

# **STRUCTURAL INTEGRITY OF FASTENERS**

**PIR M. TOOR** EDITOR

STP 1236 

**STP 1236**

# ***Structural Integrity of Fasteners***

*Pir M. Toor, editor*

ASTM Publication Code Number (PCN)  
04-012360-30



ASTM  
1916 Race Street  
Philadelphia, PA 19103

Printed in the U.S.A.

## Library of Congress Cataloging-in-Publication Data

Structural integrity of fasteners. Pir M. Toor, editor.

p. cm.—(STP; 1236)

“Papers presented at the symposium of the same name held in Miami, Florida on 18 Nov 1992 ... sponsored by ASTM Committee E-8 on Fatigue and Fracture”—CIP foreword.

“ASTM publication code number (PCN): 04-012360-30.”

Includes bibliographical references and index.

ISBN 0-8031-2017-6

1. Fasteners. 2. Structural stability. I. Toor, Pir M.

II. ASTM Committee E-8 on Fatigue and Fracture. III. Series: ASTM special technical publication; 1236.

TJ1320.S77 1995

621.8'8—dc20

95-12078

CIP

Copyright ©1995 AMERICAN SOCIETY FOR TESTING AND MATERIALS, Philadelphia, PA. All rights reserved. This material may not be reproduced or copied, in whole or in part, in any printed, mechanical, electronic, film, or other distribution and storage media, without the written consent of the publisher.

### Photocopy Rights

Authorization to photocopy items for internal or personal use, or the internal or personal use of specific clients, is granted by the AMERICAN SOCIETY FOR TESTING AND MATERIALS for users registered with the Copyright Clearance Center (CCC) Transactional Reporting Service, provided that the base fee of \$2.50 per copy, plus \$0.50 per page is paid directly to CCC, 222 Rosewood Dr., Danvers, MA 01923; Phone: (508) 750-8400; Fax: (508) 750-4744. For those organizations that have been granted a photocopy license by CCC, a separate system of payment has been arranged. The fee code for users of the Transactional Reporting Service is 0-8031-2017-6 / 95 \$2.50 + .50.

### Peer Review Policy

Each paper published in this volume was evaluated by three peer reviewers. The authors addressed all of the reviewers' comments to the satisfaction of both the technical editor(s) and the ASTM Committee on Publications.

The quality of the papers in this publication reflects not only the obvious efforts of the authors and the technical editor(s), but also the work of these peer reviewers. The ASTM Committee on Publications acknowledges with appreciation their dedication and contribution to time and effort on behalf of ASTM.

Printed in Philadelphia, PA

May 1995

# Foreword

The Symposium on Structural Integrity of Fasteners was held in Miami, Florida on 16–19 Nov. 1992. The symposium was sponsored by the American Society for Testing and Materials through Committee E08 on Fatigue and Fracture. Members of Subcommittee E08.04 on Structural Applications and specifically the Task Group on Fracture Mechanics of Fasteners selected papers for the program. Organizational assistance from Dorothy Savini and Shannon Wainwright was most helpful. Pir M. Toor of Bettis Laboratory, Reactor Technology, West Mifflin, Pennsylvania served as technical program chairman. Those who served as session chairmen were J. L. Rudd, Air Force Wright Laboratory, Dayton, Ohio; H. S. Reenszynder, Bethlehem Steel Corporation, Bethlehem, Pennsylvania; G. T. Embley, Knoll Laboratory, Schenectady, New York; Alan Liu, Rockville International, California; and R. E. Johnson, US-NRC, Washington, DC.

## A Note of Appreciation to Reviewers

The quality of the papers that appear in this publication reflects not only the obvious effort of the authors but also the unheralded, though essential, work of the reviewers. On behalf of ASTM Committee E08, I acknowledge with appreciation their dedication to high professional standards and their sacrifice of time and effort.

*Pir M. Toor*  
Technical Program Chairman

# Contents

<b>Overview</b>	ix
<b>Introduction</b>	xxv

## FATIGUE IN FASTENERS

<b>Effects of Nonuniformities in Fasteners on Localized Vibration and Fatigue—</b> DARYOUSH ALLAEI	3
Introduction	3
Role of Fasteners in Localized Vibration	5
What Is Localized Vibration	6
Mathematical Model	9
General Receptance Formulation of the Interfaces	11
Special Features of the Proposed Approach	15
Tasks in Progress	16
Conclusions and Recommendations	17
<b>Establishment of Fatigue Test Method for Turbine Blade Fastener—</b> TADAYOSHI ENDO, YOSHIYUKI KONDO, AND YOSHIKI KADOYA	20
Introduction	20
Testing Apparatus	23
Test Procedure	25
Test Results	26
Conclusion	27
<b>Review of Factors That Affect Fatigue Strength of Low-Alloy Steel</b> <b>Fasteners—</b> GEORGE W. SKOCHKO AND THOMAS P. HERRMANN	32
Nomenclature	32
Introduction	32
Summary	33
The Database	33
Evaluation of Variables that Affect Fatigue Strength	35
Mean Stress Effects in Derivation of Fatigue Failure Curves	41

Conclusions	43
Appendix	44

FAILURE EVALUATION AND CRITERIA

<b>The Regulatory Approach to Fastener Integrity in the Nuclear Industry—</b> RICHARD E. JOHNSON AND JAMES A. DAVIS	51
Introduction	51
Regulatory Aspects of Fasteners	53
ASME Requirements for Fasteners	54
Nondestructive Examination Prior to Use	55
In-Service Inspection of Fasteners	57
<b>Failure Criteria and Limiting States of Stress for Cracked Bolts/Studs—VAL</b> KAGAN	60
Introduction	60
Applications	60
Prediction of Cyclic Strength and Life (Service Time)	62
Fracture Mechanics of Threaded Joints	65
Nonlinear Effects in Threaded Joints	72
Conclusion	80
<b>The Effect of Grain Boundary Carbon on the Hydrogen-Assisted</b> <b>Intergranular Failure of Nickel-Copper Alloy K-500 Fastener Material—</b> MARJORIE ANN E. NATISHAN AND WILLIAM C. PORR, JR.	81
Introduction	81
Procedure	83
Results and Discussion	86
Conclusions	91

FRACTURE MECHANICS IN FASTENERS

<b>Stress Intensity Factors for Surface and Corner-Cracked Fastener Holes by</b> <b>the Weight Function Method—WEI ZHAO AND SATYA N. ATLURI</b>	95
Introduction	95
Three-Dimensional Weight Function Method	96
Results and Discussion	99
Concluding Remarks	106
<b>Stress Intensity Factor Approximations for Cracks Located at the Thread</b> <b>Root Region of Fasteners—RUSSELL C. CIPOLLA</b>	108
Nomenclature	108
Introduction	109
Fracture Mechanics Applications for Fasteners	110
Model Representation of Thread Root	111
Stress Analysis Applicable to Thread Region	113

Weight Function for Edge-Crack in a Cylindrical Bar	115
Calculation of Stress Intensity Factors	119
Summary and Conclusions	124
<b>Behavior of Fatigue Cracks in a Tension Bolt—ALAN F. LIU</b>	<b>126</b>
Nomenclature	126
Introduction	126
Crack Geometry Consideration	127
Selection of Independent Variables	130
Analytically Determined Stress Intensity Factors	131
Empirically Determined Stress Intensity Factors	134
Conclusion	138
<b>STRUCTURAL INTEGRITY CRITERIA FOR FASTENERS</b>	
<b>Early Stages of Fatigue Damage of Fastener Holes Monitored by Laser Speckle—FU-PEN CHIANG, MING-LIUNG DU, AND SHEN LI</b>	<b>143</b>
Introduction	143
Specimen and Experiment	144
Evaluation of Spectrum Half Width and Cross Correlation	144
Results and Discussion	146
Conclusions	151
<b>Development of Fracture Control Methodology for Threaded Fasteners in the Space Program—JULIE A. HENKENER, ATTIBELE R. SHAMALA, PAUL L. CARPER, ROYCE G. FORMAN, AND CHARLES L. SALKOWSKI</b>	<b>155</b>
Introduction	155
Fracture Control Methodology	156
Nonfracture Critical Fasteners	156
Fracture Critical Fasteners	159
Nondestructive Evaluation of Threaded Fasteners	160
Summary	163
<b>The Effect of a Tensile Load on the Ultimate Shear Capacity of a Fastener Shank—SEAN M. OLSON</b>	<b>166</b>
Introduction	166
Experimental Procedure	167
Preliminary Experiments	170
Procedure	170
Results	171
Conclusions	173
<b>Pitch Diameter Measurement of Threaded Gages Using a Coordinate Measuring Machine—RALPH VEALE, EDGAR ERBER, AND BRUCE BORCHARDT</b>	<b>175</b>
Nomenclature	175
Introduction	176

Three-Wire Pitch Diameter Method	176
Coordinate Measuring Machines (CMMs)	178
External Thread Measurement Results	180
Internal Thread Measurement Results	183
Conclusion	185

<b>Summary</b>	<b>187</b>
----------------	------------

# An Overview of Structural Integrity of Fasteners

---

## **Introduction**

Threaded members are important structural elements and influence significantly the strength and endurance of the whole structure. Further, because of high demands to structural reliability during the design and analysis of threaded members, there usually arises the tasks of achieving static strength and durability under variable internal and external loads on the stages of crack initiation and propagation.

Indeed, bolts have unique material requirements among the structural elements of an engineering component. Mechanical loads require the use of threads, and functional requirements demand low resistance to sliding motion between thread contact surfaces. Additionally, fabrication and processing operations can introduce unfavorable material properties, residual stresses, and undetected flaws. Also, actual service conditions can be quite different from those postulated for normal design consideration. Hence, bolts used in any system must have certain mechanical properties that are stipulated by specifications.

In spite of the fact that design procedures specify minimum yield strength levels, minimum tensile properties, and resistance to stress corrosion cracking, there are documented cases of stud cracking. Indeed, fracture evaluation of defects (cracks) occurring in the threaded portions of studs and bolts is a recurring problem in structures. Currently there is no explicit procedure for fracture analysis of bolting applications. Fracture analyses have been conducted according to specific industry need. Due to the complex stress state at the root of a thread, the procedure is complicated and time consuming. Hence, a more realistic and uniform fracture procedure for analysis of threaded members is needed.

The principal parameters required for fracture mechanics analysis are:

1. Stress state in the region of interest.
2. Initial flaw shape that may exist.
3. Initial flaw size that may exist.
4. Fracture toughness for the bolt material.
5. Crack growth rate data for the material.
6. Design factor.

The above parameters are discussed in detail in the sections that follow.

## **Fracture Phenomenon**

### *Brittle Fracture*

Brittle fracture generally occurs without prior plastic deformation. The fracture surface associated with this type of failure is flat (cleavage) with no shear lips. This type of failure typically occurs very quickly.

Usually, brittle fracture occurs in a component that has an existing crack in a tensile stress field. Fracture toughness is the material property that measures the fracture resistance of a given material and is affected by temperature.

Small initial flaws become large under cyclic loading (a fatigue process) and reach a critical size, eventually resulting in brittle fracture. In the case of fasteners, the most likely place to initiate brittle fracture are the regions of high stress concentration or stress gradient. These locations are thread root radius, thread to shank fillet, and head to shank fillet.

### *Ductile Fracture*

Ductile fracture is generally accompanied by large amounts of plastic deformation. The transition from brittle fracture to ductile fracture generally occurs with changes in service conditions, for example, the state of stress, temperature, and the strain rate.

Ductile fracture can result in either complete separation of the component into two or more fragments or in simply a reduction in functional or load-carrying capability of the component due to gross yielding. Brittle and ductile fracture morphologies are generally distinct in that the former is frequently cleavage and flat and the latter is dimple rupture accompanied by included (“slant”) fracture surfaces adjacent to the component surface. These inclined surfaces are sometimes referred to as “shear lips.” This type of fracture involves both crack initiation and crack propagation.

This type of fracture becomes complex when the component contains notches or grooves. The triaxial state of stress at these locations restricts the plastic flow in the components at these discontinuities. Hence the resulting fractured surfaces would show similar shear lips and will look more like a fibrous or cleavage-type surface. Such fractures tend to appear more like a brittle fracture.

The most likely location for ductile failure is the minimum sectional area. This is the region where gross yielding of the region can occur. In the case of a fastener, it is not likely that ductile failure will occur at the thread root because here the plastic flow will be restricted as mentioned in the previous paragraph.

### *Corrosion Fatigue*

Most structural components are subjected to fluctuating load and invariably operate in various environments. This type of behavior of metals in various environments is of primary importance. Corrosion fatigue behavior of a given environment-material system refers to the characteristics of the material under fluctuating loads in the presence of a particular environment.

### *Load Relaxation*

This is a time-dependent phenomenon causing a decrease in stress in a component that is held to a certain fixed deformation. The load relaxation is a creep-related process characterized by the change of elastic strain to plastic strain resulting in stress reduction. In the case of threaded members (bolts, studs), preload will be reduced gradually with time. This process is a function of the temperature involved and the initial load.

In order to avoid joint failure, it is necessary to account for loss of preload due to stress relaxation in the initial design.

Stress relaxation can occur if the following conditions exist:

1. Material that is susceptible to stress relaxation.
2. High service temperature during operation.
3. Component having irradiation exposure.

Loss of preload can be minimized or eliminated by taking proper account of these factors into design.

## **Parameters Influencing Fracture**

### *Introduction*

There are many parameters that influence the fracture behavior of bolts. For low and intermediate strength steels, temperature-induced changes in metal grain ductility are known to introduce fracture state transition. Fracture-state transition temperature for most steels covers a wide range. Therefore, material characterization from a linear elastic fracture mechanics point of view is necessary. An appropriate material must be selected to meet structural requirements at the specified lowest service temperature for the section size of interest.

The role of environment has received a great deal of attention in most engineering designs. If environment effects are significant, then environment becomes an important reference for material characterization and analysis in the brittle fracture criterion. In addition to temperature and environment influence, the influence of loading condition is also an important factor in a design to resist fracture.

Indeed, a detailed study of fracture state, service temperature and environment effect, and loading condition and strength levels must be performed to evolve a fracture-resistant design.

### *Material Characterization*

All engineering materials contain imperfections. Subsequent manufacturing and processing operations may produce additional cracks, inclusions, and other deficiencies. Such flaws can range in size from the microscopic to the very large. Surprisingly, large cracks often do not represent as serious a threat to structural integrity because they are more easily detected. Undetected smaller cracks, however, can grow to critical size as a result of service loading and environmental conditions. In ductile materials, once a crack has grown to critical size, it can result in catastrophic failure of the component.

In view of the above phenomena, ductile materials should be used for fabrication of critical parts. Although these materials have a greater tolerance for flaws, they also have a lower strength. Ductile materials, therefore, offer an alternative for the problem of material fracture, but this advantage is paid for by heavier, bulkier, and less efficient designs.

Most often, materials used in design are such that when service conditions are considered, they typically fail in a brittle manner. Under these conditions, stresses very near a flaw exceed the strength of the material even though the average design stresses in a part are very low. Therefore, the safe design of a component demands thorough understanding of the behavior of a material in the presence of flaws. In other words, the integrity of the material must be assessed for its intended use.

The plain-strain fracture toughness,  $K_{Ic}$ , quantitatively relates the critical crack size to applied load and geometry of a component. This material property is used to estimate minimum component loads, to compare candidate materials, and to assist in new alloy development. Therefore, the material's integrity must be established for its intended use.

### *Temperature Effect*

Temperature is another important parameter that can cause brittle fracture. Ferritic steels and some titanium alloys have a temperature below which they become brittle. Materials that are ductile at room temperature become brittle at temperatures below the ductile brittle temperature transition range. In this low temperature range, these materials have very low energy absorption capability.

In addition, heat treatment and cold working of materials are processes used to increase a material's ductile strength properties, but such processes can also result in a drastic drop in fracture toughness.

Therefore, comprehensive investigation must be made to understand the influence of the temperature range at which the component will operate. The true limiting factor in the temperature application is the estimate of the lowest service temperature.

### *Environment*

Many materials experience accelerated crack initiation and propagation under the joint action of a corrosive environment. For certain materials, the presence of corrosive environment can greatly reduce fracture toughness. In the presence of a corrosive environment, the metal surface affected fails to develop a protective oxide or corrosive oxide film and hence corrosion pits are formed.

Corrosion control often starts with material selection. To establish material performance that can be expected in service, it is necessary to compare candidate materials with other materials for which long-term service experience is available. This is generally achieved by accelerated laboratory tests as these tests generally represent an extreme condition. Generally, crack propagation tests of precracked fracture mechanics specimens in aggressive environments are used. These types of tests give information to obtain: (1) a limiting stress intensity factor,  $K_{ISCC}$ , below which crack initiation and growth will not occur, and (2) the rate of environmental crack growth at higher stress intensity factor values.

The information obtained from these environmental tests is then used to select a material suitable for the intended service application. Also, limitations are determined on stress, temperature, and other parameters affecting the fracture strength of the material.

### *Loading Condition*

*Tensile Loads*—If the bolt is perfectly symmetrical, the faces of the head and nut are exactly perpendicular to the axis of the threads, joint surfaces are flat and parallel, and loading the bolt by a hydraulic tensioner will produce a pure tension condition. Finite element analysis of bolts has shown that the tensile stress is zero at the free end of the bolt and that it rises uniformly through the head to the stress level found in the body. A similar pattern is observed in the threaded end, but the average stress in the threaded section is higher than the average stress in the body because the cross-sectional area is less in the threads. However, in real structure, consideration should be given to the effects of misalignments and non-perpendicularities, methods of applying preload, and variation in the coefficient of friction. For most practical applications, there is no uniform stress level, even in the body. This has a variety of implications when we are computing such things as stress levels, preloads, spring constants, etc.

In general, there is a concentration of the load at the first engage thread. The first three engaged threads carry most of the load in any case. This means that most of the nut is not

doing its share of the work. This situation can be improved by tapering the threads or altering the pitch on either nut or bolt to have more uniformity in load distribution. The most popular way is to use a nut that is partially in tension.

A bolt is always put into service tension when it is properly tightened. Subsequent external loads usually do not modify this basic tension load very much if the joint is properly designed. However, it is important to estimate the magnitude of other types of loads that can be imposed on a bolt in use. These are considered in the following sections.

*Bending*—Because joint and nut surfaces are never exactly perpendicular to the thread axis, a bolt almost never stretches uniformly when it is tightened; instead, it bends to some degree. Thermal loading conditions produce stresses in fasteners when there is either a thermal gradient through the different components clamped in the joint or there are materials with different coefficients of thermal expansion subjected to a uniform temperature condition.

Thermal differential between the fastener and the clamped components will produce tensile stress in the fastener. This stress is in addition to the initial assembly preload tensile stress. In addition, if there are non-perpendicularities and non-parallelisms between the various parts, bending stresses will be produced. The bending condition takes the form of a transverse stress gradient that is additive to the bolt tensile stress for elastic behavior. For this type of thermal bending condition to exist it is necessary that the head not rotate to relieve the bending movement. The bending stresses vary linearly across the bolt diameter and achieve their highest magnitudes at the surfaces. Lateral deflections and end rotations also cause bending stresses in bolts.

*Torsional Shear Stress*—When fasteners are preloaded by torque, a torsional shear stress is induced throughout the various cross sections of the fastener. The value of the torsional shear stress varies with respect to the radial distance from the center line of the fastener. It is a function of the frictional constraints between the threads of the nut and the threads of the bolt, as well as between the clamping surfaces of bolt heads and nuts and their respective contact surfaces. An average value of the shear stress due to preloading by torquing is normally used for stress calculations.

### *Cyclic Loading*

Generally, threaded members do not experience direct cyclic loading. However, pressure and thermal loading, which are cyclic in nature, can introduce cyclic load conditions through the joint components. Due to both linear motions and rotation in the joints, loads are of tension and bending type. Cyclic loads can cause fastener failure by crack propagation of an initial flaw that may be present in the material as well as initiation and subsequent propagation of a crack from an initially unflawed region of material.

### *Combined Loading*

In the preceding sections, the causes and effects of individual loading conditions (tensile, bending, and torsion) were discussed. However, in real situations, these loads interact and have a combined effect on the integrity of the component. Therefore, any realistic analysis must account for all the loads acting on a component in a combined manner. Tensile, bending, and torsional loads acting on a circular cyclic containing an external circumferential notch are shown in Fig. 2.

*Stress Relaxation*

Stress relaxation is a time-dependent phenomenon in which stress decreases in a structural component that is restrained to a fixed deformation. It is a creep-related phenomenon in which elastic strain changes to plastic strain, resulting in stress reduction.

The stress relaxation process is a function of initial stress level and applied temperature. For worst case combination of temperature, stress level, and material, preload can be reduced significantly in threaded joints. For brittle fracture evaluation, it is necessary to account for loss of preload due to stress relaxation.

**Types of Flaws**

*Introduction*

In order to apply fracture mechanics, it is assumed that a crack or flaw exists in the structure in a threaded member; the most likely location at which the crack will initiate is the highly stressed region of thread root. It is generally recognized that the first engaged thread in a bolt/stud is usually the location of the highest stress. Fracture analysis procedure also requires definition of the shape and size of the assumed crack or flaw. The initial size of the flaw is usually controlled by the inspection capability, and the shape is governed by structural configuration and state of stress. Realistically, the shape of a flaw is established from either laboratory specimens or in-service failure observations and the size is established from the nondestructive examination (NDE) capabilities. However, from the design verification point of view, simplicity of basic assumptions are important considerations. At the root of a thread, the flaw shape is usually assumed as either a circumferential flaw or a part-through edge crack as shown in the following sections.

The initial size and shape of a flaw in the evaluation of structural integrity plays an important role. The stress intensity factor solutions are different for various types of crack configurations, and under similar stress fields structures can have different strengths. Therefore, it is important that before developing a brittle fracture procedure, the size and shape of the flaw used in the analysis be established. In this paper four types of flaw configurations will be discussed. A bolt under tensile load is shown in Fig. 1. The stress intensity solutions in the literature are calculated assuming a single groove in a cylindrical bar under complex load conditions as shown in Fig. 2.

*Semi-Circular Surface Defect Model*

The geometry for this defect shape is given in Fig. 3. The stress intensity factor solution is obtained by line-averaging the axial stress component over the crack depth. The stress intensity factor solution for this case is given below.

$$K_I = 1.22 \bar{\sigma} \frac{\sqrt{\pi a}}{\phi} \tag{1}$$

where

- $K_I$  = the stress intensity factor,
- $\bar{\sigma}$  = the average stress over defect,
- $a$  = the initial flaw size, and
- $\phi$  = the complete elliptic integral of the second kind;  
 $\phi$  is  $\pi/2$  for a semi-circular flaw.

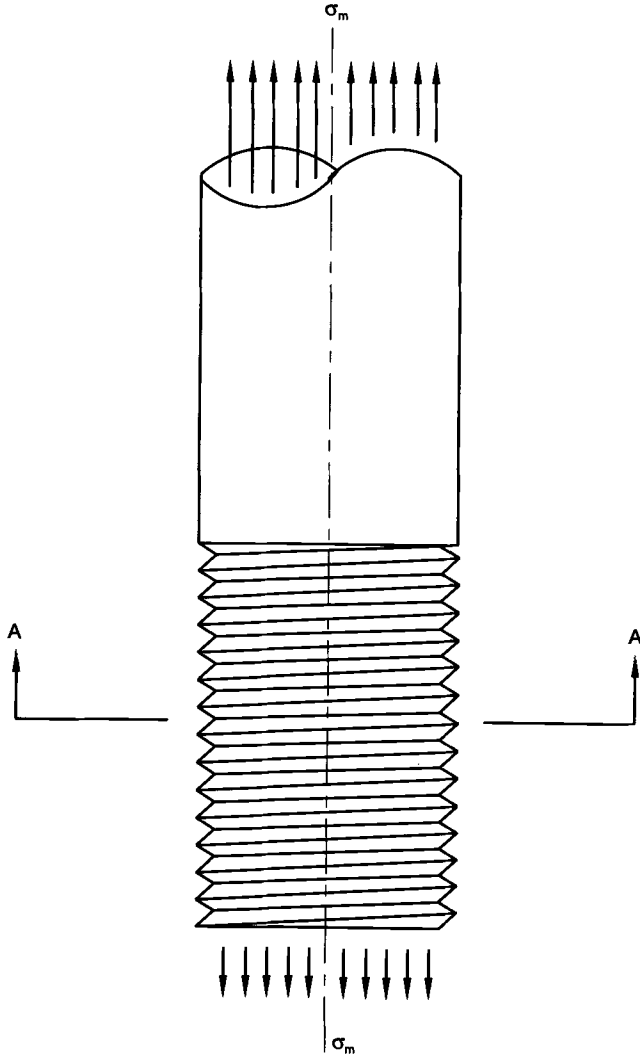


FIG. 1—Bolt under tension load.

*Single Edge Notch Model*

This model is illustrated in Fig. 4. Assessment of cracked solid cylinder was carried out by Johnson [1], and an edge crack model was developed. This model is also used by PVRC AD Hoc Group on Toughness Requirement. The stress intensity solution for this model is given as

$$K_I = \sigma \sqrt{\pi a} F(a/D_m) \tag{2}$$

where

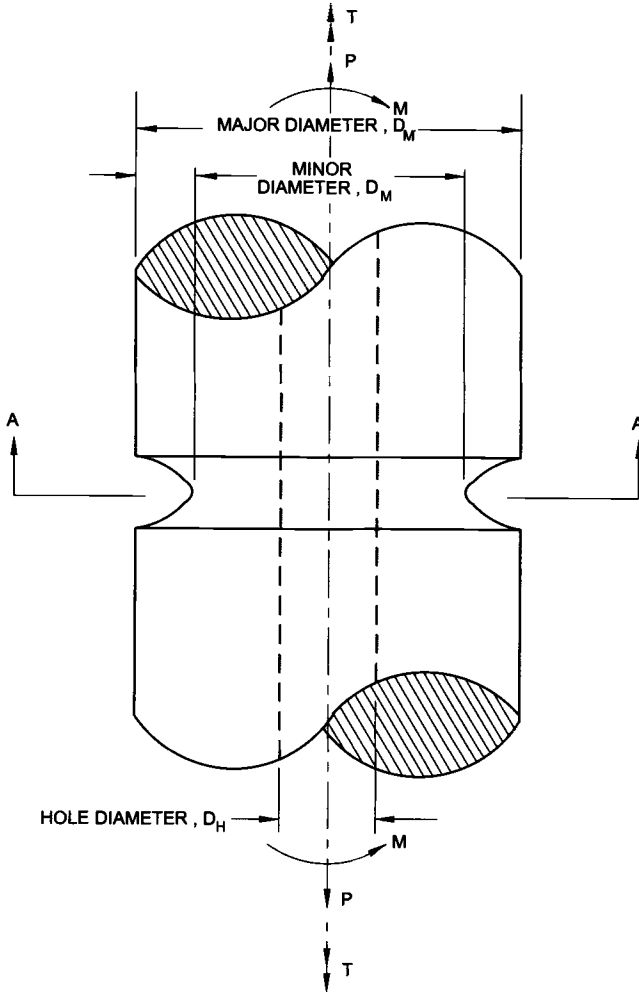


FIG. 2—Circular cylinder containing external circumferential notch under combined loading.

$$F(a/D_m) = 1.12 - 0.231 (a/D_m) + 10.55 (a/D_m)^2 - 21.72 (a/D_m)^3 + 30.39 (a/D_m)^4, \text{ and } \sigma = \text{gross stress.}$$

For application in the thread region:

- $a = a_i + a_n,$
- $a_i = \text{initial flaw size,}$
- $a_n = \text{thread depth, and}$
- $D_m = \text{major diameter of the threaded region.}$

*Circumferential Crack Model*

This model is shown in Fig. 5. Harris [2] has given a solution for stress intensity factor for this type of model as

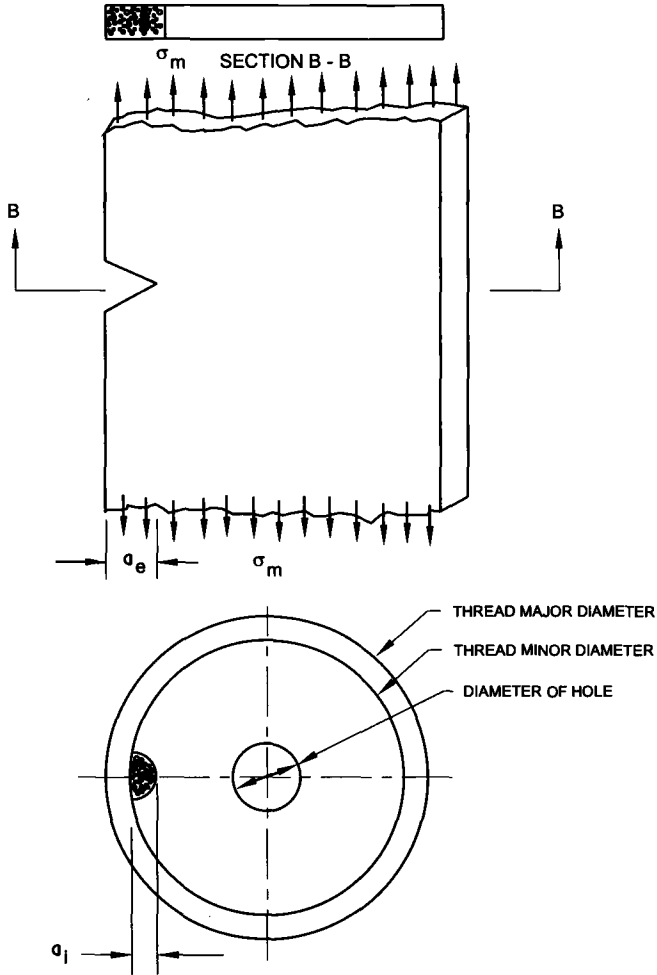


FIG. 3—Single-edge cracked plate in tension representing an asymmetric crack configuration in a circular cylinder.

$$K_1 = \sigma_m M_m \sqrt{\pi a} \tag{3}$$

where

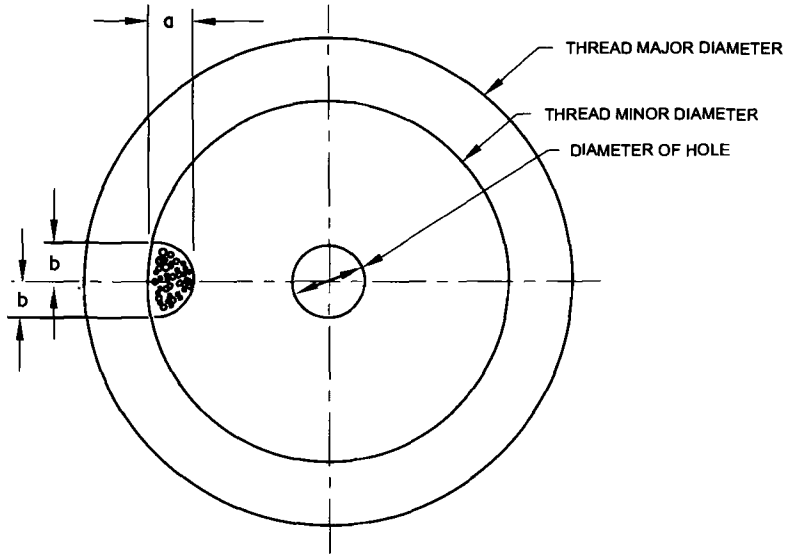
$\sigma_m$  = gross membrane stress,

$$\sigma_m = \frac{4P}{\pi(D_m^2 - D_h^2)}$$

$M_m$  = geometric correction factor.

$$M_m = \frac{1 - (D_h/D_m)^2}{[(1 - 2a/D_m)^2 - (D_h/D_m)^2] \left[ 0.8 + \frac{2a/D_m}{1 - 2a/D_m} \left( 4 + \frac{1.1 D_h/D_m}{1 - D_h/D_m - 2a/D_m} \right) \right]^{1/2}} \tag{4}$$

where



SECTION A - A ON FIGURE 2  
 FIG. 4—Semi-circular crack configuration.

- $a$  = total crack length initial crack length plus thread depth,
- $D_m$  = major diameter,
- $D_h$  = diameter of the hole, and
- $P$  = tensile load.

This model is more valid and versatile as it accounts for the presence of a central hole.

The above solution is applicable only to the membrane case. A suggested limit of applicability of this solution is  $D_h/D_m \leq 0.5$ .

*Sickle Shape Model*

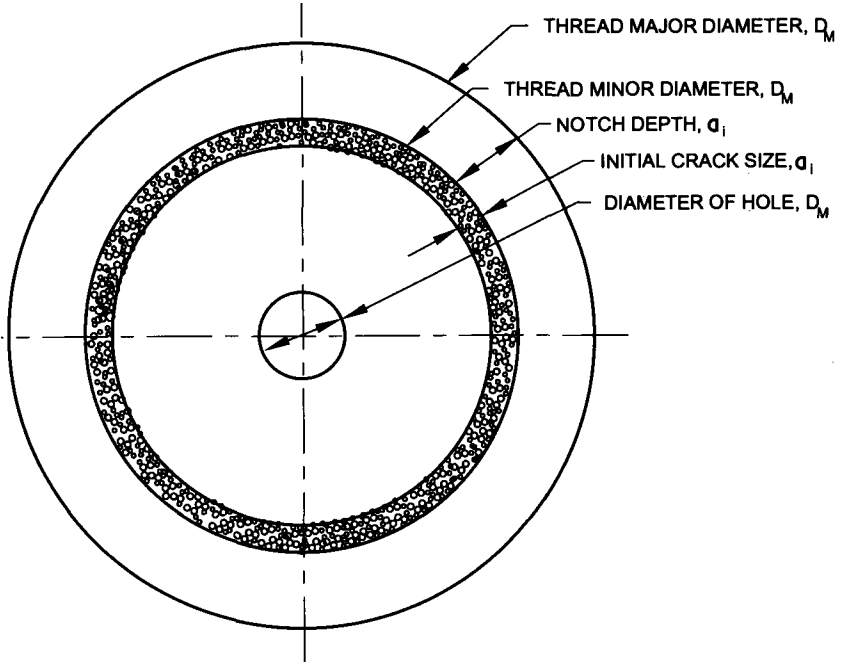
In notched cylinders, a sickle-shaped crack often develops that may cover the whole circumference of the bolt (Fig. 6). Mattheck et al. [3] have developed a solution for the stress intensity factor for this type of model at the deepest point, A, as

$$K = \int_0^a b(x, a) \sigma(x) dx \tag{5}$$

where  $b(x, a)$  is the weight function that is obtained from the stress intensity factor,  $K_r(a)$ , and the corresponding crack opening displacement,  $u_r(x, a)$ , for a reference load case

$$b(x, a) = \frac{H}{K_r(a)} \cdot \frac{\partial u_r(x, a)}{\partial a} \tag{6}$$

where



SECTION A - A OF FIGURE 2

FIG. 5—Circumferential crack configuration.

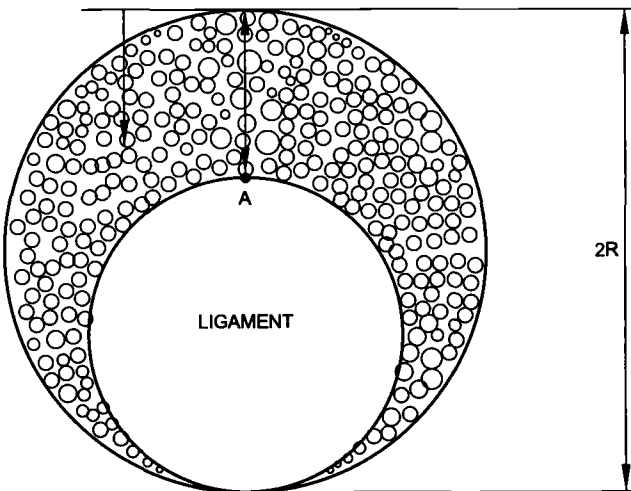


FIG. 6—Sickle-shaped crack fully surrounding the cylinder circumference.

$$H = \left( \frac{E}{1 - \nu^2} \right) \text{ for plane strain, and}$$

$$H = E \text{ for plane stress.}$$

$$K_r = \sigma_0 \sqrt{\pi a} F_r(a/R) \quad (7)$$

where  $\sigma_0$  is the tensile stress.

and

$$F_r(a/R) = 1.1215 + 0.1644 (a/R) + 5.1396 (a/R)^2$$

$$- 15.932 (a/R)^3 + 24.746 (a/R)^4 - 10.986 (a/R)^5 \quad (8)$$

The crack opening displacement  $U_r(x, a)$  as a function of  $x$  and  $a$  is calculated assuming the following relationship.

$$u(x, a) = u_{\max}(a) = (1 - x/z)^{1/2} \quad (9)$$

$u_{\max}$  is calculated by 3-D finite element analysis at  $x = 0$  under a tensile stress, and the normalized displacement expression is given as

$$\frac{u_{\max} E}{(1 - \nu^2) \sigma_0 R} = \sum_{i=1}^4 C_i (a/R)^i \quad (10)$$

with  $C_1 = 0.1965$ ,  $C_2 = 22.515$ ,  $C_3 = -44.317$ , and  $C_4 = 39.088$ .

From the above equations,  $K_r$  is obtained as

$$K_r = \sigma_0 \sqrt{\pi a} F_r(a/R) \quad (11)$$

where  $F(r)$  is given

$$F(r) = 1.1215 + 0.1644 (a/R) + 5.1396 (a/R)^2 - 15.932 (a/R)^3$$

$$+ 24.746 (a/R)^4 - 10.986 (a/R)^5 \quad (12)$$

The weight functions for the special cases of linear stress distribution  $\sigma_0(1 - x/a)$  and quadratic stress distribution  $\sigma_0(1 - x/a)^2$  are given as

$$F_{\text{lin}}(a) = 0.4446 + 1.1086 (a/R) - 3.4582 (a/R)^2$$

$$+ 5.396 (a/R)^3 + 0.2057 (a/R)^4 - 1.4844 (a/R)^5 \quad (13)$$

$$F_{\text{qua}} = 0.6048 + 1.2542 (a/R) - 3.4095 (a/R)^2 + 4.6189 (a/R)^3$$

$$+ 2.4984 (a/R)^4 - 2.6806 (a/R)^5 \quad (14)$$

These equations are valid and applicable for  $0 \leq a/R \leq 1$ . The superposition method can be used to determine the stress intensity factors.

### *Empirical Approach to Stress Intensity Factors*

An empirical approach to determine the stress intensity factor has been proposed by James and Mills [4]. They developed a function based on the analytical and experimental data for straight front crack, semi-circular crack front, and threads for tension and bending load conditions. They agreed that there are regimes of  $a/D$  where each of the solutions is applicable. The stress intensity factor subjected to tension is given as:

$$K = \sigma(\pi a)^{1/2} F(a/D) \quad (15)$$

where

$$F(a/D) = A_2^B(a/D) + C + D(a/D) + E(a/D)^2 + F(a/D)^3 + G(a/D)^4 \quad (16)$$

where

$$A = 2.043, B = 31.332, C = 0.6507, D = 0.5367, E = 3.0469, F = -19.504, G = 45.647$$

The authors claim the above equation is reasonably accurate for  $a/D > 0.004$ . A similar solution is proposed for loads subjected to bending. An additional discussion on this approach is given by A. F. Liu and R. C. Cipolla in this volume (STP 1236).

### *Loading Rate Effect*

In general, fracture toughness of structural materials, particularly steels, decreases with loading rate. For a given temperature, the fracture toughness measured in an impact test,  $K_{Ia}$ , generally is lower than the fracture toughness measured in a static test,  $K_{Ic}$ . In other words, it shows that at a constant temperature, fracture toughness tests conducted at higher loading rates generally result in lower toughness values.

The loading rate effect is significant for materials that exhibit strain rate effects, such as structural steels having yield strengths less than about 140 ksi. The loading rate at a given temperature can affect the notch toughness significantly for such materials. Ideally, the fracture toughness values should be determined at loading rates that are experienced by the actual structure. Variation of loading rate throughout the structure will affect the allowable stress through its dependence on plane strain fracture toughness,  $K_{Ic}$ .

Thus, the actual service loading rate will have a significant influence on any fracture criterion specified, either static or dynamic.

### **Crack Growth Equation**

The use of the concept of fracture mechanics in the design and analysis of structures assumes the existence of initial flaws or cracks. These cracks under repeated service loading conditions propagate and become unstable (fast-fracture) when a critical crack length is reached. The rate of crack propagation depends on many factors, such as: (1) material, (2) environment, (3) service load history, (4) crack geometry, (5) local structural configuration. It is known from Ref 5 that for a particular material the crack growth rate,  $da/dN$ , can be described as a function of the stress intensity factor range,  $\Delta K$ . At present there is a large number of crack growth equations. The Forman crack growth equation, Ref 6, as described below is widely used in the industry.

$$da/dN = \frac{c(\Delta K)^n}{(1 - R)K_c - \Delta K} \quad (17)$$

where  $da/dN$  is the rate of crack growth,  $c$  and  $n$  are material constants,  $\Delta K$  is the stress intensity factor range,  $R$  is the stress ratio defined as minimum stress divided by maximum stress, and  $K_c$  is the critical stress intensity factor.

The stress intensity factor range  $\Delta K$  is defined as

$$\Delta K = \Delta\sigma \sqrt{\pi a} \cdot F(a/D) \quad (18)$$

where  $\Delta\sigma$  is the stress range,  $a$  is the half crack length, and  $F(a/D)$  is the product of various geometric and boundary condition correction factors.

The values of  $c$  and  $n$  (material constants) are calculated from constant amplitude test data by the following technique derived from the Forman equation.

$$\log[(1 - R)K_c - \Delta K] + \log(da/dN) = \log c + n \log \Delta K \quad (19)$$

For any two points, which represent a segment of the crack growth rate curve, two simultaneous equations are solved for  $c$  and  $n$ .

### Design Safety Factor

A safety factor is required in a brittle fracture analysis procedure to account for possible variability due to unknowns and inaccuracies at various stages. A decision has to be made not only on the magnitude of the safety factor but also on how and when it should be applied. There are various possibilities that exist and that should be considered before a final decision is made. These possibilities are:

1. Safety factors on fatigue stresses.
2. Safety factors on basic data.
3. Safety factor on initial crack size.
4. Safety factor on final life (cycles).
5. Safety factor on failure load.

### Acknowledgment

The work reported in this paper was done over a number of years by the author as the chairman of ASTM Task Group E08.04.07 on Fracture Mechanics of Fasteners. I would like to thank the task group members for their many lively discussions on the structural integrity of fasteners. The author also wants to thank Westinghouse-Bettis Laboratory for its continuous support, which has made it possible for the author to participate in ASTM committee activities. The views expressed are entirely those of the author and do not reflect the views of the ASTM or the Westinghouse-Bettis Laboratory.

### References

- [1] Johnson, R. N., "Fracture of Cracked Solid Circular Cylinder," Ph.D. thesis, University of Wisconsin, 1972.
- [2] Harris, D. O., "Stress Intensity Factors for Hollow Circumferentially Notched Round Bars," *Transactions of ASME, Journal of Basic Engineering*, March 1967, pp. 49-54.

- [3] Mattheck, C., Morawietz, P., and Munz, D., "Stress Intensity Factors of Sickle Shaped Cracks in Cylindrical Bars," *International Journal of Fracture*, No. 1, 1985, pp. 45–47.
- [4] James, L. A. and Mills, W. J., "Review and Synthesis of Stress Intensity Factor Solutions Applicable to Cracks in Bolts," *Engineering Fracture Mechanics*, Vol. 30, 1988, pp. 641–654.
- [5] Paris, P. and Erdogan, F., "A Critical Analysis of Crack Propagation Laws," *Journal of Basic Engineering*, December 1963, pp. 528–534.
- [6] Forman, R. G., Kearney, V. E., and Engle, R. M., "Numerical Analysis of Crack Propagation in Cyclic-Loaded Structures," *Journal of Basic Engineering*, September 1967, pp. 459–464.

# Introduction

---

In 1986, ASTM Committee E24 concluded that there was enough interest to establish a Task Group (E24.06.04) under Subcommittee E24.06, the Application of Fracture Mechanics. The scope included providing analysis procedure, test methods, and criteria for structural integrity evaluation of fasteners. Two study groups were created under this task group, one engaged in assimilating references on fatigue and fracture mechanics application and the second to compile stress intensity factors applicable to fasteners. (In 1993, E24 merged with Committee E09 to form Committee E08 on Fatigue and Fracture.)

The symposium on Structural Integrity of Fasteners, held in Miami, Florida, on 18 Nov. 1992, was conceived a year previously at the ASTM Committee Week in Dallas, Texas. At this meeting, a workshop on fatigue and fracture of fasteners was held. Participants showed an interest in a one-day symposium on structural integrity of fasteners.

The quest for more efficient structures has prompted the development of improved materials, stress analysis, and fabrication and inspection techniques. Higher allowable stress usually results from the use of these improved techniques. Higher stresses are generally acceptable from the standpoint of static stresses; however, when these stresses are cyclic in nature, crack initiation may occur. Generally speaking, for fasteners, testing is used to predict crack initiation.

In order to review the latest developments in dealing with fatigue and fracture behavior of fasteners, the Miami symposium was held. The symposium was specifically concerned with fatigue (crack initiation), fracture (of crack growth) failure, and evaluation and criteria for structural integrity of fasteners. The symposium consisted of four sessions. This volume, which resulted from the symposium, contains the text of the papers presented plus the text of other submitted papers.

Many people contributed time and energy to make the symposium a success. Special thanks are due to: (a) *the speakers*, for the time and effort spent in preparing their presentation and final manuscripts; (b) *the session chairmen*, for their effort in keeping the sessions moving in a timely manner; and (c) *the reviewers*, for their careful editing of the manuscripts.

The papers in this volume are state-of-the-art on fatigue and fracture mechanics for fasteners. These papers are useful for engineers, scientists, and researchers whose interests lie in the structural integrity of fasteners.

*Pir M. Toor*

Editor

# **Fatigue in Fasteners**

# Effects of Nonuniformities in Fasteners on Localized Vibration and Fatigue

---

**REFERENCE:** Allaei, D., "Effects of Nonuniformities in Fasteners on Localized Vibration and Fatigue," *Structural Integrity of Fasteners, ASTM STP 1236*, P. M. Toor, Ed., American Society for Testing and Materials, Philadelphia, 1995, pp. 3–19.

**ABSTRACT:** The purpose of this paper is to report on an ongoing project that combines recent developments in the fields of vibrations and modeling to increase the service-free life and the quality of performance and reliability of fasteners and to reduce unnecessary maintenance and failure in aircraft structures. In this project, the feasibility of developing an efficient and effective mathematical model capable of incorporating the dynamic characteristics of fasteners, their interfaces with the host structure, and the host structure itself is being investigated. Such a combination will result in a significant gain in computational speed and an improvement in the accuracy of the numerical results, producing a better prediction. The model will be adaptive based on the closed-loop dynamic relation between fasteners and the host structure. The main contribution of this work is to include the effect of fasteners on vibration phenomena such as loci veering and mode localization and the application of the receptance method, which makes the model compatible with existing computer models, to the dynamics of fasteners.

**KEYWORDS:** fasteners/joints, mode localization, structures, receptances, vibrations, fatigue

Increased application of light-weight and thin plates/shells in structures and the demand for higher speeds, better quality, and more precise structural response have made engineers and researchers develop more accurate prediction models. Lack of effective dynamic models of combined fastener-structure systems are among the shortcomings of the present computer models used for vibration analysis.

Fasteners (such as adhesives, bolts and nuts, and welded joints) are an integrated and very crucial part that holds together the structural elements of machinery and space, air, ground, and marine vehicles. Since all machinery and vehicles are subjected to continuous vibration during operation, fasteners tend to wear out and loosen much faster than usually expected. Fastener failure can result in reduction (or loss) of performance, unexpected destruction of systems (such as machinery and vehicles), and devastating and costly consequences. In particular, this problem is more severe in high-speed vehicles with light-skin structures such as aircraft. The purpose of this work is to develop an effective mathematical model that can be used to gain a better understanding of the dynamics of fasteners and thus to better predict their useful life cycle and to increase their service-free life, their quality of performance, and their reliability, thereby reducing unnecessary maintenance and the risk of structure failure.

It appears that, as the need for faster maneuvering aircraft has increased, fastener wear and dynamics have received more attention in recent years. Even though this problem has

---

<sup>1</sup> Senior scientist, ORDC, Inc., Box 562, Excelsior, MN 55331-0562. Also, program manager, Sound and Vibration Engineering Technology Program, Hutchinson Technical College, Two Century Ave., Hutchinson, MN 55350.

probably been studied as early as the development of the first airplane, this discussion is focused on recent advances in the subject (1980 to the present).

Investigation of hole preparation and fastener installation effects on graphite/epoxy laminates was reported by Condon [1] in 1980. Of interest were the effect of various hole irregularities on the static and fatigue strength of the laminate and the influence of the room temperature (65 to 250°F) (18 to 121°C), moisture (dry and wet) in specimens, and type of fasteners. His test results showed that interply delaminations caused a significant strength reduction and that blind bolts and solid rivets caused installation damage. No damage was reported when blind rivets, threaded rivet pins, and pull-type lock bolts were installed. It should be noted that most of his analysis was based on extensive testing but very little analytical work. The loosening effect of fasteners was not addressed.

In Refs 2 and 3, several fastener parameters were investigated while developing a durability test method. The goal was to use fractographic data to quantify the initial fatigue distribution or equivalent initial flaw-size cumulative distribution for clearance-fit fastener holes. Their variables were material, spectrum level, fastener diameter and fit, percent bolt load transfer, and geometry. The authors used either an F-16 or a B-1 bomber in their experimental work. In Refs 4 and 5, the results of a comprehensive series of flight-by-flight fatigue tests on Mirage III0 wing main spar were reported. The authors indicated that the most promising option was the use of interference-fit steel bushes in holes. An investigation of add-on damping treatment to F-15 upper-outer wing skin was reported [6] in 1991. The authors of the paper concluded that damage accumulates due to the resonant vibration of local stiffener modes. Furthermore, cracks initiate at the fastener holes adjacent to the "T" stiffeners, and they propagate parallel to the stiffeners. According to Defense Technical Information Center (DTIC) reports, there is ongoing research [7,8] that could be related to the subject, but only brief summaries were available. None of the above work has mentioned the occurrence of the mode localization and its applications in structure-fastener systems. Their method of analysis was not based on the receptance method as described in this paper. Furthermore, the effects of fastener nonuniformities on the dynamic response of the combined structure-fastener systems have not previously been reported in the open literature.

Structures do not respond in the predicted manner nor do they function properly unless their parts have the correct size and shape relative to one another and they are connected (and remain connected) according to system specifications. However, it is not possible to make a part of any exact size or shape, nor it is possible to maintain perfect contact between parts throughout the operating life of structures. In the case of structural components, due to unavoidable manufacturing processes, even if a number of parts are made with the same process, their dimensions will vary. Such variations are known as *tolerances*. In the case of fasteners, even if their amount of variation due to manufacturing can be reduced and assumed negligible, their dynamic response variations are usually significant because they are subjected to a wide range of different magnitudes and types of vibration. It has been shown [10,16,17,21,23,28,34,38,39] that such parameter variations could result in drastic changes in the dynamic response of structures and thus in rapid failures. Therefore, the analyst and the designer must carefully plan the amount of variation that is acceptable in the system to gain the best possible balance between cost, function, and failure.

The objective of this project is to investigate the feasibility of developing an efficient and effective mathematical model capable of incorporating the dynamic characteristics of fasteners, their interfaces with the host structure, and the host structure itself. Such a combination will result in a significant gain in computational speed and improvement in accuracy of the numerical results, producing a better prediction. The model will be adaptive based on the closed-loop dynamic relation between fasteners and the host structure. Parameters more cru-

cial in the vibration response of fasteners and the host structure will be identified and incorporated in the model.

The main contributions of this work are the inclusion of the effect of fasteners on vibration phenomena such as loci veering/crossing and mode localization/transition and the application of the receptance method to the dynamics of fasteners. These vibration phenomena have been shown to have a significant effect on the performance of mechanical components and structures as described in the next section.

### **Role of Fasteners in Localized Vibration**

Tolerances and parameter variations cannot be reduced to zero and therefore must not be avoided in the design, analysis, and control of mechanical components and structures. A small increase in the dimensions of parts, their tolerances, and their parameter variations can result in significant accumulations of randomness that could propagate through out the system. In the case of fasteners, not only are their initial parameter variations (such as their location, type, and applied load) unavoidable, but also some of these variations are functions of time if the fasteners are placed in a vibrating environment. Costly failure and down-time can result if the fastener parameters are within their specifications but they have values that cause drastic changes in the dynamic response of the entire assembly.

Recent published papers regarding frequency curve veering/crossing and mode localization/transition [9–40] have raised many fundamental questions. The authors have shown that design tolerances and parameter variations in structures may result in drastic changes in vibration characteristics of structures and may be the cause for an unpredicted failure of the system. Why these phenomena occur in vibrating systems and how they can be implemented in the design process and active control of structures are among the issues that researchers have begun to address. It is very important that a full understanding of these phenomena (i.e., loci veering/crossing and mode transition/localization) is gained so that their full potential for various engineering applications can be explored. In this project, an effort is being made to address the above issues in fastener-structure systems. In particular, for the first time, the application of these phenomena to fasteners is being investigated.

This astonishing dynamic behavior has been reported in many engineering problems. Examples of such problems are free vibrations and buckling of beams, plates and shells, turbine blades and compressor rotors, electromagnetic waves in waveguides, fluid flow in nonrigid conductors, potential curves and surface for molecules, rings and tires, and large space structures. Because of the widespread application and importance of the phenomena, the author believes that the presence and severity of these rapid and violent changes in the vibration characteristics of structures need to be examined in fastener-structure systems.

Irregularity in periodic and symmetric structures has also been reported as the cause of frequency curve crossing and veering and mode localization and transition. Examples of such cases are asymmetric rings due to localized mass and stiffness nonuniformities [14,17,18,23], nonuniform tires [23], differences in the individual blades of turbine and compressor rotors [22,26], and irregularities in nearly periodic structures [10,16] that have and will have increased space applications. In general, all structures can experience drastic changes in their dynamic response if irregularities are within a specified range. Such changes in their dynamic characteristics will cause either rapid failure or improper function.

Fasteners of all types (such as adhesives, welded joints, and bolts and nuts) can be another source causing localization of the modes of vibration. To the best knowledge of the author, no report addressing the effect of fasteners on the mode localization phenomenon has ap-

peared in the open literature. There is a need to study the relationship between fastener parameters and the above-mentioned vibration phenomena.

The purpose of this project is to establish the feasibility of utilizing and incorporating these vibration phenomena in a systematic way in the prediction model and design procedure of fasteners. Other goals of the proposed research are to investigate the advantages that such dynamic characteristics may have on improving the performance of fasteners and, therefore, of the host structure, and on better predicting the life cycles of both fasteners and the host structure.

Fastener parameters such as tolerances, irregularities, material nonuniformities, locations, and static/operational loads will be studied. First, the role and contribution of such parameters to the above-mentioned dynamic characteristics will be identified and classified. Next, a methodology will be developed to integrate these factors in the structure-fastener computer model and design procedure.

The feasibility of this concept is being established by demonstrating a few classical cases in the first phase of the project. Extended research and the full development of the computer model will be conducted during the second phase of the project. The successful completion of this project will result in a more precise life prediction and design of aircraft fasteners and, perhaps, in developing more effective methods of controlling the dynamic response of structure-fastener systems. Such advancements in the field of fastener modeling, life prediction, and design will increase the quality of U.S. air, sea, and ground vehicles, and thus give the United States a better change in global competition.

### What Is Localized Vibration?

Localization of modes of vibration has been observed and reported since 1958 and has received extensive attention in structural vibrations during the last ten years. The previously reported studies were concerned with the basic understanding of these astonishing phenomena, reasons for their occurrence in structures, and the parameters that control them. The purpose of this project is to investigate the feasibility of incorporating these phenomena in a prediction model and design of fasteners in aircraft structures.

Several vibration characteristics were reported by the author and other researchers [9–40]. Two types of curves were used to present the results of such studies: loci (or frequency curves) and mode shapes. Examples of typical frequency curves are shown in Fig. 1. These curves (loci) represent the natural frequencies of the structure versus selected parameter(s). At certain values of the parameter, the frequency curves cross (CC point shown in Fig. 1). In this case, the structure has two mode shapes at a single frequency. When two frequency curves come close but do not cross, they veer away (VA) or veer together (VT). The latter is known as curve veering or loci veering. The main significance of the above characteristics of the loci are noticed when the corresponding mode shapes of the structure are examined. It was reported [38,39] that in some instances when the CC, VA, or VT occur, the mode shapes undergo drastic changes referred to as mode localization and mode transition. In the case of mode localization, the vibrations are confined to a limited region of the structure (Fig. 2). Consequently, the vibration energy cannot propagate very far from its source but is confined to a region around the source. This feature of mode localization (which is very similar to the effect damping has on vibration) has significant effects on the forced vibration of structures. Mode localization controls (or reduces) the vibration response by confinement of energy rather than dissipation, whose rate is determined by the amount of damping in the system. In the case of the mode transition, the mode with higher frequency replaces the mode shape with lower frequency and vice versa (Fig. 3). What parameters control the

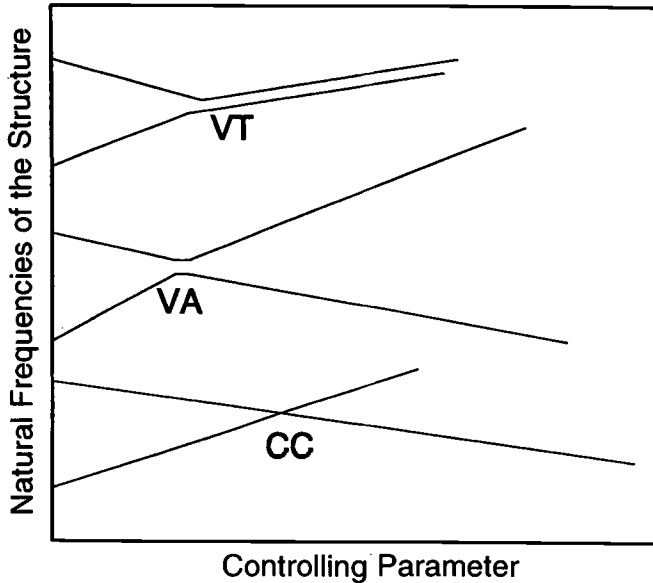


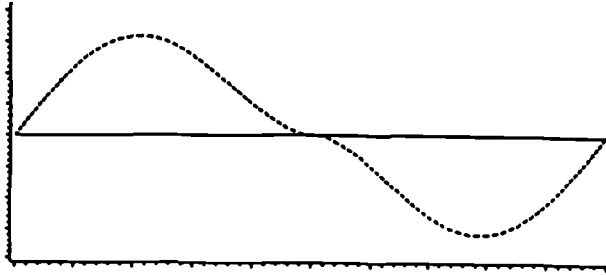
FIG. 1—Typical frequency curves. VT = veer together, VA = veer away, and CC = crossing.

occurrence of these phenomena, how they can be predicted, and how they can be utilized for life prediction and design of fasteners are of interest to this project.

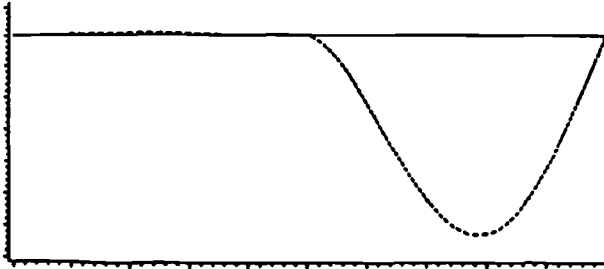
Even though quite a few papers have appeared in the open literature [9–40] and many of the questions have been addressed, several fundamental considerations still need to be investigated. It is clear that the importance of the phenomena in the field of vibration analysis, design, structural failure, and control systems has become evident to researchers around the globe.

One of the basic questions is: In which systems do the phenomena occur? A wide variety of problems have been investigated. Examples are: blade mistuning in turbomachinery, disordered multispan beams, random mass-spring-damping systems, chains of coupled pendula, columns with uncertainties in boundary conditions and axial load, misaligned fins in rocket engines, nonuniform rings, circular plates with discontinuities, nonuniform tires, frame structures, buried pipelines, railroad tracks, space structures, cylindrical shells, plates, and antennas. The author believes that the phenomena can occur in any structure (periodic or non-periodic, regular or irregular) if structural parameters are in the proper range. A corollary is that design parameters can be selected so that the phenomena occur in a controlled manner. These conclusions form the basis for the proposed concept to be applied to fastener life prediction.

The second question is: What is the significance of these phenomena in the vibrations of structures and their interaction with fasteners? Some of the consequences of the presence of the phenomena in structures have been found to be: (1) localization leads to relatively large amplitude vibration and therefore larger stress concentrations in the localized region; (2) drastic changes in the mode shapes and frequencies could deteriorate the performance of the control system; (3) in the case of solid state physics, localization results in a reduction in metallic conductivity; (4) confinement of vibration energy to a small region is achieved by localization rather than the traditional method of dissipation of energy by adding damping



(a) normal mode



(b) localized mode

FIG. 2—Natural mode shapes of a simply supported beam with a torsional spring located (a) at the middle, (b) near the middle.

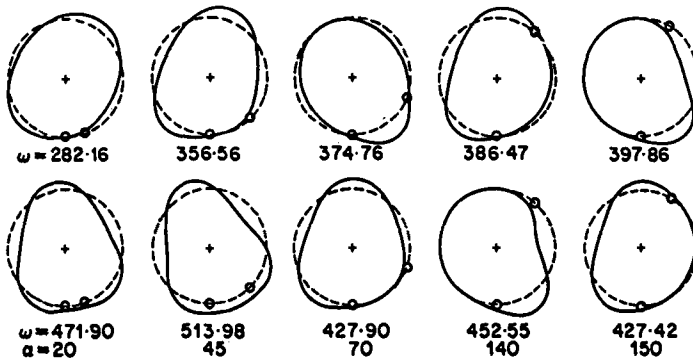


FIG. 3—Examples of a mode shape exchange (transition) for a circular ring supported by two springs.

to the system; (5) errors in measuring damping factors increase; (6) localization is also related to the reflection of waves; (7) the assumption of simple mode shapes in approximate methods might not be valid in the vicinity of the occurrence of the phenomena; and (8) rapid changes of the vibration characteristics of the structures are likely to significantly change their flutter characteristics. Some of these important factors will be examined in a selected group of fasteners mounted on structures such as beams, rings, and plates. A preliminary study of the occurrence of mode localization in a more realistic fastener-structure system, such as an aircraft, will also be part of the project. In future research projects, the phenomena will be investigated not only on beam, ring, and plate-type structures (component approach), but also on submarine, aircraft, ship, and civil structures (system approach).

There will be other issues to be addressed in this project. For example, identifying controlling parameters that are most effective in incorporating or preventing the occurrence of the phenomena in fastener-structure systems will be one of our main objectives. Another concern will be to develop a methodology to implement our findings in optimizing the design of fastener-structure systems and the prediction of the service-free life of fasteners.

### Mathematical Model

The mathematical model is composed of three distinct parts: fastener model, fastener interfaces with the host component (or structure), and the host component. Two main advantages of this approach are: (1) the developed prediction model can be incorporated in any existing structural model, and (2) rigid body modes can be added to the model to account for the loosening of the fasteners (i.e., bolts and nuts). The dynamic characteristics of every fastener and the host structure are assumed to be known in terms of their natural frequencies and mode shapes. Next, the interfaces between the fasteners and the host structure are modeled by employing the receptance method. Finally, the fasteners and the host component are connected by the developed interface models.

As an example, an aircraft bolts-wing structure is considered Figures 4 to 6 show the basic concept of the proposed model applied to an aircraft bolts-wing structure that is free at one end and fixed to the fuselage at the other end. The structure is partitioned into three segments as shown in Fig. 5. The receptance method is employed to connect the three segments to resemble the bolts-wing structure. After the dynamic analysis of the structure is examined, the prediction of the service-free life of the bolts is determined. Every time the program goes through these steps, it keeps a record of the given conditions and the outcome

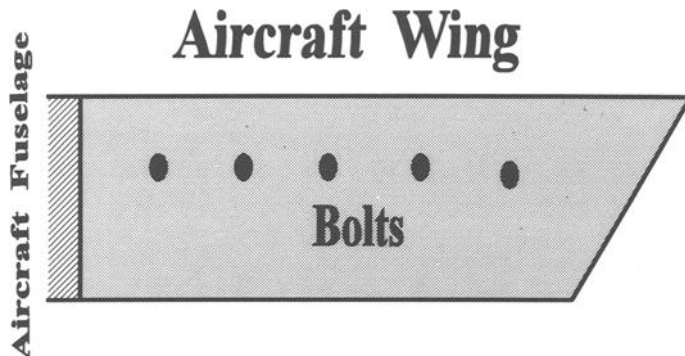


FIG. 4—A simple model of an aircraft wing-bolts structure.

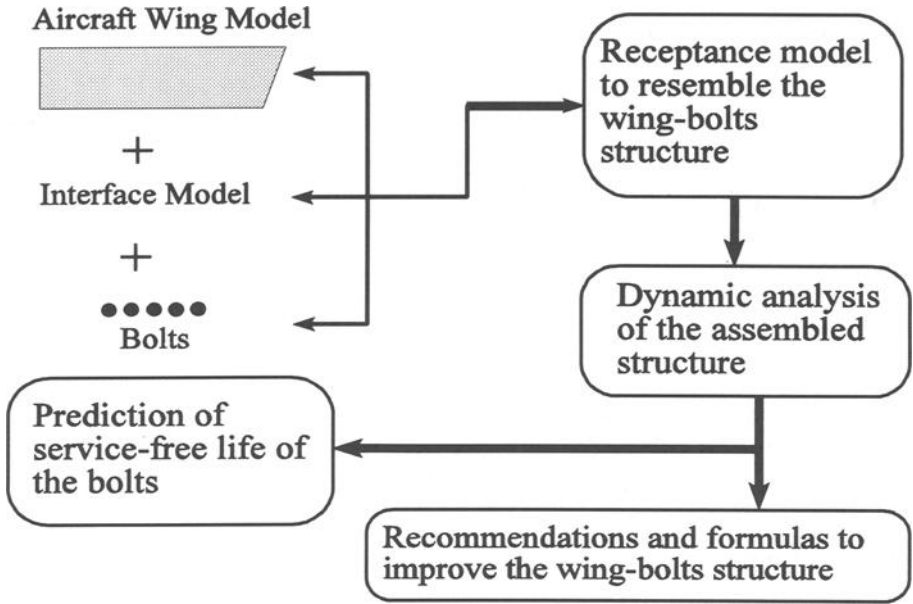


FIG. 5—Basic concept of the proposed model applied to an aircraft wing-bolts structure.

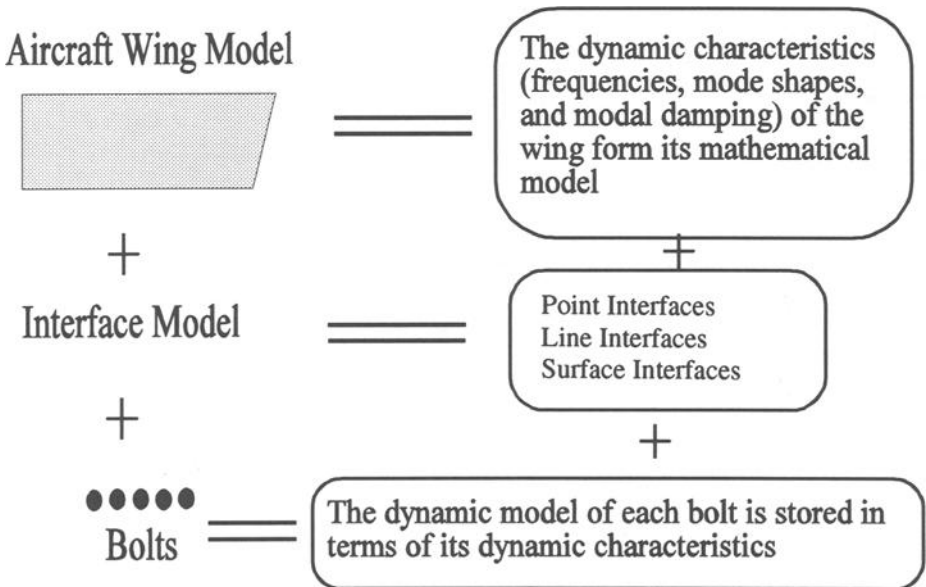


FIG. 6—The dynamic model of each segment of the proposed model.

of the analysis so that it can make recommendations on how to improve the original design (i.e., layout, type, number, etc.) of the fasteners (or bolts in this case). This portion of the model acts as neural software that is capable of learning as the model is used. The two segments, the wing and bolts, will be stored in the computer model in terms of their dynamic characteristics, which are natural frequency, mode shapes, and modal damping factors (see Fig. 6). This feature makes the model very flexible in interacting with other existing models of substructures since such vibration characteristics can be obtained by any method (i.e., finite element, vibration testing, or closed-form solutions in the case of simple models).

Other advantages of this approach (see Ref 39) are in memory savings and computational speeds. There will be neither any large stiffness, mass, and damping matrices, nor any geometric mesh matrices. The only required geometry of the substructures is their contact region. The latter will reduce the degrees-of-freedom of the total structure by a large factor [38,39]. Such features will significantly reduce the memory requirement of the computer model. On the other hand, the first output of the analysis portion of the program will be in terms of the vibration characteristics (natural frequencies and mode shapes) of the assembled structure. These data are then utilized to do a forced dynamic analysis of the total system. The author has shown [23,33] that such modeling processes significantly increase the computational speeds of the computer model.

**General Receptance Formulation of the Interfaces**

In this section, the general formulation of the receptance method applied to interfaces between the fasteners and the host structure is demonstrated. Next, the reduction of the formulation for simplified parametric study and design purposes is discussed. Finally, various features of the approach are addressed.

The system under consideration consists of an arbitrary number of substructures (i.e., fasteners) attached to a host (or main) structure. Figure 7 represents a main structure (A) carrying substructures (B,C,...). To demonstrate the basic concept, the fasteners (i.e., bolts) are modeled as spring-mass systems, and therefore only point receptances are considered. Line and surface receptances will be formulated in the case of continuous models of fasteners during the second phase of the project and will be reported in a follow-up paper. Rigid body

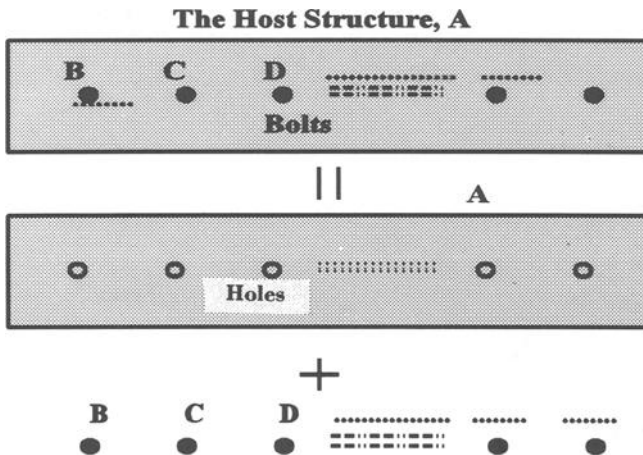


FIG. 7—A plate with attached fasteners (bolts, for example).

modes of the bolts can easily be incorporated in the model allowing for the loosening of their grip. The host structure is modeled as a thin plate capable of vibrating in all three directions (two in-plane and one transverse). It is assumed that all bolts are connected to the midsurface of the plate through a finite number of discrete points. This assumption is made to simplify the formulation and can be relaxed by connecting the fasteners at any point along the thickness of the host structure. It is also assumed that the free undamped vibration characteristics (natural frequencies and mode shapes) of the individual structures are known in a closed form, by a numerical method, or in the form of experimental data. The two systems (plate and bolts) are separated as shown in Fig. 8. Note that only one of the holes, in which the bolts fit, is shown on the plate. The interaction forces between the plate and the bolt are harmonic forces at the point of contact as shown by Eq 1.

$$\begin{aligned}
 f_{iA}(t) &= F_{iA}e^{j\omega t}, & iA &= 1, 2, \dots IA3 \\
 f_{iB}(t) &= F_{iB}e^{j\omega t}, & iB &= 1, 2, 3 \\
 IA3 &= 3 \times IA, & \bar{j} &= \sqrt{-1}
 \end{aligned}
 \tag{1}$$

where

$f_A(t)$  and  $f_B(t)$  = interaction harmonic forces between the plate and bolts,  
 $IA$  = the number of bolts attached to the plate,

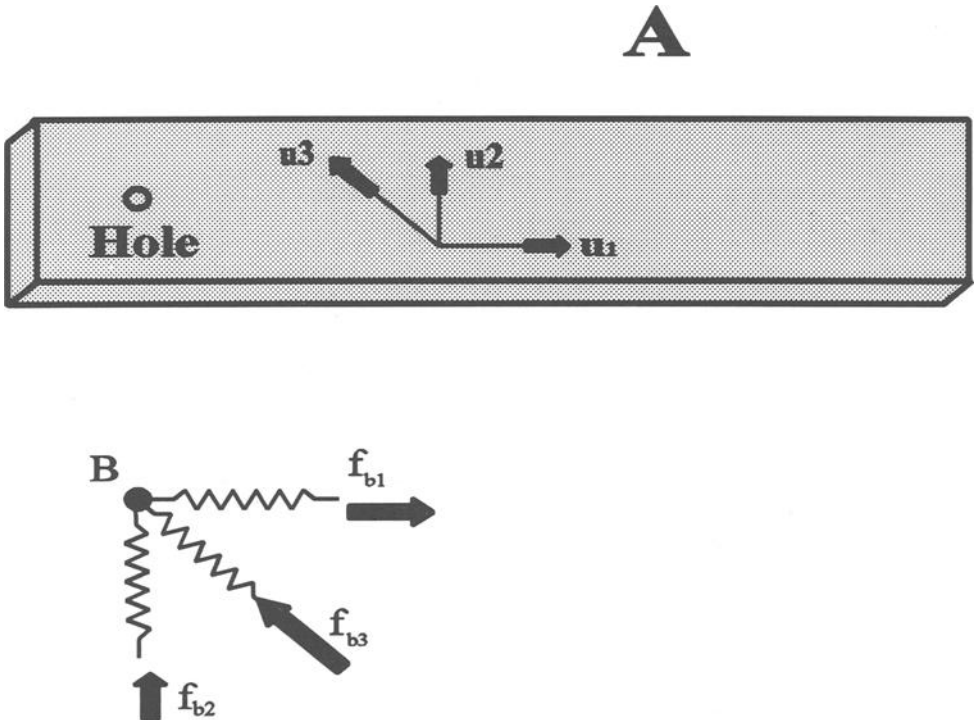


FIG. 8—The host structure (plate in this case) and a dynamic model of a typical bolt.

- $iB$  = principal direction of motions,  
 $\omega$  = excitation frequency or in this case the natural frequency of the composite structure (i.e., composed of the plate and the bolts),  
 $x$  and  $y$  = represent the plate coordinate system along  $U_1$  and  $U_2$  directions, and  
 $e$  = exponential function.

The problem is now converted to two forced vibration cases, and the objective is to solve for the steady state response of the substructures. It should be pointed out that the receptances of the substructures can be formulated by other means; what is presented here, however, seems to be the logical approach for the described problem. Utilizing the modal expansion method, the general vibration response of the plate and the bolts may be written as:

$$\{u_A(x, y, t)\} = [U_A(x, y)] \{\eta_A(t)\} \quad (2)$$

$$\{u_B(x, y, t)\} = [U_B(x, y)] \{\eta_B(t)\} \quad (3)$$

where

$\{u\}$  =  $3 \times 1$  displacement vector in three directions,

$\{U\}$  =  $3 \times N$  mode shape vector,

$\{\eta\}$  =  $N \times 1$  modal participation factor vector of the substructures, and

$N$  = number of the selected modes that describe the dynamics of the substructures.

To avoid repetitive formulation, the Subscripts  $A$  and  $B$  are eliminated in the rest of this section. For the case of no damping, the  $n$ th modal participation factor is related to the applied forces by Eq 4, and the  $n$ th term of the force vector is given by Eqs 5–7.

$$\ddot{\eta}_n(t) + \omega_n^2 \eta_n(t) = \bar{f}_n(t) \quad (4)$$

$$\bar{F}_n(t) = \frac{1}{\rho h M_n} \int_x \int_y [q(x, y, t) U_n(x, y)] dy dx \quad (5)$$

$$M_n = \int_x \int_y [U_n^2(x, y)] dy dx \quad (6)$$

$$q(x, y, t) = F \delta(x - x_i) \delta(y - y_i) e^{j\omega t} \quad (7)$$

where

$M_n$  = normalized modal mass,

$\rho$  = density,

$h$  = thickness,

$\omega_n$ 's = natural frequencies of the substructures,

$q(x, y, t)$  = applied pressure load,

$(x_i, y_i)$  =  $i$ th contact point between the substructures (the plate and the bolts), and

$\delta(x - x_i)$  = Dirac delta function.

Equations 5 to 7 can be explicitly described for a given dynamic model of the plate and the bolts. The steady state response of the problem described by Eq 4 can be written as:

$$\eta_n(t) = \frac{\bar{F}_n}{\omega_n^2 - \omega^2} e^{j\omega t}, \quad \bar{f}_n(t) = \bar{F}_n e^{j\omega t} \quad (8)$$

By substituting Eq 8 into Eqs 2 and 3, the steady state vibration responses of the substructures are obtained as shown by Eq 9.

$$\begin{aligned} \{u_A(x, y, t)\} &= [U_A(x, y)] \left\{ \frac{\bar{F}_A}{\omega_A^2 - \omega^2} e^{j\omega t} \right\} \\ \{u_B(x, y, t)\} &= [U_B(x, y)] \left\{ \frac{\bar{F}_B}{\omega_B^2 - \omega^2} e^{j\omega t} \right\} \end{aligned} \quad (9)$$

The receptances are defined as the ratio of the displacement at Point  $i$  over the applied force at Point  $j$  in the absence of all other forces as given by Eq 10. In other words, the displacements at the contact points are only due to one interface force at a time. The displacements can be related to the applied harmonic forces as they are shown by Eq 11. Note that  $[\alpha]$  and  $[\beta]$  are  $IA3$  symmetric receptance matrices of the substructures  $A$  and  $B$ , respectively. Recall that  $IA3 = 3XIA$  since each bolt interacts with the plate in the three principal directions.

$$\alpha_{ij} = \frac{u_A(x_i, y_i, t)}{f_{jA}(t)}, \quad \beta_{ij} = \frac{u_B(x_i, y_i, t)}{f_{jB}(t)} \quad (10)$$

$$\{U_A\} = [\alpha]\{F_A\}, \quad \{U_B\} = [\beta]\{F_B\} \quad (11)$$

At the points of contact, force and displacement conditions are enforced by Eqs 12 and 13.

$$\{U_B\}^T = \{U_A\}^T, \quad \{F_B\}^T = -\{F_A\}^T \quad (12, 13)$$

Combining Eqs 11 through 13 leads to Eq 14.

$$([\alpha] + [\beta])\{F_B\} = 0, \quad [R]\{F_B\} = 0, \quad [R] = ([\alpha] + [\beta]) \quad (14)$$

Where  $[R]$  is the  $IA3$  by  $IA3$  total receptance matrix of the assembled structure (the plate and bolts). Since the trivial solution  $\{F\} = 0$  is not desired, the determinant of the total receptance matrix,  $[R]$ , should be set to zero. Equation 15 is the characteristic equation whose roots are the natural frequencies of the structure. Equation 9 can be used to extract the mode shapes of the substructures (plate and the bolts). For a calculated natural frequency,  $\omega$ , of the assembled structure, the mode shape are given by Eq 16.

$$\det [R] = 0 \quad (15)$$

$$\begin{aligned} \{U_{sA}(x, y, t)\} &= [U_A(x, y)] \left\{ \frac{\bar{F}_A}{\omega_A^2 - \omega_s^2} \right\} \\ \{U_{sB}(x, y, t)\} &= [U_B(x, y)] \left\{ \frac{\bar{F}_B}{\omega_B^2 - \omega_s^2} \right\} \end{aligned} \quad (16)$$

Note that  $\{U_s\}$ 's are the eigenvectors representing the  $s$ th mode shape of the connected

structure.  $\{U\}$ 's are, on the other hand, the eigenvectors representing the first  $N$  mode shapes of the lowest  $N$  natural frequencies ( $\omega_A$  and  $\omega_B$ ) of the substructures.  $\omega_s$  is the  $s$ th natural frequency of the assembled structure, and it is the same for all the substructures after they are connected.

It should be noted that the above formulation is general and can be applied to any combination of connected substructures and fasteners. Also, note that the natural frequencies appear in the denominator of the receptances (Eqs 9 and 10) and the mode shapes (Eq 16) of the assembled structure. Therefore, assuming that the natural frequencies of the assembled structure are not significantly different from the frequencies of the host structure (i.e., plate), both formulations can be reduced to a single-term series solution that involves the dominating mode. Such reduced formulations can be used for simple parametric study and design purposes [38,39]. Also, the solution (frequencies and mode shapes of the assembled structure) has very low sensitivity to the accuracy of the higher modes of the substructures. So the propagation of the numerical error of higher frequencies, which is due to inaccurate models of substructures, does not have a significant effect on the solution of lower modes of the assembled structure (i.e., plate-bolt system).

### Special Features of the Proposed Approach

A summary of the advantages of the proposed approach is given in this section. The outlined features are composed of two main parts: application of model localization in the study of fastener wear and vibration, and application of the substructuring concept by employing the receptance method.

1. *Application of mode localization on service-free life of fasteners:* For the first time in the open literature, the presence and influence of the internal coupling of structural modes, which force the vibration energy to be localized, will be investigated in structure-fastener systems. It is anticipated that the results of this study will significantly improve the service-free life of fasteners.

2. *Memory savings:* The memory requirement is controlled by the number and type of fasteners rather than by the complexity of the host structure and fasteners. It has been shown [14,15,17] that the memory savings of the proposed substructuring concept based on the receptance method is seven to ten times better when compared with the full finite element method.

3. *Computational speed:* The computational speed is significantly faster than the full numerical approaches, such as the finite element method, since the analysis does not involve large matrix operations. Free vibration analysis of the substructures is performed only once, and the results are input in the proposed interface model to study the assembled structure. The author has shown [14,15] that the receptance method improves the computational speed by a large factor.

4. *Accuracy of the numerical results:* The accuracy of the numerical results depends on the vibration characteristics of the substructures, which are obtained independently by any suitable method. Assuming that the stored vibration characteristics of the substructures are accurate, the number of the required substructure modes should be double the number of modes of interest of the assembled structure [14] to have reasonable accuracy.

5. *Reduced design formulas:* In certain ranges of system parameters, it is possible to reduce the equations to closed-form formulas that can be used for simple parametric study and design purposes.

6. *Efficient parametric study:* Since the host structure and the fasteners are independently modeled and then connected via the proposed interface model, the parameters will be

grouped in three parts: host structure, fasteners, and interface parameters. Dynamic models of host structures are covered in the open literature. Our focus is on fasteners and their interfaces with the host structure. While keeping two of the three sets of parameters constant, the influence of the third group of parameters on the life prediction of fasteners will be studied.

7. *Reduced sensitivity of the numerical results of the substructure:* As was previously shown, natural frequencies appear in the denominator of the receptance and mode shape equations. Therefore, the inaccuracy of the higher natural frequencies of substructures generated by their independent dynamic models will not affect the calculated vibration characteristics of the assembled structure, whereas in conventional numerical models, such as finite element, the accuracy of the results depends on the number of degrees of freedom, the generated mesh, and the type of elements.

8. *Inclusion of rigid body modes:* In order to trace the loosening effect of fasteners, rigid body modes need to be incorporated in the model. The receptance method provides the capability of including the rigid body modes as well as the nonrigid body modes. Multidirectional rigid body modes will be implemented in the model.

9. *Compatibility with existing models:* Since the three parts of the proposed model can be independently developed and only the vibration characteristics of the substructures are required, it will have full compatibility with other dynamic models of the substructures.

10. *Neural capability:* The model will record the significant results of each analysis and will incorporate them in making recommendations for future improvement of the system.

### Tasks in Progress

To demonstrate the feasibility of the described concept, three major tasks are planned to be completed during the first phase of the project. The three tasks are described in this section, and the results will be reported in the next paper.

A preliminary study of the fasteners of a fighter aircraft (such as F/A-18 or F-15) is being conducted, and the potential contributing parameters controlling the vibration response and service-free life of the fasteners is being identified during the first task. Some of the candidate parameters are types of fasteners, their relative and absolute locations on the host structure, their material properties, static and dynamic loads, operating conditions, the frequency range they are subjected to, and their duty cycles. The goal is to incorporate these controlling parameters in the proposed mathematical model. After identification of the types of fasteners, their different dynamic models and interfaces with the host structure will also be studied.

A preliminary mathematical model based on the described concept is being developed in the second task. The fasteners, their interfaces, and the host structure are being separately modeled and connected by employing the receptance method. Application of the receptance method to the problem of optimizing and predicting the service-free life of fasteners is one of the main focuses of this project. The most significant parameters identified in Task 1 will be incorporated in the preliminary model.

To prove the feasibility of the approach, the host structure is modeled as a thin beam, plate, or cylindrical shell. The boundary conditions of the host structure are selected so that closed form solutions generating their free vibration characteristics are obtained and therefore the objectives of the project are more efficiently met. Bolts are modeled as lumped masses that are attached to the host structure via massless springs or as elastic solid bars with elastic interfaces. In both cases, rigid body modes are allowed in the model so that the loosening of their grips can be traced. In the first phase of the study, only point receptances are utilized to model interfaces between the fasteners and the host structure. Line and surface receptances will be developed during the second phase.

Finally, a sample parametric study will be conducted to demonstrate the effectiveness and validity of the model. The model will be tested on skin structures, such as thin plates and shells, under controlled conditions. Computer simulation of aircraft vibration will be imposed on the test structures with attached fasteners. Effects of variations in fastener parameters on frequency curve veering and mode localization will be studied.

A preliminary study of the presence and effects of localized vibrations of the fastener-host structure system will be conducted. The goal is to show that certain fasteners and host structure parameters can force the vibration energy to be localized. By mapping the localized regions on the host structure and knowing their effects on the service-free life of the fasteners, it will be possible to optimize the fastener-structure system parameters. It is anticipated that the fasteners located in regions with less vibration energy will last longer. The outcome of this project, on one hand, will significantly improve fastener technology, and, on the other hand, weight savings will be possible since fewer and lighter fasteners will be needed in regions with less vibration energy.

The latter task will be accomplished, for example, by tuning a set of parameters responsible for occurrence of such phenomena. Localizing the vibrational energy within a specified section of the structure could result in a huge reduction of the number of required fasteners and collected data for monitoring purposes. It has been shown [9-40] that it is possible to force various structures to exhibit such vibration characteristics. However, no systematic method has been identified on how one can control these phenomena in structures that have different components, that are made of composite materials, and that have various geometries and shapes. In particular, no paper on the occurrence of the phenomenon in the fastener-structure system has appeared in the open literature.

Localizing the vibrational energy within the host structure is one of the main thrusts of this project. The purpose is to design the fastener-structure system so that it will have the maximum vibration activities in a small portion of the structure. The specified region will be identified as the critical part of the structure and must be monitored more closely. Such localization will make the detection of any undesired dynamic response of the structure much faster and more precise. It will also provide areas where the fasteners are subjected to less vibrations and therefore less failure.

## Conclusions and Recommendations

The completion of this project will result in a much better understanding of the dynamics of fasteners, significantly improved modeling capabilities to predict their service-free life, and advanced design criteria for fasteners. In particular, it is anticipated that the occurrence of loci veering and mode localization in fastener-structure systems will have a major impact on fastener technology and analysis. The outcome of this work could be a major step toward developing the next generation of computer software to optimize fastener-structure systems.

A better understanding of the above-mentioned vibration phenomena in structures is the key to more effectively applying them to fastener-related problems. One of the outcomes of this research will be a fundamental knowledge and understanding of these characteristics, which will be well documented so that other researchers and engineers can use this information in their particular applications. For the first time, a link between all fastener parameters and these phenomena will be established. The relation between each of the four phenomenon will also be identified. The most significant of the anticipated benefits of this project will be a systematic method of integrating this basic knowledge in the design and life prediction of fasteners in fighter aircraft structures.

The potential application of the proposed approach in the field of dynamics of fasteners is tremendous. Once the implications of mode localization, loci crossing and veering, and

how one can implement them in fastener-structure systems becomes clear, the means of effectively optimizing and predicting the service-free life of fasteners will be identified. The knowledge gained during the first phase of the project will be utilized in conducting a detailed investigation of the fasteners and developing a full prediction model for determining their service life. Verification against field data and commercialization will be performed during the second phase of this research work.

Fasteners have widespread applications in systems used by NASA, the U.S. Army, the U.S. Air Force, and the U.S. Navy. In particular, the outcome of this project will enhance the capabilities of U.S. fighter aircraft. An effective fastener model will prevent unnecessary maintenance and surprise failures.

Commercial applications of such development can be directed to aircraft, ships, and automobiles. Other versions of the developed model can be applied to civil structures such as buildings and bridges, commercial products such as engines, and other engineering systems that use fasteners extensively.

### *Acknowledgment*

This work has been funded by the U.S. Air Force through the Fasteners, Actuators, Connectors, Tools and Subsystem (FACTS) Laboratory at Wright-Patterson Air Force Base in Ohio. Their continuous support of this project is greatly appreciated.

### **References**

- [1] Condon, E. F., "Investigation of Hole Propagation and Fastener Installation for Graphite/Epoxy Laminates," final report, McDonnell Aircraft Co., St. Louis, Contract No. N00019-79-C-0293, 1980.
- [2] Speaker, S. M., et al., "Durability Methods Development, Test and Fractography Data," final report, General Dynamics, Fort Worth, TX, Contract No. F33615-77-C-3123, 1982.
- [3] Gordon, D. E., et al., "Advanced Durability Analysis, Fractographic Test Data," final report, General Dynamics, Fort Worth, TX, Contract No. F33615-84-C-3208, 1986.
- [4] Mann, J. Y., et al., "Improving the Fatigue Life of the Mirage III0 Wing Main Spar," a report by Aeronautical Research Labs in Melbourne, Australia, Report No. ARL-STRUC-R-398, 1984.
- [5] Bowles, S., "Crack Distribution and Growth Rates for Critical Fasteners Holes in Mirage Wing RH79," report, Aeronautical Research Labs, Melbourne, Australia, Report No. ARL-MAT-TM-396, 1987.
- [6] Levraea, et al., "Add-On Damping Treatment for Life Extension of the F-15 Upper-Outer Wing Skin," final report, Wright Patterson AFB, OH, Report No. WL-TM-91-307-FIBG, 1991.
- [7] Schaefer, W. H., "Advanced Composite Wing and Expennage to Fuselage Attachment Fittings," ongoing work, Accession No. DF671780.
- [8] Pritchett, L. D., "Reliable NDT Methods and Procedures to Detect Cracks under Installed Fasteners Connected with AF Aircraft Structures," ongoing work, Accession No. DF672970.
- [9] Kuttler, J. R. and Sigillito, V. G., "On Curve Veering," *Journal of Sound and Vibration*, Vol. 75, No. 4, 1981, pp. 585-588.
- [10] Hodges, C. H., "Confinement of Vibration by Structural Irregularity," *Journal of Sound and Vibration*, Vol. 82, p. 82.
- [11] Huang, W., "Vibration of Some Structures with Periodic Random Parameters," *AIAA Journal*, Vol. 20, No. 7, 1982, pp. 1001-1008.
- [12] Hodges, C. H. and Woodhouse, J., "Vibration Isolation from Irregularity in a Nearly Periodic Structure: Theory and Measurement," *Journal of the Acoustical Society of America*, Vol. 74, No. 3, 1983, pp. 894-905.
- [13] Perkins, N. and Mote, C., "Comments on Curve Veering in Eigenvalue Problems," *Journal of Sound and Vibration*, Vol. 106, No. 3, 1986, pp. 451-463.
- [14] Allaei, D., Soedel, W., and Yang, H. T. Y., "Natural Frequencies and Modes of Rings and Deviate from Perfect Axisymmetry," *Journal of Sound and Vibration*, Vol. 111, No. 1, 1986, pp. 9-27.

- [15] Allaei, D. and Soedel, W., "Documentation of Software Used to Study Vibration of Nonuniform Tires," Report No. 0810-3 HL 86-31p, Ray W. Herrick Laboratories, Purdue University, 1986.
- [16] Bendiksen, O. O., "Mode Localization Phenomena in Large Space Structures," *AIAA Journal*, Vol. 25, No. 9, 1987, pp. 1241-1248.
- [17] Allaei, D., Soedel, W., and Yang, T. Y., "Eigenvalues of Rings with Radial Spring Attachments," *Journal of Sound and Vibration*, Vol. 121, No. 3, 1987, pp. 547-561.
- [18] Allaei, D., Soedel, W., and Yang, T. Y., "Free Vibration of Rolling Structures Carrying Local Non-uniformities by the Receptance Method," *Proceedings*, Twentieth Midwestern Mechanics Conference, presentation and proceeding publication, September 1987, pp. 1347-1353.
- [19] Allaei, D., "Vibration Analysis of Circular Plates Using Axisymmetric Finite Element," *Proceedings*, Twentieth Midwestern Mechanics Conference, September 1987, pp. 330-336.
- [20] Pierre, C., Tang, D. M., and Dowell, E. H., "Localized Vibrations of Disordered Multispan Beams: Theory and Experiment," *AIAA Journal*, Vol. 25, No. 9, 1987, pp. 1249-1257.
- [21] Ibrahim, R. A., "Structural Dynamics with Parameter Uncertainties," *Applied Mechanics Review*, Vol. 40, No. 3, 1987, pp. 309-328.
- [22] Pierre, C. and Dowell, E. H., "Localization of Vibrations by Structural Irregularities," *Journal of Sound and Vibration*, Vol. 122, No. 1, 1987, pp. 549-564.
- [23] Allaei, D., Soedel, W., and Yang, T. Y., "Vibration Analysis of Non-axisymmetric Tires," *Journal of Sound and Vibration*, Vol. 122, No. 1, 1988, pp. 11-29.
- [24] Allaei, D. and Shih, T. S., "Vibration Analysis of Annular Plates Carrying Cocenter Circular Dynamic Elements," *Proceedings*, Applied Mechanics and Engineering Science Conference, full presentation and published abstract, 20-22 June 1988.
- [25] Allaei, D., Soedel, W., and Yang, T. Y., "Vibration Characteristics of Rings on Nonuniform Elastic Support," abstract, *Proceedings*, 7th ASCE-EMD Specialty Conference, May 1988.
- [26] Pierre, C., "Mode Localization and Eigenvalue Loci Veering Phenomenon in Disordered Structures," *Journal of Sound and Vibration*, Vol. 126, No. 3, 1988, pp. 485-502.
- [27] Cornwell, P. and Bendiksen, O., "Localization of Vibrations in Large Space Reflectors," *AIAA Journal*, Vol. 27, No. 2, 1989, pp. 219-226.
- [28] Shih, T. S. and Allaei, D., "On the Free Vibration Characteristics of Annular Plates With Ring-Type Elastic Attachments," *Journal of Sound and Vibration*, Vol. 140, No. 2, 1990, pp. 239-257.
- [29] Triantafyllou, M. and G., "Frequency Coalescence and Mode Localization Phenomena: A Geometric Theory," *Journal of Sound and Vibration*, Vol. 50, No. 3, 1991, pp. 485-500.
- [30] Labadi, M. and Allaei, D., "Loci Veering and Mode Localization in Elastic Linkages and Frames," *Proceedings*, Southeastern Conference on Theoretical and Applied Mechanics (SECTAM XVI), The University of Tennessee Space Institute, Nashville, Tennessee, April 1992.
- [31] Labadi, M. and Allaei, D., "Free and Forced Vibration of the Human Body," *Proceedings*, SECTAM XVI, Nashville, Tennessee, April 1992.
- [32] Allaei, D., "Mode Localization Due to Tire Non-uniformities," *Proceedings*, Eleventh Annual Meeting and Conference on Tire Science and Technology, Akron, Ohio, 24-25 March 1992.
- [33] Allaei, D., "An Advanced Approach for Vibration Analysis of Nonuniform Tires," *Proceedings*, Eleventh Annual Meeting and Conference on Tire Science and Technology, Akron, OH, March 1992.
- [34] Allaei, D., "Application of Localized Modes in Vibration Control," *Proceedings*, Second International Congress on Recent Developments on Air and Structure Borne Sound and Vibration, full paper is included in the *Proceedings*, December 1992.
- [35] Jei, Y. and Lee, C., "Does Curve Veering Occur in the Eigenvalue Problem of Rotors?," *Journal of Vibration and Acoustics, Stress & Reliability*, Vol. 114, 1992, pp. 32-36.
- [36] Cornwell, P. and Bendiksen, O., "Numerical Study of Vibration Localization in Disordered Cyclic Structures" *AIAA Journal*, Vol. 30, No. 2, 1992, pp. 473-481.
- [37] Luongo, A., "Mode Localization by Structural Imperfections in One-Dimensional Continuous Systems," *Journal of Sound and Vibration*, Vol. 155, No. 2, 1992, pp. 249-271.
- [38] Allaei, D., "Application of Localized Vibration and Smart Materials in Controlling the Dynamic Response of Structures, Part I," submitted to Advanced Research Project Agency (ARPA), 1992.
- [39] Allaei, D., "Application of Localized Vibration and Smart Materials in Controlling the Dynamic Response of Structures, Part II," submitted to ARPA, October 1992.
- [40] Bouzit, D. and Pierre, C., "Vibration Confinement Phenomena in Disordered, Mono-Coupled, Multispan Beams," *Journal of Vibration and Acoustics*, Vol. 114, 1992, pp. 521-530.

# Establishment of Fatigue Test Method for Turbine Blade Fastener

---

**REFERENCE:** Endo, T., Kondo, Y., and Kadoya, Y., "Establishment of Fatigue Test Method for Turbine Blade Fastener," *Structural Integrity of Fasteners, ASTM STP 1236*, P. M. Toor, Ed., American Society for Testing and Materials, Philadelphia, 1995, pp. 20–31.

**ABSTRACT:** The design of a long, wide blade for a large-sized steam turbine required the development of new design methodology. The most important consideration to ensure the integrity of a blade attachment is to evaluate the stress at the local point of a blade root. The major difficulties in stress evaluation are the three-dimensional effects and the contact problem at the fastening point between the blade root and the disk steeples. Because of these complexities, the design method based on the linear elastic finite-element method (FEM) analysis has to be verified experimentally.

For this purpose, a new fatigue testing apparatus was developed that simulates the operating loads for the steam turbine, including centrifugal forces, untwisting moments, and bending moments. The results of the strain measurement and the low-cycle fatigue tests verified the use of the peak stress, which was calculated by three-dimensional elastic FEM analysis using linear elastic connection of blade root and disk steeples and Neuber's rule for the evaluation of the strain range. If the strain is evaluated correctly, the low-cycle fatigue life can be obtained using a Langer's-type equation.

**KEYWORDS:** steam turbine, blade attachment, strain measurement, three-dimensional finite-element method, low-cycle fatigue

The increasing demand for electricity has promoted an increase in the size of steam turbines for power generation. The design of a large-sized steam turbine required the development of a new design methodology. Especially in a low-pressure steam turbine, the blade in the last row has become longer and wider [1]. The increase in the height and width of the blade has caused an increase in local stress at the blade attachment portion by three-dimensional effects. In addition, recent changes in the operating mode have promoted frequent start-stops. These factors may result in an increase in the stress level and cyclic stress. Hence, fatigue failure can be a potential problem at the blade root [2].

An example of a modern long blade is shown in Fig. 1. These blades have fir-tree-type roots for the blade attachment. The blade is attached to the turbine rotor by the blade root and disk steeples connection as shown in Fig. 2. The various kinds of forces that act on the blade when operating are summarized in Fig. 3. The large centrifugal forces ( $F_c$ ) and untwisting moments ( $M_u$ ) of a three-dimensionally twisted blade can cause high local stress at the corner of a blade root. The most important consideration to ensure the integrity of a blade attachment is to evaluate the stress at the local point of a blade root. The major

---

<sup>1</sup> Chief engineer, Koryo Engineering Corporation, 2-1-1, Shinhama, Arai-cho, Takasago, Japan.

<sup>2</sup> Assistant chief research engineer, Takasago R & D Center, 2-1-1, Shinhama, Arai-cho, Takasago, Japan.

<sup>3</sup> Professor, Setsunan University, 17-8, Ikedanakamachi, Neyagawa, Japan.

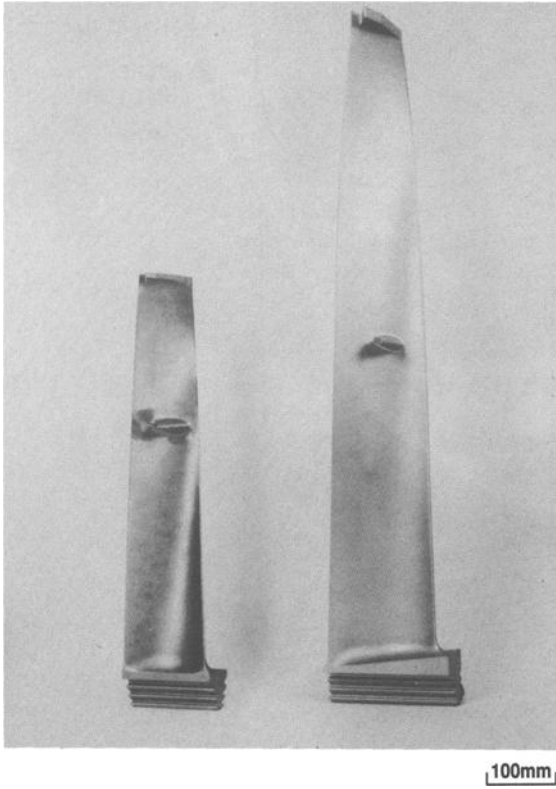


FIG. 1—Example of a modern long blade.

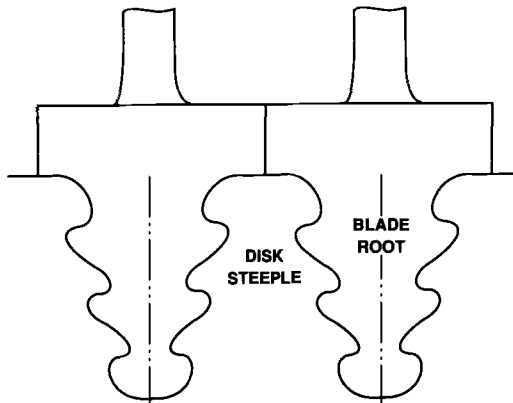
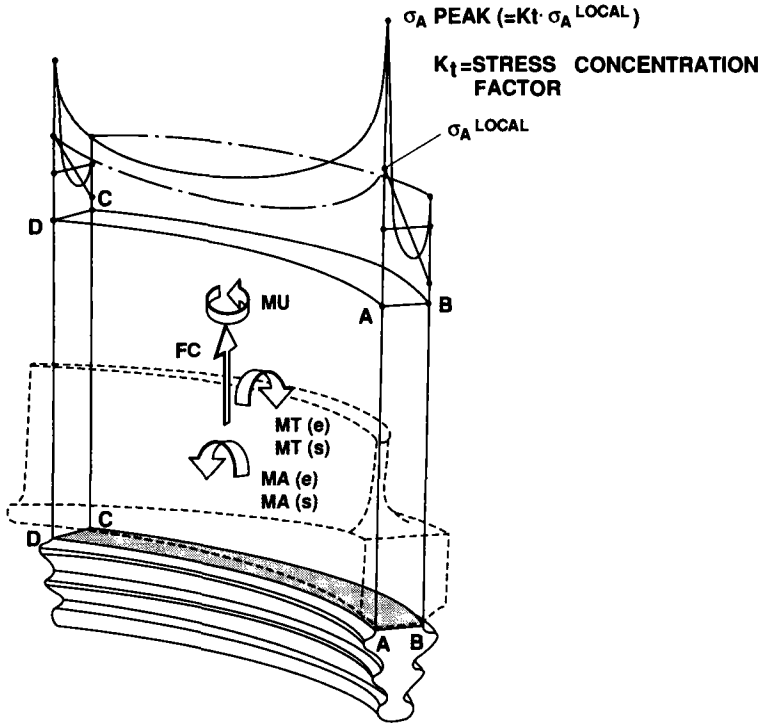


FIG. 2—Connection between blade root and disk steeples.



**NOTATION :**

$\left\{ \begin{array}{l} F_C = \text{CENTRIFUGAL FORCE} \\ M_U = \text{UNTWISTING MOMENT} \\ M_T = \text{TANGENTIAL MOMENT} \\ M_A = \text{AXIAL MOMENT} \end{array} \right.$	$\left\{ \begin{array}{l} (s) - \text{STEAM FORCE} \\ (e) - \text{ECCENTRICITY} \end{array} \right.$
--	--

FIG. 3—Summary of loads that act on a blade.

difficulties in stress evaluation are three-dimensional effects and the contact problem at the fastening between blade root and disk steeple. The evaluation of the stress at a local point caused by three-dimensional effects using a rotating test is quite difficult and unrealistic. Therefore, the development of a new design method and its experimental verification is the key technology for the development of new blades.

The current design methodology for blade uses the three-dimensional finite-element method for stress analysis as shown in Fig. 4. There are several ways of connecting the blade root and disk steeple. Among these, a linear connection using an arrangement of linear springs is the simplest and most common.

There happens to be a case where the peak stress at the stress concentration exceeds the yield point of the material. In such a case, the evaluation of low-cycle fatigue is done as

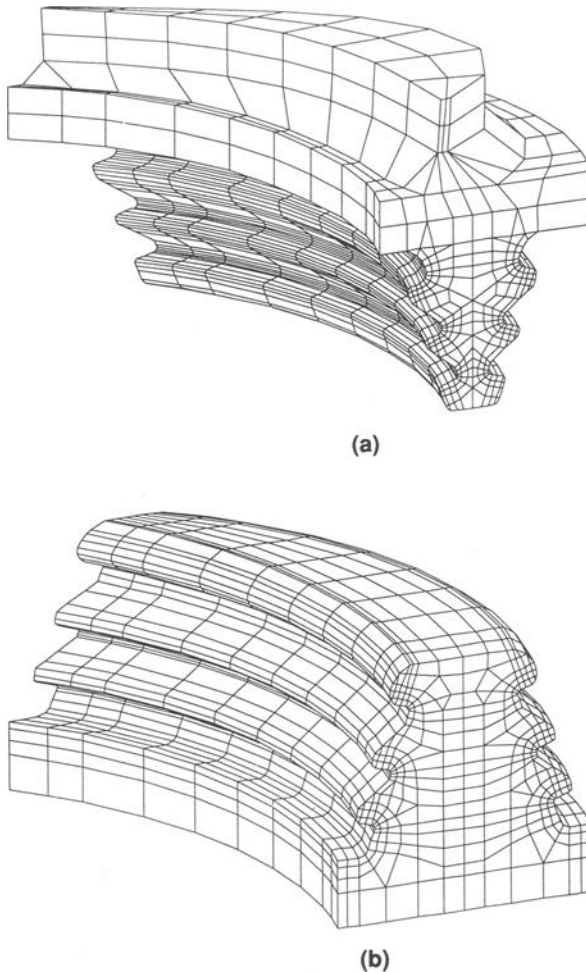


FIG. 4—Example of FEM mesh: (a) blade root, (b) disk steeple.

follows. The total strain range ( $\Delta\epsilon_f$ ) is estimated using the fictitious peak elastic stress calculated by FEM and Neuber's rule [3]. It is substituted into the Langer's equation [4], and then we can obtain the fatigue life. In the above-mentioned evaluation method, several assumptions are made. Therefore, experimental verification of the precision of the strain estimation and the low-cycle fatigue life is needed. In this paper, the verification test results are reported using newly developed fatigue testing apparatus for an actual steam turbine blade.

### Testing Apparatus

The general appearance of the newly developed fatigue testing apparatus for an actual blade is shown in Fig. 5. Fundamentally, this apparatus is composed of a frame for the application of simulated centrifugal forces, an arrangement for the application of untwisting moments and an electrohydraulic servo actuator for the application of lateral bending mo-

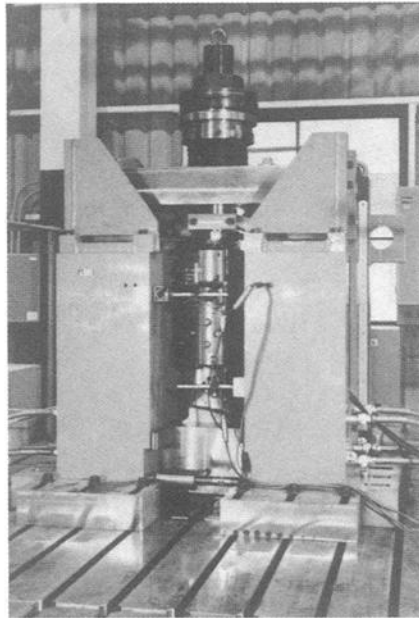
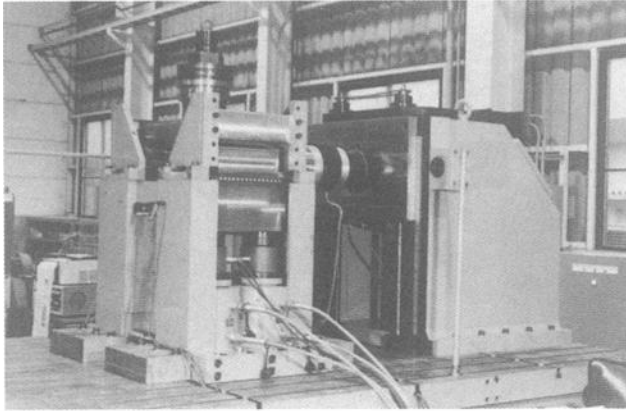


FIG. 5—General appearance of a fatigue testing machine for the blade.

ments. The schematic view of the test apparatus is shown in Fig. 6. A test blade was set into the groove formed in the base, which simulated the disk steeple. The airfoil portion was gripped by a specially designed holder. The holder was connected to the upper crosshead through a set of belleville springs and thrust bearings to remove reaction moments and reaction torques caused by the motion. The crosshead was driven cyclically in the vertical direction by four hydraulic cylinders using a controlled sequence. The capacity of the simulated centrifugal force was up to 400 tons (3.92 MN). The holder can be intentionally twisted to simulate the untwisting moment. The laterally located electrohydraulic servo ac-

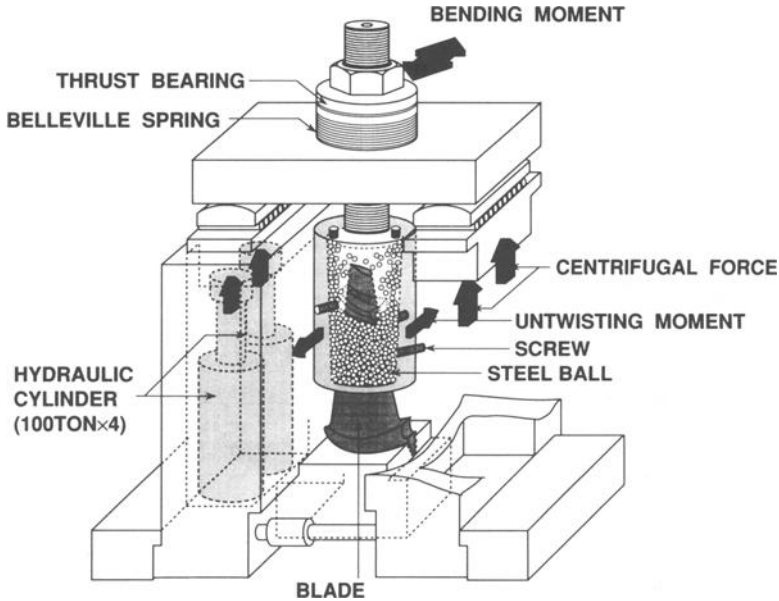


FIG. 6—Schematic view of fatigue testing apparatus.

tuator was connected to the holder to apply the bending moment, which simulated the gas bending caused by steam flow and the cyclic blade vibration. The capacity of the lateral force was  $\pm 20$  tons (196 kN). The maximum frequency was 70 Hz at the displacement of  $\pm 1$  mm.

One of the most important parts in this apparatus is the blade holder. Since the airfoil of the blade is three-dimensionally twisted and the thickness is usually thin, the application of a large centrifugal force is not easy. For this purpose, the specially designed holder shown in Fig. 7 was developed. The hollow cylinder has a conical hole inside. The airfoil portion was inserted into the hole, and the gap between the blade and the hole was filled with small steel balls. Then the steel balls were compressed by multiple screws. Stiff support was achieved using this holder. Stresses were simulated on the blade that were similar to operating stresses using this apparatus.

### Test Procedure

Multiple strain gages (gage length 1 mm) were bonded on the notch root at the corner of the test blade as shown in Fig. 8. Additional strain gages were also bonded on the airfoil portion for verification of the load application. Then the test blade was set into the groove formed in the base as shown in Fig. 9.

The test procedure is shown in Fig. 10. The purpose of the test was to see the response at a local point of the blade root when the load was applied to determine if the measured stress distribution at a nominal section correlated with the calculated stress distribution. A nominal section was selected a little bit away from the root so that the stress condition would not be influenced by the supporting condition. Firstly, the centrifugal force was applied. Then, the bending moment and untwisting moment were added until the measured strain distribution met the stress distribution calculated by three-dimensional FEM at the nominal

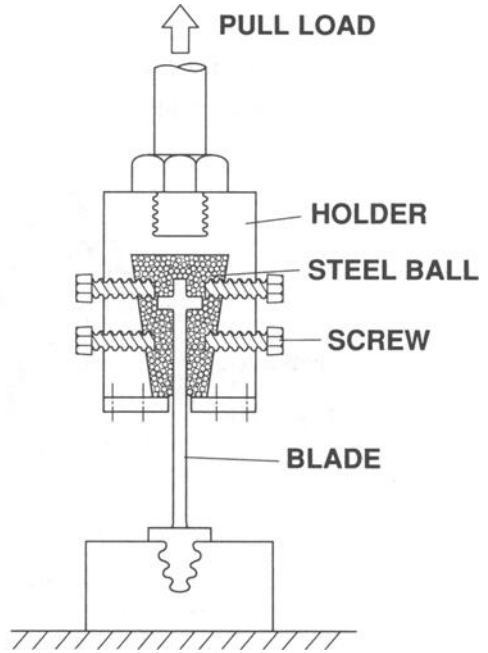
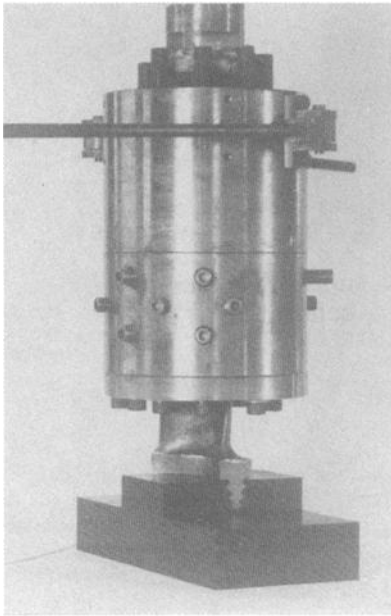


FIG. 7—Specially designed holder to grip the blade profile.

section. Test load was determined through this procedure. After applying a few loading cycles for the measurement of strain, the low-cycle fatigue test was continued.

**Test Results**

An example of the comparison between the measured stress and the calculated stress distribution at the nominal section is shown in Fig. 11. Figure 11 indicates that the stress

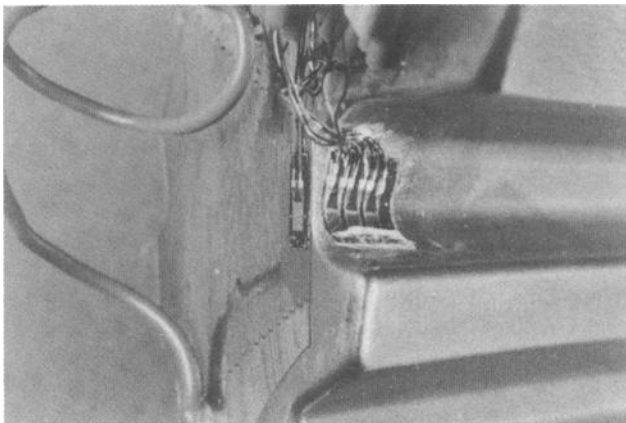


FIG. 8—Strain gages bonded at the corner of the blade root.

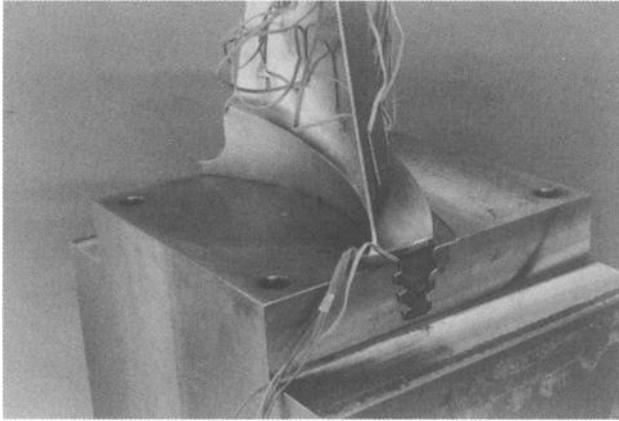


FIG. 9—Blade and disk assembly for test.

distribution when operating was successfully reproduced at the nominal section. Therefore, it can be concluded that the method of load application using the apparatus was valid.

An example of the estimated stress-strain hysteresis loop at a blade root corner is shown in Fig. 12. The strain range for the second cycle was used for the evaluation. The comparison between the measured strain range and the estimated strain range using the calculated peak stress and Neuber's rule for the test blade is shown in Fig. 13. Irrespective of the contact at the blade root and disk steeples, the measured strain was in good agreement with the estimated strain based on linear elastic calculations. This seems to be a result of the fact that the blade root was fixed to the disk steeples at a relatively low load and a substantial sliding motion did not occur.

Low-cycle fatigue test results under various strain ranges at the blade root are shown in Fig. 14. The fatigue life for the initiation of a 1-mm-deep crack could be expressed using a Langer's-type equation in terms of the total strain range. An example of the fracture surface of a test blade is shown in Fig. 15. The fatigue crack initiated at the corner of the blade root.

## Conclusion

1. A low-cycle fatigue testing apparatus has been developed for a turbine blade that simulates operating loads for the steam turbine including centrifugal forces, untwisting moments, and bending moments. This apparatus was used to verify the stress analysis method for long, wide turbine blades, which have the complexities of three-dimensional effects and a contact problem.

2. The measured strain at the blade root corner was in good agreement with the estimated strain calculated using the peak stress predicted by three-dimensional FEM and Neuber's rule.

3. Test results on the low-cycle fatigue life of the turbine root can be evaluated using a Langer's-type equation in terms of total strain range.

4. Based on these results, it was verified as appropriate to use the peak stresses calculated by three-dimensional elastic FEM analysis using linear elastic connection of the blade root and disk steeples and Neuber's rule for the evaluation of the strain range. If the strain is evaluated correctly, the fatigue life can be obtained using a Langer's-type equation.

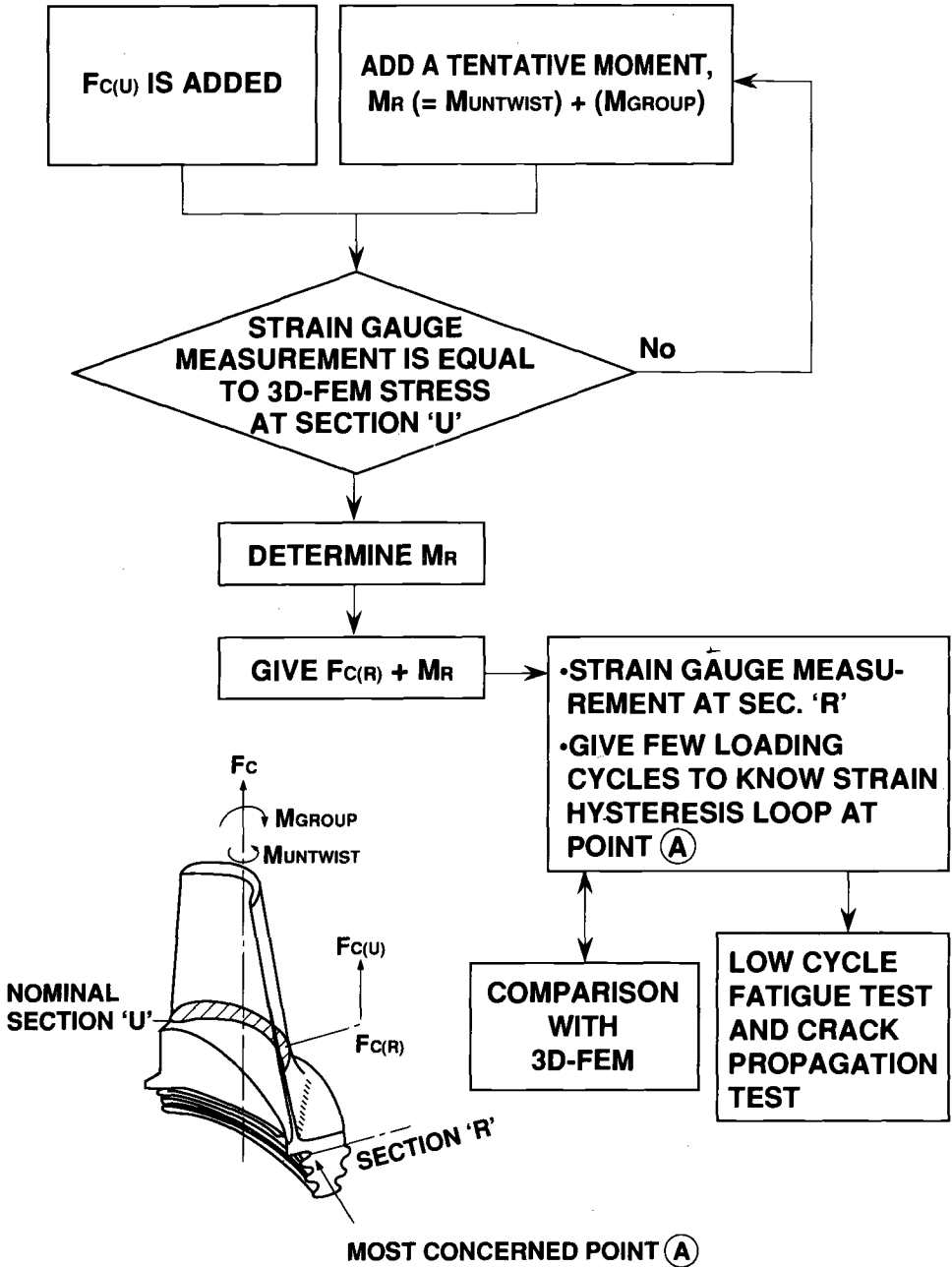


FIG. 10—Procedure of the load application in the blade pull test.

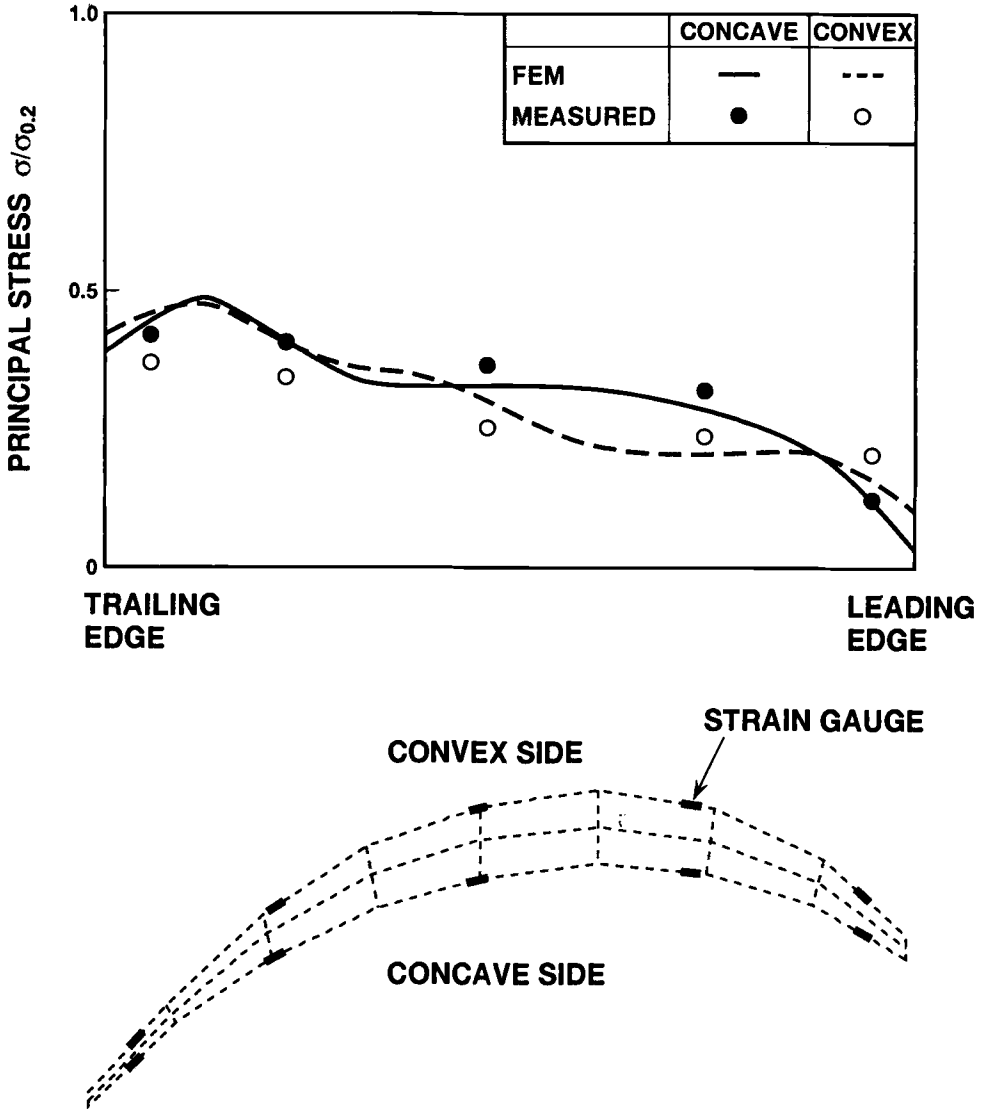


FIG. 11—Comparison between the measured strain and the calculated strain at a nominal section.

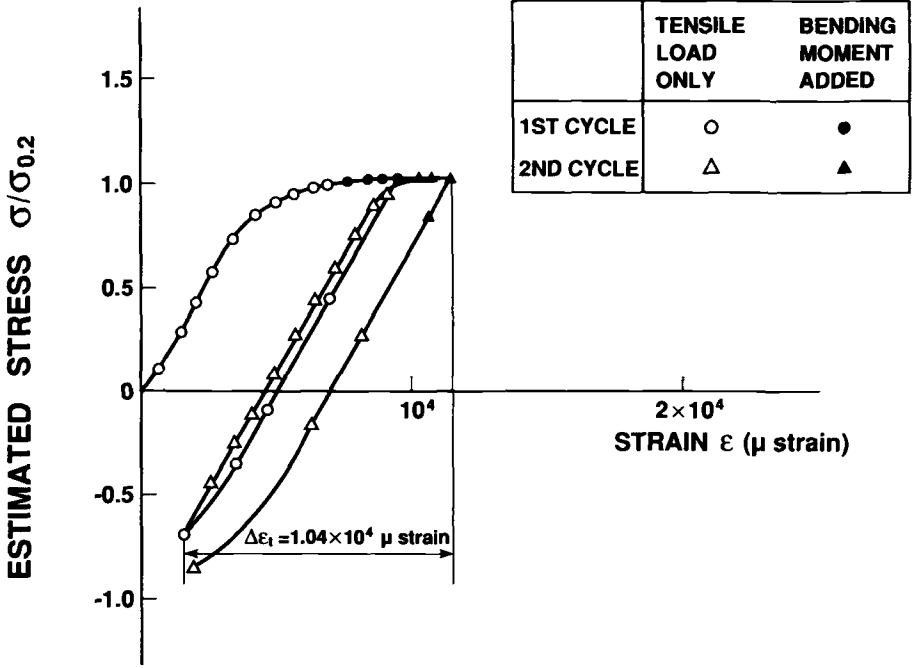


FIG. 12—Estimated stress-measured strain hysteresis loop.

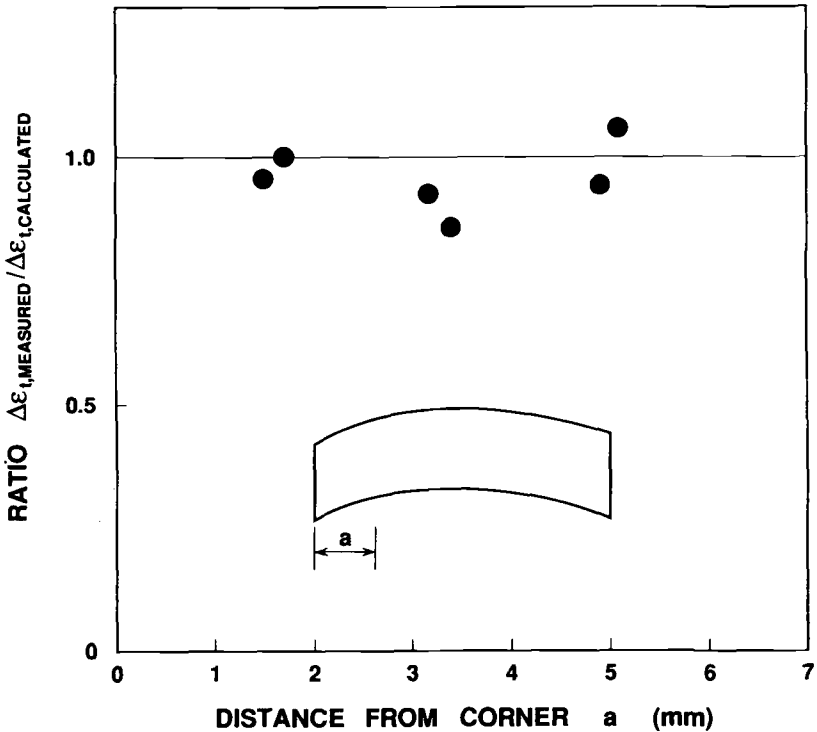


FIG. 13—Comparison between the measured strain and the calculated strain at the blade root.

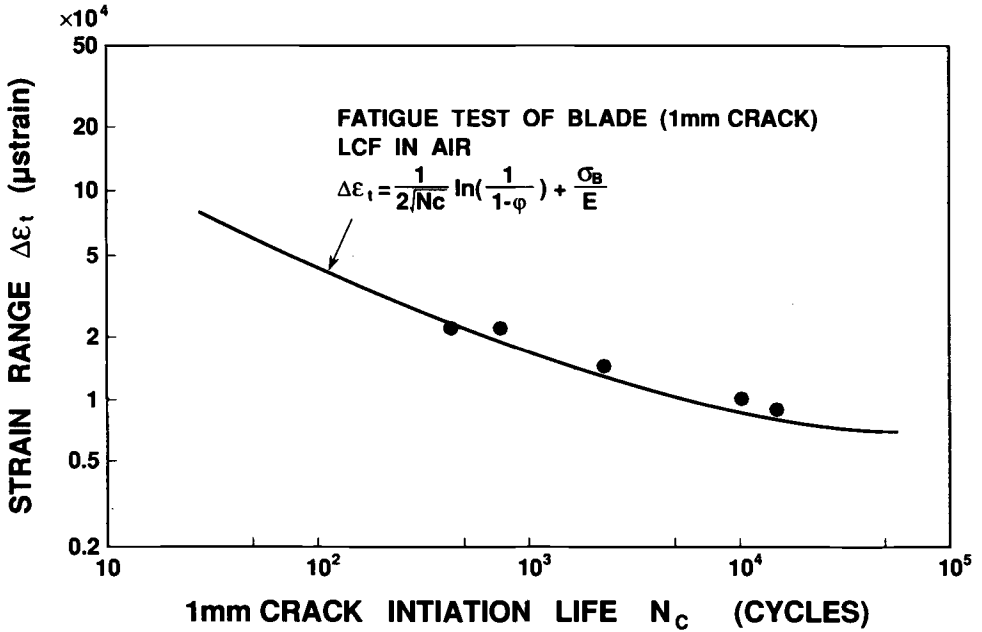


FIG. 14—Test results of fatigue crack initiation at the blade root.

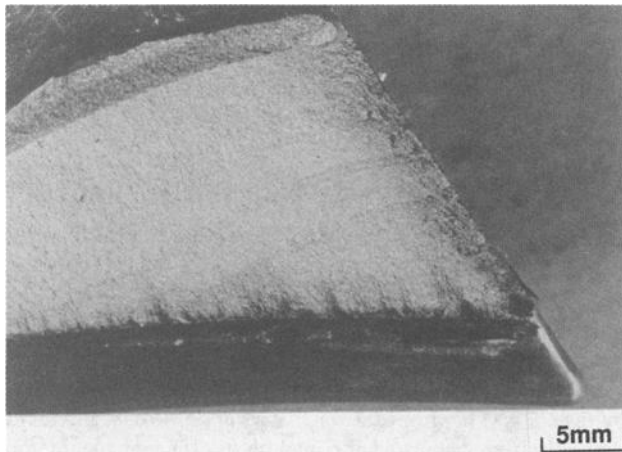


FIG. 15—Example of crack that initiated at the corner of the blade root.

**References**

- [1] Kadoya, Y., "Recent Trend and International Cooperation in Research and Development of Steam Turbine," in Japanese, *Turbo Machinery*, Vol. 19, No. 1, 1991, p. 16.
- [2] Dewey, R. P. and Rieger, N. F., "Survey of Steam Turbine Blade Failure," EPRI CS-3891, 1985.
- [3] Neuber, H., "Theory of Stress Concentration for Shear-Strained Prismatical Bodies with Arbitrary Nonlinear Stress-Strain Law," *Transactions of ASME, Journal of Applied Mechanics*, Vol. 28, No. 4, 1961, p. 544.
- [4] Langer, B. F., "Design of Pressure Vessels for Low-Cycle Fatigue," *Transactions of ASME*, Vol. 84, Series D, 1962, p. 389.

# Review of Factors That Affect Fatigue Strength of Low-Alloy Steel Fasteners

---

**REFERENCE:** Skochko, G. W. and Herrmann, T. P., “Review of Factors That Affect Fatigue Strength of Low-Alloy Steel Fasteners,” *Structural Integrity of Fasteners, ASTM STP 1236*, P. M. Toor, Ed., American Society for Testing and Materials, Philadelphia, 1995, pp. 32–47.

**ABSTRACT:** Axial-load-cycling fatigue tests of threaded fasteners are useful in determining fastener fatigue failure or design properties. By using appropriate design factors between the failure and design fatigue strengths, such tests are used to establish fatigue failure and design parameters of fasteners for axial and bending cyclic load conditions. This paper reviews the factors that influence the fatigue strength of low-alloy-steel threaded fasteners, identifies those most significant to fatigue strength, and provides design guidelines based on the direct evaluation of fatigue tests of threaded fasteners. Influences on the fatigue strength of the thread manufacturing process (machining and rolling of threads) and the effect of fastener membrane and bending stresses, thread root radii, fastener sizes, fastener tensile strength, stress relaxation, mean stress, and test temperature are discussed.

**KEYWORDS:** load-controlled fatigue; thread fatigue; machined, ground, rolled threads; low-alloy steel fasteners; mean stress effects

## Nomenclature

$A_s$	Tensile area of fastener thread = $0.7854 (D - 0.9743/n)^2$ , in. <sup>2</sup>
$D$	Basic major thread diameter, in.
$n$	Threads per inch
$N_f$	Cycles to failure
$S_a = S_{alt}$	Nominal alternating stress on tensile area of thread, $A_s$ , exclusive of stress concentration factors, ksi
$S_{mean}$	Nominal mean stress on tensile area of fastener thread, $A_s$ , exclusive of stress concentration factors, ksi
$S_{max}$	Nominal maximum stress on tensile area of fastener thread, $A_s$ , exclusive of stress concentration factor, ksi
$S_u$	Ultimate tensile strength, ksi

Snow and Langer [1] evaluated threaded fastener test data and proposed a fatigue design curve for low-alloy fasteners. The proposal was based upon  $K_f = 4$  and an unnotched fatigue failure curve for low-alloy steel adjusted for maximum effect of mean stress using a cubic correction for mean stress. Design factors of 1.5 on stress and 5.7 on cycles were used to account for significant crack initiation. That evaluation was followed by Fritz [2], who summarized and evaluated 198 fatigue tests of 1 to 5<sup>1</sup>/<sub>16</sub>-in. (25.4 to 128.6-mm) diameter, eight-thread series, low-alloy steel fasteners and proposed using a zero mean stress design fatigue

---

<sup>1</sup> Senior engineer, Westinghouse Electric Corp., Schenectady, NY.

<sup>2</sup> Manager, Mechanical Analysis, Westinghouse Electric Corp., Schenectady, NY.

curve, accounting for the effects of mean stress with cubic correction and using a high-temperature correction multiplier. The data summarized by Fritz are reevaluated here with the objective of separating the variables into those that significantly affect fatigue strength and those that are of lesser significance and thus could be neglected when establishing fatigue design properties of such fasteners.

**Summary**

This paper presents a means of evaluating significant variables that affect the fatigue strength of low-alloy steel fasteners. The data are first segregated into the machined thread, rolled thread, and rolled head fillet populations. By utilizing the derived least squares fits of each data population, all data can be adjusted either to the machined or to the rolled thread data baselines, reducing the data scatter and allowing the effects of significant variables to be quantified. The most significant factors in the fatigue of evaluated fasteners are the thread manufacturing process and the mean stress effects.

**The Database**

References 1 and 2 summarize the low-alloy (AISI 4140 and AISI 4340) steel-threaded fastener data. That test data population consists of 198 fastener fatigue tests, shown plotted in Fig. 1, with 69 machined, ground, machined and ground, and machined, ground, and

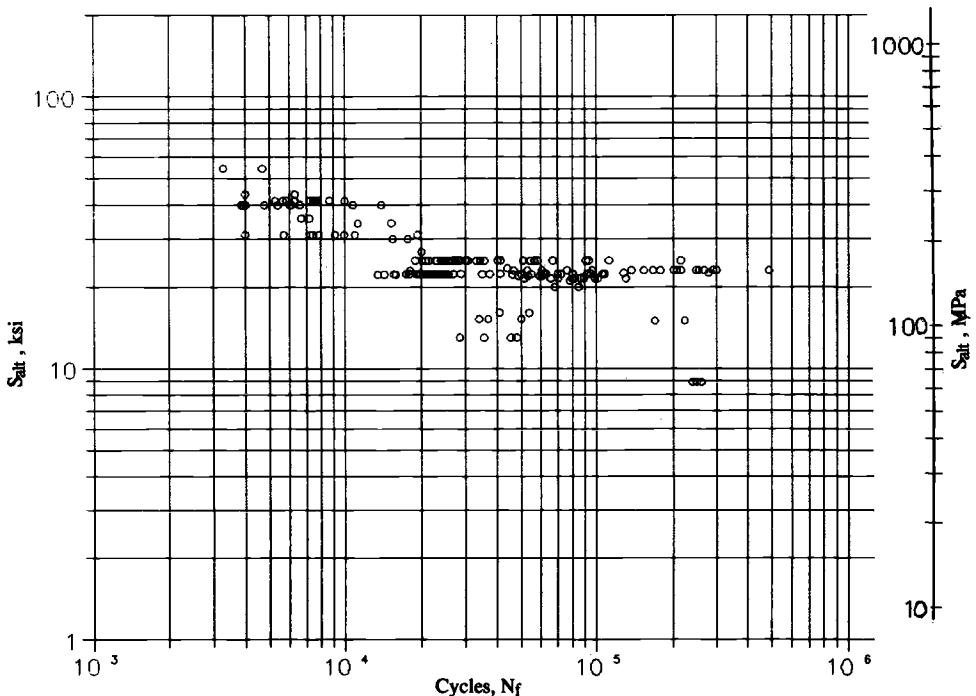


FIG. 1— $S_{alt}$  versus cycles  $N_f$  plot for machined and rolled threads and rolled bolt head fillets tested with  $0.248 \leq S_{max}/S_u \leq 0.822$ .

TABLE 1—*Low-alloy steel threaded fastener data summarized in Refs 1 and 2.*

	Rolled	Machined	Ground	Machined and Ground	Machined and Ground and Polished	Total Tests
Threads failed	50	2	44	13	4	113
Threads runouts	0	1	0	0	0	1
Bolt heads failed	62	0	5	0	0	67
Bolt heads runouts	17	0	0	0	0	17
Totals	129	3	49	13	4	198

polished fasteners, 79 rolled head fasteners, and 50 rolled thread fasteners. Twelve tests were run at high temperature [500°F (260°C)], and the remaining 186 were tested at 70°F (21.1°C). The data are summarized in Table 1.

The bolts that failed in threads have been treated as thread failures. Of the 186 fatigue tests at 70°F (21.1°C), 67 bolts failed in bolt head fillets, with 5 failures in ground head fillets, and 62 bolt head failures in rolled head fillets. Although, because of differences in loading and stress concentration effects, rolled bolt head fillet failures could be expected to differ in fatigue strength from thread failures, we will demonstrate in this evaluation that these failures happen to be comparable in fatigue strength to rolled thread failures. The thread data population contains 17 bolt head runouts and 1 machined thread runout. Of the 500°F (260°C) tests, 3 failed in machined threads and 9 failed in rolled threads.

The reported ultimate and yield tensile strengths of fastener materials fell into the ranges shown in Table 2.

Fatigue tests were conducted with alternating load control with dimensionless mean nominal stresses  $S_{\text{mean}}/S_u$  ranging from 0.14 to 0.50 and dimensionless maximum nominal stresses  $0.341 \leq S_{\text{max}}/S_u \leq 0.724$  for machined threads and  $0.248 \leq S_{\text{max}}/S_u \leq 0.822$  for rolled threads and head fillets. Failure cycles, at complete separation, ranged between 3285 and 487 000.

The fatigue tests of the database in Ref 1 include the following variables that need to be assessed as to their significance to allow meaningful evaluation of the fatigue data.

- studs or bolts
- rolled or machined threads
- different mean stresses
- tests at 70°F (21.1°C) and at 500°F (260°C)
- thread root radii and bolt head fillets radii
- fatigue runouts

TABLE 2—*Reported tensile strengths of fastener materials shown in Table 1.*

T test, °F	$S_u$ range, ksi (MPa)		$S_y$ range, ksi (MPa)		$S_{u \text{ Ave}}^a$ ksi (MPa)	$S_{y \text{ Ave}}^a$ ksi (MPa)
	Max	Min	Max	Min		
70	170 (1172)	128 (883)	164 (1131)	106 (731)	149 (1028)	135 (931)
500	166 (1145)	130 (897)	147 (1014)	106 (731)	148 (1021)	126.5 (872)

NOTE: °F = 32 + 9/5°C.

- fastener diameter (1 to 5<sup>1</sup>/<sub>16</sub> in.) (25.4 to 128.6 mm)
- fasteners of different ultimate and yield strengths
- tapered nut threads
- modulus
- relaxation

We grouped the machined, ground, and machined and ground and/or polished thread data and treated them as machined thread data. As shown in Table 2, machined thread data alone constitute only a third of the data population. Thus, they are judged insufficient to develop a design fatigue curve in the high-cycle regime. To sort the test variables into significant and insignificant variables, we need to use the combined rolled and machined database.

The following, along with the work of Snow and Langer [1] and Fritz [2], evaluates the impact of variables that influence fastener fatigue strength. No systematic tests were conducted to segregate each of the variables. We assessed them based on engineering judgment, categorizing them into significant (need to adjust for) and secondary (within scatter band) categories relative to their impact on fatigue strength.

### Evaluation of Variables that Affect Fatigue Strength

The following categorizes the test data variables into those that are significant and those that are not. The test data were segregated according to the location of the fastener failure, i.e., stud and bolt thread or bolt head fillet and whether the thread was machined, ground, machined and ground, or rolled. We assumed that bolts that failed in threads, as well as fatigue runouts, could be conservatively grouped with thread failures.

#### *Effect of Material Strength*

Figure 1 shows a plot of nominal alternating stress,  $S_{alt}$ , versus cycles to failure,  $N_f$ , for all 198 data without segregating the data according to fastener type. Figure 2 also shows a plot of the 198 nonsegregated data after normalizing the data relative to the reported tensile strength of fastener material. Normalization of nominal alternating stresses by  $S_u$  reduces the scatter at low cycles without affecting it at high cycles. Thus, the following uses normalized data to account for different tensile strengths among the specimens.

#### *Fastener Type (Stud or Bolts) and Manufacturing Process, Rolled or Machined Threads*

Figure 3 shows a plot of the 198 fatigue test data segregated according to the location of the failure, i.e., machined threads and rolled thread and bolt head fillets. Although machined thread data are limited, Fig. 3 shows both an apparent benefit of rolling the threads and the bolt head fillets on high-cycle fatigue strength when compared to machined threads. Also, rolled thread and bolt fillet data fall into a relatively narrow scatter band, suggesting that there is little difference in fatigue behavior between rolled threads and rolled bolt head fillets. Therefore, the distinction between rolled bolt head fillets and threads is considered minor compared to machined, ground, and/or polished threads.

Figure 4 identifies and compares the least squares fits (LSFs) of different data populations of Fig. 3. That figure, and the LSFs of the data shown in the Appendix, show that, above 10 000 cycles, the machined threads fall considerably both below the rolled head fillet or the rolled thread data, while rolled head fillets and rolled threads are of comparable fatigue strength.

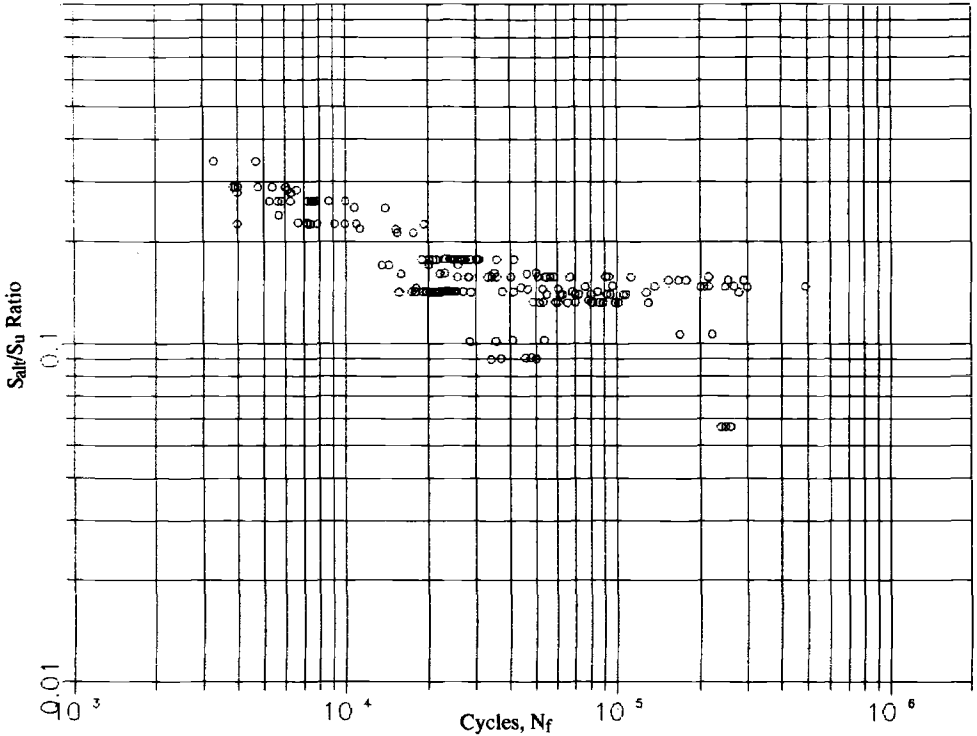


FIG. 2— $S_{alt}/S_u$  plot versus cycles  $N_f$  for machined and rolled threads and rolled bolt head fillets tested with  $0.248 < S_{max}/S_u < 0.822$ .

The differences in fatigue strength due to the thread manufacturing process and the location of failures (head fillet versus threads) are clearly shown by the least square fits (defined in the Appendix) of the different data populations, plotted in Fig. 4. Figure 4 shows that rolled thread and rolled bolt head fillets are of comparable strength, while the machined threads are the most limiting in fatigue. The thread manufacturing process is thus seen to be a significant variable.

Having the LSFs of segregated data populations, the individual test data of any of the fastener types could be adjusted to any other fastener-type baseline by a cycle-dependent function of the ratio of their least squares fits. This offers an opportunity to study the effects of variables such as mean stress as a function of cycles based on a larger population base than could be made if each population were treated separately. Consequently, we used the following adjustment process:

1. We established LSFs of the data populations and used ratios of LSFs to define cycle-dependent adjustment functions.
2. We operated on each  $S_{alt}/S_u$  data point by the adjustment function to get the desired population, i.e., machined threads.
3. To assess the effectiveness of the adjustment process, we compared the adjusted data with LSFs originally determined in Fig. 4 and in the Appendix.

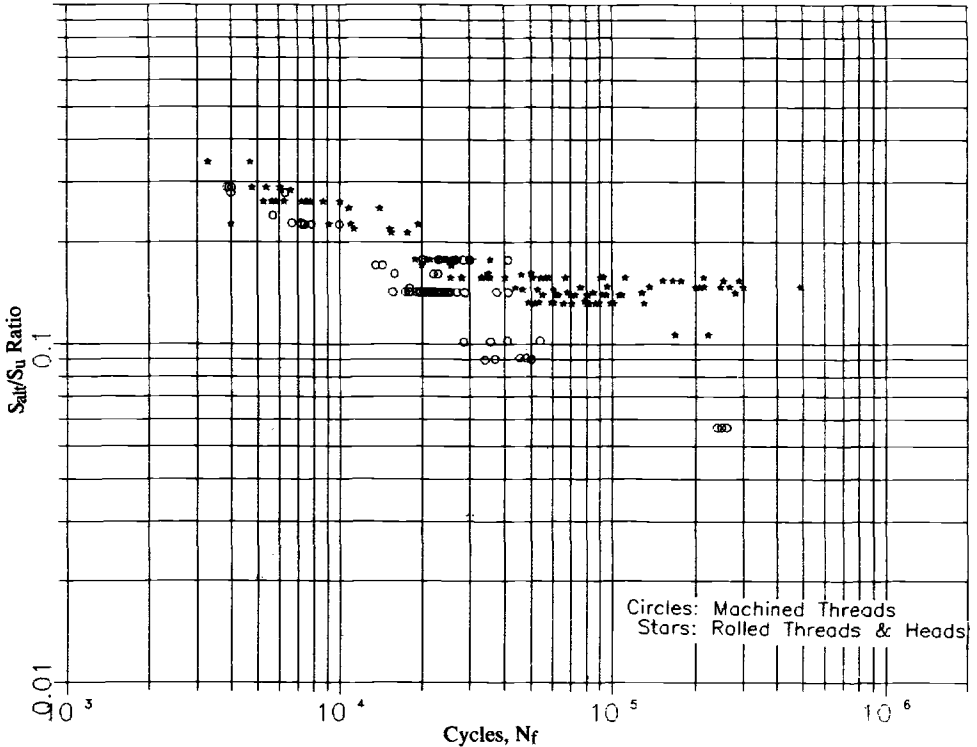


FIG. 3—Plot of  $S_{alt}/S_u$  versus cycles  $N_f$  for machined threads versus rolled threads and bolt head fillets tested with  $0.248 \leq S_{max}/S_u \leq 0.822$ .

Figure 5 shows all 198 test data adjusted to the machined database line compared to the least squares fit of the original, unadjusted machined thread data from Fig. 4. It shows that the adjusted data scatter bands are reasonably narrow and that the LSF curve of the machined data population is reasonably representative of the mean of the adjusted data. We propose to develop a fatigue failure curve only for machined data. Being a lower bound of all the data, such a curve can then be used conservatively for the rolled threads and for bolt head fillets as well.

#### *Treatment of Runouts*

The data population contains 18 runouts, 17 at 70°F (21.1°C) and 1 at 500°F (260°C). The fatigue runouts were conservatively assumed to be, and were counted as, failures at the runout cycles. They were not considered a significant test variable since they fall within the data scatter band.

#### *Mean Stress*

The fatigue tests have been conducted with  $0.25 \leq S_{max}/S_u \leq 0.82$  and  $0.14 \leq S_{mean}/S_u \leq 0.50$ . Such a large range of  $S_{max}/S_u$  values suggests that the mean stress could be a

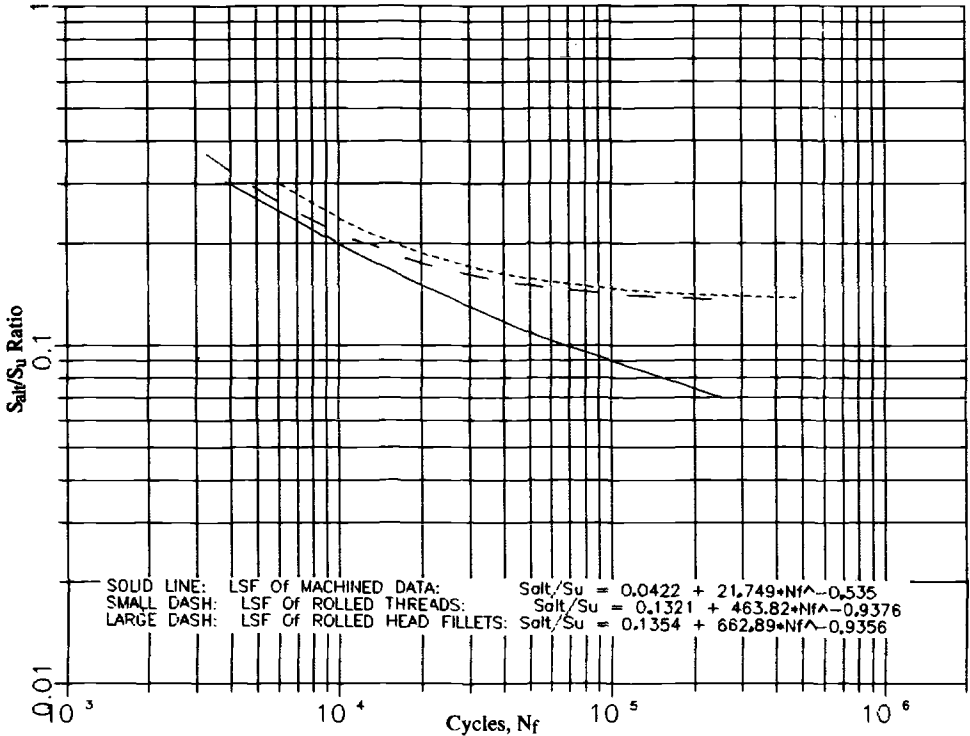


FIG. 4—Least squares fits of  $S_{alt}/S_u$  versus cycles  $N_f$  for machined and rolled threads and rolled bolt head fillets tested with  $0.248 \leq S_{max}/S_u \leq 0.822$ .

significant variable on fatigue strength of fasteners; this will be further evaluated later in this paper.

**Test Temperature**

Figure 6 shows how the twelve high-temperature tests, adjusted for the manufacturing process to the machined database line, compare to the least squares fit of the machined data from Fig. 4. These test results appear to follow the room-temperature LSF of machined data, but apparently represent two different populations, i.e., those below 28 000 cycles and those with failures above 50 000 cycles. The few test data at 500°F (260°C) are believed to be insufficient to allow meaningful assessment of high-temperature effects on fatigue strength of rolled and/or of machined threads.

**Nut Thread Taper**

As mentioned by Haywood [3] and Forrest [4], tapered threads of mating nuts could enhance fatigue strength of fasteners by redistributing the thread loads. The data of Refs 1 and 2 on tapered threads is neither systematic nor extensive enough to quantify the benefits of nut thread tapers on the increase of fatigue strength. The benefits of tapered nut threads are believed to depend on stress amplitude and material and are most likely of the order of the test data scatter band. Although 41 ground thread fasteners and 39 rolled thread fasteners

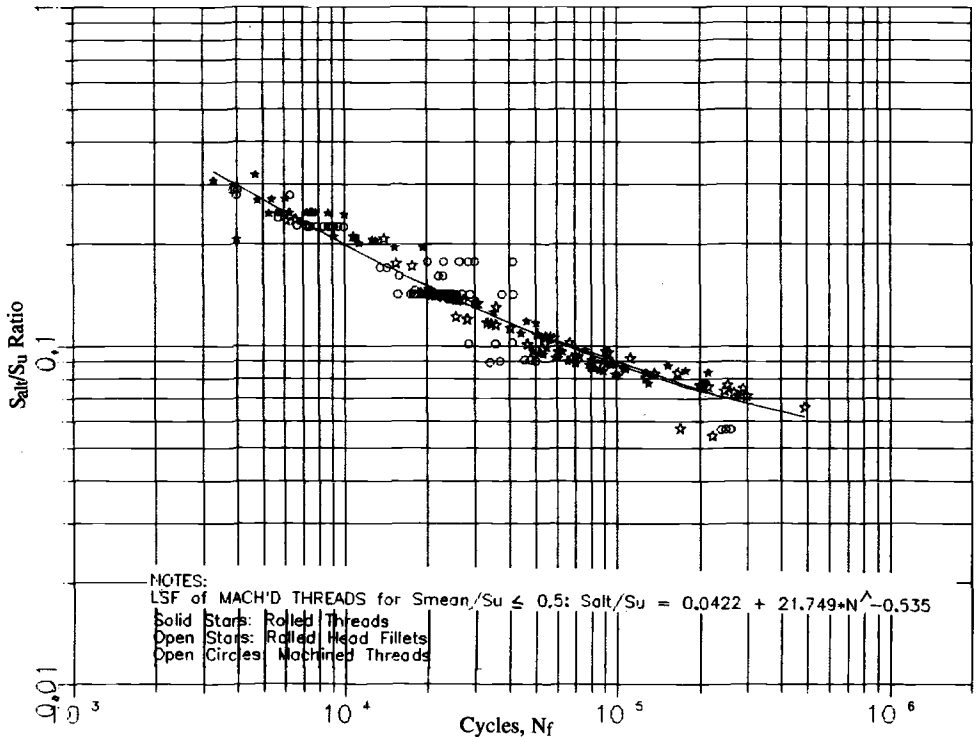


FIG. 5—LSF of machined thread data and  $S_{alt}/S_u$  of all data versus cycles  $N_f$ , adjusted to machined data baseline, tested with  $0.298 < S_{max}/S_u \leq 0.82$ .

were tested with nut threads tapered 0.004 in./in., without carefully controlled fatigue tests of fasteners loaded by tapered nut threads, the existing data do not permit quantification of this variable.

#### Fastener Size

Data in Fig. 5 represent fatigue strengths of 1 through  $5\frac{1}{16}$ -in. (25.4 through 128.6-mm)-diameter fasteners and fall into a reasonably narrow and well-behaved scatter band. Detailed segregation of the test data according to fastener size is not feasible because of the limitations of the available database. The available data do not allow quantifying size effect because this effect could be masked by other test variables. Although, based on Ref 3, it could be expected that smaller fasteners are likely to be more fatigue resistant than the larger fasteners, the use of a single-failure fatigue curve is more practical than multiple curves based on fastener size. We had examined the 198 data by segregating them into three different fastener size populations to qualitatively assess the fastener size effect. We found that the differences in fatigue strengths of small (less than  $1\frac{1}{2}$  in. (38.1 mm) in diameter), medium ( $1\frac{1}{2}$  to  $2\frac{1}{2}$  in. (38.1 to 63.5 mm) in diameter) and of large (greater than  $2\frac{1}{2}$  in. in diameter) fasteners fall within the scatter band of the test data. As shown in Fig. 12.4 of Ref 3 for bolts 1 to 3 in. (63.5 mm) in diameter, we found that, for the data in this evaluation, fastener size is of secondary importance and is of the order of data scatter.

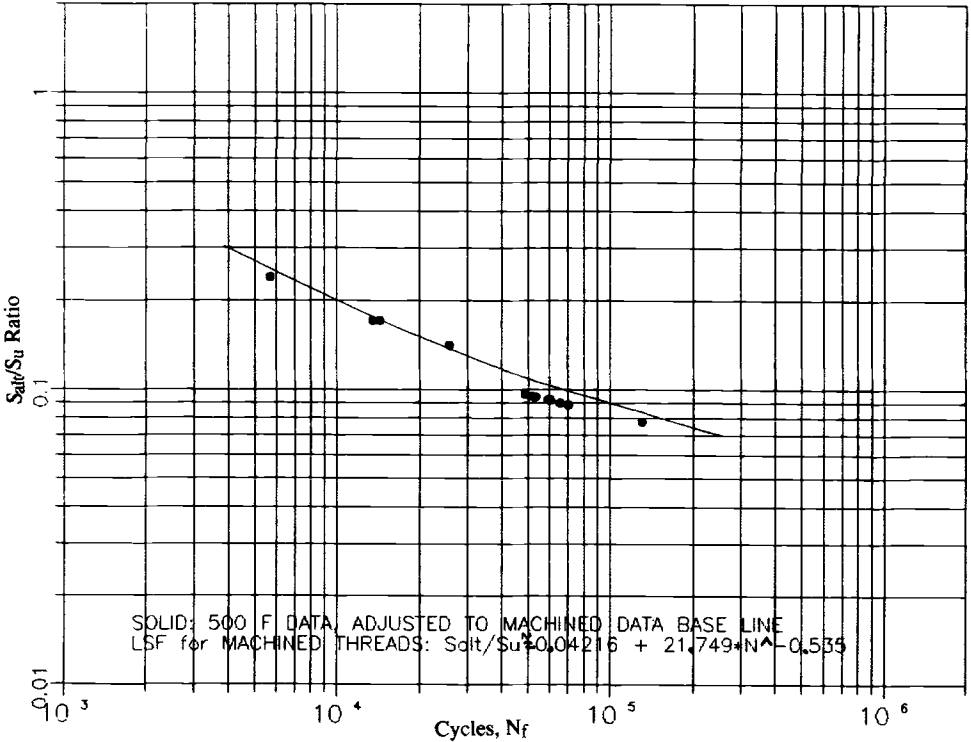


FIG. 6—LSFs of machined data compared to 500°F (260°C) data adjusted to machined data baseline.

*Thread Root Radius or K<sub>t</sub> Factor*

In Refs 1 and 2, no systematic, well-controlled tests were done examining the effects of thread root radii. The tests in the database have been made on fasteners with reported root radii of 10 to 21 mils (0.25 to 0.53 mm) in 1 through 5 1/16-in. (25.4 through 128.6 mm)-diameter, 8-thread-series fasteners. These are typical thread root radii for such threads. Root radii are commonly accepted as significant for crack initiation, but they are unlikely to affect crack propagation. Once crack growth is started in the thread root, the geometric effect of the thread root radii on the stress intensity factor diminishes. Although the investigation in Ref 1 attempted to determine fatigue strength reduction factors for threads, that in Ref 2 considered fatigue as a multistage process (crack initiation, crack propagation, and final fracture) and based the investigation on nominal stresses. We consider that any significance of the narrow range of root radii on fatigue strength of 1 through 5 1/16-in. (25.4 through 128.6 mm)-diameter fasteners is perhaps masked by other variables, making such typical root radii of secondary importance.

Also, because root radii are a variable inherent in the nominal stress-based fatigue curve being derived, extrapolations to very small root radii must be based on engineering judgment. Consequently, our evaluation was based on the assumption that the stress concentrations due to root radii are inherent in the data evaluated on a nominal stress basis.

### *Young's Modulus*

Young's modulus is not a significant variable in load-controlled fatigue tests of low-alloy steel fasteners loaded by steel nuts or threaded blocks since the moduli of fasteners and of mating threads are either comparable or nearly the same. The use of a Young's modulus ratio to correct load-controlled fatigue data and failure or design fatigue curves for temperature does not appear to be justified because in load-controlled fatigue tests, the local stresses at the thread roots are independent of Young's modulus. Test data at different temperatures are needed to show if notched fatigue strength under load control degrades with increased temperature and if degradation is related to Young's modulus of the fastener materials.

### *High-Temperature Stress Relaxation*

High-temperature stress relaxation is unlikely to influence the fatigue strength of machined threads. However, as heat treatment after thread rolling, stress relaxation could be expected to reduce the fatigue strength of rolled threads because high temperature is likely to lower the beneficial residual stresses in rolled threads which account, at least partially, for their increased fatigue strength. Thus, although, high-temperature stress relaxation could be a significant variable for rolled threads, especially at higher cycles to failure, we do not consider it a significant variable on fatigue strength of machined and/or ground threads. Also, the low-temperature test data are insufficient to quantify this effect either for rolled or for machined threads.

### **Mean Stress Effects in Derivation of Fatigue Failure Curves**

The review of the data in the last section identified the significant variables that could affect the fatigue strength of fasteners. Specifically, the thread manufacturing process and the mean stress have been identified as being significant variables whose effects need to be quantified. Temperature has also been identified as potentially significant, but data are insufficient to assess the effect.

The following method is used to quantify the effects of the thread manufacturing and mean stress. The nominal alternating stress data, normalized by  $S_u$ , are systematically segregated according to thread manufacturing method and location of fastener failure (bolt head fillet or thread). Then, the ratios of LSFs of the segregated data representing different manufacturing processes, shown in the Appendix, form cycle-dependent adjustment functions for thread manufacturing variables. Using these functions, the data can be adjusted either to machined thread, to rolled thread, or to bolt head fillet baselines. We chose to adjust the rolled thread and head fillet data to machined thread data baseline by the ratio of LSFs shown in Fig. 4 and in the Appendix, respectively. The adjusted data are shown in Fig. 7 as a function of  $S_{\text{mean}}/S_u$ . Note that data adjustment was made only to  $S_{\text{alt}}/S_u$  while holding  $S_{\text{mean}}/S_u$  constant, so that the adjustment reflects a change only in the stress range.

From Fig. 7, it is observed that data fall below the notched tensile strength,  $S_u^{\text{notched}}/S_u \cong 1.1$  and are lacking at mean stress levels above  $S_{\text{mean}}/S_u \cong 0.5$ . Hence, our conclusions about mean stress effect are limited by the data  $S_{\text{mean}}/S_u \leq 0.5$ .

To examine the effect of  $S_{\text{mean}}$ , the data of Figs. 5 and 7 are grouped by  $S_{\text{alt}}/S_u$  and cycle ranges in Fig. 8. Figure 8 replots data of Fig. 5, showing five arbitrary cycle ranges for grouping the data between 30 200 and 487 000 cycles. The data within each of these cycle ranges are examined for mean stress effects at the average of each cycle range. At low cycles and high  $S_{\text{alt}}/S_u$  values, below 30 200 cycles, mean stress effects were found either not to

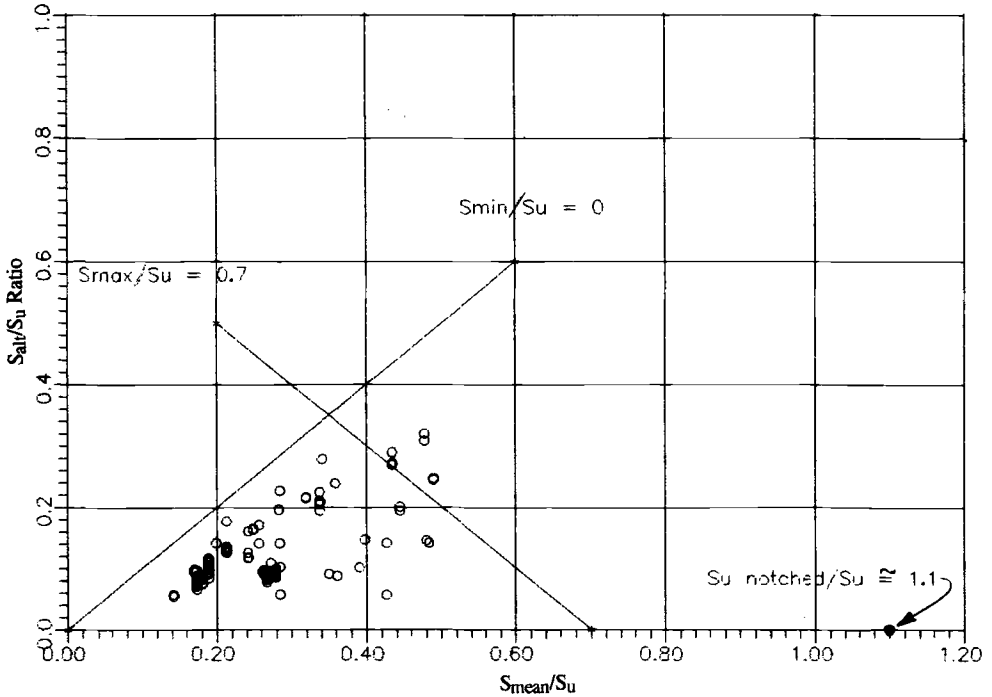


FIG. 7—Plot of  $S_{alt}/S_u$  data versus  $S_{mean}/S_u$  for all data adjusted to machined data baseline for  $0.248 \leq S_{max}/S_u \leq 0.820$ .

exist or are perhaps masked by data scatter. Figures 9 through 13 show that, in the cyclic range from 30 200 to 487 000 cycles, linear least squares fits of the form  $S_{alt}/S_u = A - B \cdot S_{mean}/S_u$  apply; the exception is an LSF at 138 300 cycles, which showed nearly no dependence on mean stress. These LSFs indicated a reduction of  $S_{alt}/S_u$  with increased  $S_{mean}/S_u$ .

The evaluation of the LSF sets shown in Figs. 9 through 13 showed that they intersect the abscissa at approximately  $S_{mean}/S_u = 1.54$ , well beyond the notched tensile strength of low-alloy steel,  $S_{mean}/S_u = 1.1$ . Fitting linear LSFs between the coordinates  $S_{alt}/S_u$  at  $S_{mean}/S_u = 0.2$ , given by the LSF expressions shown in Figs. 9 through 13 and  $S_{mean}/S_u = 1.54$ , allows adjusting the originally computed LSFs to a common intercept  $S_{max}/S_u = S_{mean}/S_u = 1.54$ . These adjusted LSFs were then used to determine the maximum mean stress correction ( $S_{max}/S_u = 0.7$ ) to be applied to the failure curve shown in Fig. 5. The ratio of the original LSF ordinates to those corrected for maximum effect of mean stress equals 1.52. Thus, for  $S_{max}/S_u = 0.7$ , the mean stress effect is significant and the failure curve should equal  $S_{alt}/S_u = (0.04216 + 21.749 \cdot N^{-0.535})/1.52 \approx 0.028 + 14.31 \cdot N^{-0.535}$ . Figure 14 compares the data to the LSF curve of Fig. 5 and shows the failure curve (dashed), which has been adjusted for maximum effect of mean stress,  $S_{max}/S_u = 0.7$ .

The above procedure could be applied to the data to adjust them to the rolled thread and bolt head fillet radii baselines. Also, if needed, failure curves for different  $S_{max}/S_u \leq 0.7$  could be developed as an alternative to a single, maximum mean-stress-effect adjustment.

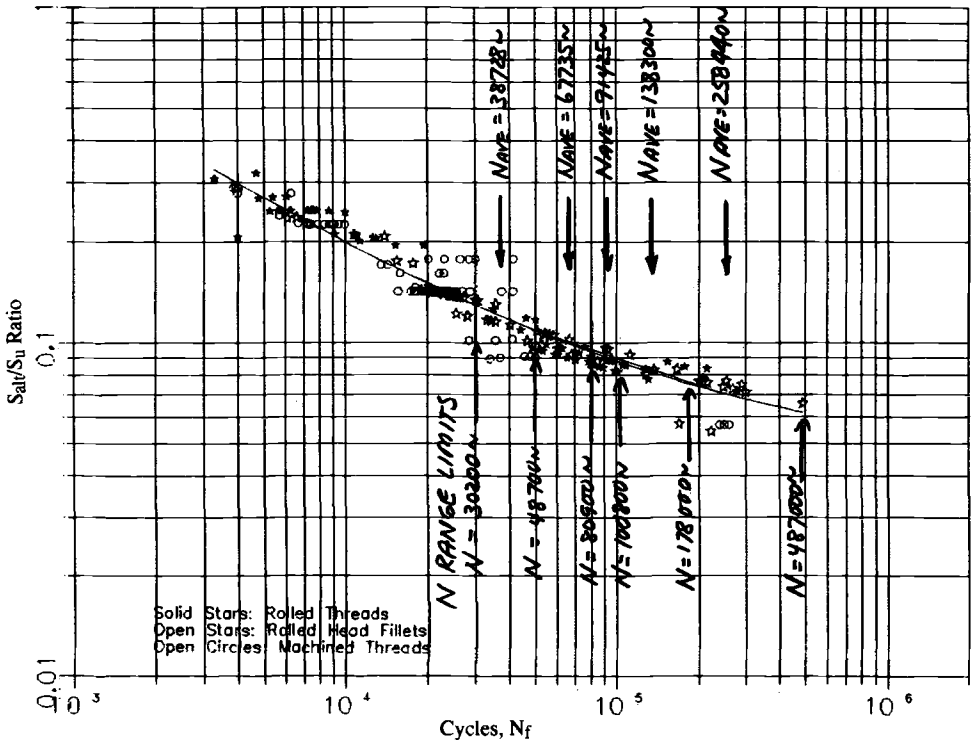


FIG. 8—LSF of machined thread data and  $S_{alt}/S_u$  of all data versus cycles  $N_f$  adjusted to machined data baseline tested with  $0.248 \leq S_{max}/S_u \leq 0.82$ .

## Conclusions

1. Data evaluations have shown that by segregating the data, the effects of thread manufacturing can be quantified. By adjusting the data for these effects, different sets of 198 data were examined for effects of mean stress. Least squares fits of data showed mean stress dependence; however, tests with high mean stresses at  $S_{max}/S_u$  are needed to confirm predictions made from tests at lower mean stresses and to quantify mean stress effects.

2. Fastener strength is not a significant variable on fatigue strength, and the derived fatigue failure curve adequately accounts for size effect. Evaluation of these issues showed the following:

1. Inclusion of rolled data in the evaluation did not bias the derived failure curve for machined threads unconservatively upwards.
2. For low-alloy steel fasteners, the tensile strength of fastener material is not a significant variable that could influence the fatigue strength of fasteners.
3. For the machined thread fasteners of 1 to  $5\frac{1}{16}$  in. (25.4 to 128.6 mm) in diameter, size effect is not a significant variable.

3. A single, nominal stress-based fatigue failure curve for 70°F (21.1°C) was determined for low-alloy steel-machined threaded fasteners, as shown in Fig. 14. This curve incorporates a correction for maximum effect of mean stress.

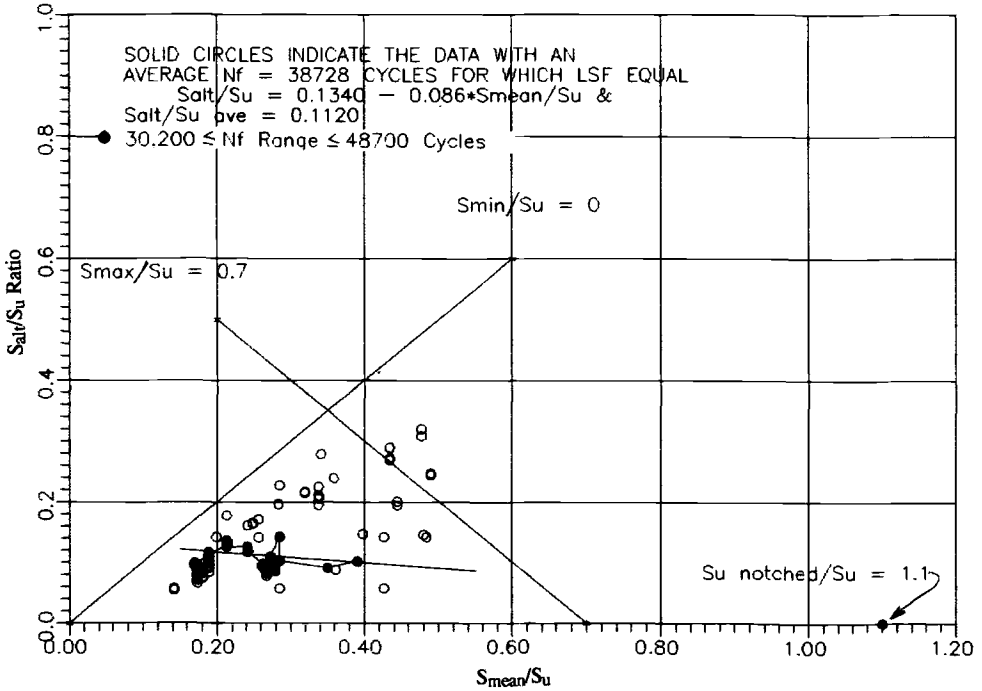


FIG. 9—Plot of  $S_{alt}/S_u$  data versus  $S_{mean}/S_u$  for all data adjusted to machined data baseline for  $0.248 \leq S_{max}/S_u \leq 0.820$ .

4. The procedure used to develop the failure curve for machined threads could also be used to develop similar failure curves for rolled thread fasteners as well as for fatigue evaluation of rolled bolt head fillets.

5. Test data at 500°F (260°C) are insufficient to provide corrections needed to account for high temperature. Additional data at high temperatures are needed to quantify adjustments to fatigue evaluations that account for high temperatures.

6. A fatigue failure curve (dashed) such as developed in Fig. 14 could be further adjusted downward and used to predict crack initiation in threaded fasteners for the start of crack growth calculations or with appropriate design factors could be used for fatigue design of fasteners.

## APPENDIX

### Least Square Fits of Data Populations

The following least squares fits of low-alloy, load-controlled fastener fatigue test data obtained by using program ENPLOT:

1. Machined, ground, and/or polished thread data:

$$S_a/S_u \text{ at } 70^\circ\text{F (21.1}^\circ\text{C)} = 0.04216 + 21.749 \cdot N_f^{-0.535}$$

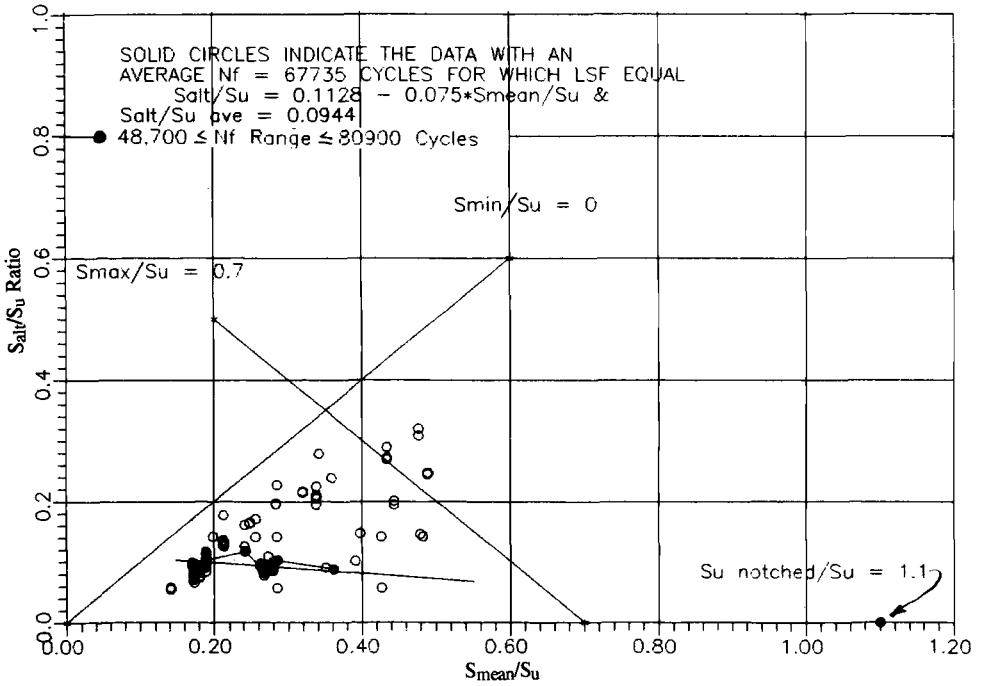


FIG. 10—Plot of  $S_{alt}/S_u$  data versus  $S_{mean}/S_u$  for all data adjusted to machined data baseline for  $0.248 \leq S_{max}/S_u \leq 0.820$ .

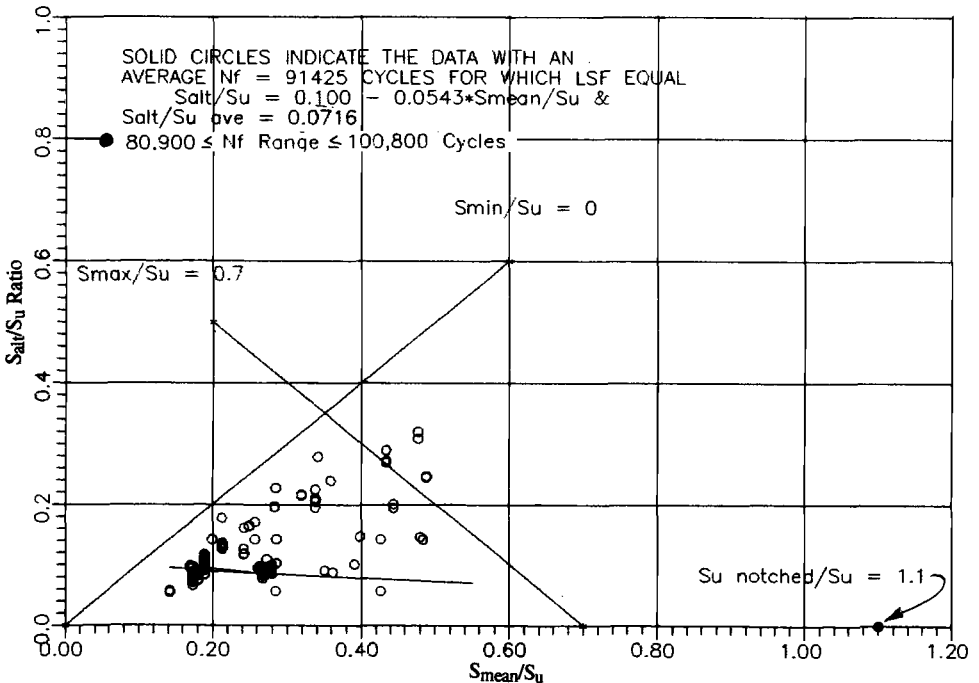


FIG. 11—Plot of  $S_{alt}/S_u$  data versus  $S_{mean}/S_u$  for all data adjusted to machined data baseline for  $0.248 \leq S_{max}/S_u \leq 0.820$ .

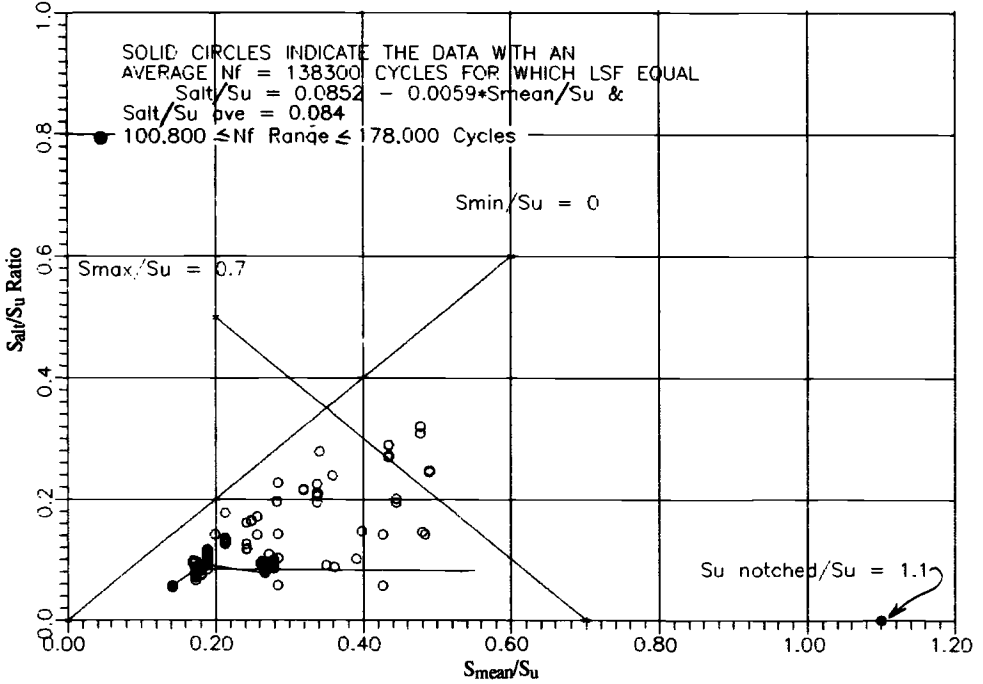


FIG. 12—Plot of  $S_{alt}/S_u$  data versus  $S_{mean}/S_u$  for all data adjusted to machined data baseline for  $0.248 \leq S_{max}/S_u \leq 0.820$ .

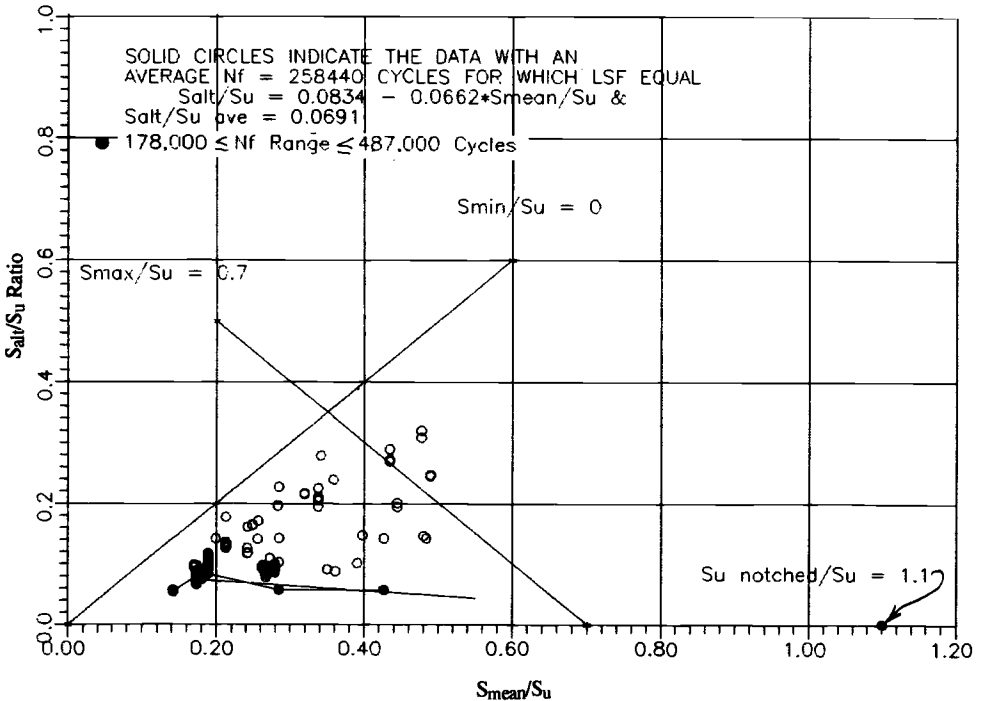


FIG. 13—Plot of  $S_{alt}/S_u$  data versus  $S_{mean}/S_u$  for all data adjusted to machined data baseline for  $0.248 \leq S_{max}/S_u \leq 0.820$ .

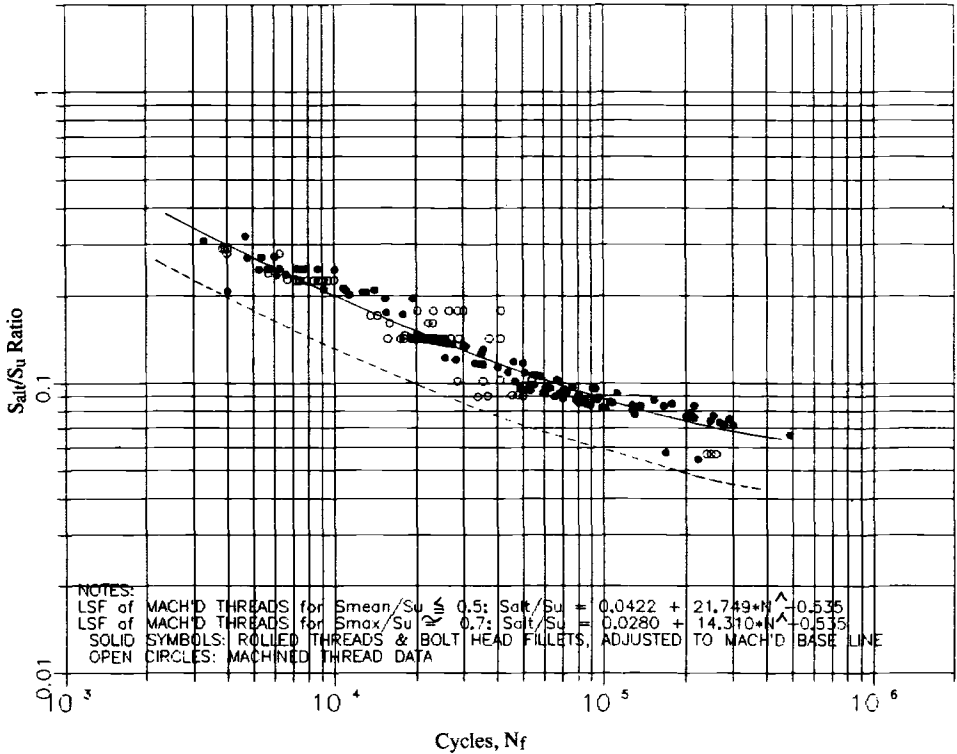


FIG. 14—LSF for  $S_{mean}/S_u \leq 0.5$  and for  $S_{max}/S_u \approx 0.7$  and data adjusted to machined data baseline.

2. Rolled thread data:

$$S_a/S_u \text{ at } 70^\circ\text{F (21.1}^\circ\text{C)} = 0.1321 + 463.82 \cdot N_f^{-0.9376}$$

3. Rolled bolt head fillet radii data:

$$S_a/S_u \text{ at } 70^\circ\text{F (21.1}^\circ\text{C)} = 0.1354 + 662.89 \cdot N_f^{-0.9356}$$

References

[1] Snow, A. L. and Langer, B. F., "Low Cycle Fatigue of Large Diameter Bolts," ASME Paper 66-Pet-8, American Society of Mechanical Engineers, New York, September 1966.  
 [2] Fritz, R. J., "Cyclic Stress Limits for Bolts and Studs," ASTM Paper 67-Met-23, American Society of Mechanical Engineers, New York, April 1967.  
 [3] Heywood, R. B., "Designing Against Fatigue of Metals," Reinhold Publishing Corp., New York, 1962, pp. 267-271.  
 [4] Forrest, P. G., *Fatigue of Metals*, Pergamon Press, Elmsford, NY, 1962, pp. 267-268.

# **Failure Evaluation and Criteria**

James A. Davis<sup>1</sup> and Richard E. Johnson<sup>1</sup>

# The Regulatory Approach to Fastener Integrity in the Nuclear Industry

---

**REFERENCE:** Davis, J. A. and Johnson, R. E., "The Regulatory Approach to Fastener Integrity in the Nuclear Industry," *Structural Integrity of Fasteners, ASTM STP 1236*, American Society for Testing and Materials, Philadelphia, PA, 1995, pp. 51–59.

**ABSTRACT:** Fasteners used in operating nuclear power plants are subjected to specific design rules. The regulatory basis for these rules is contained in Part 50 of Title 10 of the *Code of Federal Regulations* (10 CFR Part 50). The Code specifies that safety-related components in an operating nuclear power plant be designed in accordance with the American Society of Mechanical Engineers (ASME) Boiler and Pressure Vessel Code. Section III of the Code sets design rules for tensile loads, bending loads, fatigue stresses, and stress-corrosion-cracking load limits for fasteners larger than 1 in. (2.54 cm) in diameter. The ASME Code also permits design of fasteners by analysis using generally accepted methods such as finite element analysis in place of the ASME Code recommended methods. Section XI of the ASME Code describes inspection requirements for fasteners. Typical inspection methods covered by this code are visual inspection, magnetic particle inspection, liquid penetrant inspection and ultrasonic inspection.

There has been a great deal of interest in safety-related fasteners in nuclear power plants because of the many fasteners that failed in the 1970s and early 1980s. In the early 1980s, the U.S. Nuclear Regulatory Commission (NRC) established Generic Safety Issue 29, "Bolting Degradation or Failure in Nuclear Power Plants." The industry responded to this generic safety issue by forming a Joint Task Group on Bolting that included the Atomic Industrial Forum, the Materials Properties Council, and the Electric Power Research Institute (EPRI). Generic Safety Issue 29 was resolved in October 1991 as a result of the work of the Joint Task Group on Bolting and numerous NRC actions.

Typical examples of fastener degradation will be discussed in this paper along with the regulatory response that was taken to minimize the probability of reoccurrence.

**KEY WORDS:** fastener, nuclear, stress corrosion cracking, boric acid, fatigue, counterfeit, ASME Boiler and Pressure Code, nondestructive examination, in-service inspection

A typical nuclear power plant contains approximately 40 000 fasteners including bolts, washers, nuts, studs, cap screws, and machine screws. With this large number of fasteners, it is not surprising that problems develop over the years with fasteners. In 1983, the U.S. Nuclear Regulatory Commission (NRC) issued a summary report describing the experience in the nuclear industry with fasteners [1]. The most common cause of failure of fasteners in the nuclear industry was stress corrosion cracking (SCC). Many of the SCC incidents involved steam generator manway hatch studs of overly hard alloy steel exposed to a moist environment rich in oxygen. Other SCC incidents involved the use of a molybdenum disulfide lubricant that decomposed at high temperatures, forming hydrogen sulfide, which enhances the SCC process. Other SCC failures were attributed to the use of ferritic or maraging

---

<sup>1</sup> Task manager and materials engineer, respectively, U.S. Nuclear Regulatory Commission, Mail Stop 7D4, Washington, DC 20555.

stainless steel fasteners that were improperly heat treated, resulting in a microstructure very susceptible to SCC. SCC was also observed in steam generator supports and piping restraints. Finally, many SCC fasteners failed inside valve bodies and in reactor vessel internal supports.

The second most common cause of fastener failure was corrosion by boric acid, which is used as the moderator in pressurized water reactors [1]. In general, boric acid can accumulate in sufficient amounts to cause corrosion when borated water leaks from closure gaskets or seals, the water evaporates, and boric acid accumulates, causing accelerated corrosion of carbon or alloy steel fasteners. In one case, boric acid corroded a 3.5-in. (89-mm) fastener to a thickness of 1.1 in. (28 mm).

The third most common cause of fastener failure was fatigue [1]. All of the fatigue failures occurred in supports inside the reactor vessel. The fatigue failures were caused by improper pretorque of the bolts or flow-induced vibration.

In NUREG-0943 [1], the NRC also reported that fasteners failed for the following reasons: (1) fasteners contained quench cracks as a result of improper heat treatment; (2) fasteners were made of the wrong material (carbon steel instead of low-alloy steel); (3) fasteners were improperly torqued because uncalibrated torquing equipment was used; and (4) bolts were not properly sized.

The number of fastener failures each year increased during the late 1970s and early 1980s, prompting the NRC to establish Generic Safety Issue (GSI) 29, "Bolting Degradation or Failure in Nuclear Power Plants." Responding to the establishment of GSI-29, the Atomic Industrial Forum (AIF), the Materials Properties Council (MPC), and the Electric Power Research Institute (EPRI) formed the Joint Task Group on Bolting to address the bolting issue. EPRI led the Joint Task Group on Bolting, which completed 19 general bolting tasks as detailed in EPRI NP-5769 [2]. The Task Group also published EPRI NP-5067, "Good Bolting Practices Manuals," in two volumes, publishing Vol. 1 [3] in 1987 and Vol. 2 [4] in 1990. Finally, EPRI produced three videotapes, "Pressure Boundary Bolting Problems," Parts I, II, and III [5], to aid in training licensee personnel.

The NRC issued generic letters, bulletins, and information notices to help resolve GSI-29. From 29 Dec. 1986 to 19 Nov. 1987, the NRC issued IE Information Notice No. 86-108, with Supplement 1 and 2 on boric acid corrosion [6]. On 17 March 1988, the NRC issued Generic Letter 88-05 on boric acid corrosion [7]. In the information notices, the NRC described instances in which boric acid corroded ferritic components including bolts. In the generic letter, the NRC requested that the licensee of each pressurized water reactor develop a program to find boric acid corrosion.

On 19 July 1989, the NRC issued Bulletin 98-02 on Anchor Darling swing check valves [8]. Some of these swing check valves had Type 410 stainless steel bolts tempered at 900°F (480°C), producing a bolt that is very susceptible to stress corrosion cracking. The proper heat treatment is conducted at a temperature of 1100°F (590°C), which produces a microstructure much less susceptible to stress corrosion cracking. Anchor Darling also suggested that Type 17-4 PH stainless steel tempered at 1100°F would also be an acceptable alternative material for the bolts.

One of the major issues of the 1980s was the increase in the number of counterfeit or fraudulently marketed fasteners not only in the nuclear industry, but also in the aerospace, military, and transportation systems. The most frequently counterfeited fasteners are ASTM A-193, Grade 8 and Grade 5 bolts that are replaced with less expensive Grade 8.2 and Grade 5.2 bolts. The Grade 8.2 bolts embrittle at a lower temperature than the Grade 8 bolts and may fail prematurely. On 6 Nov. 1987, the NRC issued Compliance Bulletin 87-02 to determine the extent of the problem of counterfeit or fraudulently marketed fasteners in the nuclear power industry [9]. The NRC requested each licensee to test ten safety-related fasteners and ten nonsafety-related fasteners for mechanical properties and chemistry. The NRC

published the results of these tests in NUREG-1349 [10]. The NRC determined that 8% of the safety-related fasteners were nonconforming and 12% of the nonsafety-related fasteners were nonconforming. Most of the nonconforming fasteners had minor variations in chemistry or had mechanical properties that were slightly out of specification. Only 2% of the safety-related fasteners were more than 10% out of specification, either for mechanical properties or chemistry. In this report, the NRC concluded that fraudulently marketed or counterfeit bolts are not a safety concern in the nuclear industry. However, the NRC issued a series of information notices and a generic letter in 1989 and 1990 listing suppliers of fasteners that had supplied nonconforming fasteners to the nuclear industry and giving guidance to licensees to minimize the possibility of purchasing fraudulent fasteners.

The NRC issued NUREG-1339 [11], which includes NRC's evaluation of EPRI NP-5769 and NRC's exceptions to this industry report. The NRC staff agrees with EPRI that the licensees should develop and implement plant-specific fastener integrity programs on all safety-related fasteners. NUREG-1339 and EPRI NP-5769 give guidelines for a comprehensive bolting integrity program. In a letter of 6 July 1989, the Nuclear Management and Resources Council (NUMARC) informed its members that EPRI had published EPRI Reports NP-5769 and NP-5067 and that these reports contain the basis for resolving GSI-29. On 17 Oct. 1991, the NRC issued Generic Letter 91-17 [12] to close GSI-29.

### **Regulatory Aspects of Fasteners**

For regulatory purposes, fasteners are divided into two classes: (1) safety-related and (2) nonsafety-related. The NRC has established guidelines for the purchase and use of safety-related fasteners. The NRC does not regulate nonsafety-related fasteners; thus, the purchase and use of these fasteners is the responsibility of the nuclear power plant licensee. The safety-related fasteners are divided into three classes. Class I includes the fasteners on all components within the reactor coolant pressure boundary up to the second isolation valve outside of the nuclear reactor containment. Class II includes all components from the outermost containment isolation valve up to but not including the turbine stop and bypass valves and connected piping up to and including the first valve that is either normally closed or is capable of automatic closure during all modes of normal operation for boiling water reactors. Class II includes all fasteners on the secondary side of the steam generator for pressurized water reactors; Class II also includes the fasteners in systems or portions of systems for emergency core cooling, removing containment heat after an accident, or removing fission products after an accident. Finally, Class II includes systems or portions of systems designed to shut down the reactor or remove residual heat. Class III components include water, steam, and radioactive-waste-containing pressure vessels, heat exchangers, storage tanks, piping, pumps, and valves which are not part of the reactor coolant pressure boundary or included in Class II. A more detailed discussion of Class I, II, and III components is given in Regulatory Guide 1.26 [13]. Class I components are in Quality Group A, Class II are in Quality Group B, and Class III are in Quality Group C. Quality Group D includes nonsafety grade components.

The regulatory basis for rules pertaining to fasteners is found in the *Code of Federal Regulations*, 10 CFR Part 50 [14]. Section 10 CFR 50.55a(a)(1) states that structures, systems, and components of a nuclear reactor shall be designed, fabricated, erected, constructed, tested, and inspected to quality standards commensurate with the importance of the safety function to be performed. Section 10 CFR 50.55a(a)(2) states that systems and components must meet the requirements of the American Society of Mechanical Engineering (ASME) Boiler and Pressure Vessel Code [15]. This section also lists the latest edition of the ASME Code that has been endorsed by the NRC. The licensee of an operating nuclear power plant

normally uses the edition of the ASME Code in effect when the utility docketed its construction plan with the Federal government (the NRC). Each licensee produces a final safety analysis report that may permit the licensee to use later editions of the ASME Code for reanalyses, repairs, or inspection. Section 10 CFR 50.55a(a)(3) states that alternative requirements may be used when approved by the NRC. The licensee must show that the proposed alternatives to the ASME code would provide an acceptable level of quality and safety or that compliance with the specified requirements of this section would result in hardship or unusual difficulties without a compensating increase in the level of quality and safety.

## ASME Requirements for Fasteners

### *Class I Fasteners*

The design requirements for bolts are found in Section III of the ASME Code [15]. Materials specifications for fasteners are found in Section II of the ASME Code. Section III, Paragraph NB-2128 states that Class 1 bolts shall conform to the requirements of one of the specifications listed in Section III, Appendix I, Table I-1.3, "Design Stress Intensity Values  $S_m$  For Bolting Materials." Table I-1.3 lists the minimum tensile strength, the minimum yield strength, and the design stress intensity for low-alloy steels, high-alloy steels, nickel-base alloys, and nickel-copper alloys as functions of metal temperature. The ASME Code requires that nuts conform to SA-194 in Section II of the ASME code or one of the specifications in Table I-1.3. Washers are optional but, if used, shall be compatible with the nuts. Class 1 fasteners also must comply with Paragraph NB-3230, "Stress Limits for Bolts." Paragraph NB-3230 includes methods for establishing design conditions, determining the average stress, maximum stress or maximum stress intensity, and the method for designing to avoid fatigue failure. The number and cross-sectional area of bolts for a given application are determined using Appendix E of Section III of the ASME code. Appendix E describes in detail the method for determining the minimum number and cross-sectional area of bolts for gasketed joints based on the design of the gasketed joint, the system operating pressure and temperature, and the characteristics of the gasket material. Appendix E also allows the use of the methods given in Appendix A-6000, "Discontinuity Stresses," if the methods given in Appendix E are inadequate. The stresses calculated using Appendix E or A must satisfy the requirements for maximum stress or maximum stress intensity and fatigue stress in Sections NB-3230.

Paragraph NB-3232 states that the service stresses in bolts may be higher than the stresses given in Table I-1.3. The maximum average cross-sectional stress may be as much as twice the stress given in Table I-1.3. The maximum stress at the periphery of the bolt may be as much as three times the stress given in Table I-1.3 as long as the fatigue stresses are not exceeded. These stresses arise from direct tension and bending, neglecting stress concentrations.

Paragraph NB-3232.3 describes the fatigue analysis to be performed on bolts. A fatigue analysis does not have to be performed if all the requirements of Paragraph NB-3222.4(d) are satisfied. This paragraph lists service conditions that result in stresses below the design fatigue curves given in Appendix I-9.4. Bolts with tensile strengths below 100 ksi (690 MPa) are evaluated using Paragraph NB-3222.4(e). This paragraph lists factors such as local structural discontinuities, thermal- and pressure-induced stresses, the effect of elastic modulus, and the cumulative damage assessment to be used with the design fatigue curves in Appendix I-9.4. This paragraph also requires the use of a fatigue strength reduction factor as described in NB-3232.3(c), which states that the fatigue strength reduction factor can be no less than 4.0 unless determined by analysis. The same analysis is conducted for high-strength alloy

steel bolting (tensile strength over 100 ksi) with several additional requirements. The maximum stress shall not exceed  $2.7 S_m$  if the higher of the two design curves from Fig. I-9.4 is used. The maximum stress of  $2 S_m$  is used for direct tension loading. The threads must be V-type with a minimum radius no smaller than 0.003 in. (0.01 cm). The fillet radii at the end of the shank can not be less than 0.060 in. (0.15 cm).

### *Design of Bolted Flanged Joints*

Appendix XI of the ASME code contains the methodology for designing bolted, flanged joints. The ASME code also allows flanged joints to be designed using the American National Standards Institute (ANSI) Standard 16.5, the American Petroleum Institute (API) Standard 605, or the Manufacturer's Standardization Society of the Valve & Fitting Industry (MSS) SP-42.

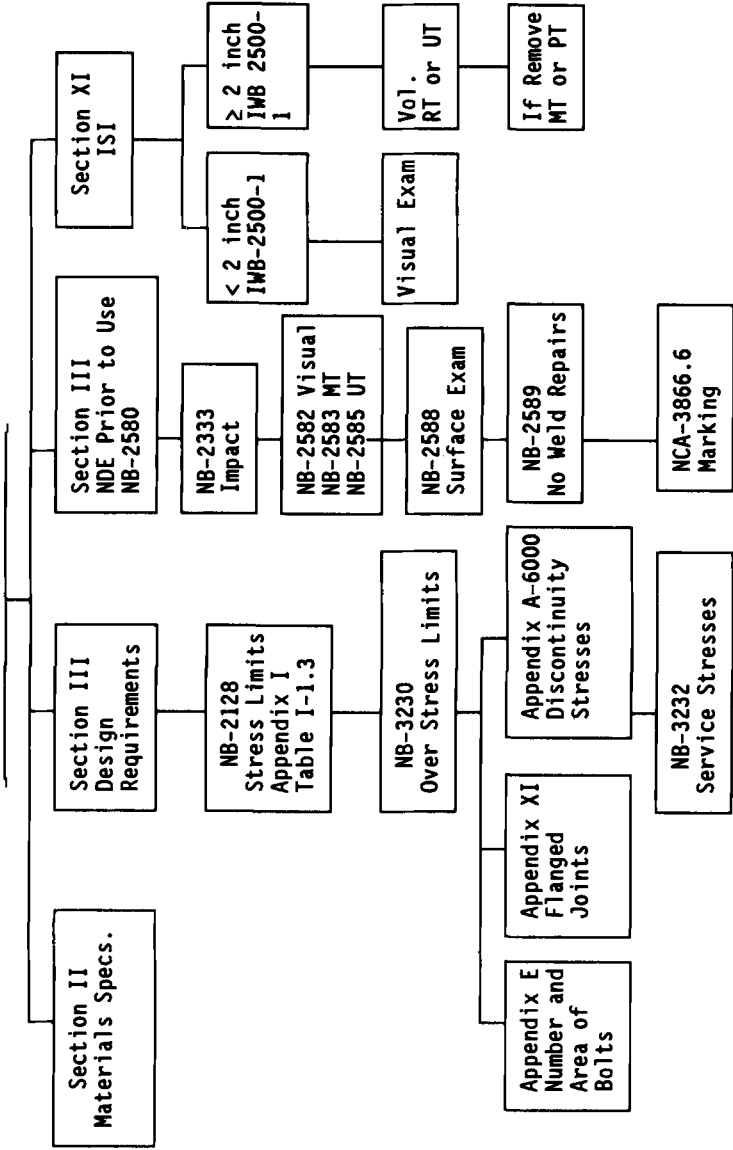
### *Mechanical Testing of Fasteners*

Section III of the ASME code requires impact testing of fasteners including bolts, studs, and nuts. Paragraph NB-2333 requires that three impact tests be conducted at the preload temperature or lowest service temperature, whichever is lower. Table NB-2333-1 gives the impact test result requirements for bolts. Section III specifies no requirements for bolts less than 1 in. in diameter (25 mm). Bolts between 1 and 4 in. (25 to 100 mm) in diameter must have a lateral expansion of 25 mils (0.6 mm) or more. Bolts over 4 in. (100 mm) in diameter must have a lateral expansion of 25 mils (0.6 mm) or more and an absorbed energy of at least 45 ft-lb (61 N-m). Paragraph NB-2345 requires that impact tests be conducted on each lot of material, in which a lot is one heat of material treated in one charge or as a continuous operation. The frequency of testing can be no less than one set of tests for each 1500 lb (680 kg) of material for 1¾ in. (44.5 mm) in diameter and less, 3000 lb (1360 kg) for over 1¾ to 2½ in. (44.5 to 63.5 mm) in diameter, 6000 lb (2721 kg) for 2½ to 5 in. (127 mm) in diameter, and 10 000 lb (4535 kg) for diameters over 5 in. (127 mm). Figure 1 summarizes the requirements for fasteners found in the ASME Code.

### **Nondestructive Examination Prior to Use**

Section III, Paragraph NB-2580, of the ASME code gives the preinstallation, nondestructive examination requirements for bolts, nuts, and studs. These examinations normally are conducted by the manufacturer of the fasteners. The threads, shanks, and heads of all bolts, nuts, and studs are to be visually examined as described in Paragraph NB-2582. Any harmful discontinuities such as laps, seams, or cracks are unacceptable. Nuts, bolts, and studs over 1 in. (25 mm) in diameter must be examined by magnetic particle examination (MT) using the ASTM Test Method for Magnetic Particle Examination of Steel Forgings (A 275-78) as described in Paragraph NB-2583. Paragraph NB-2583 permits the use of liquid penetration (LP) examination in place of MT using the procedure described in Paragraph NB-2584. Linear axial indications longer than 1 in. (25 mm) are unacceptable; no linear nonaxial indications are acceptable. All bolts, nuts, and studs with a nominal diameter of 2 in. (50 mm) or larger must also be evaluated using straight-beam, radial-scan ultrasonic examination (UT) before threading according to Paragraph NB-2585 of the 1986 and later editions of the ASME Code. Earlier editions of the ASME Code did not include this requirement. Any indication greater than 20% of the height of the first back reflection or any discontinuity that prevents the production of a first back reflection of 50% of the calibration amplitude is unacceptable. Any bolts, nuts, or studs over 4 in. (100 mm) in diameter are also examined

ASME CODE-FASTENER REFERENCES



RT - X-Ray Radiography  
 UT - Ultrasonic

MT - Magnetic Particle  
 PT - Liquid Penetrant

FIG. 1—ASME code requirements for fasteners.

using a straight-beam, longitudinal-scan UT either before or after the threads are produced. A calibration test block having the same nominal composition and diameter as the production part and at least half as long is prepared by drilling a flat-bottomed hole that is  $\frac{3}{4}$  in. (19 mm) in diameter by 3 in. (75 mm) deep in one end of the bar. The hole is plugged after drilling. Any indication in excess of the test hole indication is unacceptable. These acceptance tests are to be conducted after final heat treatment as specified in Paragraph NB-2587 of the 1986 and later editions of the ASME Code. Earlier versions of the ASME Code did not include this requirement. Surface defects on finished bolts, nuts, and studs are not acceptable and are grounds for rejection as specified in Paragraph NB-2588. Finally, Paragraph NB-2589 specifies that defects in bolts, nuts, or studs may not be repaired by welding.

All bolts, studs, and nuts larger than 1 in. (25 mm) in diameter are marked in accordance with NCA-3866.6. The marking identifies the grade of material, the manufacturer, and a marking that can be traced to the heat number, mechanical properties, thermal treatment, and in-service inspection results for the bolt, stud, or nut.

### *Class II and Class III Fasteners*

Class II fasteners must meet the same requirements as Class I fasteners except that the fasteners are visually examined before use and the MT, LP, and UT requirements do not apply. Class III fasteners have the same requirements as Class I fasteners except the impact requirements are relaxed and the MT, LT, and UT requirements are eliminated. Class I fasteners can be used in Class II and III applications, and Class II fasteners can be used in Class III applications. Many licensees order Class I fasteners exclusively to avoid the possibility that a fastener would inadvertently be used in an application with higher requirements than that for which the fastener was qualified; for example, a Class II fastener can not be used in a Class I application.

### **In-Service Inspection of Fasteners**

Section XI of the ASME code gives the in-service inspection requirements for fasteners. Table IWB-2500-1 summarizes the Class I fastener inspection requirements. Fasteners that are 2 in. (50 mm) in diameter and smaller are examined visually. Nuts, bushings, and washers for bolts greater than 2 in. (50 mm) in diameter must be visually examined for defects and examined volumetrically using either X-ray radiography or UT. When removed, such as for refueling, reactor vessel closure studs that are removed are also given a surface examination using MT or PT. All of the fasteners in the reactor vessel, pressurizer, steam generator, heat exchangers, piping, pumps, and valves are examined with 100% of the fasteners examined within an inspection interval of usually ten-year periods. Class II fastener examination requirements are limited to bolts and studs greater than 2 in. (50 mm) in diameter using volumetric examinations. Class III fasteners have no inspection requirements.

### *Procurement of Nuclear Grade Fasteners*

Nuclear grade fasteners are procured from a supplier or manufacturer that has a Quality System Certificate issued by ASME. Before issuing a Quality System Certificate, ASME verifies that the vendor has an adequate Quality Program and Identification and Verification Program as specified in Paragraph NCA 3820(a) of Section III of the ASME Code. The number of suppliers or manufacturers having Quality System Certificate has decreased over the years since few nuclear power plants are being constructed and the demand for nuclear grade components has diminished. The ASME code permits a nuclear power plant licensee

to receive a Quality System Certificate and to buy commercial grade components that are "dedicated" as nuclear grade by the licensee. Paragraph NB-2130 of Section III of the ASME Code specifies that all material to be used in a safety-related component must have a Certified Material Test Report (CMTR) as described in Paragraphs NCA-3867.4 and NCA-3867.5 or a Certificate of Compliance (CC) as described in Paragraph NCA-3867.4(b). Only the party holding the Quality System Certificate can issue the CMTR or CC, but the material may have been supplied by a subcontractor or consultant and tested under the direction of the Quality System Certificate holder. This permits a nuclear power plant licensee to buy a commercial grade component and dedicate it by following the rules of Section III of the ASME Code. EPRI has issued a report containing guidance for using commercial grade items in nuclear-safety-related applications [16].

Safety-related components for use in nuclear power plants are purchased subject to Part 21 and Appendix B of Title 10 CFR 50. Part 21 requires the licensee to report promptly to the NRC findings about components regarding detected defects or failure to comply with the requirements of 10 CFR 50 or the ASME Code if the defects or noncompliance result in a significant safety hazard. The supplier of the defective or nonconforming part must notify all nuclear grade purchasers and the NRC that the part is defective or nonconforming. The supplier is also required to describe the corrective action to be taken and the length of time it will take to complete the action. Appendix B describes the quality assurance criteria imposed on suppliers by nuclear power plant licensees. Appendix B includes requirements for: independent design reviews of safety-related components; procurement document control; control of purchased material, equipment, and services; identification and control of materials, parts, and components; records; and audits. Appendix B requires that nuclear power plant licensees conduct scheduled and unscheduled audits of suppliers of safety-related components. In May 1990, EPRI issued EPRI NP-6629 [17] to clarify the procurement of safety-related components.

## References

- [1] "Threaded-Fastener Experience in Nuclear Power Plants," NUREG-0943, U.S. Nuclear Regulatory Commission, Public Document Room, 2120 L Street, NW, Lower Level, Washington, DC 20555, January 1983.
- [2] Nickell, R. E., "Degradation and Failure of Bolting in Nuclear Power Plants," EPRI NP-5769, Vols. 1 and 2, Research Reports Center, P.O. Box 50490, Palo Alto, CA 94303, April 1988.
- [3] Bickford, J. H. and Looran, M. E., "Good Bolting Practices," Vol. 1: Large Bolt Manual, EPRI NP-5067 V1, Research Reports Center, P.O. Box 50490, Palo Alto, CA 94303, 1987.
- [4] Van Duyne, D. A., "Good Bolting Practices," Vol. 2: Small Bolts and Threaded Fasteners, EPRI NP-5067 V2, Research Reports Center, P.O. Box 50490, Palo Alto, CA 94303, 1990.
- [5] "Pressure Boundary Bolting Problems," Parts I, II, and III, EPRI Videotapes, Research Reports Center, P.O. Box 50490, Palo Alto, CA 94303.
- [6] "Degradation of Reactor Coolant System Pressure Boundary Resulting from Boric Acid Corrosion," IE Information Notice No. 86-108, with Supplement 1 and 2, U.S. Nuclear Regulatory Commission, Public Document Room, 2120 L Street, NW, Lower Level, Washington, DC 20555, 29 Dec. 1986 to 19 Nov. 1987.
- [7] "Boric Acid Corrosion of Carbon Steel Reactor Pressure Boundary Components in PWR Plants," Generic Letter 88-05, U.S. Nuclear Regulatory Commission, Public Document Room, 2120 L Street, NW, Lower Level, Washington, DC 20555, 17 March 1988.
- [8] "Stress Corrosion Cracking of High-Hardness Type 410 Stainless Steel Internal Preloaded Bolting in Anchor Darling Model S350W Swing Check Valves or Valves of Similar Design," Bulletin 89-02, U.S. Nuclear Regulatory Commission, Public Document Room, 2120 L Street, NW, Lower Level, Washington, DC 20555, 19 July 1989.
- [9] "Fastener Testing to Determine Conformance with Applicable Material Specifications," Compliance Bulletin 87-02, U.S. Nuclear Regulatory Commission, Public Document Room, 2120 L Street, NW, Lower Level, Washington, DC 20555, 6 Nov. 1987.

- [10] "Compilation of Fastener Testing Data received in Response to NRC Compliance Bulletin 87-02," NUREG-1349, NRC Public Document Room, 2120 L Street, NW, Lower Level, Washington, DC 20555, June 1989.
- [11] "Resolution of Generic Safety Issue 29: Bolting Degradation or Failure in Nuclear Power Plants," NUREG-1339, NRC Public Document Room, 2120 L Street, NW, Lower Level, Washington, DC 20555, June 1980.
- [12] "Bolting Degradation or Failure in Nuclear Power Plants," Generic Letter 91-17, NRC Public Document Room, 2120 L Street, NW, Lower Level, Washington, DC 20555, 17 Oct. 1991.
- [13] Regulatory Guide 1.26, "Quality Group Classifications and Standards for Water-, Steam-, and Radioactive Waste-Containing Components of Nuclear Power Plants," NRC Public Document Room, 2120 L Street, NW, Lower Level, Washington, DC 20555, February 1976.
- [14] *Code of Federal Regulations*, Title 10, Parts 0 to 50, revised as of 1 Jan. 1992, available from the U.S. Government Printing Office, Superintendent of Documents, Mail Stop: SSOP, Washington, DC 20402-9328.
- [15] *ASME Boiler and Pressure Vessel Code*, ASME, United Engineering Center, 345 East 47th Street, New York, NY 10017, 1971 to 1992 editions plus addenda.
- [16] "Guideline for the Utilization of Commercial Grade Items in Nuclear Safety Related Applications (NCIG-07)," EPRI NP-5652, June 1988, Research Reports Center, P.O. Box 50490, Palo Alto, CA 94303.
- [17] "Guidelines for the Procurement and Receipt of Items for Nuclear Power Plants (NICG-15)," EPRI NP-6629, May 1990, Research Reports Center, P.O. Box 50490, Palo Alto, CA 94303.

## Failure Criteria and Limiting States of Stress for Cracked Bolts/Studs

---

**REFERENCE:** Kagan, V., "Failure Criteria and Limiting States of Stress for Cracked Bolts/Studs," *Structural Integrity of Fasteners, ASTM STP 1236*, P. M. Toor, Ed., American Society for Testing and Materials, Philadelphia, 1995, pp. 60–80.

**ABSTRACT:** Service time and the strength of high-stressed threaded connections under cyclic nonlinear stress-strain conditions are determined by the behavior of the fatigue crack's initiation and propagation stages in local stress-strain concentration areas of threaded components. The ultimate states and failure criterion of cracked bolts/studs have been determined by analysis of the parameters of linear and nonlinear deformation and fracture mechanics. Evaluation of the number of cycles of fatigue crack initiation  $N_i$  and the number of cycles to final failure  $N_f$  for different design joints required an all-round consideration of cyclic nonelastic (nonlinear) stress-strain behavior. It also needed the further study of the influence of the conditions of cyclic, mechanical, and thermal loadings, as well as assembly and manufacturing based on the theoretical stress concentration factor  $K_t$  (elastic deformation), stress  $K_\sigma$ , and strain  $K_\epsilon$  (non-elastic deformation) factors' values in the mated-loaded (engaged) and unloaded (free) thread turns. The analysis indicated a linear relation between critical value  $h_{max}$  of the fatigue crack's depth and the cycle amplitude's stress  $\sigma_a$ , as well as a correlation with the limiting value of the stress (strain) intensity factor. The remaining strength and fatigue life of the cracked threaded components are evaluated taking into consideration the values of the current thresholds and the limiting stress and strain intensity factor. The conditions of their applicability depend on the applicability of linear (elastic) or nonlinear (elastic-plastic) fracture mechanics criteria.

**KEYWORDS:** threaded connections, cracked bolts/studs, fatigue, linear and nonlinear deformation and fracture mechanics, stress-strain factor, stress and strain intensity factors

### Applications

#### *Advantages of Threaded Fasteners*

Threaded joints find wide application in all areas of the national economy. It is difficult to find a machine or an installation without threaded joints. Intense use of threaded joints in aircraft and machinery, as well as in engineering structures, accounts for the reduced use of rivet joints in recent years. Comparatively small-sized threaded joints applied in a range of structural steels and alloys in many different manufacturing procedures are finding applications in constructions of unique buildings and machines.

The number of components in threaded joints in specific constructions varies. For instance, in a wing-to-fuselage junction of a large airplane or in a high-pressure vessel there are 10 to 100 threaded joints. In the construction of a car or in the whole body fuselage of a large airplane, there are from 2000 to 1 000 000, respectively. In the United States, the annual production of threaded fasteners is about 250 billion; two thirds of that number are used in

---

<sup>1</sup> Senior design engineer, Engineering Materials Sector, AlliedSignal Inc., 101 Columbia Rd., Morristown, NJ 07962-2332. Formerly principal research scientist and professor, Experimental Mechanics and Material Science Center, Technical University, Vilnius, Lithuania.

the automotive and tractor industries. Such factors as operating conditions, methods of manufacture, and assembly, as well as reliability in service time and life (duration) exert a major effect on the design patterns of threaded connections.

### *Design Consideration*

Maximum attention is being paid to design, manufacturing, assembling, and maintenance of threaded joints in aerospace, transportation, energy, and nuclear power industries because the failure of a single threaded joint can lead to serious consequences. The material costs due to the fracture of a threaded joint can be considerable. For example, due to the fracture of threaded components, repair costs to a diesel engine and a turbo generator are \$4,000 and \$160,000, respectively, with no allowance for idling losses [1]. A still greater danger involves failure of a threaded joint serving as a load-carrying (bearing) element and ensuring both the proper tightness of junction and the integrity of the construction as a whole (high-pressure vessels, aerospace, and petrochemical construction) because of the danger of chemical or radioactive contamination. The reduction of the overall dimensions for construction due to the growth of the unit capacity leads to the increase in size of the threaded joints. Increases in threaded joints can be 300 to 1000 mm in diameter in heavy-duty presses, high-pressure engineering, and testing constructions, 150 to 250 mm in diameter in nuclear and chemical vessels and anchors, and 50 to 180 mm in diameter in aircraft and aerospace industries, submarines, and deep-water apparatus, etc.

### *Mechanical Properties and Selection of Materials for High-Stressed Joints*

The ultimate tensile strength ( $S_u$ ) of employed threaded joints lies within a large range, starting from 300 MPa (construction of metal structures) to 2100 MPa (aerospace structures, in individual cases for shear-loaded bolts even up to 3000 MPa). The percent of the reduction in the area varies from 10 to 70%. As a rule, steels and alloys with an ultimate strength of 1000 to 1400 MPa are used for production of high-stressed threaded components. The selection of a specific alloy or steel grade depends on the bolt (stud) diameter since the greater the diameter the more alloying constituents are required to provide identical mechanical properties over the whole cross section of a threaded component.

Martensite-aging steels feature prolonged durability and material plasticity and have been used recently for the manufacture of threaded components. A threaded component with an ultimate tensile strength  $S_u$  of up to 1700 MPa is made of chrome-magnesium-silicon, and chrome-magnesium-nickel steels are subjected to thermal-mechanical treatment, as well as cold treatment to obtain an ultimate tensile strength  $S_u$  of up to 2100 to 2600 MPa. Nickel-containing steels are used to manufacture corrosion-resistant threaded joints, employable at elevated temperatures. Threaded components made of medium-alloy, high-strength steels may be used for temperature-loaded constructions of up to 437 to 500 K. Chrome-molybdenum, chrome-molybdenum-vanadium, and chrome-nickel-molybdenum (723 K) steels are used in the turbine-machinery industry with temperatures in the range of 500 to 673 K. When the operating temperature is 823 to 1073 K, thermal-resistant and high-temperature nickel-based steels are utilized.

Further temperature increase necessitates the use of refractory molybdenum (1921 K), niobium (1801 K), tantalum (1921 K), and tungsten (2255 K) alloys. Chrome-nickel, chrome-molybdenum, and chrome-nickel-molybdenum threaded joints can be used at lower temperatures such as 200 K. However, when operating at lower temperatures, measures should be taken to provide resistance to brittle failure.

*Loading and Stress-Strain Conditions*

When selecting a grade of a tensile strength of a threaded material, its price and production effectiveness should be taken into consideration, giving preference to high-stressed threaded joints and minimizing material and labor expenses, as well as decreasing the weight of the structures. Thus, the cost of bolts with an ultimate strength  $S_u = 700$  MPa is 30% of the cost of bolts with  $S_u = 1000$  MPa. To maintain uniform tightening over the junction of the same construction, it is possible to have 20% less high-strength threaded joints (with identical dimensions), which naturally reduces assembly losses. However, the tendency toward crack resistance has been gaining strength along with improvement of the tensile strength of the materials used and the growth of pretension stresses [2,3].

A general tendency to an increase in working parameters (pressure, temperature, speed, load, etc.) of contemporaneous machines and structures has given rise to the enhancement of stationary and nonstationary mechanical and thermal effects on the basic load-carrying members. This evokes a buildup of global and local tensions within the elements of the construction, including threaded joints, with the probable occurrence of cyclic elasto-plastic strains in local stress concentration areas. In light of the above circumstances, the traditional calculation of static, cyclic (fatigue), and long-term (creep) strengths of threaded joints, based on an estimation of nominal stresses, becomes insufficient. Due to the limitation induced on the overall dimensions and the weight, it is not always possible to increase the longitudinal and lateral dimensions of such heavy-load threaded joints (aerospace constructions and high-pressure vessels) with the goal of reducing local loads and nominal stresses (in threaded components). Under such operating conditions of mechanical and thermal loadings, limiting states (judging either by the initiation of cracks or by final/complete failure) occur when the number of cycles is measured in hundreds or thousands, i.e., fracture takes place in the range of a small number of cycles (low-cycle fatigue) prior to failure.

**Prediction of Cyclic Strength and Life (Service Time)**

The problem of estimating cyclic strength and life of a threaded joint based on the final/complete failure and the initiation of cracks is discussed in Refs 3-5. Through analytical and experimental investigations of regularities and conditions favoring fatigue crack formation (initiation stage) in the thread root undertaken in accordance with the standards, it has been proven that the feasibility of application of the following expression is used to estimate either the permissible (design) number of cycles  $N_d$ , according to stress amplitudes present by the operation mode, or the available (design) alternating stress amplitudes  $\sigma_{a,d}$  over the number of cycles defined by the operation modes [5]:

$$\sigma_{a,d} = 2.3 E_t \log \{100/[100 - (RA)]\} / \{n_\sigma [4N_d^m + (1 + R)/(1 - R)]\} + \sigma_{-1} / \{A + \sigma_{-1}/S_u [(1 + R)/(1 + R) - 1]\} \quad (1)$$

$$\sigma_{a,d} = 2.3 E_t \log \{100/[100 - (RA)]\} / \{4[n_N N_d]^m + (1 + R)/(1 - R)\} + \sigma_{-1} / \{A + \sigma_{-1}/S_u [(1 + R)/(1 - R) - 1]\}$$

where

$\sigma_{a,d}$  = design alternating stress amplitude, MPa,  
 $N_d$  = design number of cycles,

- $E_t$  = modulus of elasticity, MPa,  
 $R$  = stress ratio,  $R = \sigma_{\min} / \sigma_{\max}$ ,  
 $RA$  = reduction in area, %,
- $\sigma_{-1}$  = fatigue limit, MPa,  
 $S_u$  = ultimate tensile strength, MPa,  
 $n_\sigma$  = safety factor (by conditions of cyclic strength),  
 $n_N$  = safety factor (by conditions of cyclic fatigue life at crack initiation stage),  
 $A$  = coefficient of  $\sigma_{sa} - S_m$  fatigue failure data schematization,  
 $\sigma_a$  = alternating stress amplitude, MPa, and  
 $\sigma_m$  = mean stress, MPa.

For chrome-nickel-molybdenum steel with an ultimate tensile strength  $S_u = 700$  to  $1250$  MPa, the coefficient of schematization  $A$  in Eq 1 equals 1.2 to 1.3. For the estimation of design fatigue strength, we should take into account the minimum values of  $\sigma_{a,d}$ , calculated in the two above equations (by conditions of safety factors  $n_\sigma$  or  $n_N$  for both equations).

Figure 1 presents estimated fatigue  $\sigma_{a,d} - N_c$  curves for threaded joints made from chrome-nickel-molybdenum steel, with values of the ultimate strength  $S_u$  varying from 780 to 1280 MPa (at room temperature conditions—293 K). In the given range of the ultimate strength  $S_u$ , the fatigue crack initiation stage  $N_c$  ( $N_c$  = the number of cycles required for a fatigue crack nucleus at the surface of the root thread to grow to such an extent as to become visible: equals 1 to 1.5 mm) depends on  $S_u$ . It has been confirmed, considering the resistance of fatigue fracture in the identical threaded joint design and manufacture (with guaranteed values of root radius  $R_h$  affecting the stress factor and damage accumulation in the threads). Higher values of the ultimate strength  $S_u$  correspond to a smaller number of cyclic stresses  $N_c$  for the same level  $S_u = \text{constant}$ . Nevertheless, for the lower values of  $N_c = (1.5 \text{ to } 2.5) \times 10^4$ , the fatigue curves intersect, and the threaded joints, which are made of higher-strength steels, are featured for larger values of fatigue limit.

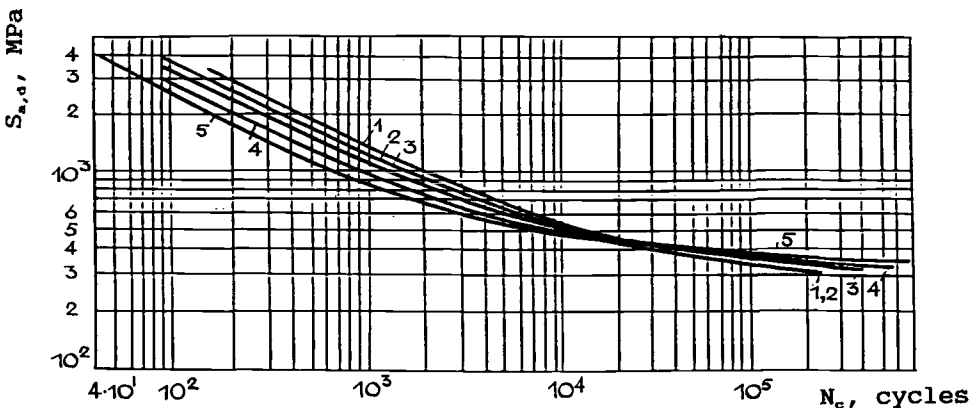


FIG. 1—Fatigue strength ( $S_{a,d}$ )-life ( $N_c$ ) computation curves for threaded joints M52 at the fatigue macrocrack initiation stage. Chrome-nickel-vanadium steel. Room temperature (293 K) conditions. Variation of ultimate tensile strength  $S_u$  from 780 to 1280 MPa: 1 = 780 MPa; 2 = 880 MPa; 3 = 990 MPa; 4 = 1150 MPa; 5 = 1280 MPa;  $S_{a,d}$  = alternating stress amplitudes, MPa;  $N_c$  = fatigue life at crack initiation stage, cycles.

*Experimental Methods of Fatigue Crack Determination and Measurement in the Circular Bars and Threaded Joints*

The experimental investigation of the fracture process in the circular bars and threaded joints has been carried out by employing special fatigue crack detection procedures, which helped to determine the shapes, sizes, and locations of cracks and defects. The methods facilitating the investigation of fatigue crack evolution in threaded joints were selected by following the analysis of recommendations for the use of nondestructive testing and evaluation (NDTE). To determine fatigue cracks on the surface, electromagnetic and fluorescent magnetic methods were used. However, the estimation of the depth of fatigue crack depth without disassembly in the engagement threads using NDTE methods presents certain difficulties. Therefore, the crack depth has been defined by utilizing the methods of paints, as well as thermal and cyclic markings without disassembly. Complex methods of fractography were also employed. The coordinates (for the determination of shapes and sizes of fracture) of kinetics of the fracture front were set on a toolmaker's microscope.

*Fatigue Crack Initiation (Formation) and Propagation Stages*

While estimating a fatigue crack's formation and propagation stages, it has been shown that the processes are greatly influenced by alternating stress amplitude and mean stress level and the presence of alloying elements: an excess of nickel promotes a fatigue crack propagation stage. The relation (fatigue test data for threaded joints M52) between the fatigue crack initiation stage  $N_c$  and fatigue life  $N_f$  (the number of cycles to final failure) shows (Fig. 2) that for the stress amplitude level  $\sigma_a = 0.4 S_y$  (where  $S_y =$  yield strength), the ratio  $N_f/N_c$  approaches 6 to 7, and for  $\sigma_a = 0.15 S_y$ , the ratio amounts to 2.0 to 3.5.

For the reduction of values of thread pitch ( $P$ ) for the same diameter  $d$  of joint, the ratio  $P/d$  increases (where  $d =$  the nominal diameter of the thread) the ratio  $N_f/N_c$  due to the change of the fatigue crack propagation mechanism.

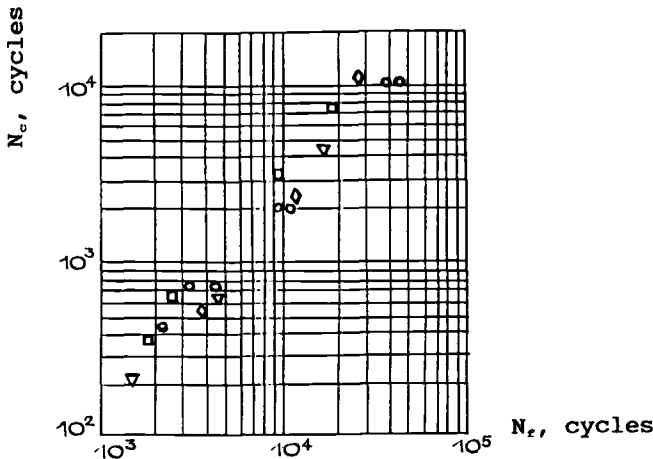


FIG. 2—Fatigue life on the crack initiation  $N_c$  stage and by final failure  $N_f$  for threaded joints M52 from: chrome-nickel (○, ◇) and chrome-nickel-molybdenum-vanadium (▽, □) steels. Room temperature (293 K) conditions.  $N_c =$  fatigue life at crack initiation stage, cycles.  $N_f =$  fatigue life (number of cycles to final failure).

### *Stress Concentration Factors for the Bolts/Studs Joints in the Elastic Range*

When calculating the values of alternating stress amplitude  $\sigma_{a,d}$ , an allowance for stress factor (for elastic deformation conditions) has been made based on the data for the theoretical ( $K_t$ ) and effective ( $K_{ef}$ , the cyclic loading conditions) stress concentration factor values, together with applying the interpolation procedure to the discrete material constant values  $C_q$  in dependence on the  $S_y/S_u$  ratio (where  $S_y$  and  $S_u$  equal the yield ultimate tensile strength, correspondingly).

The calculation of a theoretical stress concentration factor for threaded joints was made according to the following relation:

$$K_t = 1 + \varphi_1 (P/R_{th})^{0.5} \quad (2)$$

where

$\varphi_1$  = the reduction factor varying within the range of 1.1 to 1.57,

$P$  = thread pitch, mm, and

$R_{th}$  = thread root radius, mm.

However, this relation doesn't take into account the influence of design and distribution of loads (stresses) in mating areas. Considering the dependence of the response factor to the stress concentration  $K_t$  on root radius  $R_{th}$ , the ultimate strength  $S_u$ , and the design version of threaded joints under elastic deformation conditions, the theoretical ( $K_t$ ) and the effective ( $K_{ef}$ ) stress factors can be calculated using the following expressions:

$$K_t = \beta_d \varphi_{th} (1 + R_{th}) (P/R_{th})^{0.5(1+R/P)} \quad (3)$$

$$K_{ef} = [\beta_d \varphi_{th} (1 + R_{th}) (P/R_{th})^{0.5(1+R/P)} - 1] (1 + C_q/R_{th})^{-1} + 1 \quad (4)$$

where

$\beta_d$  = the design version, varying from 0.8 to 1.4,

$\varphi_{th}$  = the factor, taking the influence of the load's (stresses) distribution factor, varying from 0.9 to 1.2, and

$C_1$  = the material constant versus the value of ultimate strength  $S_u$ , which is defined by a polynomial of the second or third degree.

Figure 3 illustrates an interrelation of the theoretical  $K_t$  and the effective  $K_{ef}$  stress factors versus the thread pitch  $P$  for bolt-nut joints of a standard design based on results obtained from Eq 3. Within the thread pitch variation in the range from 1.0 to 2.5 mm, the effective  $K_{ef}$  stress factor approaches its maximum value when the theoretical stress factor  $K_t = 6$ ; further increase of pitch  $P$  leads to the monotonous growth of  $K_{ef}$  factor values.

## **Fracture Mechanics of Threaded Joints**

### *Damage and Failure of Threaded Joints*

An important complex analysis of strength and life (service time) problems under low-cycle, elasto-plastic deformation at different evolution stages of fatigue damage and in brittle failure states is based on such failure cases when at a definite stage of evolution fatigue cracks evolve into brittle cracks. Low cycles and brittle failures of components of threaded

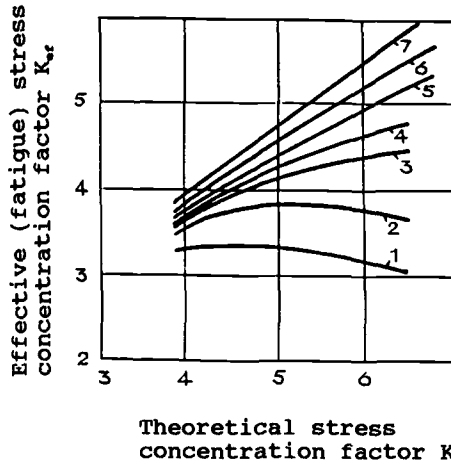


FIG. 3—Interrelation of theoretical  $K_t$  and effective (fatigue)  $K_{ef}$  stress concentration factors for bolt-nut joints with an influence of value of the thread pitch  $P$ (mm): 1 = 1.0; 2 = 1.75; 3 = 2.5; 4 = 3.0; 5 = 4.0; 6 = 6.0; 7 = 8.0.  $K_t$  = theoretical stress concentration factor.  $K_{ef}$  = effective (fatigue) stress concentration factor.

joints (mainly of bolts and studs) have been detected in manufacturing (assembly, testing of thermal energy and nuclear energy equipment, and in high-pressure vessels of petrochemical, gas, aircraft, and aerospace industries).

The major reasons for damages and failures are related to the errors at the design stages and to violations of manufacture, assembly, repair technology, etc. Such failures can develop from more pronounced stress-strain concentration areas of threaded components and from primary defects originating in the design and manufacturing stages. Fatigue cracks and mechanical and corrosion damages can accumulate during storage, assembly, and maintenance. To successfully conduct the analysis of a crack's propagation in high-stressed threaded components and to prove the adequacy of fracture factors to the strength and life calculation procedures, the investigation of fracture propagation peculiarities within a threaded joint and a fatigue crack's trajectories within the joint is of prime importance [5–7].

### Fatigue Crack Propagation Mechanism

The analysis of operative damages and failures of threaded joints has shown that, generally, fracture propagation can take place in nine different areas of stud (bolt) joints (Fig. 4). The failure of a bolt head in a bolt assembly is also possible (Fig. 4, Area 10). Laboratory analysis of damages and failures in threaded joints while employed in a wide range of mechanical (axial, axial-flexural) loading and elevated temperature (up to 773 K) conditions for different design versions with a variety of sizes (M8 to M130) and mechanical properties of material (ultimate strength  $S_u$  from 400 to 2400 MPa) has demonstrated that, under static and cyclic deformation, failure both in a threaded bar body (Fig. 4B) and in thread fillets (Fig. 4C) is the most typical.

Fatigue failure in the thread mating (engagement), nonengagement, and bolt head areas in service time presents the most serious danger because it can lead to abrupt failure of the joints without any warning factors such as partial unsealing, noise resulting from mutual collision of engaged parts, etc. The failure of threads of bolts or nuts (Fig. 4B, 4C) can take

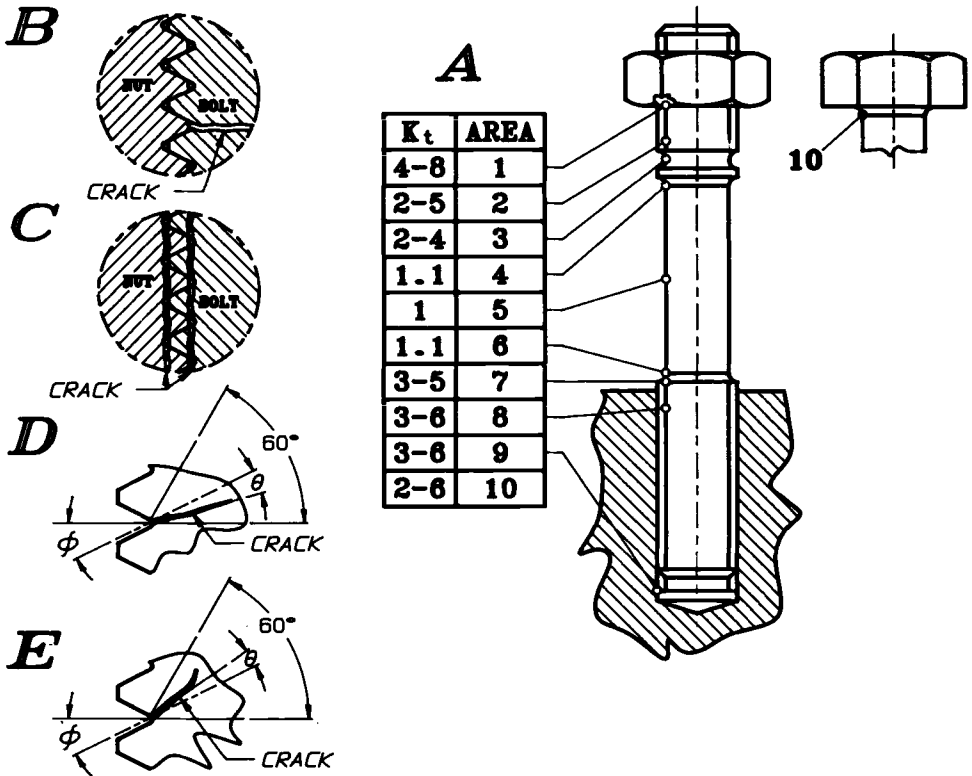


FIG. 4—Damage areas in threaded joints and fatigue crack trajectories: (A) values of theoretical stress concentration factors  $K_t$  in threaded components; (B) failure of body of bolt/stud; (C) failure of a thread fillet; (D) fatigue crack propagation in a coarse-thread joint; (E) fatigue crack propagation in a fine-thread joint;  $K_t$  = theoretical stress concentration factor;  $\varphi$  = area of crack initiation, rad;  $\Theta$  = crack propagation trajectory, rad.

place in accordance with the ratio of mechanical parameters of the material (ultimate strength for bolt/stud  $S_{u,b}$  and nut  $S_{u,n}$ , respectively). This behavior of failure is typical for joints with the small size of pitch  $P$  (fine thread) as well as in the case of insufficient length of the engaged thread, and it is valid for design when the ultimate strength (or yield strength) of bolt/stud and nut materials differs by more than twice.

For coarse-pitch thread joints, failure in the engagement area takes place due to fatigue crack propagation at the root of the most highly loaded (stressed) threads, progressing over the cross section (Fig. 4C, Areas 1 and 8). The origin of cracks at the root of a bolt/stud thread is always in the direction of a loaded thread side at angle  $\varphi$ , depending on the accuracy of manufacture, the peculiarities of stress distribution in the contact area, and  $\varphi$  within the range of 20 to 50°. The crack, having originated in the area of plastic strain, follows the trajectory shown in Figs. 4D and 4E, then makes a smooth turn and further propagates in the plane tilted toward the axis of a threaded bar by an amount equal to 90°.

The direction and amount of the angle is dependent on peculiarities of a fracture process specified by the design version and the mechanical properties of the material. When the crack is generated, it propagates around the root of a bolt thread with a tendency to an inside

propagation. The crack front is controlled in accordance with the number of cycles and loading conditions. Based on the axial loading, the ratio of the fatigue life to crack initiation stage and the fatigue life to final failure ( $N_f/N_c$ ) is reduced upon decreasing the loading level (i.e., upon increasing the number of cycles prior to final failure  $N_f$ ). The longitudinal crack propagation at the root of the thread that takes place within low cycles of loading and the service time (fatigue life) of threaded joints is defined mainly by the means of fatigue crack propagation (penetration) in the depth of the cross section of a bolt/stud.

Following the basic modes of crack displacement [8,9], the field of stresses around the tip of a crack is divided into three basic categories corresponding to fracture procedure and is characterized by the breakaway, lateral, and longitudinal shear (sliding mode) found within Schemes I, II, and III. By combining all three mechanisms, insight can be gained into the regularities of the fracture propagation process. The mechanism representing a fracture process in smooth bolt areas (Fig. 4A, Area 5) comprises the origination of a crack at the point of imperfection (either as a metallurgical or technological origin) and its propagation into a cross-section plane, i.e., the I mechanism is involved. In threaded (notched) areas and over the radius  $R_{th}$  of transfer from a smooth to a threaded part, the cyclic fracture process is also controlled by a breakaway mechanism acting in a cross section of a bolt.

In an unloaded (nonengaged) thread portion (Fig. 4A, Area 2), the behavior of fracture propagation is the same as observed in the grooves cut over the radius; however, the fracture plane is tilted by an amount equal to the right angle. In the thread engagement area at the stage of fatigue macrocrack initiation, the cracking process is controlled by a shear mechanism that is substituted by a breakaway mechanism in the case of fracture propagation over the thread bar (bolt) body (for coarse-pitch thread joints). In the unloaded (nonengaged) thread portion, along the fillet, the tension remains unchanged and the crack propagation over the circumference is controlled by the longitudinal shear mechanism. For threads in engagement areas, a nonuniform longitudinal tension is estimated taking into consideration regularities in distribution of stresses over the depth of engagement.

Crack propagation along the thread root depends, first of all, upon the gradient of the tension, and, secondly, on the torque moment  $T$  exerted during axial loading (during assembly time). The value of the moment  $T$  makes a larger contribution to crack propagation over nonengaged threads, and in a cutter exit groove it offers a thread in engagement.

The comparison of experimental test results obtained by the author with the data on estimation [4] of the angle  $\theta$ , specifying the fatigue crack propagation path, has shown (Fig. 5) that its absolute value increases with an increase of the ratio  $K_{II}/K_I$  (from 0 to 1.0) and with a decrease of the  $K_I/K_{II}$  ratio (from 1.0 to 0) and approaches its maximum value (Fig. 5) at  $K_I/K_{II} = 0$ .

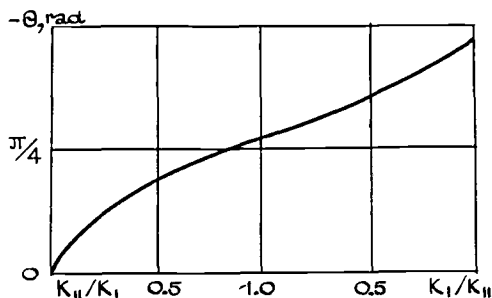


FIG. 5—Influence of the stress intensity factor  $K_I/K_{II}$  ratio on a fatigue crack propagation trajectory.

*Stress Intensity Factors (for Circular Bars)*

An application of the conditions valid for linear elastic fracture mechanics (LEFM) is associated with an estimation of the stress intensity factors ( $K_I, K_{II}, K_{III}$ ), taking into consideration the variations of design, material properties, and loading variety for high-stressed threaded joints. For coarse-pitch threaded joints, as well as under the same tensile strength grades of bolt/stud and nut materials, both engaged and nonengaged thread fractures take their course following a normal breakaway scheme, which calls for the calculation of the threshold ( $K_I$ ) and the critical ( $K_{IC}$ ) stress-intensity-factor values.

The stress intensity factor's  $K_I$  estimation procedure, which is applicable to threaded joints, has been selected on the basis of thorough investigation of shapes of the crack front and the sizes of the areas affected by fatigue damage at different cyclic loading stages (Fig. 6). The investigation has been carried out by employing special fatigue crack detections and recording procedures helping to determine the shapes, sizes, and locations of cracks and defects (see earlier under *Experimental Methods of Fatigue Crack Determination in the Circular Bars and Threaded Joints*). In the typical configuration of fatigue fracture, the fatigue-damage front contour in the test of threaded joints (M8 to M130) and the stage-wise crack propagation low-cycle tensile fatigue conditions have not undergone any changes within the scale. Basically, the two types of contours, circular and ellipsoidal (Fig. 7), have been disclosed. The majority of relations of defined values of  $K_I(K_{IC})$  in circular straight bars are derived for a concentric circular contour of a crack front, while the minority are valid for eccentric circular as well as ellipsoidal contour (of nondamaged neck). The relation (Eq 5) presents a convenient way [6] of calculating  $K_I(\beta)$  and  $K_{IC}(h = h_{max})$  values both for ellipsoidal and eccentric contours of a neck:

$$K_I(\beta) = \pi R(\beta) (1 + \chi)^{0.25} / 2 \{ [\sigma_t / (1 + g)^{0.5}] + [3\sigma_b / 4 (1 + 0.562g)^{0.5}] \} \tag{5}$$

where

$R(\beta)$  = radius vector of a crack contour in the polar coordinates, mm, and  
 $\sigma_t$  = nominal tensile stresses equal to MPa

$$\sigma_t = Q / \pi ab \text{ for ellipsoidal} \tag{6}$$

$$\sigma_t = Q / \pi R^2 \text{ for circular contours of a crack front} \tag{7}$$

$Q$  = tensile force applied to the bar, kN, and  
 $\sigma_b$  = bending (flexural) stresses equal to MPa.

$$\sigma_b = 4 / \pi ab [M_y \sin(\beta) R(\beta) / a^2 + M_x \cos(\beta) R(\beta) / b^2] \tag{8}$$

For ellipsoidal contour, and when substituting the value of the area by  $\pi R^2$ , the result for circular contour is obtained.  $M_x, M_y$  = bending moments relative to the  $x$  and  $y$  axes, kNm.

Parameters  $\chi$  and  $g$  are calculated according to Eqs 9 and 10:

$$\chi = R^{-1}(\beta) (dR/d\beta) \tag{9}$$

$$g = 0.199 h^{-1} R(\beta) (1 + \chi)^{0.5} \tag{10}$$

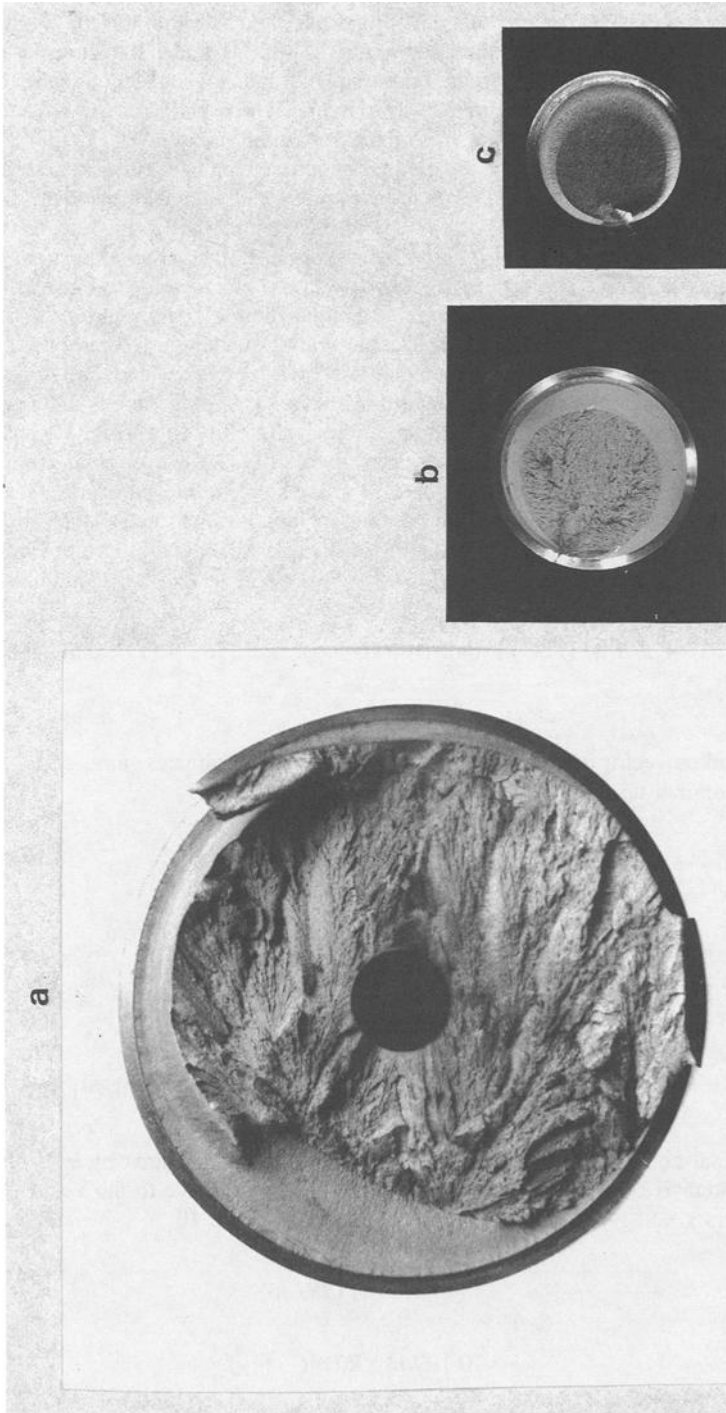


FIG. 6—Examples of fatigue failure of threaded joints M20 to M110 (by laboratory fatigue testing, room temperature conditions): (a) M110×6; (b) M52×4; (c) M20×2.5 (mm).

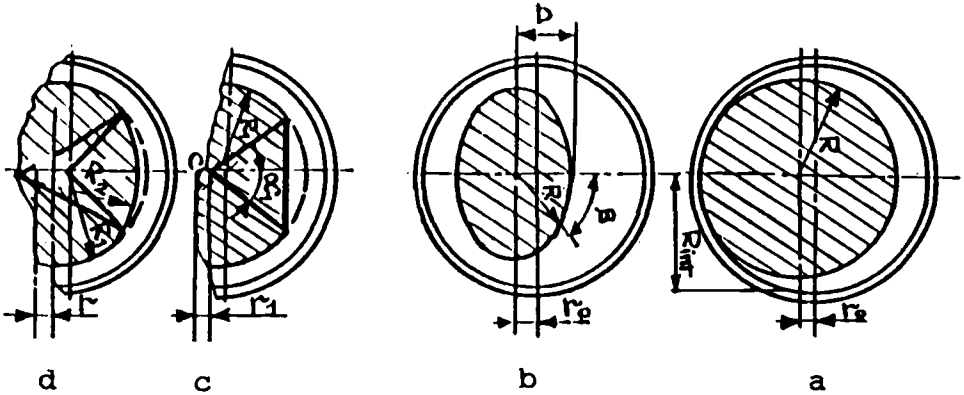


FIG. 7—Typical configurations of fatigue crack contours: (a) circular; (b) ellipsoidal; (c) segment-shaped; (d) convex crescent-shaped.

where

$h$  = crack depth (normal to its contour), mm, and  
 $a, b$  = the axes of ellipse, mm.

It is well known [5,6] that more than ten relations are used to estimate the stress intensity factor  $K_I(K_{IC})$  for the concentric circular (nondamaged) neck version, giving a perfect mutual agreement at  $1.0 \geq (R_{int}/R) \geq 7.0$ , while at  $(R_{int}/R) \approx (0.3 \text{ to } 0.4)$  a discrepancy in design values  $K_I(K_{IC})$  in terms of various procedures is two or three times larger. It is worth noticing that for laboratory test results, the investigation of resistance of cyclic loading (under the low and classical fatigue conditions) in threaded joints, the minimum value of the relation  $(R_{int}/R) \approx 0.6$  has been obtained only when a fatigue crack propagation over a cross section has come to its final steady state. Judging by the final failure, the ratio  $R_{int}/R$  may reach approximately 0.4 (for bolt/stud materials under negligible tightening stresses and cyclic loading conditions), where  $2R_{int}$  is the internal diameter of a nondamaged circular bar.

#### Stress Intensity Factor for Cracked Bolts/Studs (LEFM)

Generally, the estimation of  $K_I(K_{IC})$  values in threaded joints is made for the concentric circular contour of a fatigue crack front, specific only to initial crack propagation stages at high tightening stresses for high-strength threaded joints (with the ultimate strength  $S_u$  for material as large as 1000 MPa), which doesn't embrace the total variety of fracture modes.

Figure 8 illustrates the  $K_I(\beta)$  variation mode for eccentric circular and the ellipsoidal contour of neck. The stress intensity factor  $K_I(\beta)$  reaches its critical value  $K_{IC}$  at the maximum depth of a crack ( $h_{max}$ ). Only the maximum (critical) values of sizes over the front of an ellipsoidal eccentric crack ( $h_{max}$ ,  $a_{max}$ ,  $b_{max}$ , and  $r_0$ ) are used to estimate the critical value of stress intensity factor  $K_{IC}$  or the loading capacity (ultimate load  $Q_c$ ) for cracked threaded joints. In this case, the relation (Eq 5) becomes

$$K_{IC} = Q_c (\pi b_{max})^{0.5} [h_{max}/(h_{max} + 0.199 b_{max})]^{0.5} + (3r_0/b_{max}) [h_{max}/(h_{max} + 0.112 b_{max})]^{0.5} \quad (11)$$

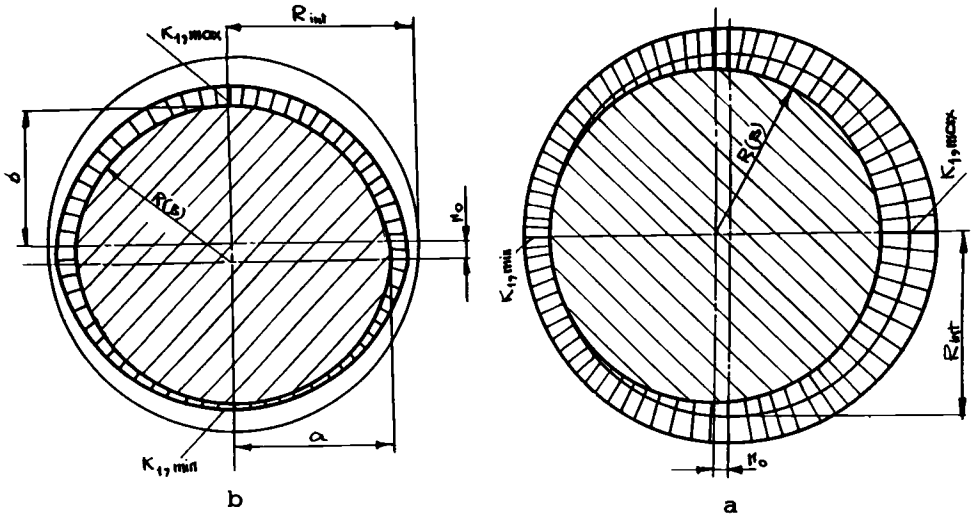


FIG. 8—Variation of stress intensity factor  $K_I$  over the fatigue crack contour: (a) circular eccentric; (b) ellipsoidal eccentric.

where

- $r_0$  = eccentricity of the neck's locations, mm, and
- $b_{max}$  = an axis of the ellipse in the direction of the crack.

An estimation of  $K_I$  or  $K_{IC}$  for the eccentric circular and concentric ellipsoidal or circular neck of a cracked bolt/stud can also be made by following Eq 11 with regards to  $a_{max} = b_{max}$  or to  $r_0 = 0$ , respectively.

For an eccentric circular neck partially flat, as a segment-shape (Fig. 7c) or convex crescent-shaped (Fig. 7d) front of a crack, the factors  $K_I$  or  $K_{IC}$  can also be calculated by interchanging the expressions for  $\sigma_r$  (Eqs 6 and 7) and for  $\sigma_b$  (Eq 8), making respective allowances for the shape of a cross section (nondamaged neck) of a cracked bolt/stud. An extra allowance for the local segment and crescent front shaping of an eccentrically located circular neck gives 4 to 18% smaller value of stress intensity factor  $K_{IC}$  in comparison with that obtained on the calculation of the inscribed (into the front of the fatigue crack contour) ellipse or circumference.

### Nonlinear Effects in Threaded Joints

#### Efforts of Clamp Load

Equations 5 to 11 can be used to calculate the  $K_I(K_{IC})$  values in nonengaged (nonmating) areas (Fig. 4, Areas 2 to 7) by making the effective effort of  $Q_v(N)$  to be defined with the allowance for pretightening  $Q_{vo}$ , external load  $F$ , and basic external load factor  $\chi_1$  for threaded joints under consideration [2]:

$$Q_v(N) = Q_{vo} + \chi_1 F(N) \tag{12}$$

where

$\chi_1$  = external load factor [2].

$$\chi_1 = \lambda_b / (\lambda_b + \lambda_j) \quad (13)$$

where

$\lambda_b, \lambda_j$  = coefficients of compliance of the components of threaded joints, m/kN.

Considering kinetics in the reduction of tightening loads, its preliminary value can be calculated following the relationship shown below:

$$Q_{vo}(N, t, \tau) = [Q_{v,\min} + Q_t + F(1 - \chi_1) + \Delta Q_d]M_t \quad (14)$$

where

$Q_{v,\min}$  = minimum tightening load (by requirement of design), kN,

$Q_t$  = influence of the temperature loading effects within time,  $\tau$ , kN,

$\Delta D$  = total reduction of tightening load due to plastic  $\Delta D = \Delta Q_p + Q_w$ , the strain of mating surfaces  $\Delta Q_p$  and wear  $Q_w$ , kN, and

$M_t$  = effect of friction conditions, lubrication, and assembly methods.

In service time, the pretightening load  $Q_{vo}$  can be decreased to 10 to 80% (even exposing the joint) depending on the design version and operating conditions, which at cyclic loading conditions extend the range of stress intensity factor values  $\Delta K_1 = (K_{1,\max}$  to  $K_{1,\min})$  and intensify the propagation of fatigue cracks.

#### *The Influence of Fatigue Crack Location in a Mating Area*

When calculating factor  $K_1(K_{1C})$  in the damaged area under the bolt head, one should make an extra allowance for eccentricity of load applied to the head of the bolt, equal to the values of moments  $M_x, M_y$ , and  $\sigma_b$  affecting bending stresses.

The calculation of  $K_1(K_{1C})$  for matting (engaged) threads over load  $Q$  acting upon the bolt/stud is done using the same conservative method since lesser load holds in the section of intensive fatigue crack propagation. The comparison of design values  $K_{1C}$  for a specimen of material and for threaded joints of the same shape and size under static and cyclic loading conditions has shown that for threaded joints the values are higher due to supporting effects of the female (nut) part thread fillet, located between the section in which the main fatigue crack propagation (causing unavoidable failure) and the supporting surface of the nut acts (Figs. 4A, 4B).

The nominal stresses  $\sigma$ , acting in the fatigue crack propagation section and depending upon kinetic interacting axial loads are defined in Eqs 6 and 7 as follows [5]:

$$\sigma = Q_c / A_c$$

where

$A_c$  = area of bolt/stud, damaged by fatigue crack, mm<sup>2</sup>.

$$Q_c(N, t, \tau, \Theta) = Q_v(N, t, \tau) - P/2\pi \int_{2\pi-\Theta}^{2\pi} q(P\Theta/2\pi, N, t, \tau) \quad (15)$$

where

$q(P\Theta/2\pi, N, t, \tau)$  = load intensity factors in the cracked threads engagement area, kN/mm

$q(P\Theta/2\pi, N, t, \tau) =$

$$[P^2/4\pi\gamma(P\Theta/2\pi)] \int_0^\Theta \beta(P\Theta_1/2\pi) \int_0^{81} q(P\Theta_2/2\pi, N, t, \tau) d\Theta_2 d\Theta_1$$

$$+ 2\pi/P [\gamma(P\Theta/2\pi) \int_0^{2\pi n} d\Theta / \gamma(P\Theta/2\pi)]^{-1} Q(N, t, \tau)$$

$$- P/8\pi^3 \int_0^{2\pi} [\gamma(P\Theta/2\pi)]^{-1} \int_0^\Theta \beta(P\Theta_1/2\pi) \int_0^{81} q(P\Theta_2/2\pi) d\Theta_2 d\Theta_1 d\Theta \quad (16)$$

where

$\Theta$  = helix angle, rad,

$P$  = thread pitch, mm,

$n$  = the number of threads (where there is intensive fatigue crack propagation),

$N$  = number of cycles,

$\beta(P\Theta/2\pi)$  = coefficient characterizing compliance of the male and female parts, and

$\gamma(P\Theta/2\pi)$  = parameter specifying compliance of thread fillets.

Analysis of local tension of the length of mating fillets and of the nature of propagation of cyclic fracture has shown that, in threaded joints of standard design, the section involving an intensive propagation of fatigue crack (deep into a cross section of a bolt) is to be found inside the female (nut) part and the angle  $\Theta$  (with readings taken from the mating point of the full-formed fillets) varies within  $\pi/6$  to  $\pi/2$ . In addition, some part of the load is undertaken by an incomplete profile of thread of the female part, its rigidity being dependent upon dimensions of the countersink.

An evaluation of the load  $Q_c(N)$  has shown (Fig. 9) approximately 6% reduction in  $Q_c$  for the ratio  $P/d = 0.06$  at  $\Theta = \pi/3$ . Taking into account the load applied to the incomplete profile fillet carrying approximately 40% load of analogous full-formed fillet, one can observe the effect  $Q_c^* = 0.92$ .  $Q_c$  acts in the main crack location place (where  $Q^* = Q_c/Q_v$ ).

Kinetics of the value  $Q_c$  in the section involving the propagation of a fatigue crack causes a variation of the values of  $K_1$  over the full front of the crack contour (Fig. 8). For the

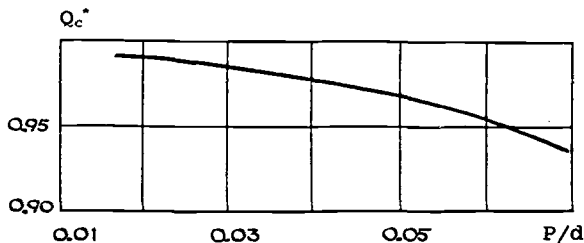


FIG. 9—The efforts of clamp load  $Q_c^*$  in cracked bolt-nut joints:  $P$  = thread pitch;  $d$  = bolt/stud diameter.

fatigue crack circular arrangement, the link between  $Q_c$  and  $K_1$  is almost of linear nature. It is worth noting that for shallow cracks the contour of the front is a circular eccentric shape, and for  $R(\beta)/R = (0.8 \text{ to } 1.0)$ , the calculation with no allowance for eccentricity gives up to 10% error.

*Stress and Strain Concentration Factor for the Plastic Range*

For nonlinear (elasto-plastic) deformation conditions, the alternating strain amplitude  $\epsilon_{ba}$  in the thread's root using the strain concentration factor  $K_\epsilon$  is given by [4,5]:

$$\epsilon_{ba} = \sigma_{ba} K_\epsilon E^{-1} \tag{17}$$

where

- $\sigma_{ba}$  = the alternating stress amplitude in the bolt/stud, MPa, and
- $E$  = modulus of elasticity, MPa.

The amplitude of nominal cyclic stresses in the bolt/stud with area  $A_b$  is [2]:

$$\sigma_{ba} = (Q_{max} - Q_{min}) \chi / 2A_b \tag{18}$$

Strain concentration factors are defined by interpolation of Eq 19, calculated by N. Makchutov [4,5]:

$$K_\epsilon = K_t^{2/(1+m)}, \text{ at } (\sigma_{nom}/S_y) \geq 1 \tag{19}$$

where

- $K_t$  = theoretical stress concentration factor, defined by Eqs 2 and 3,
- $\sigma_{nom}$  = nominal stresses, MPa, defined by Eq 7,
- $S_y$  = yield strength, MPa, and
- $m$  = strengthening index of the stress-strain relation for threaded materials.

Using materials with slight strengthening, stress  $K_\sigma$  and strain  $K_\epsilon$  concentration factors may be calculated using Eqs 20 and 21 in the case of elastic strain,  $K_\epsilon = K_\sigma$ :

$$K_\sigma = (\sigma_{nom}/S_y)^{-1} \tag{20}$$

$$K_\epsilon = K_t^2 (\sigma_{nom}/S_y) \tag{21}$$

with a low influence of the theoretical stress concentration factor ( $K_t \leq 3.5$ ) values [4]. At these conditions the pretightening level growth causes substantial effects of strain concentration (Fig. 10), a determining ultimate state for static and cyclic deformation on ultimate local strain, Eq 17.

*Stress and Strain Intensity Factors for Cracked Bolts/Studs (Elastic-Plastic Fracture Mechanics)*

The values obtained for  $K_I(K_{IC})$  have been checked for correctness by satisfying the plane-strain state with regard to the ratio of typical cross-section dimensions of nondamaged ( $R_{int}$ ) and damaged ( $2a, 2b; a, b =$  ellipse axis) bolts/studs, i.e.:

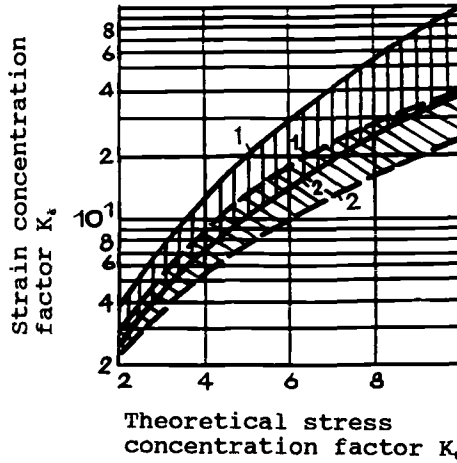


FIG. 10—Influence of elasto-plastic properties of material ( $m =$  strengthening index) on theoretical stress  $K_{\sigma}$  and strain  $K_{\epsilon}$  concentration factors in threaded bolt-nut joints: (1) =  $S_{vo} = S_y$ ; (2) =  $S_{vo} = 0.6 S_y$ ; (III) =  $m = 0$ ; \\\ =  $m = 0.2$ ;  $S_{vo}$  = level of pretightening.

$$d(2R_{int}) \geq 2.3 (K_{IC}/S_y)^2, 2b(2a)_{min} \geq 1.6 (K_{IC}/S_y)^2 \tag{22}$$

The effect of a crack depth with circular eccentric contour of its front on the value of stress intensity factor  $K_I$  in threaded joints M20x1 – M300x6 has shown that the range of correct values of factor  $K_I$  relative to dimensions of the joints varies within 95 to 340 MPa  $m^{1/2}$  and is valid for the  $(2R_{int}/h) \approx (15 \text{ to } 20)$  relation; therefore, for the analysis of basic regularities on crack propagation within threaded joints, the assumptions of linear fracture mechanics are true (Fig. 11).

The limiting-state and fatigue-crack-intensive propagation stage, causing the final fracture and taking place under elasto-plastic strain deformation, do not satisfy the conditions in Eq 22, and the intensity distribution of stresses and strains can be described at loading conditions specified for threaded connections in Refs 4 and 5 with utilization of strain ( $K_{I\epsilon}^*$ ) and stress ( $K_{I\sigma}^*$ ) intensity factors.

To ensure the proper tightness and service time, the level of a nominal stress in threaded components (bolts or studs) usually doesn't exceed the value of the yield strength of material  $S_y$  and for such conditions

$$K_{I\sigma}^* = (K_I/S_y)^{Pk_{\sigma}} \tag{23}$$

For nominal stresses  $\sigma_{nom}$  above the yield limit  $S_y$ , strain intensity factor is:

$$K_{I\epsilon}^* = (Q_c/A_b)^{(1-m)/(m(1+m))} (K_I/S_y)^{Pk_{\epsilon}} \tag{24}$$

Strengthening factor  $m$ , exponents  $Pk_{\epsilon}$  and  $Pk_{\sigma}$  are determined on the basis of a stress-strain diagram (elasto-plastic deformation conditions) [5]. The appearance of comparatively small-sized plastic strain areas in the tip of the crack on the stage of failure has been considered by introduction of the correction factor into the typical dimension ( $2b, a =$  the axes of ellipse;  $h =$  depth of crack) of a fatigue crack front:

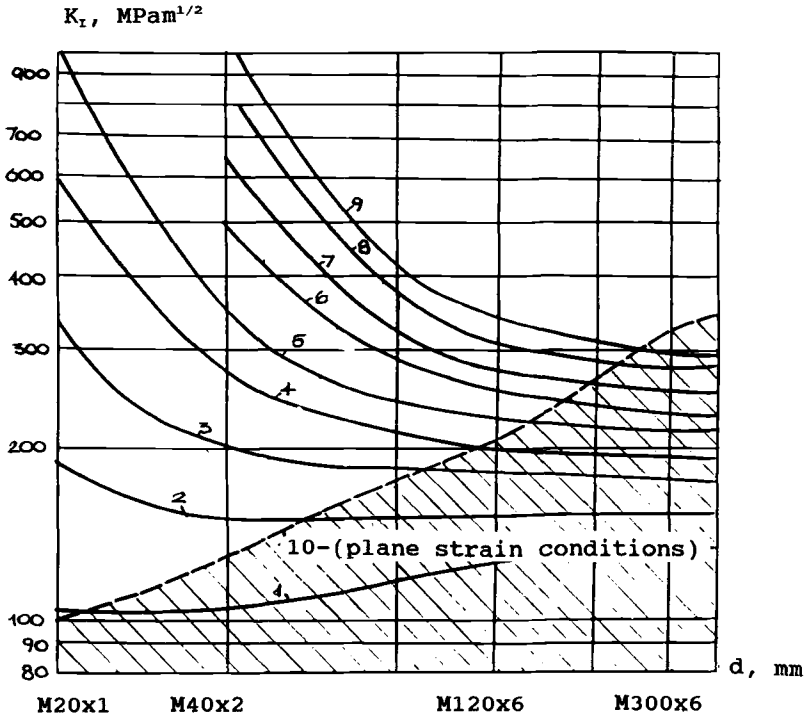


FIG. 11—Stress intensity factor  $K_I$  in threaded joints M20x1 to M300x6 and the area (\\) of correct values of  $K_I$  satisfying the plane strain conditions by Eq 22. Curves 1 to 9 with the influence of fatigue crack depth (mm) for eccentric front of a contour: 1 = 2.0; 2 = 4.0; 3 = 6.0; 4 = 8.0; 5 = 10.0; 6 = 12.0; 7 = 14.0; 8 = 16.0; 9 = 18.0 (mm). 10 = values of stress intensity factor  $K_I$  satisfying the plane strain conditions (Eq 22).  $d$  = diameter of bolt/stud.

$$\begin{aligned}
 a_y &= a - (1/6\pi) (K_I/S_y)^2 \\
 b_y &= b - (1/6\pi) (K_I/S_y)^2 \\
 h_y &= h + (1/6\pi) (K_I/S_y)^2
 \end{aligned}
 \tag{25}$$

*Ultimate State of Cracked Threaded Joints (by Load Capacity)*

The load capacity under static strength conditions may be evaluated by the fatigue crack (or defect) detection data, including crack locations, shapes, and sizes, and also according to the equation:

$$Q_{bc}(N, t, \tau) = 2K_{10C}A_c/\varphi_k[\pi b_y h_{\max,y}/(h_{\max,y} + 0.2b_y)]^{0.5} + Q(N, t, \tau, \Theta_c)
 \tag{26}$$

where

$\varphi_k$  = the correction function of crack location and eccentricity,

$$\varphi_k = 1 + 3(r_0/b)[1 + 0.10(h_{\max,y} + 0.10b_y)^{-1}]^{0.5}
 \tag{27}$$

$\Theta_c$  = angular location coordinate of a damaged thread fillet, rad,  
 $A_c$  = area of bolt, damaged by fatigue crack, mm<sup>2</sup>, and  
 $r_0$  = the neck location, mm (see Figs. 7 and 8).

The load  $Q_c$ , acting in the fatigue crack propagation section, is determined by Eq 15.

For high-strength threaded joints, the ultimate load capacity in the case of elasto-plastic tightening and extreme deformation conditions is determined by the equation:

$$Q_{bc}(N, \tau, T) = K_{IeC}^{*[m(1+m)]/(1-m)} / (A_p S_y)^{[m+(1+m)]/(1-m)} \{[\pi b_y h_{max,y} / (h_{max,y} + 0.2b_y)]^{0.5} 0.5\varphi_k / A_c S_y\}^{pk} + Q_c \quad (28)$$

The critical values of stress  $K_{IeC}^*$  and strain  $K_{IeC}^*$  intensity factors and the limiting load  $Q_{bc}$  for cyclic-damaged threaded joints can be determined by Eqs 23 to 28 on the database test results or can be calculated taking into consideration design versions, the results of investigation of NDTE, and the elastoplastic properties of the material.

The estimation of the limiting state of threaded joints made from chrome-nickel-molybdenum ( $S_y = 1260$  MPa) and chrome-nickel-molybdenum-tungsten ( $S_y = 1920$  MPa) steels following the stage of final failure and threshold stage of fracture (the transition from stable to unstable fatigue crack propagation stage) has shown that an increase in  $S_y$  evokes a reduction of strain intensity factor  $K_{Ie}^*$ . Consequently, any growth of  $S_y$  promotes more extensive disperse of  $K_{Ie}^*$  values, which may be three times as large.

#### *Prediction of Remaining Fatigue Life (Service Time) of Cracked Threaded Joints*

Under cyclic loading conditions, the crack propagation rate in threaded joints can be presented by an S-shaped (on logarithmic scale) fatigue crack diagram consisting of three areas: two extreme curvilinear zones and a single middle part approximated by a straight line. The length of the areas changes with the loading and the environmental conditions, design version, and bolt/stud material properties (Fig. 12).

Experimental investigation of the diagram representing kinetics of cyclic fracture of threaded joints demonstrated that the initial curvilinear area (in the range of the small values for  $\Delta K_I$ ) is responsive to conditions of mechanical and temperature loading. The middle area is sensitive to the asymmetry of a loading cycle, while the second curvilinear area is affected by the variation of the thread size. In the linear area of the fatigue fracture diagram for the threaded connection, the rate of crack propagation in comparison to its depth is described excluding the effects of asymmetry of loading by a Paris-type relation (Paris law):

$$dh/dN = C_p (\Delta K_I)^{n_p} \quad (29)$$

where

$n_p$  ( $n_p$ ) = the slope of the log  $dh/dN$  versus log  $\Delta K$  plot, and

$C_p$  = a parameter that depends upon bolt/stud material properties, asymmetry of loading (mean stress), frequency, etc.

For the definition of a crack propagation rate in the threaded joints with influence of effects of asymmetry of loading ( $R$  load or stress ratio), Forman-type equations are used:

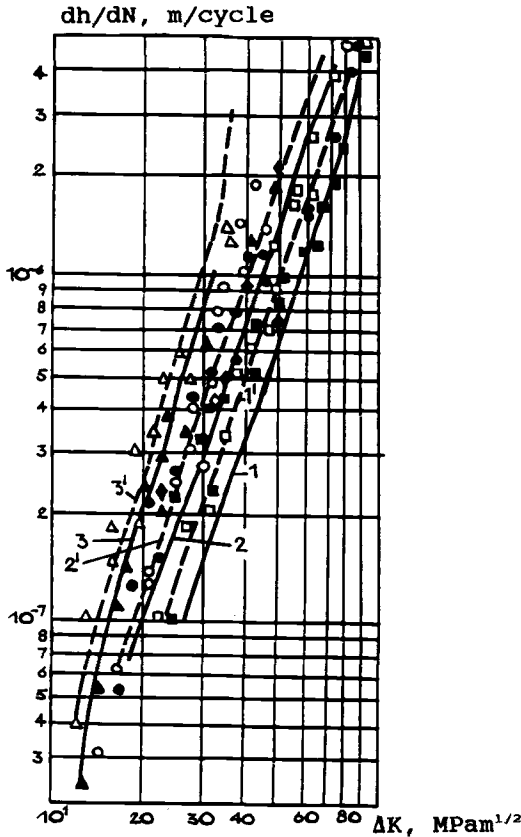


FIG. 12—Fatigue crack propagation in threaded joints M20x6 and M130x6 (♦) made from chrome-nickel-molybdenum-vanadium steels: room temperature conditions; stress ratio  $r = 0$  (■, □),  $r = 0.3$  (●, ○, ◆),  $r = 0.6$  (▲, △), (1') to (3') = average.  $\Delta K$  = stress intensity factor range,  $MPa\ m^{1/2}$ .  $dh/dN$  = fatigue crack growth rate, m/cycle.

$$dh/dN = C_F(\Delta K_I)^{n_f} / [(1 - R)K_{IC} - \Delta K_I] \tag{30}$$

where

$C_F, n_f(n_f)$  = parameters to be determined by test results, and  
 $\Delta K_I = (K_{I,max} - K_{I,min})$  = the range of stress (strain) intensity factors.

The remaining fatigue life-operating time (by number of cycles  $N$  or hours) can be calculated starting from an initial crack depth  $h_0$  to design (or critical) crack size  $h_{cr}$  by condition of values of limiting load  $Q_{bc}$ , Eqs 26 to 28, and employing, for instance, integration of the relation (Eq 29), or:

$$N = C_p^{-1} \int_{h_0}^{h_{cr}} \Delta K^{n_p} dh \tag{31}$$

## Conclusion

This paper presents an original method of determining the strength and durability of threaded joints on fatigue crack initiation and propagation stages. The above calculation takes into consideration the dependence of the joint's design version, load conditions, and behavior of material used on nonlinear effects of fracture and deformation mechanics of threaded joints. The suggested method sets limits of usage of linear and nonlinear fracture conditions for cracked bolts/studs. The calculation of the remaining fatigue life on the crack's propagation stage can be made using Paris and Forman equations combined with the results of NDTE (of shapes and locations of fatigue cracks).

## Acknowledgments

The author appreciates the help on his AlliedSignal colleagues and ASTM in the preparation of this paper.

## References

- [1] Blume, D., "Schadensfälle bei Schrauben-Verbindungen," *VDI—Berichte*, Berlin, 1983, No. 478, pp. 143–150.
- [2] Bickford, J. H., *An Introduction to the Design and Behavior of Bolted Joints*, 2nd ed., rev., and expanded. Marcel Dekker, Inc. New York, 1990.
- [3] Raymond, L., "Fracture Mechanics Applied to Tensile Fasteners, Part I—Failure Mode," *American Fasteners Journal*, October/November 1989. "Part II—Material Selection," *American Fasteners Journal*, January/February 1990.
- [4] Makhutov, N., Kagan, V., and Zatsarinny, V., "Initiation and Propagation Mechanics of Low Cycle Fatigue Cracks in Bolts," *Proceedings*, Fifth International Conference on Fracture, ICF-5, Cannes, 1981, Vol. 2, pp. 605–612.
- [5] Kagan, V., Makhutov, N., and Filatov, V., "Non-Linear Effects in Threaded Joints Under Low-Cycle Loading," *Proceedings*, Eighth International Conference on Structural Mechanics in Reactor Technology, Vol. 2, Inelastic Behavior of Materials and Constitutive Equations, Brussels, 1985, pp. 161–166.
- [6] Jarema, S. Y., "Stress Intensity Factors for Cylindrical Specimens with External Crack of Variable Depth," *Physic-Chemicheskaya Mehanika Materialov*, Vol. 6, No. 1, Lvov, Ukraine, 1970, pp. 87–89.
- [7] Liu, A. F., "Evaluation of Current Analytical Methods for Crack Growth in a Bolt," *Proceedings*, Seventeenth I.C.A.F. Symposium, Stockholm, May 1993, pp. 1–12.
- [8] Westergaard, H. M., "Bearing Pressures and Cracks," *Journal of Applied Mechanics*, *ASME Transactions*, Series A, Vol. 66, 1939, p. 49.
- [9] Irwin, G. R., "Analysis of Stresses and Strains Near the End of a Crack Traversing a Plane," *Journal of Applied Mechanics*, *ASME Transactions*, Vol. 24, 1957, p. 361.

Marjorie Ann E. Natishan<sup>1</sup> and William C. Porr, Jr.<sup>1</sup>

## The Effect of Grain Boundary Carbon on the Hydrogen-Assisted Intergranular Failure of Nickel-Copper Alloy K-500 Fastener Material

---

**REFERENCE:** Natishan, M. E. and Porr, Jr., W. C., "The Effect of Grain Boundary Carbon on the Hydrogen-Assisted Intergranular Failure of Nickel-Copper Alloy K-500 Fastener Material," *Structural Integrity of Fasteners, ASTM STP 1236*, P. M. Toor, Ed., American Society for Testing and Materials, Philadelphia, 1995, pp. 81–92.

**ABSTRACT:** A recent failure analysis of nickel-copper K-500 fasteners that failed in air associated the rate-dependent, intergranular fracture mode with the presence of grain boundary carbon films and precipitates. The exact mechanism of rate-dependent fracture in that instance was unknown. However, mechanisms such as hydrogen-assisted cracking and creep are known to be consistent with the circumstances of that failure. To determine whether hydrogen-assisted cracking could be affected by grain boundary carbon amount and morphology, the present study examines the influence of intergranular carbon precipitates and various levels of hydrogen on the fracture behavior of nickel-copper Alloy K-500. Dichotomous results indicate that hydrogen-assisted intergranular fracture associated with carbon precipitates may occur in this alloy at lower bulk hydrogen levels than previously reported, yet carbon precipitates may inhibit susceptibility to hydrogen embrittlement under cathodic charging conditions. The latter result is discussed with respect to a possible competitive interaction between hydrogen-assisted and carbon-precipitate-induced intergranular fracture modes.

**KEYWORDS:** nickel-copper K-500, grain boundary carbon, intergranular failure, fasteners, hydrogen embrittlement, slow loading rate properties

### Background

Nickel-copper alloy K-500 is a face-centered cubic (FCC) solid solution of copper and nickel that is strengthened upon aging at 593°C by a fine dispersion of  $\gamma'$  precipitates ( $\text{Ni}_3\text{Al/Ti/Fe}$ ) and carbides to an approximate yield strength of 620 MPa [1]. Due to the high strength, toughness, and resistance to general corrosion, Alloy K-500 is commonly used in marine and other corrosive environments. Its fracture mode on overload failure is usually transgranular microvoid coalescence; however, Alloy K-500 has been shown to be susceptible to intergranular failure when exposed to hydrogen [2,3]. Intergranular failures have recently occurred in Alloy K-500 fasteners during testing despite the absence of a hydrogen-producing test environment.

Previously, a failure analysis was conducted on three high-pressure drain system fasteners that failed during testing to determine the mode and metallurgical cause of failure. The detailed results of this analysis are presented in Ref 4.

---

<sup>1</sup> Senior project engineer and research engineer, respectively, Carderock Division, Naval Surface Warfare Center, Annapolis Detachment, Code 614, Annapolis, MD 21402-5067.

The fasteners had been torqued into a high-pressure drain system valve for an unknown period of time prior to failure. The exposure environment of the fasteners included temperatures of approximately 150 to 260°C from conductive heating due to system fluid within the valves. The fasteners were not directly exposed to the system fluid until after failure. The loading on the fasteners due to the internal valve pressure was far below the loading from the torque preload and was not thought to play a role in the failures.

The failure analysis included detailed scanning electron fractographic analysis of the fracture surfaces, high-resolution optical metallography to characterize the microstructures, scanning Auger spectroscopy for detailed elemental distribution analysis, and mechanical testing to simulate the service conditions and duplicate the mode of failure. It was found that at low loading rates and high temperatures (260°C), the K-500 failed in an intergranular mode, whereas at high loading rates and low temperatures, the failure mode was transgranular microvoid coalescence.

The conclusion of the failure analysis was that the K-500 fasteners failed in an intergranular fracture mode due to an undetermined loading-rate and temperature-dependent mechanism associated with grain boundary carbon precipitation [4]. That uncertainty in the failure mechanism has led to the current research, described as follows.

### *Current Research*

As just reported, initial study of fastener failures indicated a loading rate and temperature-dependent fracture mode transition in K-500 at temperatures between 21 and 260°C. Traditional loading-rate and temperature-dependent phenomena that occur in metals include hydrogen embrittlement, creep, and dynamic strain aging (DSA). Substantial creep in metals, and any resulting intergranular cavitation, is usually associated with temperatures above  $T_m/2$  [5] and thus is not expected in environments where temperatures do not exceed 260°C ( $T_m/2$  for K-500 is 530°C). DSA associated with solid solution C has been reported to occur in nickel alloys at temperatures above 200°C [6,7], but a specific mechanism for this phenomenon in the nickel-carbon (Ni-C) system has not been identified and general DSA theories are disputed. Dynamic strain aging is a deformation phenomenon; it is uncertain how DSA would result in brittle, intergranular fracture. A mechanism of intergranular, loading-rate-dependent fracture attributable to DSA is not believed to be applicable in this case. In the previously described fastener failure, no external source of hydrogen was identified and levels of bulk hydrogen were measured to be below that associated with hydrogen embrittlement in K-500 [3]. Additionally, it is uncertain how any of these three phenomena might be associated with the intergranular carbon precipitation.

Since creep and dynamic strain aging mechanisms are typically associated with higher temperatures in nickel alloys, while hydrogen-assisted cracking has been observed at (and below) room temperature, possible hydrogen embrittlement was further examined.

A large research program is underway at the Carderock Division of the Naval Surface Warfare Center to study the susceptibility of alloy K-500 to low-load intergranular failure. The objective of this program is to determine the mechanism of intergranular fracture both with and without a hydrogen-producing environment. The end goal of this research is modification of processing standards to alter grain boundary carbon precipitation and reduce the intergranular cracking susceptibility of K-500. The scope of this program covers forging processes, precipitate kinetics, and the evolution of fracture in K-500 manufactured by various melters. This paper presents preliminary results of a study to determine the susceptibility of K-500 to hydrogen-assisted, intergranular fracture as a function of the amount and nature of grain boundary carbon precipitates.

## Procedure

To characterize the effect of grain boundary precipitate morphology on hydrogen embrittlement susceptibility of alloy K-500, slow-loading-rate tension tests were performed on bar stock of varying amounts of grain boundary carbon precipitation. Material containing predominantly film-type grain boundary precipitates, material containing predominantly discrete grain boundary precipitates, and material containing very little grain boundary precipitation of any kind were studied to determine whether the amount and morphology of grain boundary carbon precipitate play a role in hydrogen embrittlement susceptibility.

## Materials

Four different heats of alloy K-500, produced by four different manufacturers using various melt practices, were examined in this study with the different heats designated HJ, ET, DT, and VT. The chemical compositions and microstructural features of the four heats are indicated in Table 1. The chemical compositions of the four are nominally the same. The materials were received as forged bar stock that varied microstructurally with individual manufacturer's melt practices. Heat HJ had a uniform, small-grain distribution with very little or no grain boundary precipitation of carbon (Fig. 1). The other three heats had larger grain sizes with nonuniform grain-size distributions. The grain boundary carbon precipitates ranged from predominantly films for Heats ET and DT (Fig. 2) to predominantly discrete (spherical) precipitates in the heat marked VT (Fig. 3). Variations in the percentage of grain boundaries with carbon precipitates ranged from negligible in Heat HJ to upwards of 50% for Heat VT.

## Mechanical Testing

Slow-loading-rate tensile experiments were conducted using a screw-driven tensile machine at an applied displacement rate of  $4.2 \times 10^{-4}$  mm/s. This rate was selected to promote brittle, intergranular fracture, based on the previously described results of the effect of load-

TABLE 1—Chemical composition, grain boundary precipitate morphology, and associated percentage grain boundary carbon for selected heats of Alloy K-500.

Heat	HJ	ET	DT	VT	Military Specification QQ-N-286F
Grain Boundary, % Carbon Coverage	1-3	10-15	15-20	>20	Not Specified
Precipitate Morphology	Discrete Particles	Films	Films	Discrete Particles + Some Films	Not Specified
Ni	65.40	64.43	66.71	64.9	63.0 (min)
Cu	29.24	30.03	28.50	29.9	27.0-33.0
Al	2.96	2.71	2.95	3.00	2.30-3.15
Fe	0.96	1.02	0.60	0.76	2.0 (max)
Mn	0.70	0.68	0.60	0.61	1.5 (max)
Ti	0.49	0.49	0.45	0.46	0.35-0.85
C	0.17	0.13	0.13	0.14	0.18 (max)
Si	0.08	0.21	0.06	0.13	0.50 (max)
S	0.001	0.001	0.003	0.001	0.010 (max)

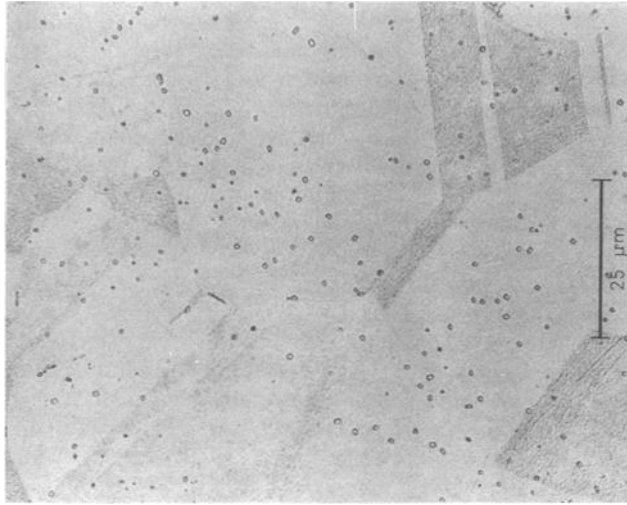


FIG. 1—Optical micrograph of Alloy K-500, Heat HJ illustrating little or no grain boundary carbon precipitation.

ing rate on fracture behavior of heat DT [4]. Three specimens from each of the four heats (representing four different levels of grain boundary carbon) were tested in air and while cathodically charged at a potential of  $-1.0 V^2$  to introduce hydrogen to the specimen. ASTM

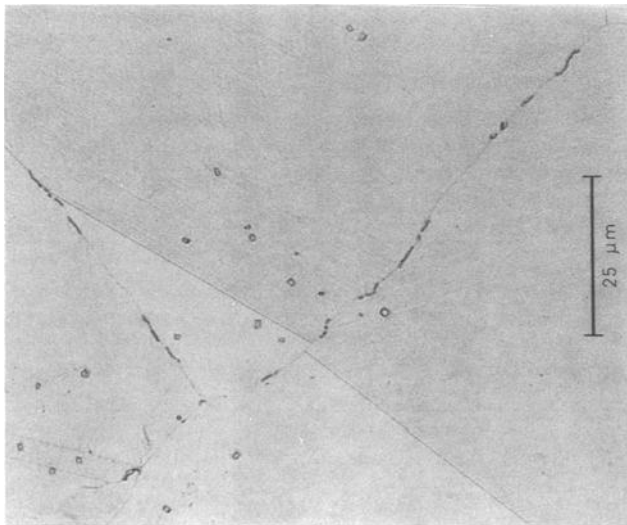


FIG. 2—Optical micrograph of Alloy K-500, Heat ET illustrating film-like grain boundary carbon precipitates.

---

<sup>2</sup> All cathodic charging potentials indicated in this paper are referenced versus the standard calomel electrode (SCE).

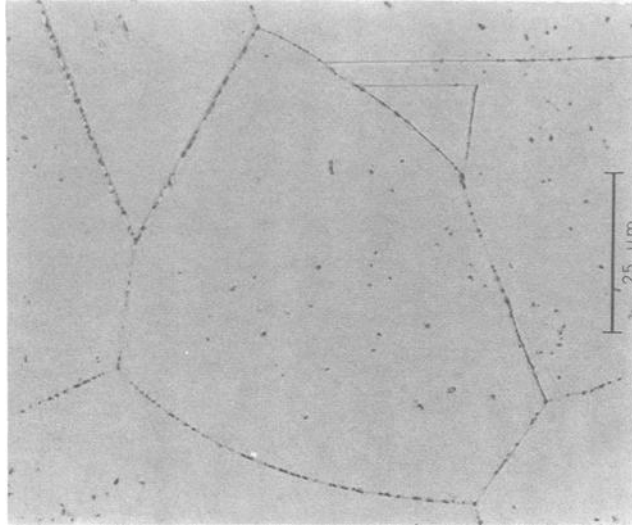


FIG. 3—Optical micrograph of Alloy K-500, Heat VT illustrating discrete, spherical grain boundary carbon precipitates.

Specification for substitute Ocean Water (D 1141-90) [8] was used as the electrolyte. Only one specimen each from the 1 to 3% grain boundary carbon and 15 to 20% grain boundary carbon heats were tested at  $-1.5$  V due to limitations in material. Specimens were charged for several hours prior to testing, with continued charging for the duration of each test. Specimen geometry was a continuously threaded stud to simulate the fasteners that had failed during testing. The studs were 9/16-12 UNC with a 12-mm gage section (exposed length, not threaded into grips). Notched tensile strength (load divided by initial notch root cross-sectional area,  $P/A_n$ ) was measured for each test, and the amount of intergranular fracture was quantified using scanning electron microscope (SEM) fractography in conjunction with a digital image analyzer.

To examine possible hydrogen-assisted intergranular cracking resulting from bulk hydrogen, heat treatments at  $425^\circ\text{C}$  for 10 h were performed on several specimens machined from K-500 Heat DT (the same heat of K-500 as the failed fasteners described in [4]), and subsequently specimens were tested under slow-displacement-rate conditions at room temperature. Assuming a diffusivity of hydrogen in K-500 of approximately  $10^{-1}$   $\text{cm}^2/\text{s}$  at this temperature, this baking treatment should have been sufficient to offgas mobile bulk hydrogen from the 9/16-12 UNC stud specimens.<sup>3</sup> Following testing, the fracture surfaces of these specimens were examined for changes in the fracture mode.

<sup>3</sup> This is based upon time for hydrogen to diffuse from the center of the specimen to the surface given by

$$t = \frac{x^2}{2D}$$

where  $t$  is the diffusion time,  $x$  is the diffusion distance (0.714 cm), and  $D$  is the diffusivity of hydrogen in K-500 estimated from the diffusivity of hydrogen in nickel [9]

$$D \left( \frac{\text{cm}^2}{\text{s}} \right) = 1.07 \times 10^2 e^{-5050/T}$$

where  $T$  is temperature in K.

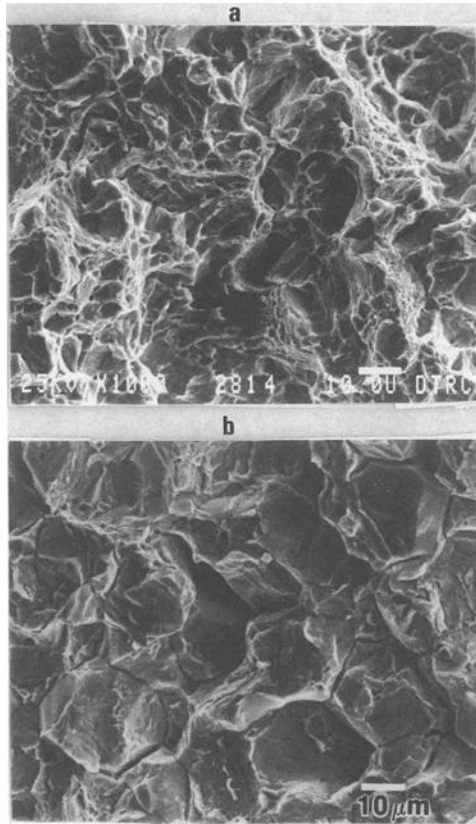


FIG. 4—SEM fractographs illustrating (a) the mixed transgranular microvoid coalescence and intergranular fracture mode of notched tension specimens heat treated at 425°C prior to testing at 21°C, and (b) the intergranular fracture mode of as-received notched tension specimens tested at 21°C.

## Results and Discussion

### Baking Treatments

Figure 4 shows fracture surfaces of specimens loaded to failure with and without pretest heat treatments. The amount of intergranular fracture observed in these experiments was not quantified. However, the amount of brittle, intergranular failure observed on the baked specimens (Fig. 4a) was greatly reduced from the as-received specimens (Fig. 4b), with only very localized regions of intergranular failure. This observation is consistent with a low-hydrogen, loading-rate-dependent mechanism of failure for this heat of K-500. Speculatively, the heat treatments caused outgassing of retained hydrogen (approximately 4 ppm in the as-received material), reducing intergranular embrittlement. The baking temperature of 425°C was insufficient to cause evolution of the microstructure<sup>4</sup> during the heat treatment; hence, hydrogen outgassing represents the most likely cause of the reduced amount of intergranular

<sup>4</sup> Notched tensile strength (NTS) was unaffected by the heat treatment: with heat treatment, NTS  $\approx$  1100 MPa; without heat treatment, NTS  $\approx$  1125 MPa.

fracture. Previously, bulk hydrogen levels below 5 ppm were not believed to cause hydrogen-related embrittlement in K-500 [3]; these results suggest that grain boundary carbon precipitates may enhance hydrogen-assisted embrittlement in some way, such that low-bulk hydrogen levels ( $<5$  ppm) are sufficient to cause intergranular embrittlement.

These preliminary results are of great interest for two reasons, the first being that a number of failures of alloy K-500 fasteners in seawater environments, under cathodic protection, have been observed over the last few years and attributed to hydrogen embrittlement. These fasteners were never evaluated for the presence of grain boundary carbon precipitation, and so it is not known if grain boundary carbon could have been an accelerating factor in their failure. This is of interest because of the wide use of Alloy K-500 for fasteners in seawater applications. If grain boundary carbon plays a role in hydrogen embrittlement susceptibility, it may be possible to decrease susceptibility by controlling the microstructure of this alloy.

The other reason for interest in these results is the apparent contradiction with the results of Lee and Latanison [10] which indicated that spherical grain boundary precipitates of carbon in nickel decrease the degradation in fracture behavior attributable to hydrogen embrittlement. Lee and Latanison concluded that spherical carbon precipitates on grain boundaries act as traps for hydrogen, inhibiting hydrogen diffusion along grain boundaries to regions of high stress and hence reducing embrittlement from hydrogen. The results from the current study would indicate that bulk hydrogen is mobile in K-500 and participating in the embrittlement mechanism despite the presence of grain boundary carbon precipitates. It is important to consider that the results of Lee and Latanison indicated that the amount of embrittlement attributable to hydrogen was reduced by the presence of grain boundary carbon precipitates; however, the overall ductility in this condition was lower than the ductility under the conditions of hydrogen embrittlement without the grain boundary precipitates. The grain boundary precipitates themselves had an embrittling effect. This implies that the embrittling effects of grain boundary precipitates and hydrogen may be additive. Precipitates might not reduce hydrogen embrittlement susceptibility; the K-500 may show a reduced fraction of embrittlement attributable to hydrogen because the material is already fully embrittled.

Considering the low mobility of hydrogen in nickel at room temperature, an alternate interpretation for the results of the current study, consistent with the conclusions of Lee and Latanison, can be introduced: the 425°C heat treatment provided sufficient thermal energy to allow weakly trapped hydrogen to diffuse to stronger precipitate traps such that intergranular fracture in subsequent experiments is reduced. How a low concentration of weakly trapped, immobile atomic hydrogen would participate in an intergranular fracture mode at room temperature, however, is not obvious.

The difference in morphology between the grain boundary precipitates studied by Lee and Latanison and those characterized in this study suggested that while discrete precipitates may act to inhibit diffusion of hydrogen, semicontinuous, film-type precipitates may actually provide a pathway for hydrogen diffusion along grain boundaries and result in a greater relative mobility of atomic hydrogen in Alloy K-500. The crystal structure of the grain boundary carbon has not been identified, but it was suspected that the unalloyed carbon was present in the form of graphite, which has large interplanar spacings that could allow rapid diffusion of hydrogen. These speculations cannot be further examined with the limited data presented here; detailed study of hydrogen mobility and trapping in K-500, as a function of precipitate content and morphology, is required.

### *Mechanical Testing*

The tests in air indicated that grain boundary carbon precipitation may have an effect on notched tensile strength (NTS): strength increased with increasing amounts of grain boundary

carbon. Figure 5 shows the average NTS of the three specimens tested at each condition in air and at  $-1.0$  V and the single specimens values for  $-1.5$  V. Variation of NTS values in air and  $-1.0$  V for each heat was less than 10%. Heat HJ (lowest grain boundary carbon) did not follow this trend, but the grain size for this material was substantially smaller, which could account for the increased strength exhibited by this material. It is not obvious that the moderate increase in tensile strength with increasing amount of grain boundary carbon precipitates is associated with the grain boundary carbon precipitates. This trend in NTS may simply be the result of varying chemistry and processing for the four heats.

The tests in a hydrogen-charging environment showed that hydrogen had a much larger effect on the properties of the low-grain-boundary carbon precipitate specimens that it did on specimens containing 10% or more grain boundary carbon precipitation (Fig. 5). At  $-1.0$  V there was very little effect of hydrogen charging on the notched tensile strength for the higher-grain-boundary carbon specimens. At the highest charging level, a similar decrease in notched tensile strength was observed in both the very low-grain-boundary carbon material and the 15 to 20% grain boundary carbon material. These results indicate that at this extreme hydrogen-charging condition grain boundary precipitation plays little role in determining the influence of hydrogen on degradation of notched tensile strength.

The amount of intergranular fracture (a qualitative measurement of embrittlement or ductility) as a function of the amount of grain boundary carbon precipitate followed the same trend as shown by notched tensile strength (Fig. 6). With the exception of Heat HJ (1 to 3% grain boundary carbon), the total amount of intergranular fracture in the notched tension

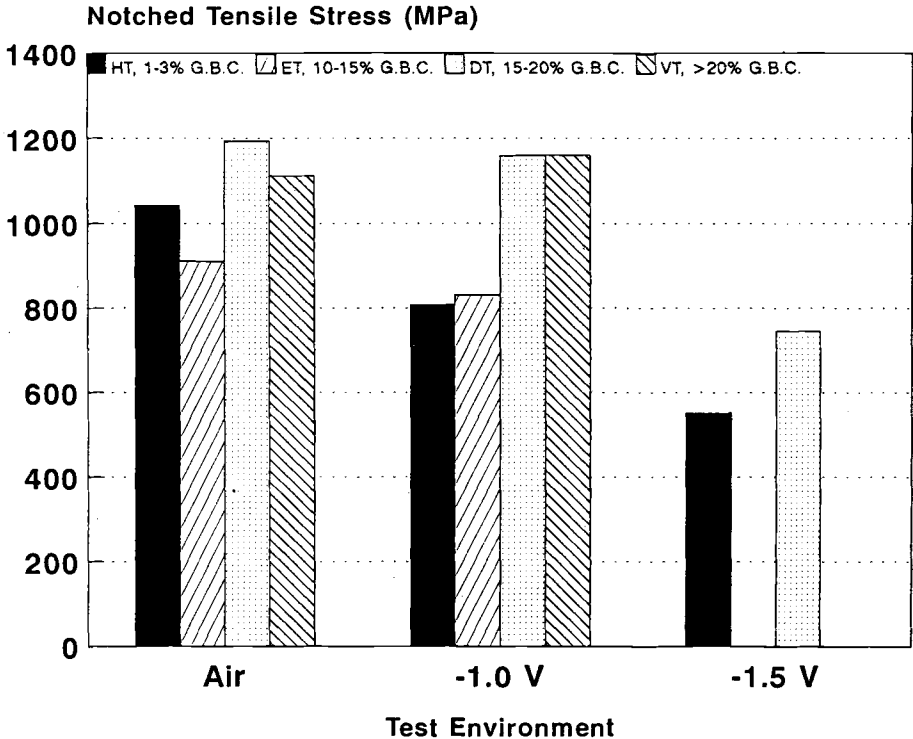


FIG. 5—Notched tensile strengths of four heats of Alloy K-500 (four different amounts of grain boundary carbon {GBC} precipitation) as a function of test environment.

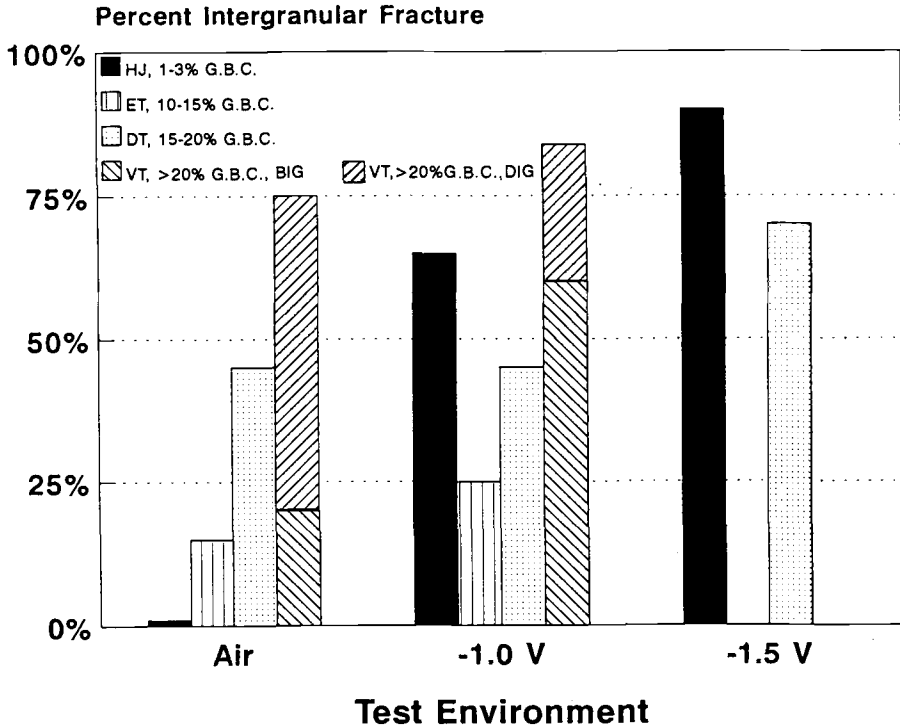


FIG. 6—Total amount of intergranular fracture (brittle [BIG], and ductile [DIG]) in four heats of Alloy K-500, with four different amounts of grain boundary carbon (GBC) precipitation, as a function of test environment.

specimens increased with increasing amount of grain boundary carbon precipitation, whether tested in air or under  $-1.0$  V cathodic charging conditions. As indicated in Fig. 6, intergranular fracture of Heat VT was observed in two different modes: (1) ductile, intergranular fracture (DIG) associated with microvoid initiation at spherical-grain-boundary carbon precipitates, and (2) brittle, intergranular fracture (BIG) associated with either film-type grain boundary carbon precipitates or hydrogen embrittlement. In previous experiments the ductile, intergranular fracture mode was observed to occur independent of displacement rate, while the brittle, intergranular mode was observed only at slow displacement rates [4]. Scatter in the measures of intergranular fracture for each heat tested in air and at  $-1.0$  V was considerable. This variation is due partly to the subjective nature of this measurement and as such is not shown in Fig. 6.

Specimens containing less than 10% grain boundary carbon precipitation showed a large effect of hydrogen (cathodic charging) on the amount of brittle, intergranular fracture observed at both  $-1.0$  and  $-1.5$  V. Specimens containing 15 to 20% grain boundary precipitation showed no effect of hydrogen on the total amount of intergranular fracture observed at  $-1.0$  V cathodic charging. However, at the highest levels of cathodic charging ( $-1.5$  V), there was a moderate increase in the amount of intergranular fracture observed in the 15 to 20% grain boundary carbon material. Specimens containing more than 20% grain boundary carbon precipitation showed little effect of cathodic charging at  $-1.0$  V on the total amount of intergranular fracture observed; however, an increase in the amount of brittle, intergranular

fracture was observed for the specimens containing a large amount of discrete carbon precipitates. This indicates that the loading-rate-dependent, hydrogen-assisted fracture mechanism and the loading-rate-independent, ductile intergranular fracture mechanism are competitive mechanisms.

These results imply that alloys containing little or no grain boundary carbon precipitation have a greater susceptibility to degradation in tensile strength and fracture mode as a function of cathodic hydrogen charging than material with moderate to extensive grain boundary carbon precipitation. This is consistent with the results of Lee and Latanison and suggests that grain boundary carbon acts to inhibit the susceptibility of Alloy K-500 to hydrogen embrittlement. Grain boundary carbon may indeed act to trap hydrogen, and semicontinuous, film-type precipitates may trap hydrogen in a manner similar to discrete carbon precipitates. In contrast, as evidenced in Fig. 6, there was an increase in the amount of brittle, intergranular fracture associated with hydrogen for the specimens containing a large proportion of discrete grain boundary carbon precipitates and only a small amount of film-type carbon precipitate (Heat VT, >20% grain boundary carbon). Yet, the total amount of intergranular fracture did not change substantially from experiments conducted in air. This is consistent with a competitive relationship between hydrogen embrittlement and intergranular fracture associated with spherical grain boundary carbon precipitates: both mechanisms are acting; however, one predominates over the other, depending upon conditions. In addition, the total amount of intergranular fracture associated with cathodic charging at  $-1.0$  V was similar for Heats HJ [1 to 3% grain boundary carbon (GBC)] and VT (>20% GBC), Fig. 6. Thus, even though Heat HJ shows a severe degradation in fracture mode associated with hydrogen charging, it is no more severe than the degradation in fracture mode of this alloy associated with large amounts of grain boundary carbon precipitation.

The effect of carbon precipitate morphology on hydrogen-assisted intergranular cracking cannot be clearly determined from the experiments conducted in this study. The implication from Fig. 6 is that Alloy K-500 heats with film-like carbon precipitates (ET and DT) and may exhibit greater susceptibility to hydrogen-assisted intergranular fracture than heats with discrete spherical precipitates (VT). However, the overall amount of intergranular fracture under cathodic polarization of these two heats at  $-1.0$  V is less than in heats with either no intergranular precipitation (HJ) or heats with predominantly spherical precipitates (VT). This idea can only be addressed by a study in which precipitate morphology is varied for a constant amount of grain boundary carbon precipitate.

#### *Implications and Future Research*

Although data presented here are limited, they are consistent with the results of Lee and Latanison when the amount of grain boundary carbon precipitation is low. Heat HJ exhibits a severe susceptibility to property degradation from hydrogen exposure. With the introduction of a small amount of grain boundary carbon precipitation (Heat ET, 10 to 15% GBC), property degradation from cathodic charging at  $-1.0$  V is much reduced; NTS is similar and the amount of intergranular fracture was lower than for Heat HJ under the same conditions. With increasing amount of grain boundary carbon precipitation (>15% GBC, Heats DT and VT), property degradation does not occur with cathodic charging at  $-1.0$  V. At very high levels of hydrogen charging, however, grain boundary precipitation had a limited effect on susceptibility to property degradation. These data contradict the theory of carbon-precipitate-enhanced hydrogen embrittlement from the preliminary hydrogen-baking heat treat study in which an improvement was observed in fracture mode after a long-term 425°C baking.

It is possible that with very low levels of bulk hydrogen, the grain boundary precipitation acts to enhance diffusion of hydrogen such that the material is fully embrittled even with

low concentrations of hydrogen, and at the hydrogen levels associated with cathodic charging at  $-1.0$  V, no additional embrittlement occurs. Future research will address this possibility. Phenomena that need to be examined in detail include atomic hydrogen partitioning and mobility in K-500 and how these are affected by heat treatment and precipitate morphology and the subsequent effect of partitioning or trapping on mechanical behavior. The question still remains as to whether there is an additive effect or a competing effect between the grain boundary fracture mechanisms attributed to hydrogen and grain boundary carbon precipitation. A micromechanistic approach will be required to study this issue.

The current research, along with that of Lee and Latanison, indicates a strong relationship between the amount and morphology of grain boundary carbon precipitates and hydrogen-assisted fracture susceptibility, yet little is currently understood about the variation in carbon precipitate morphology in different heats of Alloy K-500. A study is currently underway to determine the effect of hot forging procedures on final carbon precipitate morphology. It is hoped that an understanding of processing variables that affect carbon precipitate morphology and amount and an understanding of the susceptibility of K-500 to hydrogen-assisted intergranular fracture and mechanical property degradation will allow development of K-500 fastener material that will perform better in seawater applications under cathodic protection.

## Conclusions

1. Nickel-copper alloy K-500 is susceptible to loading-rate-dependent intergranular failure at  $21^{\circ}\text{C}$ .
2. The amount of intergranular fracture in Alloy K-500 increases with increasing amount of grain boundary carbon precipitation and hydrogen charging (via cathodic charging).
3. Grain boundary carbon inhibits the susceptibility of Alloy K-500 to increased hydrogen-assisted intergranular fracture. The total amount of intergranular failure for the highest carbon precipitate level material tested in air, however, was the same as the material with little or no intergranular carbon precipitates tested under  $-1.0$  V versus SCE cathodic charging.
4. Results from experiments involving pretest heat treatments imply that hydrogen-assisted intergranular fracture occurs with bulk atomic hydrogen levels much lower than previously thought.

## References

- [1] "Monel: Nickel-Copper Alloys," product brochure from Huntington Alloys Division of International Nickel Company, Huntington, WV, 1984.
- [2] Harris, J. A., Scarberry, R. C., and Stephens, C. D., "Effects of Hydrogen on the Engineering Properties of MONEL Nickel-Copper Alloy K-500," *Corrosion*, Vol. 28, No. 2, February 1972, pp. 57-62.
- [3] Kamdar, M. H., "Embrittlement of Nickel by Gaseous Hydrogen," *Hydrogen in Metals, Proceedings of the 2<sup>nd</sup> International Conference*, Pergamon Press, New York, Vol. 2, 1977, 3D10.
- [4] Natishan, M. E., Sparks, E. R., and Tims, M. L., "Intergranular Cracking in Nickel-Copper Alloy K-500 Due to Grain Boundary Carbon," *Proceedings, International Symposium for Testing and Failure Analysis*, ASM International, Materials Park, OH, 1991, pp. 385-392.
- [5] Dieter, G. E., *Mechanical Metallurgy*, 2nd ed., McGraw-Hill, Inc., New York, 1976, p. 452.
- [6] Sung, J. K., Jones, J. W., and Was, G. S., "Effect of Carbon on the Low-Temperature Creep Behavior of Ni-16Cr-9Fe," *Metallurgical Transactions, A*, Vol. 23A, March 1992, pp. 1033-1037.
- [7] Miner, R. V. and Castelli, M. G., "Hardening Mechanisms in a Dynamic Strain Aging Alloy, HASTELLOY X, During Isothermal and Thermomechanical Cyclic Deformation," *Metallurgical Transactions, A*, Vol. 23A, February 1992, pp. 551-561.

- [8] "Specification for Substitute Ocean Water, Designation: D 1141-90," *Annual Book of ASTM Standards*, ASTM, Philadelphia, PA, Vol. 11.02, 1992, pp. 423-424.
- [9] Betteridge, W., *Nickel and Its Alloys*, Ellis Horwood Limited, West Sussex, England, 1984, p. 25.
- [10] Lee, T. S. F. and Latanison, R. M., "Effects of Grain-Boundary Segregation and Precipitation on the Hydrogen Susceptibility of Nickel," *Metallurgical Transactions, A*, Vol. 18A, Sept. 1987, pp. 1653-1662.

# **Fracture Mechanics in Fasteners**

# Stress Intensity Factors for Surface and Corner-Cracked Fastener Holes by the Weight Function Method

---

**REFERENCE:** Zhao, W. and Atluri, S. N., "Stress Intensity Factors for Surface and Corner-Cracked Fastener Holes by the Weight Function Method," *Structural Integrity of Fasteners*, ASTM STP 1236, P. M. Toor, Ed., American Society for Testing and Materials, Philadelphia, 1995, pp. 95–107.

**ABSTRACT:** The paper presents stress intensity factor solutions for surface and corner-cracked fastener holes by using an efficient and accurate three-dimensional weight function method. The approach is briefly described. Stress intensity factors for crack-face pressure loads of the type  $(x/r)^n$  are provided, where  $n$  varies from 0 to 4. The geometry parameters considered are as follows: the ratio of the hole radius to plate thickness  $r/T = 1.5$  ( $T = t$  for corner cracks,  $T = 2t$  for surface cracks); the crack aspect ratio  $a/c = 0.5, 1, \text{ and } 1.5$ ; the ratio of crack depth-to-plate thickness  $a/t = 0.1, 0.3, \text{ and } 0.5$ . Based on the given solutions and the superposition principle, stress intensity factors for other load cases may be easily obtained. Examples are given for remote tension, biaxial tension, wedge loading in the hole, and simulated pin loading. Also, the effect of the residual stress field following cold expansion is considered for the remote tension loading condition.

**KEYWORDS:** surface crack, corner crack, stress intensity factor, stress concentration, residual stress, weight function, cold expansion

Surface and corner-cracked fastener holes have been identified as a common source of failure in aircraft structures. In addition to a wide range in multi-geometry parameters, stress analysis of such cracked configurations also involves a variety of loading conditions, different load transfers, and residual stress fields, such as those introduced by cold expansion and by interference fit.

A great effort has been made to determine the controlling parameters—the stress intensity factors for such cracked configurations. Among others, Raju and Newman [1] analyzed corner-cracked holes by a three-dimensional finite-element method. Using the same method, Newman and Raju [2] solved the problem of surface-cracked holes, in addition to several other cracked configurations. Grandt [3] and Grandt and Kullgren [4] considered a single surface crack or a corner crack from fastener holes by using the finite-element alternating method. Using their improved finite-element alternating method, Nishioka and Atluri [5] analyzed corner cracks emanating from aircraft attachment lugs as well as from holes in a finite thickness plate.

---

<sup>1</sup> Post-doctoral fellow and institute professor, respectively, Computational Modeling Center, Georgia Institute of Technology, Atlanta, GA 30332-0356.

<sup>2</sup> New address: Department of Mechanical Engineering, University of South Carolina, Columbia, SC 29208.

The finite-element method [1] and the finite-element alternating method [5] are versatile and accurate and have provided very useful solutions. In particular, the finite-element alternating method [5] also cuts computational costs greatly.

With the previously mentioned varieties in mind, however, it is clear that routine applications of the three-dimensional finite-element-based methods in damage tolerance analysis of surface and corner-cracked fastener holes would be very expensive. Weight function methods, on the other hand, have an exclusive advantage in dealing with various loading conditions and residual stress fields; that is, once the weight function is known for a cracked configuration, stress intensity factors can be obtained by an integration of the product of the weight function and the crack-face stress in the otherwise uncracked body. For a general description of, and recent advances in, weight function methods, please refer to Ref 6.

A number of researchers have applied the weight function methods to solve surface and corner cracks emanating from holes. Typically, Perez et al. [7] considered a single corner crack under general loading conditions. Their weight function method, representing the most commonly used approach, gives two averaged values of stress intensity factors at the ends of crack axes. The empirical stress intensity factor equations [2] are used as a reference solution for determining the weight function. Zhao et al. considered surface cracks [8] and corner cracks [9] from holes in a finite thickness plate. Their weight function method, proven to be accurate and efficient, provides a detailed stress intensity factor distribution along the crack front, and in many cases does not require a reference solution for the cracked configuration in question. Although the method is not as versatile as the finite-element or the finite-element alternating method, it is very cost effective and is a good complement to numerical methods for analyzing typical structural configurations. This weight function method will be used in the following to provide stress intensity factors for surface and corner-cracked fastener holes, with emphasis placed on cold expansion residual stress fields.

### Three-Dimensional Weight Function Method

The development of the weight function method, based on the slice synthesis model [10] and the general weight function expressions for two-dimensional cracks [11], is described in Part I of Ref 8. Here we give a brief description of the method.

#### *Modeling and the Weight Function*

The problems are shown in Fig. 1A for surface cracks and in Fig. 1B for corner cracks. We'll take corner cracks as an illustration. The cracked body is decomposed as two kinds of orthogonal slices of infinitesimal thickness. Figures 2a and 2b give the crack plane view of decomposition. To represent the cracked body, two actions need to be considered. These are the restraining effect of the uncracked area on the cracked slices and the coupling stresses acting between the slices. As shown in Figs. 2c and 2d, these two actions are simulated, respectively, as restraining springs,  $k_a$  and  $k_c$ , on the slice's boundaries towards which the crack extends and as coupling spring forces,  $P(x, y)$ , acting on the crack faces of the slices. In this way, the three-dimensional nature of the cracked body is properly built into the slices. By employing the two bounding conditions, the weight functions for the slices are constructed as follows

$$W_i = W_{2D,i}^{\text{fixed}} + T_i(R_i)(W_{2D,i}^{\text{free}} - W_{2D,i}^{\text{fixed}}) \quad (1)$$

where,  $W_i$  is the weight function for the slices shown in Fig. 2; the subscript  $i$ , ( $i = a, c$ ), designates  $a$ - (Fig. 2c) or  $c$ -slices (Fig. 2d);  $W_{2D,i}^{\text{fixed}}$  and  $W_{2D,i}^{\text{free}}$  are the weight functions

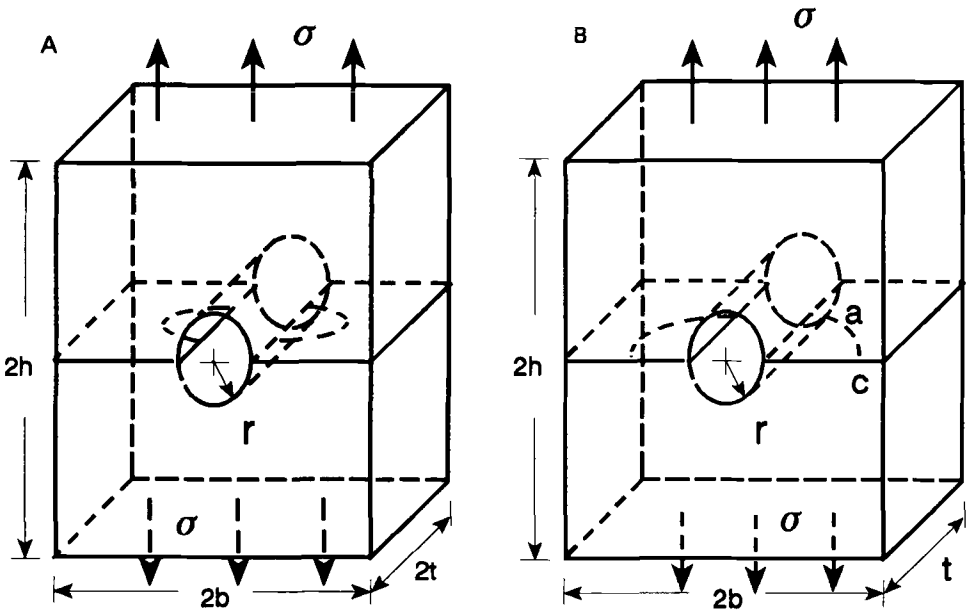


FIG. 1—Surface or corner-cracked hole: (A) surface crack, (B) corner crack.

for the two-dimensional cracks with fixed (roller constraint) boundary condition and with free boundary condition, respectively;  $T_i(R_i)$ , called the transition factor, is an unknown function of restraining area,  $R_i$ , which satisfies  $T_i(\infty) = 0$ , and  $T_i(0) = 1$ . We consider an infinite width plate, thus  $R_i = \infty$ .  $W_{2D}$  in Ref 11 is used for the analysis.

*Stress Intensity Factors*

At this stage we are ready to use the two-dimensional weight function theory [12,13] to express the stress intensity factors for the slices

$$K_a(a_x) = \int_0^{a_x} [\sigma(x, y) - P(x, y)]W_a(R_a, a_x, y) dy \tag{2a}$$

$$K_c(c_y) = \int_0^{c_y} P(x, y)W_c(R_c, c_y, x) dx \tag{2b}$$

where  $\sigma(x, y)$  is the normal stress at the crack location in the otherwise uncracked body. The unknown spring forces  $P(x, y)$  will be determined by the compatibility requirement

$$V_a(x, y) = V_c(x, y) \tag{3}$$

where the crack-face displacements  $V_i$  for the slices are expressed as follows

$$V_a(x, y) = \frac{1}{E_a} \int_y^{a_x} K_a(\xi)W_a(R_a, \xi, y) d\xi \tag{4a}$$

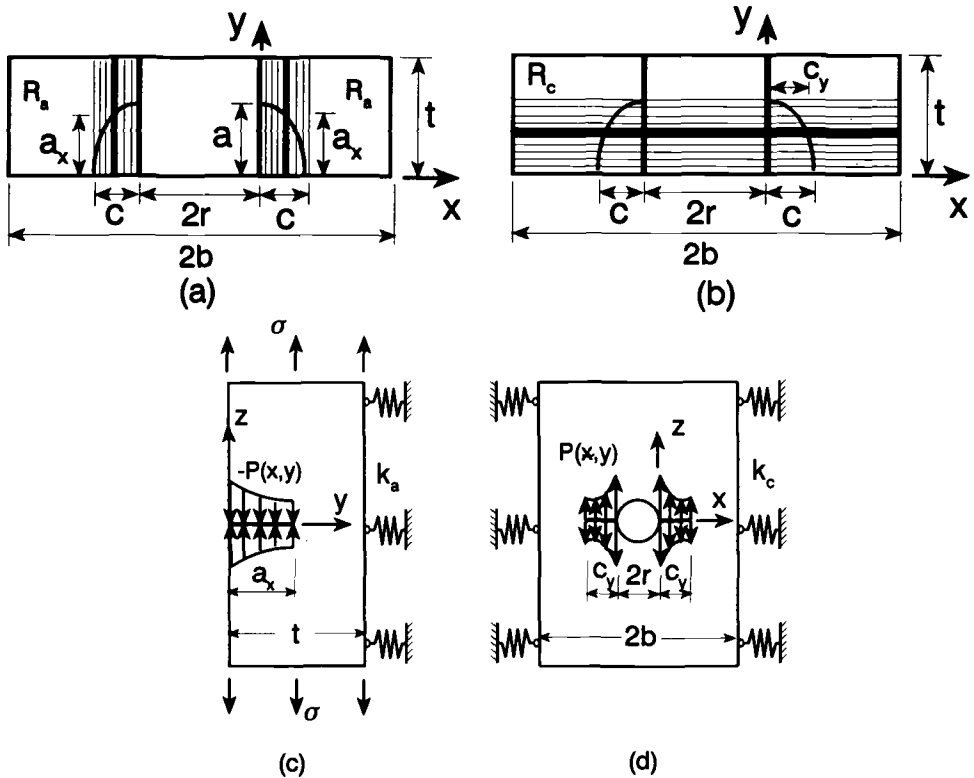


FIG. 2—Decomposition and simulation of the corner-cracked body.

$$V_c(x, y) = \frac{1}{E_c} \int_x^{c_y} K_c(\xi) W_c(R_c, \xi, x) d\xi \tag{4b}$$

in which  $E_a = E, E_c = E_s$ . With  $E$  being the Young's modulus and  $\nu$  the Poisson's ratio, we have, from Ref 8

$$\frac{E_s}{E} = \left( \frac{\Phi}{1 - \nu^2} - 1 \right) \frac{c}{a} \quad a/c \leq 1 \tag{5a}$$

$$\frac{E_s}{E} = \frac{\Phi}{1 - \nu^2} - \frac{c}{a} \quad a/c > 1 \tag{5b}$$

where  $\Phi$  is the complete elliptic integral of the second kind. Once  $P(x, y)$  is determined, the stress intensity factors for the cracked body,  $K(\varphi)$ , are obtained from the stress intensity factors for the slices,  $K_i$ , in terms of

$$K(\varphi) = \frac{(-1)^n}{1 - \eta^2} \left\{ K_a^4(a_x) + \left[ \frac{E}{E_s} K_c(c_y) \right]^4 \right\}^{1/4} \tag{6}$$

where  $\eta = \nu/(1 + \nu)$  for  $\varphi = 0^\circ$  and  $90^\circ$ ,  $\eta = \nu$  for  $0^\circ < \varphi < 90^\circ$ ,  $n = 1$  for  $K_i \leq 0$ , and  $n = 2$  for  $K_i > 0$ . The definition of crack parameters is given in Fig. 3.

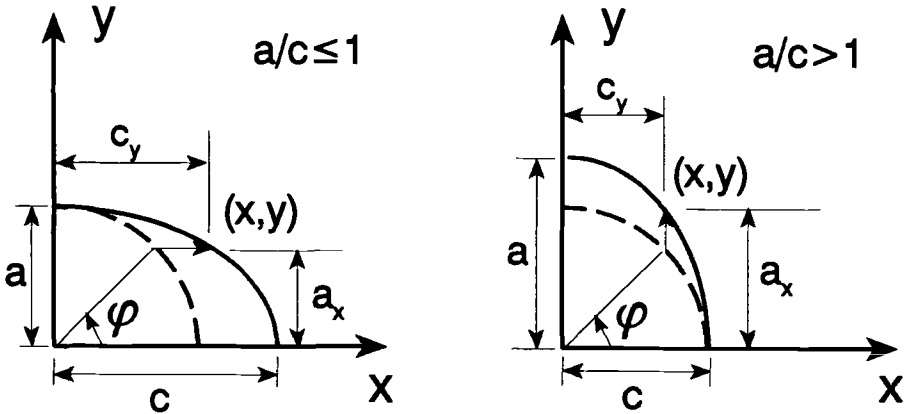


FIG. 3—Definition of crack parameters.

**Results and Discussions**

To be of general utility for different loading conditions, stress intensity factors for crack-face polynomial pressure of the type  $\sigma_0(x/r)^n$  is provided with  $n = 0$  to 4. The geometry parameters considered are as follows:  $r/T = 1.5$  ( $T = t$  for corner cracks,  $T = 2t$  for surface cracks);  $a/c = 0.5, 1, \text{ and } 1.5$ ; and  $a/t = 0.1, 0.3, \text{ and } 0.5$ . The results are presented in a dimensionless form defined as

$$M(\varphi) = K(\varphi)/(\sigma_0\sqrt{\pi r}/\Phi) \tag{7}$$

where  $\sigma_0$  is a reference stress.

*Examples of Typical Loading Conditions*

Tables 1 and 2 list the results for double surface and corner cracks, respectively. Figure 4 shows an example for double corner cracks subjected to crack-face pressure. With the superposition principle, this kind of solution can be readily used to produce solutions for other loading conditions. This is illustrated below.

The stress distribution at the crack location in the uncracked body due to an applied load case  $S$  can generally be fitted as a polynomial

$$\sigma_s(x) = \sigma_{s0} \sum_{n=0}^N Q_{sn}(x/r)^n \tag{8}$$

where  $Q_{sn}$  are the corresponding polynomial coefficients. Let  $M_n$  be the dimensionless stress intensity factors corresponding to crack-face pressure  $(x/r)^n$ . Then the dimensionless stress intensity factors  $M_s$  for the applied load can be obtained by

$$M_s = \sum_{n=0}^N Q_{sn}M_n \tag{9}$$

The results so obtained are given in Fig. 5 for corner cracks for four typical loading con-

TABLE 1—Dimensionless stress intensity factors for double surface cracks at a hole under crack-face pressure:  $100 \cdot (x/r)n$ ,  $r/t = 3$ .

<i>a/c</i>	<i>a/t</i>	<i>n</i>	$\phi^\circ$	0.09	11.25	22.5	33.75	45	56.25	67.5	82.53	89.91	
0.5	0.1	0	12.881	13.360	14.279	15.351	16.503	17.576	18.418	19.508	20.158		
		1	0.673	0.675	0.687	0.671	0.618	0.532	0.414	0.236	0.162		
		2	0.039	0.039	0.037	0.033	0.026	0.019	0.011	0.005	0.003		
		3	0.002	0.002	0.002	0.002	0.001	0.001	0.000	0.000	0.000		
	0.3	0	22.215	23.072	24.661	26.568	28.633	30.542	32.041	33.889	34.934		
		1	3.491	3.501	3.566	3.490	3.223	2.776	2.163	1.229	0.841		
		2	0.603	0.601	0.575	0.512	0.412	0.292	0.177	0.076	0.057		
		3	0.109	0.107	0.097	0.078	0.055	0.033	0.016	0.007	0.005		
	0.5	0	28.927	30.104	32.222	34.864	37.769	40.475	42.638	45.167	46.509		
		1	7.551	7.582	7.740	7.605	7.063	6.119	4.795	2.756	1.912		
		2	2.172	2.167	2.078	1.857	1.504	1.074	0.656	0.286	0.218		
		3	0.655	0.642	0.583	0.474	0.334	0.200	0.101	0.043	0.035		
	1	0.1	0	18.346	18.526	18.629	18.623	18.697	18.913	19.141	19.833	20.534	
			1	0.468	0.456	0.435	0.396	0.343	0.282	0.214	0.121	0.086	
			2	0.013	0.013	0.012	0.010	0.007	0.005	0.003	0.001	0.001	
			3	0.000	0.000	0.000	0.000	0.000	0.000	0.000	0.000	0.000	
0.3		0	31.747	32.090	32.291	32.343	32.556	32.999	33.454	34.686	35.879		
		1	2.429	2.370	2.263	2.065	1.793	1.477	1.120	0.637	0.453		
		2	0.207	0.201	0.181	0.150	0.113	0.077	0.045	0.020	0.016		
		3	0.019	0.018	0.015	0.011	0.007	0.004	0.002	0.001	0.001		
0.5		0	41.346	41.864	42.208	42.458	42.971	43.779	44.595	46.413	48.032		
		1	5.254	5.132	4.912	4.501	3.928	3.257	2.487	1.436	1.039		
		2	0.747	0.725	0.653	0.543	0.413	0.282	0.169	0.076	0.060		
		3	0.112	0.107	0.091	0.069	0.046	0.026	0.013	0.006	0.005		
1.5		0.1	0	15.192	15.253	15.094	14.721	14.279	13.882	13.533	13.627	14.182	
			1	0.243	0.237	0.222	0.198	0.166	0.132	0.097	0.055	0.042	
			2	0.004	0.004	0.004	0.003	0.002	0.001	0.001	0.000	0.000	
			3	0.000	0.000	0.000	0.000	0.000	0.000	0.000	0.000	0.000	
	0.3	0	26.278	26.399	26.139	25.536	24.823	24.172	23.600	23.785	24.739		
		1	1.264	1.230	1.156	1.029	0.865	0.691	0.510	0.292	0.221		
		2	0.070	0.068	0.060	0.048	0.036	0.023	0.014	0.006	0.005		
		3	0.004	0.004	0.003	0.002	0.002	0.001	0.000	0.000	0.000		
	0.5	0	34.171	34.367	34.079	33.411	32.618	31.885	31.252	31.605	32.896		
		1	2.731	2.660	2.505	2.236	1.888	1.515	1.126	0.652	0.501		
		2	0.252	0.243	0.216	0.175	0.129	0.085	0.050	0.024	0.020		
		3	0.025	0.023	0.020	0.015	0.009	0.005	0.003	0.001	0.001		
			4	0.002	0.002	0.002	0.001	0.001	0.000	0.000	0.000	0.000	

ditions, where Tension/Compression means that remote tension is applied in the *z*-direction and compression in *x*-direction. The reference stress is taken as  $\sigma_0 = P/2rT$  for wedge loading, with *P* being the total applied force in *z*-direction, and as remote stress for the rest. Also shown in Fig. 5 are the results for a single corner crack. There is only a slight difference between the single and the double crack configurations in this case. This is expected when

TABLE 2—Dimensionless stress intensity factors for double surface cracks at a hole under crack-face pressure:  $100 \cdot (x/r)n, r/t = 1.5$ .

<i>a/c</i>	<i>a/t</i>	<i>n</i>	$\phi^\circ$	0.09	11.25	22.5	33.75	45	56.25	67.5	82.53	89.91	
0.5	0.1	0		22.019	21.119	21.812	23.095	24.559	26.053	27.266	28.727	29.468	
		1		2.203	2.069	2.049	1.982	1.816	1.569	1.234	0.726	0.483	
		2		0.248	0.235	0.218	0.192	0.154	0.110	0.069	0.031	0.021	
		3		0.030	0.028	0.024	0.020	0.014	0.008	0.004	0.002	0.001	
	0.3	0		37.556	36.087	37.216	39.415	41.898	44.341	46.292	48.386	49.311	
		1		11.354	10.670	10.566	10.217	9.355	8.060	6.308	3.583	2.362	
		2		3.846	3.620	3.377	2.978	2.385	1.705	1.055	0.458	0.299	
		3		1.373	1.285	1.131	0.909	0.636	0.384	0.202	0.086	0.052	
	0.5	0		48.782	46.934	48.343	51.249	54.523	57.686	60.202	62.586	63.468	
		1		24.468	23.012	22.806	22.085	20.259	17.493	13.712	7.760	5.102	
		2		13.801	12.990	12.136	10.719	8.605	6.168	3.832	1.662	1.086	
		3		8.212	7.638	6.770	5.453	3.824	2.316	1.224	0.523	0.317	
	1	0.1	0		31.115	29.311	28.476	28.026	27.778	27.918	28.245	29.170	29.995
			1		1.517	1.400	1.300	1.173	1.007	0.827	0.633	0.367	0.256
			2		0.085	0.078	0.069	0.056	0.042	0.029	0.017	0.008	0.005
			3		0.005	0.005	0.004	0.003	0.002	0.001	0.001	0.000	0.000
0.3		0		53.094	50.084	48.657	47.931	47.559	47.790	48.337	49.774	51.011	
		1		7.816	7.217	6.706	6.053	5.196	4.265	3.256	1.865	1.284	
		2		1.309	1.211	1.063	0.874	0.654	0.443	0.269	0.121	0.083	
		3		0.232	0.213	0.177	0.133	0.087	0.049	0.026	0.012	0.007	
0.5		0		68.253	64.474	62.663	61.836	61.514	61.954	62.819	64.676	66.117	
		1		16.777	15.476	14.422	13.036	11.213	9.228	7.063	4.043	2.779	
		2		4.687	4.335	3.813	3.139	2.355	1.598	0.974	0.439	0.301	
		3		1.385	1.266	1.057	0.795	0.520	0.296	0.155	0.069	0.044	
1.5		0.1	0		24.923	23.613	22.687	21.828	20.897	20.160	19.665	19.733	20.388
			1		0.766	0.717	0.656	0.578	0.481	0.382	0.284	0.164	0.120
			2		0.027	0.026	0.022	0.018	0.013	0.009	0.005	0.002	0.002
			3		0.001	0.001	0.001	0.001	0.000	0.000	0.000	0.000	0.000
	0.3	0		42.486	40.095	38.733	37.313	35.771	34.521	33.684	33.755	34.798	
		1		3.944	3.676	3.380	2.983	2.481	1.967	1.463	0.897	0.576	
		2		0.430	0.402	0.347	0.280	0.203	0.132	0.079	0.037	0.608	
		3		0.050	0.046	0.038	0.028	0.018	0.010	0.005	0.002	0.002	
	0.5	0		54.388	51.638	49.687	47.964	46.105	44.601	43.634	43.769	45.042	
		1		8.447	7.879	7.253	6.410	5.339	4.243	3.163	1.810	1.313	
		2		1.538	1.428	1.244	1.003	0.729	0.476	0.285	0.131	0.096	
		3		0.298	0.275	0.226	0.167	0.106	0.058	0.030	0.014	0.010	
	4		0.060	0.054	0.042	0.028	0.016	0.007	0.004	0.002	0.001		

*l/r* is small, where *l* is the length of a through crack with the same area as that of the part through cracks. Due to this, the results for single cracks are not listed. Some detailed analysis on the difference between the single and the double surface crack configurations can be found in Ref 8. For assessing the accuracy of the weight function solutions, Fig. 6 gives comparisons of the present results with established solutions for double corner cracks under

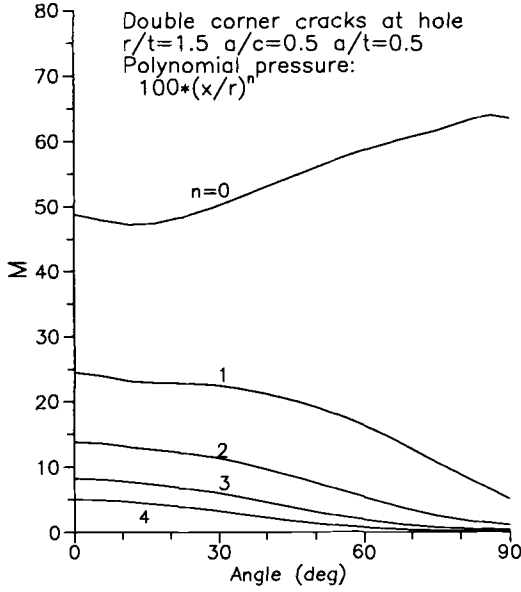


FIG. 4—Dimensionless stress intensity factors for corner cracks under crack-face pressure.

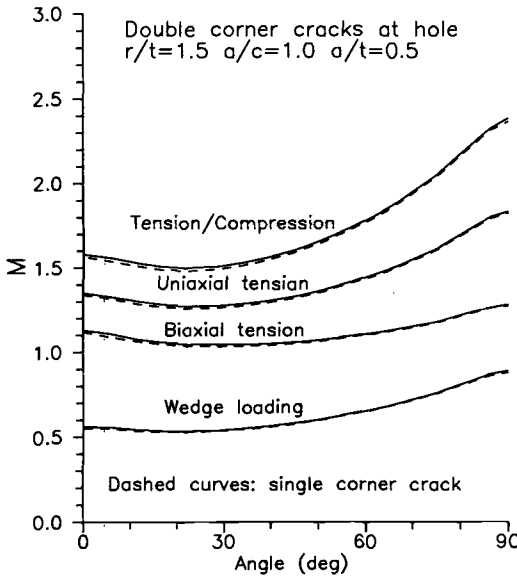


FIG. 5—Solutions for corner cracks under four typical loads.

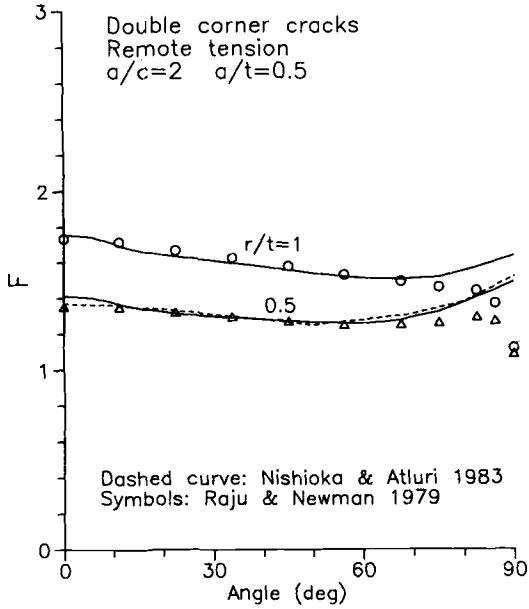


FIG. 6—Comparison with established numerical solutions for double corner cracks.

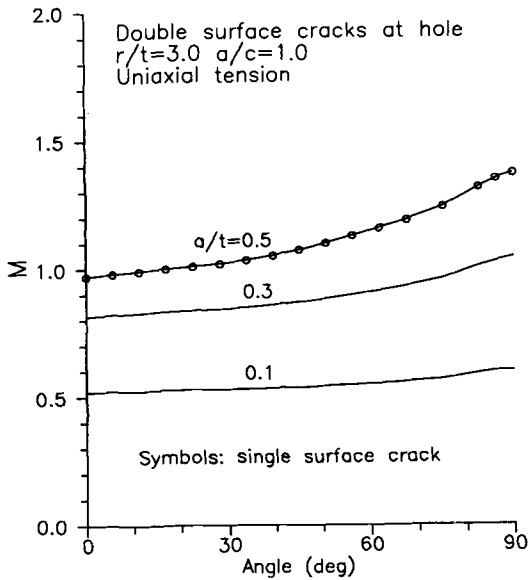


FIG. 7—Dimensionless stress intensity factors for surface cracks subjected to uniaxial tension.

uniaxial tension. As observed, the agreement is very good. (In Fig. 6,  $F$  is used, which is defined as  $F = K/[\sigma(\pi a)^{1/2}/\Phi]$ .) Figure 7 shows typical effect of crack depth for surface cracks.

Various other loading conditions can be considered in the same way. Pin loading is a case of interest in the analysis of cracked fastener holes. The dimensionless stress intensity factors for the pin-loading case,  $M_p$ , can be obtained by superposition of the cases of wedge loading and uniaxial tension

$$M_p = \frac{1}{2} \left( \frac{r}{b} M_t + M_w \right) = \frac{1}{2} \sum_{n=0}^N \left[ \left( \frac{r}{b} Q_{tn} + Q_{wn} \right) M_n \right] \quad (10)$$

### Examples of Residual Stress Effect

We consider the effect of residual stresses around the hole due to the cold expansion. The process of cold expansion of holes is an effective way to produce beneficial compressive residual stress fields near the hole surface, thus reducing the effective stress concentration under applied loads and enhancing fatigue lives of structures. In analyzing the multiple site damage problems of aging aircraft, Park and Atluri [14] considered the effect of plastic deformation due to cold-working. Assuming elastic-perfectly-plastic material behavior and the Tresca yield condition, they gave the residual stress distribution as

$$\sigma_{\theta\theta} = \sigma_{ys} \left[ \frac{1}{2} + \ln \frac{\rho}{R_y} - \left( \frac{1}{2} + \ln \frac{R_y}{r} \right) \left( \frac{r}{\rho} \right)^2 \right] \quad r \leq \rho < R_y \quad (11a)$$

$$\sigma_{\theta\theta} = \sigma_{ys} \left[ \frac{1}{2} \left( \frac{R_y}{\rho} \right)^2 - \left( \frac{1}{2} + \ln \frac{R_y}{r} \right) \left( \frac{r}{\rho} \right)^2 \right] \quad \rho > R_y \quad (11b)$$

in which  $\sigma_{ys}$  is the yield stress,  $\rho$  is the radial distance from the center of the hole, and  $R_y$  is the radius of the boundary between the elastic and the plastic zones. Figure 8 shows the residual stress distribution for the three different plastic zone sizes. The corresponding 4th order polynomial expressions are represented by solid curves.

We are now in a position to consider the residual stress effects. Take the uniaxial tension as the applied load, the remote stress  $\sigma = 0.2\sigma_{ys}$ , and the reference stress  $\sigma_0 = \sigma_{ys}$ . The residual stress effect is thus reflected in  $M$ . Let us focus on surface cracks. Figure 9A shows the effect of residual stress on semi-circular cracks for the three different crack depths. By comparing the solid and dashed curves, it can be seen that the degree of the residual stress effect varies along the crack front and is most significant at the hole surface ( $\varphi = 90^\circ$ ). As the crack gets larger, the effect decreases around  $\varphi = 0^\circ$  but remains significant near the hole surface. For  $a/t = 0.5$ , part of the crack front near  $\varphi = 0^\circ$  is already in the region where the residual stress is tensile. Figure 9B is for the same cracks, but in a larger residual stress field. As noted, the reduction in stress intensity factors becomes much more significant compared with that in Fig. 9A. The effect of residual stress on cracks of different aspect ratios is given in Fig. 10A. As  $a/c$  decreases, the crack front around  $\varphi = 0^\circ$  gets farther from the hole surface and therefore is less influenced by the residual stresses. This is the trend observed in Fig. 10A. Again in Fig. 10B, the same cracks are shown but in a larger residual stress field. The residual stress changed both the magnitudes and the distributions of stress intensity factors greatly.

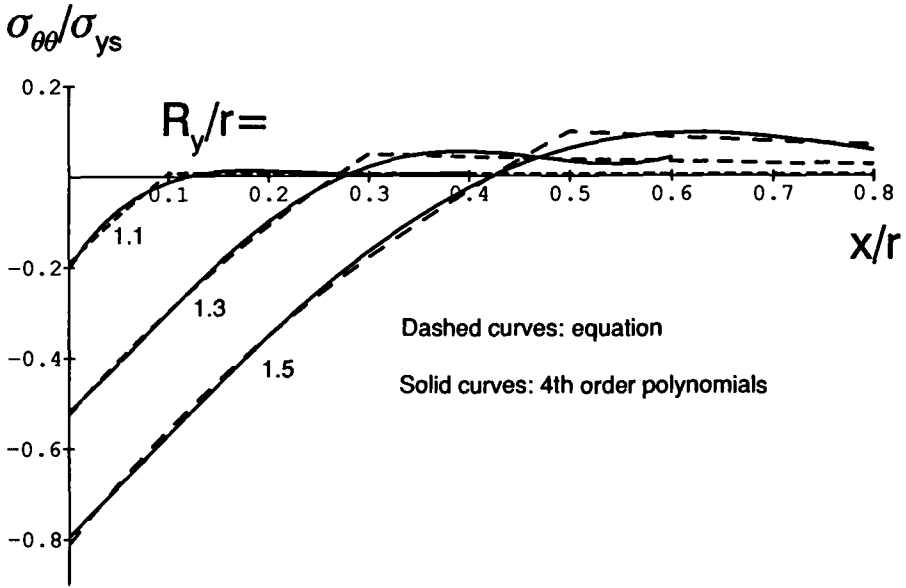


FIG. 8—Tangential residual stress distribution around a cold-expanded hole.

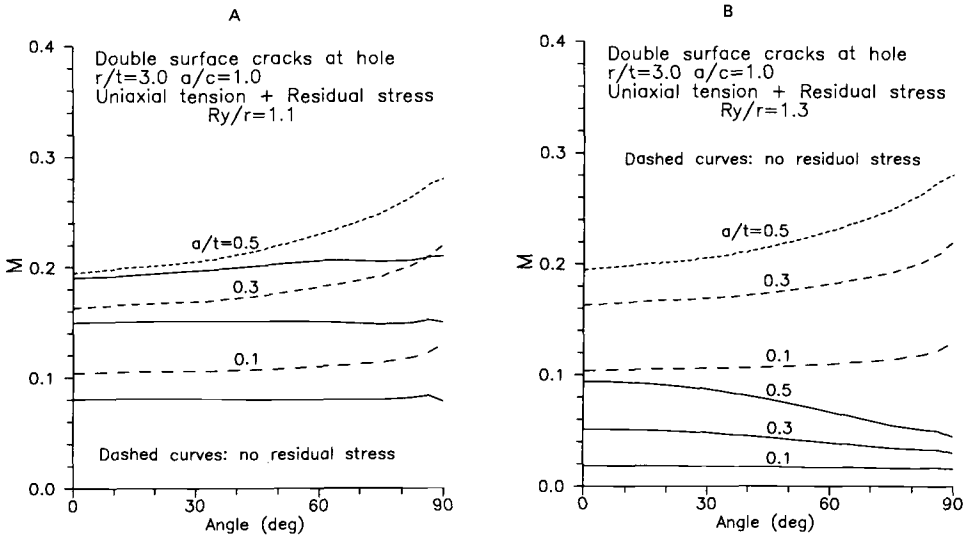


FIG. 9—Effect of the residual stress on a semi-circular surface crack of different depths: (A)  $R_y/r = 1.1$ , (B)  $R_y/r = 1.3$ .

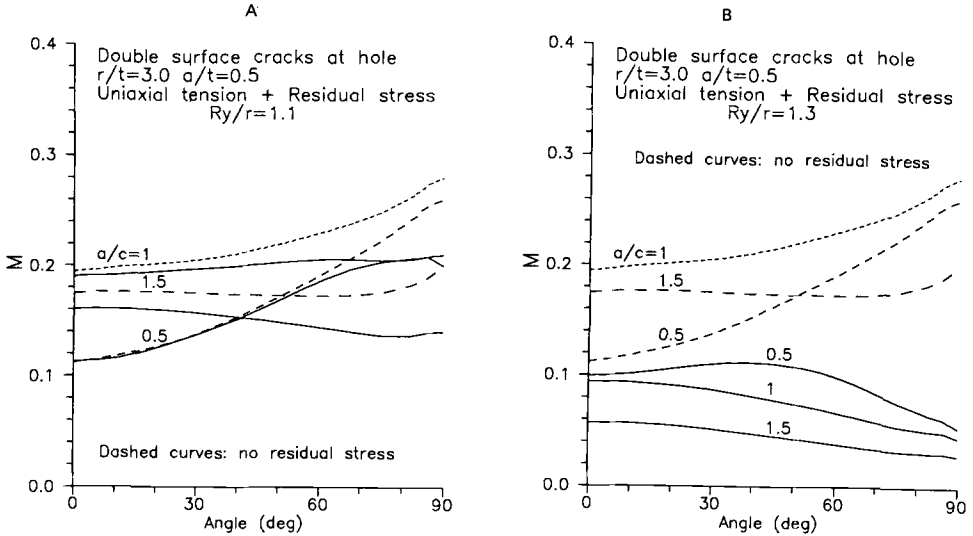


FIG. 10—Residual stress effect on surface cracks of different shapes: (A)  $R_y/r = 1.1$ , (B)  $R_y/r = 1.3$ .

### Concluding Remarks

Stress intensity factors for typical surface and corner-cracked fastener holes are determined by the three-dimensional weight function method. It takes only a few seconds to get a solution on ordinary PCs. Since the method is very accurate, cost effective and easy to use, and has been established for most of the typical cracked configurations, it is a very useful complement to the three-dimensional finite-element and the finite-element alternating methods in analyzing typical cracked configurations. The solutions provided in the paper should be useful in damage tolerance analysis of surface and corner-cracked fastener holes.

### References

- [1] Raju, I. S. and Newman, J. C., Jr., "Stress Intensity Factors for Two Symmetric Corner Cracks," *Fracture Mechanics (11th Conference)*, ASTM STP 677, C. W. Smith, Ed., American Society for Testing and Materials, Philadelphia, 1979, pp. 411–430.
- [2] Newman, J. C., Jr. and Raju, I. S., "Stress Intensity Factor Equations for Cracks in Three-Dimensional Finite Bodies," *Fracture Mechanics: 14th Symposium, Vol. 1*, ASTM STP 791, J. C. Lewis and G. Sines, Eds., American Society for Testing and Materials, Philadelphia, 1983, pp. 238–256.
- [3] Grandt, A. F., Jr., "Crack Face Pressure Loading of Semi-Elliptical Cracks Located Along the Bore of a Hole," *Engineering Fracture Mechanics*, Vol. 14, 1981, pp. 843–852.
- [4] Grandt, A. F., Jr. and Kullgren, T. E., "Stress Intensity Factors for Corner-Cracked Holes Under General Loading Conditions," *Journal of Engineering Materials and Technology*, Vol. 103, 1981, pp. 171–176.
- [5] Nishioka, T. and Atluri, S. N., "An Alternating Method for Analysis of Surface-Flawed Aircraft Structural Components," *AIAA Journal*, Vol. 21, NO. 5, 1983, pp. 749–757.
- [6] Atluri, S. N., "Simplified Computational Methods for Elastic and Elastic-Plastic Fracture Problems, in *Advances in Computational Nonlinear Mechanics in Aerospace Engineering*," S. N. Atluri, Ed., AIAA, 1992.
- [7] Perez, R., Ray, S. K., and Grandt, A. F., Jr., "Application of a Weight Function Method to Predict the Fatigue Life of Corner-Cracked Holes Loaded in Bending," *Engineering Fracture Mechanics*, Vol. 28, 1987, pp. 283–291.

- [8] Zhao, W., Wu, X. R., and Yan, M. G., "Weight Function Method for Three Dimensional Crack Problems—I & II, *Engineering Fracture Mechanics*, Vol. 34, No. 3, 1989, pp. 593–607, 609–624.
- [9] Zhao, W., Wu, X. R., and Yan, M. G., "Stress Intensity Factors for Corner Cracks at a Hole Under Remote Tension," *Acta Mechanica Sinica*, Vol. 7, No. 1, 1991, pp. 76–81.
- [10] Fujimoto, W. T., "Determination of Crack Growth and Fracture Toughness Parameters for Surface Flaws Emanating from Fastener Holes, in *Proceedings, AIAA/ASME/SAE 17th Structures, Structural Dynamics, and Material Conference*, King of Prussia, PA, ASME, New York, 1976.
- [11] Wu, X. R. and Carlsson, J., *Weight Functions and Stress Intensity Factor Solutions*, Pergamon Press, Elmsford, NY, 1991.
- [12] Bueckner, H. F., "A Novel Principle for the Computation of Stress Intensity Factors," *ZAMM*, Vol. 50, 1970, pp. 529–546.
- [13] Rice, J. R., "Some Remarks on Elastic Crack-Tip Stress Fields," *International Journal of Solids Structures*, Vol. 8, 1972, pp. 751–758.
- [14] Park, J. H. and Atluri, S. N., "Fatigue Growth of Multiple-Cracks near a Row of Fastener-Holes in a Fuselage Lap-Joint, *Computational Mechanics*, Vol. 13, No. 3, 1993, pp. 189–203.

# Stress Intensity Factor Approximations for Cracks Located at the Thread Root Region of Fasteners

---

**REFERENCE:** Cipolla, R. C., "Stress Intensity Factor Approximations for Cracks Located at the Thread Root Region of Fasteners," *Structural Integrity of Fasteners, ASTM STP 1236*, P. M. Toor, Ed., American Society for Testing and Materials, Philadelphia, 1995, pp. 108–125.

**ABSTRACT:** Nondimensional stress intensity factors have been numerically determined for a straight-fronted edge crack located at the thread root of a fastener. An influence-function or weight-function approach was used in determining  $K_I$  for several fastener sizes: diameters ranging from 1 to 6 in. (2.5 to 15.2 cm) and thread pitches of 4, 8, and 12 threads per inch. Several analytical approximations are used in simplifying the stress analysis problem and the development of the weight function. The results for the nondimensional stress intensity factor,  $K_I/\sigma(\pi a)^{1/2}$ , are provided as a function of crack depth, bolt size, and thread pitch. The effects of bolt size and thread form play an important role only when cracks are relatively small. These results indicate that local differences caused by thread form and root radius are limited to crack depths within 2% of the net section. All major contributions to elevation in  $K_I$  caused by the presence of the threads appear to diminish for cracks extending beyond 25% of the minor diameter.

**KEYWORDS:** stress intensity factors, threaded fasteners, bolting, weight functions, fracture mechanics, straight-fronted crack, stress analysis

## Nomenclature

- a* Crack depth
- a<sub>r</sub>* Crack depth for a postulated "reference" flaw
- a/l* Crack aspect ratio
- A* Net tensile area or "stress" area
- D* Nominal (major) diameter
- d* Minor diameter
- F* Nondimensional function for stress intensity factors,  $F = K/\sigma(\pi a)^{1/2}$
- H* Height of functional triangle for thread profile
- h* Influence function or weight function
- K* Stress intensity factor
- K<sub>I</sub>* Stress intensity factor for Mode I loading
- K<sub>t</sub>* Stress concentration factor
- l* Crack length
- n* Number of threads per inch
- p* Thread pitch,  $p = 1/n$
- P* Axial load
- r* Minor radius,  $d/2$

---

<sup>1</sup> Principal engineer, Aptech Engineering Services, Inc., Sunnyvale, CA 94089.

$\sigma$	Nominal applied stress based on net section
$\sigma_{\max}$	Maximum surface stress at thread root
$\sigma_{\text{nom}}$	Nominal stress
$\sigma(x)$	Stress distribution as a function of distance away from root
$\hat{\sigma}(x)$	Normalized stress, $\sigma(x)/\sigma_{\max}$
$\nu$	Poisson's ratio
$\rho$	Thread root radius

## Introduction

Over recent years, there appears to be an increasing interest in applying fracture mechanics to bolting materials used in fabricating threaded fasteners. There have been many examples of bolting failures due to corrosion-related cracking and mechanical fatigue, some of which had significant economic consequences. There are probably many other reasons for this interest; however, the key underlying factor is the increasing importance among industry users of maintaining a reliable bolted connection for service-critical closures. Examples of critical connections range from high-energy bolted closures in power plant equipment, civil-structural connections in buildings and bridges, to smaller mechanical joints in aerospace structures and satellites. Fracture control implementation for space shuttle payloads requires nondestructive inspection and safe-life analysis of bolted connection joints in order to prevent catastrophic structural failure.

A key element in the use of fracture mechanics concepts to fasteners is the determination of crack tip stress intensity factors for each potential initiation location. In a bolt or stud, the areas where cracking is most probable are the thread root, the thread run-out to the shank, and the transition region between the bolt head and shank. A rigorous analysis for determining stress intensity factors for elliptical cracks would require three-dimensional numerical stress analysis of the bolt, including detailed modeling of the thread profile, thread pitch and helix angle, and loading boundary conditions. However, with some simplified assumptions, it is possible to compute representative stress intensity factors very efficiently, which is highly desirable when repetitive  $K$  calculations are required, such as in crack growth life assessments.

In the electric power industry, fracture mechanics methods have been successfully used to evaluate the integrity of structural and pressure retaining fasteners [1,2]. These activities were in direct response to observed in-service degradation of fasteners and the industry concern for plant safety [3]. In one application, fracture mechanics was used to establish allowable bolt preloads based on an evaluation of threshold levels for crack growth in order to mitigate stress corrosion cracking failures. In developing the linear elastic fracture mechanics (LEFM) based evaluation method, a procedure was developed for estimating the stress intensity factors for a single "reference" depth for a semi-elliptical crack at the thread root for various fastener sizes. The procedure has several limitations; since the stress intensity factor solution was based on a semi-infinite half-space, both curvature and finite dimensions were not represented so the results were only accurate for relatively small crack depths. This, however, was consistent with the objective of the original work, which was to evaluate the growth potential of small preexisting fabrication flaws during early service life.

This paper presents an improvement to the previous work for approximating  $K_I$  over a much larger range in crack depths ( $0 \leq a/d \leq 0.9$ ) for fasteners under tension loads. The approach follows the same simplified method of analysis previously applied but employs a weight function whose accuracy is maintained over a wider range. At this stage in development, the solution for only a straight-fronted crack is given. However, being only an approximate analysis, the methods presented can be improved to include the effect of flaw

aspect ratio. In the meantime, the results presented herein will provide a conservative assessment in design life and failure prevention analyses.

## Fracture Mechanics Applications for Fasteners

### *Linear Elastic Fracture Mechanics Concepts*

The principles of LEFM effectively link three parameters: the flaw size and shape, the fracture resistance of the material, and the applied stress. Although the stress distribution of a cracked structure for an arbitrary loading body geometry and crack geometry can be quite difficult to determine, only three deformation modes can occur near the tip of the crack as depicted in Fig. 1: the faces can be pulled apart (Mode I) or sheared perpendicular or parallel to the leading edge of the crack (Modes II or III). The crack opening or Mode I, where the load is applied perpendicular to the crack face, is normally viewed as the most damaging of the three modes and is the mode considered relevant for evaluating flaws in threaded fasteners.

The most useful parameter for describing the character of the near crack tip stress distribution is the stress intensity factor. The stress intensity factor,  $K_I$ , defines the local crack tip response to global conditions and is calculated in terms of the applied stress,  $\sigma$ , the crack depth,  $a$ , and a factor that depends on the flaw size, flaw depth, stress distribution, and structural displacement constraints,  $F$ , from the relation

$$K_I = F\sigma(\pi a)^{1/2} \quad (1)$$

The important parameter in computing  $K$  is the function  $F$ , and in most cases  $F$  must be determined by numerical methods. Once  $F$ , and hence  $K$ , is established, the conditions for crack extension and fracture can be calculated.

### *Weight Function Method*

Although many closed form and approximate solutions exist for crack tip stress intensity factor, it is often required to use numerical analysis methods to calculate  $K$ . With the exception of some special case solutions, the determination of  $K$  as a function of crack depth is a nontrivial problem when the body dimensions are finite or when the stress distribution

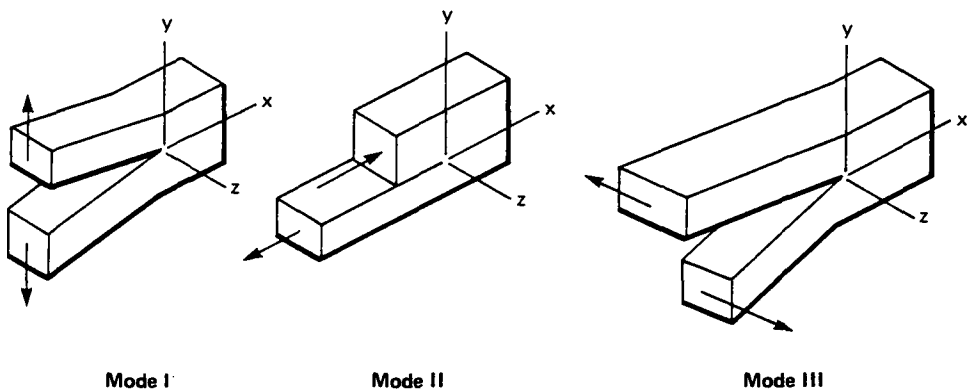


FIG. 1—Basic crack opening modes.

is varying in a nonlinear fashion as is the case for stress near a thread root. The method used in this investigation to determine  $K_I$  is based on the influence function or weight function technique. The essential features in the formulation of the weight function method are based on the following fundamentals

- The application of elastic superposition allows the use of the “uncracked” stress distributions in the  $K$  analysis.
- The weight function itself is invariant with stress and provides the means to calculate the effect of a crack in redistributing any stress field.

The principle of superposition reduces the  $K$  solution of an arbitrary and perhaps difficult crack problem to the solution of the stress analysis problem but without the crack present, and the problem of a cracked body with an applied internal pressure acting on the crack face. The applied internal pressure is that required to cancel the uncracked stress field in order to establish the traction-free boundary conditions along the crack face.

The weight function,  $h(x, a)$ , is a function of spatial position ( $x$ ) and crack size ( $a$ ) and also depends on the specified displacement boundary conditions and body geometry. The calculation of  $K$  for the general class of two-dimensional problems in Mode I is

$$K_I = \int_L h(x, a)\sigma(x) dx \quad (2)$$

where  $L$  is the crack line, and  $\sigma(x)$  is the “uncracked” stress distribution normal to the crack face. For three-dimensional problems,  $K$  becomes a function of crack front position so that Eq 2 must be replaced with more complex formulas. In applying Eq 2 to three-dimensional problems,  $K_I$  is determined on a local average basis where an average value of  $K_I$  is calculated over some defined segment of the crack front. These local averages are also related to and may be calculated directly from the strain energy release rates resulting from defined crack growth and shape changes. In either case, the solution for  $K_I$  becomes a simple integration over the crack face where only the  $\sigma(x)$  needs to be predetermined for the problem. This makes this approach very tractable for repetitive calculations involving nonlinear varying stress fields such as those that exist at threads.

### Model Representation of Thread Root

There are many factors to consider when attempting to develop a flaw model that will represent the crack-driving force for a crack located at a thread. By keeping these factors in mind, it will improve one’s understanding of why the  $K_I$  solutions presented in this paper and others are only approximations. In a comprehensive review, James and Mills [4] summarized the work of several researchers on  $K_I$  solutions applicable to bolts. Many solutions exist for cracks in unnotched round bars, but very few dealt with cracks in notched bars or threaded bolts. A number of  $K_I$  solutions have been developed for straight-fronted and semi-circular crack fronts in smooth bars for tension and bending loading conditions. It is expected that when cracks are small, they will be highly influenced by the stress concentration effect of the threads. But, as cracks propagate deeper into the bolt, the effect of the threads will become less dominant until the solution for an unnotched bar may be a reasonable approximation for a bolt.

In reality, a fastener has multiple notches created by a single groove traversing the axial length of the bolt as a continuous helix. The longitudinal profile for an external thread is

shown in Fig. 2 [5]. The thread is composed of linear flanks forming an included angle of  $60^\circ$  and a root region which will be rounded to some degree depending on the method of manufacture and sharpness of the cutting or rolling tool. Most investigators feel comfortable modeling the threaded fastener as a single groove in a round bar as illustrated in Fig. 3. The angle of axial inclination is ignored primarily on the basis that cracks, as they extend, have been observed to become planar cracks relative to the bolt axis. During crack growth, the cracks will actually cross over one to two threads to achieve an alignment perpendicular to the primary (axial) stress direction. Therefore, ignoring the helix angle seems reasonable, but the relative magnitude of  $K_{T1}$  should be studied at a later time to determine the significance of this assumption on the early stage of crack growth.

The assumption of a single groove as opposed to a series of multiple grooves will also have an effect on the magnitude of  $K_T$ . It is expected, however, that, for a multiple-grooved bar, the stress concentration factor will be less than that for a single groove of the same dimensions due to the shielding effect of neighboring grooves. The shielding effect will tend to smooth out the stress in the vicinity of the threads because the geometric discontinuity will be less severe. The expected effect is that the single notch model will be conservative for threads away from engagement with nuts or other internally threaded connectors.

The treatment of the engaged lengths of fasteners will be more complicated and will depend on the number of threads actively engaged, the load sharing among the threads, and the load distribution along the thread relative to the pitch line. Here there are two competing effects. First, the stress concentration of an engaged thread will most likely be higher due to the reasons mentioned above. However, it is doubtful even for the first engaged thread that 100% of the axial load will be carried at the thread plane. So the higher expected stress concentration will be partially compensated by a lower local nominal stress. Again, additional analytical studies would be needed to determine the difference in  $K_T$  between engaged and unengaged thread planes. In this evaluation, a single-groove bar is used to represent the basic geometry of a threaded fastener for application to both engaged and unengaged locations.

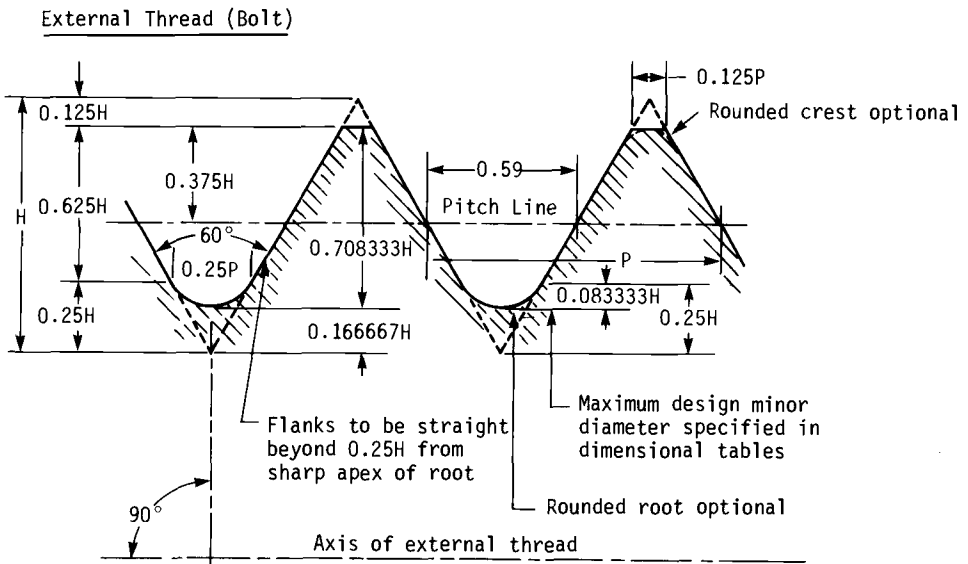
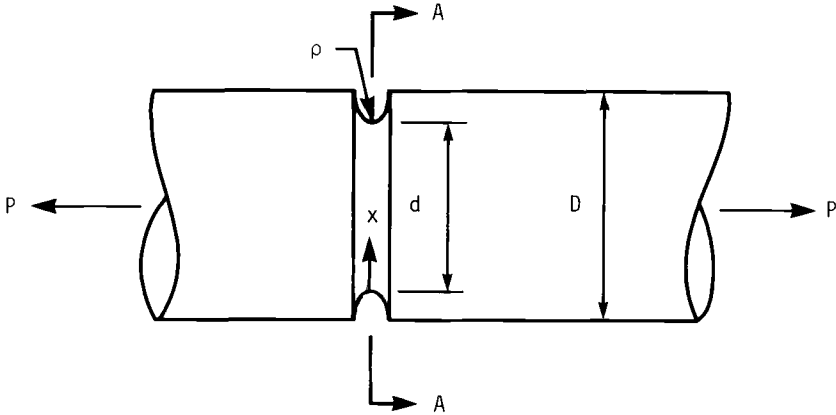
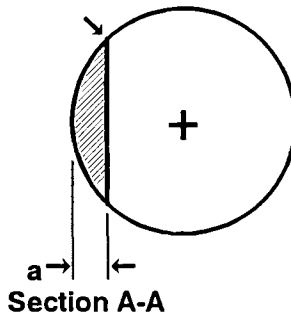


FIG. 2—Design profile for external UN thread.



(a) Grooved Bar Geometry

## Straight-Fronted Crack



(b) Thread Root Crack Geometry

FIG. 3—Single groove bar representation of (a) threaded fastener and (b) root crack.

## Stress Analysis Applicable to Thread Region

*Loading Mode*

The loading mode in fasteners is assumed to be dominated by uniaxial forces. This assumption is consistent with the general design of threaded fasteners to carry primarily tension loads. Hence, stress intensity factors for Mode I loading would be very useful in structural integrity assessments of bolting. Caution should be used when applying the methods contained in this paper when fasteners are designed to carry shear. When shear stresses are present, the effect of in-plane shear on the stress intensity factor can be negligible for small flaws since the value of these shear stresses along the cross section will be zero near the thread root surface where the flaws are postulated to occur. When mixed mode loading is anticipated (i.e.,  $K_I$  and  $K_{II}$ ), the common practice is to orient or project the flaw to the plane

of maximum principal stress. Since the principal stress plane at the stud surface will be the plane normal to the centerline (i.e., pure triaxial state of stress), the effect of in-plane shear stress on  $K$  can be neglected as long as the crack to be evaluated is a surface flaw with a depth that is very small relative to the stud diameter.

### Local Stress Variation

The design profile for an external thread, as shown in Fig. 2, is based on the unified screw thread standards. The actual profile geometry with regard to the thread root region will depend on several manufacturing variables, such as thread forming process, tool wear, and quality control practice. The determination of the stress distribution local to the thread root requires the knowledge of two quantities: the stress concentration factor,  $K_t$ , at the local discontinuity and the stress attenuation profile radially inward from the surface. The stress concentration factor is defined as the ratio of maximum surface stress to the applied nominal stress

$$K_t = \sigma_{\max} / \sigma_{\text{nom}} \quad (3)$$

and the stress attenuation normalized to the maximum surface stress, can be represented as

$$\hat{\sigma}(x) = \sigma(x) / \sigma_{\max} \quad (4)$$

where  $x$  is a spatial coordinate directed radially inward from the thread root surface. The complete "uncracked" stress distribution necessary for the numerical procedure was determined from

$$\sigma(x) = K_t \sigma_{\text{nom}} \hat{\sigma}(x) \quad (5)$$

The somewhat unusual format of Eq 5 was intentional; much information on notch stresses exist, however, it is often presented either in terms of stress concentration factors or as special case stress solutions for a few simple geometries. Hence, Eq 5 is tractable for applying stress solutions from literature sources to engineering problems involving notches, holes, or other discontinuities.

Because the objective of this work was to investigate the effect of thread profile of  $K_t$  as well as generating representative  $K_t$  factors for bolts, the solution for Eq 5 requires the stress variation to be defined in terms of bolt size and thread root radius. Stress distributions were obtained from literature sources for similar geometries that would provide a reasonable or conservative estimation for  $K_t$  and  $\hat{\sigma}(x)$  in terms relatable to bolt geometry parameters. A single groove round bar geometry, as shown in Fig. 3, has been well researched by Neuber [6]. The stress concentration factor for a grooved round bar under pure axial tension is given by

$$K_t = 1 + \left[ \frac{(K_{te} - 1)^2 (K_{th} - 1)^2}{(K_{te} - 1)^2 + (K_{th} - 1)^2} \right]^{1/2} \quad (6)$$

where

$$K_{te} = 1 + 2(c/\rho)^{1/2}$$

$$K_{th} = \{r/\rho (r/\rho + 1)^{1/2} + (0.5 + \nu) r/\rho + (1 + \nu)[(r/\rho + 1)^{1/2} + 1]\} / N$$

$$N = r/\rho + 2\nu(r/\rho + 1)^{1/2} + 2$$

$$r = d/2, c = (D - d)/2$$

$$\nu = \text{Poisson's ratio} = 0.3$$

The stress concentration factors from Eq 6 for a range of  $d/D$  and  $\rho/D$  are graphically presented in the handbook by Peterson [7].

The stress attenuation from a deep hyperbolic groove subjected to axial tension also follows the work of Neuber [6] as developed by Leven [8]. The principal stress across the transverse section of symmetry for a shaft is

$$\hat{\sigma}(x) = \frac{m(m^2 - 0.4m + 1) \cos^2 v + m^3}{(m^2 - 0.4m + 2) \cos^3 v} \quad (7)$$

where

$$m = \left(1 + \frac{r}{\rho}\right)^{-1/2}$$

$$v = \sin^{-1} \left[ \left(1 - \frac{x}{r}\right) \left(1 + \frac{\rho}{r}\right)^{-1/2} \right]$$

Plots of  $\hat{\sigma}(x)$  are given in the paper by Leven [8].

Since the stress concentration factor from Eq 6 will not necessarily be the same as the solution for the hyperbolic groove, an additional condition is applied to Eq 6 to establish an equivalent nominal stress from the average stress across the section

$$\sigma_{\text{nom}} = \frac{1}{A} \int \sigma(x) dA = \frac{8}{d^2} \int_0^{d/2} x \sigma(x) dx \quad (8)$$

An example of the resulting stress distribution for a 1½-inch (3.8-mm) 12UN threaded bar is illustrated in Fig. 4. For this geometry, the calculated elastic stress concentration of a thread with a root radius of 0.012 in. (0.3 mm) is 4.53.

An inspection of the ANSI design tables [5] showed that the ratio of minor to major diameter ( $d/D$ ) for common fasteners will fall within a tight range between 0.88 and 0.95. Since root radius ( $\rho$ ) for machined threads may vary greatly due to tool wear, a rounded contour will result, but the root contour may not be definable by a single radius value. For this reason, the effect of root radius on  $K_t$  has been studied for  $\rho$  between 0.002 in. (0.05 mm) and 0.140 in. (3.6 mm). Physical limits on  $\rho$  will naturally occur due to the depth of thread to be machined and the physical size of the cutting tool. Observations of several large structural bolts indicate that the average  $\rho$  is very close to the UNR thread profile specification where the theoretical radius for UNR threads is

$$\rho = 0.144 \ 34/p \quad (9)$$

where  $p$  is the thread pitch. The use of an average root radius in the  $K$  analysis is discussed later.

## Weight Function for Edge-Crack in a Cylindrical Bar

### Flat Plate Solution

The weight function for a straight-fronted crack in a bar of circular cross section was approximated from a series expansion for a general weight function derived for a flat plate.

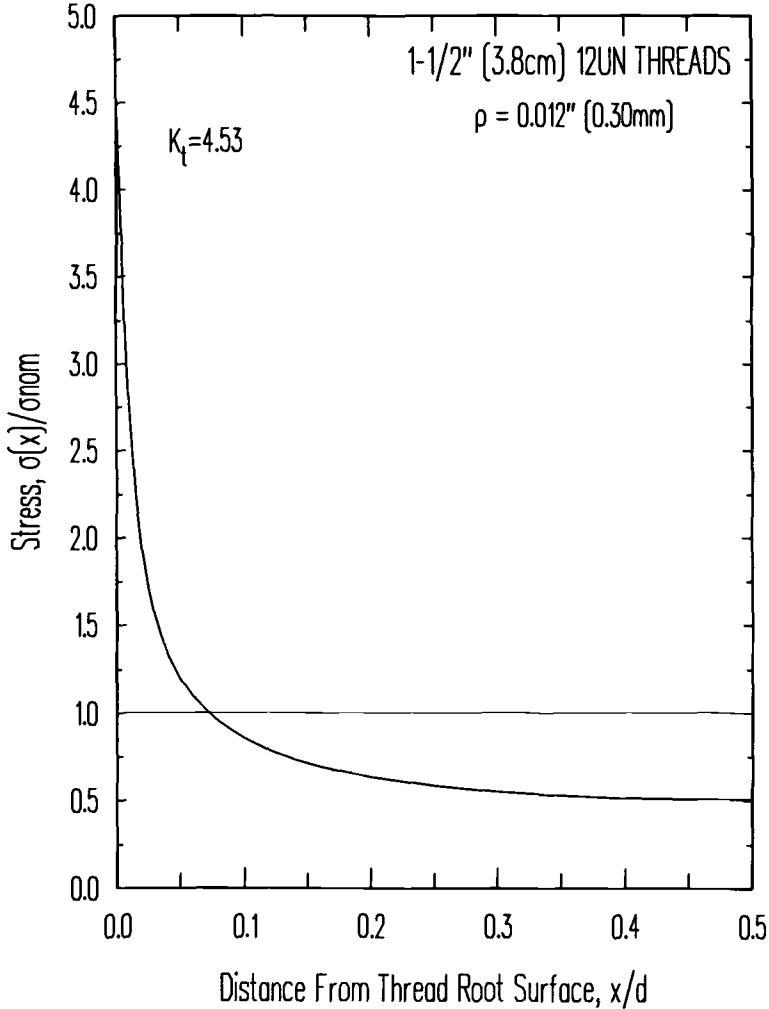


FIG. 4—Approximate stress distribution across the net section of a 1½-in. (3.8-cm)-diameter 12UN fastener.

The straight-fronted crack geometry is shown in Fig. 3b. Following the work of Glinka and Shen [9], a four-term expression for  $h(x, a)$  was used

$$h(x, a) = \frac{2}{[2\pi(a - x)]^{1/2}} \left[ 1 + M_1 \left(1 - \frac{x}{a}\right)^{1/2} + M_2 \left(1 - \frac{x}{a}\right) + M_3 \left(1 - \frac{x}{a}\right)^{3/2} \right] \quad (10)$$

where  $x$  is the distance across the crack plane relative to the outside surface of the minor diameter as shown in Fig. 3a. The four-term expression above was adequate to approximate the weight function behavior, with an accuracy better than 1% over a range of crack depths  $0 \leq a/d \leq 0.9$  [9].

The coefficients  $M_1$ ,  $M_2$ , and  $M_3$  were derived from two reference  $K$  solutions as outlined by Shen and Glinka [10]. The two reference solutions for the edge-cracked plate were extracted from Tada et al. [11] for tension and bending loadings. The third condition required for the simultaneous solution for  $M_1$ ,  $M_2$ , and  $M_3$  was formulated from the knowledge that, for surface cracks, crack face curvature at the free surface is such that the second derivative of crack opening displacement at  $x = 0$  is equal to zero [10]. Consequently, the condition that  $\partial^2 h / \partial x^2 = 0$  at  $x = 0$  is used in the derivation of the coefficients in Eq 10. The resulting expression for the coefficients are

$$\begin{aligned} M_1 &= \frac{\pi}{\sqrt{2}} \left[ -2F_t + \frac{3}{a/d} (F_t - F_b) \right] - \frac{24}{5} \\ M_2 &= 3 \\ M_3 &= \frac{2\pi}{\sqrt{2}} \left[ 3F_t + \frac{3}{a/d} (F_b - F_t) \right] + \frac{8}{5} \end{aligned} \quad (11)$$

where the relationships for the nondimensional reference  $K$  solutions for uniform tension acting on the crack ( $F_t$ ) and global bending ( $F_b$ ) acting on a rectangular plate are given by

$$\begin{aligned} F_t &= \left[ \frac{1}{\beta} \tan \beta \right]^{1/2} \frac{0.752 + 2.02(a/d) + 0.37(1 - \sin \beta)^3}{\cos \beta} \\ F_b &= \left[ \frac{1}{\beta} \tan \beta \right]^{1/2} \frac{0.923 + 0.199(1 - \sin \beta)^4}{\cos \beta} \end{aligned}$$

and where  $\beta = (\pi/2)(a/d)$ .

The reported accuracy for  $F_t$  and  $F_b$  is better than 0.5% for any  $a/d$ . The overall behavior of the weight function for the constant thickness plate is shown in Fig. 5. The variation in  $h(x, a)\sqrt{a}$  with distance  $x/a$  is graphically shown for  $a/d$  ranging from 0.1 to 0.6.

#### *Approximate Solution for Round Bar*

The effect of the variable thickness due to the circular cross section was indirectly included by modifying Eq 2 as proposed by Besuner [12]

$$K = \frac{1}{t(a)} \int_0^a h^*(x, a) t(x) \sigma(x) dx \quad (12)$$

where  $t(x)$  is the thickness of the bar as a function of the radial inward distance given by

$$t(x) = [4x(d - x)]^{1/2} \quad (13)$$

and  $h^*(x, a)$  is the weight function given by Eq 10 evaluated for an effective  $a/d$  ratio defined by the following relationship

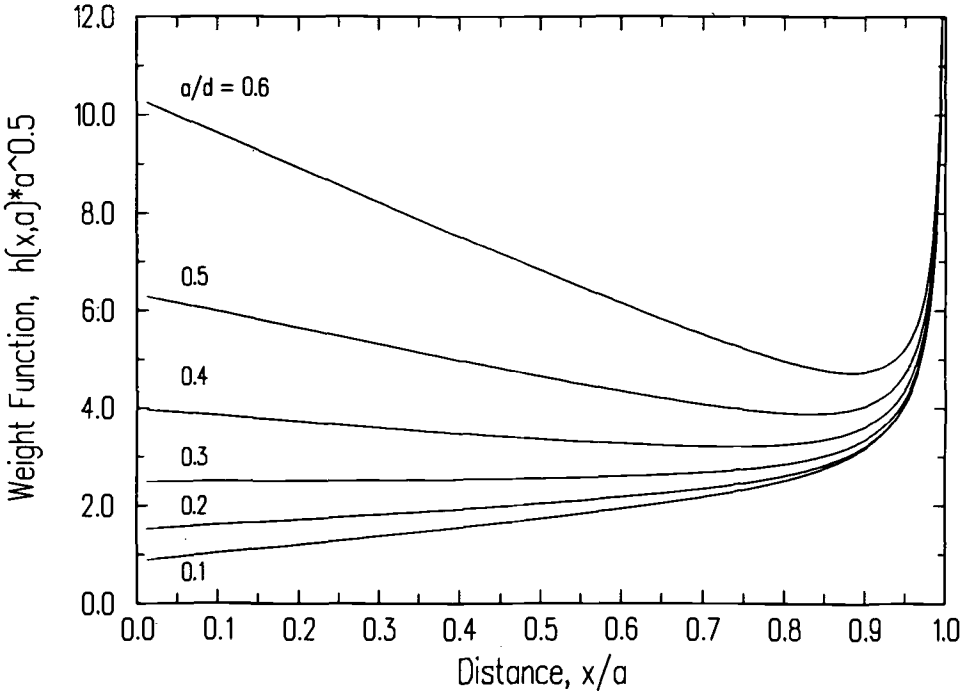


FIG. 5—Weight function for straight-fronted crack in a plate.

$$a/d_{\text{eff}} = \frac{\int_0^a [t(x)]^q dx}{\int_0^d [t(x)]^q dx} \tag{14}$$

Good correlation is achieved between three-dimensional buried and surface corner cracks and the approximation from Eq 14 when  $q$  is 0.25 as determined in the development of this paper. Note that when  $t(x) = t_0$ , a constant, Eq 14 reduces to the flat plate definition ( $a/d_{\text{eff}} = a/d$ ).

The overall behavior of the approximate weight function was verified against two-dimensional finite element analyses for an edge-cracked bar under tension and bending [13,14]. These comparisons are shown in Fig. 6. The results for the finite element analysis of Daoud et al. [13] for uniform tension are in reasonable agreement with the approximate  $K_I$  solution of Eq 12. The weight function results follow the trend reasonably well but tend to underpredict the finite element calculations when  $a/d$  exceeds 0.4. The same observations are true for the results for bending from Daoud and Cartwright [15]. It should be pointed out that the two-dimensional finite element model was itself an approximate representation to the round bar. The bar thickness was discretized by Daoud and Cartwright into precise, constant thickness segments. In general, there is reasonable agreement between the two independent methods, and the weight function appears well behaved and, therefore, well suited for use with stress distributions in notched bars.

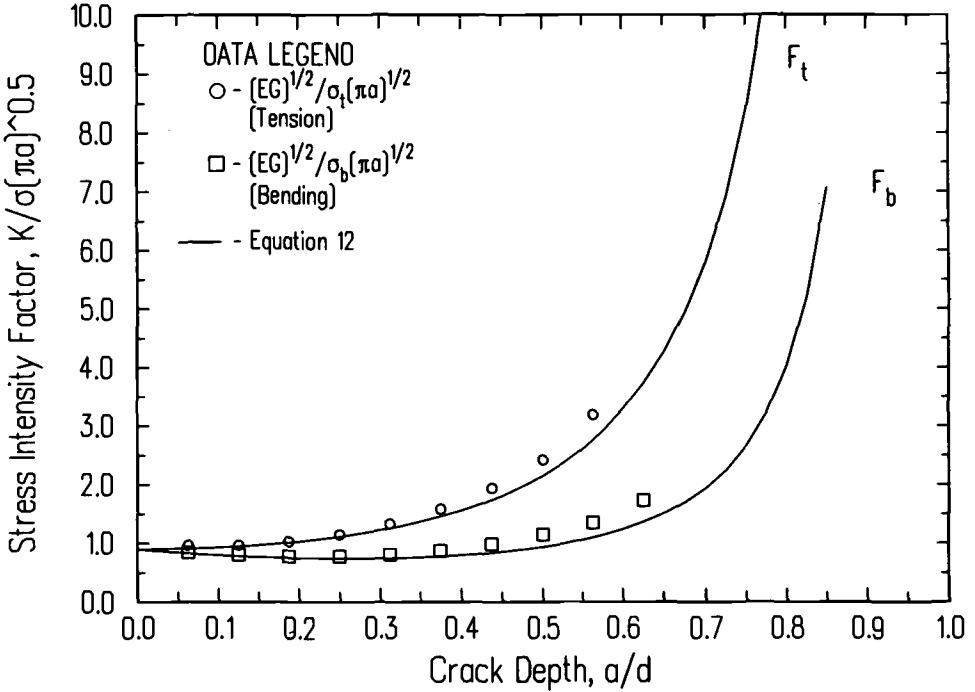


FIG. 6—Comparison of modified weight function for round bar with finite element results.

**Calculation of Stress Intensity Factors**

*Numerical Procedure and Limits*

The variation in  $K_I$  with respect to  $a/d$  was calculated from Eq 12 by applying the weight function defined by Eqs 10, 11, 13, and 14. The integration of Eq 12 was performed numerically using a standard trapezoidal rule. Accurate results were obtained with fewer than 50 integration points nonlinearly distributed with the density of points increasing as  $x/a \rightarrow 1$ . Double precision arithmetic was needed to avoid numerical precision errors in solving Eqs 10 and 11 for small  $a/d$ . In matching the correct trend as  $a/d \rightarrow 0$ , it was necessary to involve the following condition on  $F$  when  $a/d = 0$

$$F(0) = F_0 K_t = 0.898 K_t \tag{15}$$

where,  $F_0$  is the value of  $F$  at  $a/d = 0$  for the straight-front crack in a unnotched circular bar under tension (or bending) load. From Fig. 6, the value for  $F_0$  is numerically calculated to be 0.898. The imposition of Eq 15 is required because the inherent stress concentration factor for the deep hyperbolic groove is not the same as the single-groove round bar, which is more appropriate for the thread root geometry.

*Effect of Diameter*

The calculated  $K_I$  for nominal bolt diameter sizes of 2½, 3, 4, 5, and 6 in. (6.4, 7.6, 10.1, 12.7, and 15.2 cm) and a 4UN thread designation (4 threads/in.) is shown in Fig. 7. The

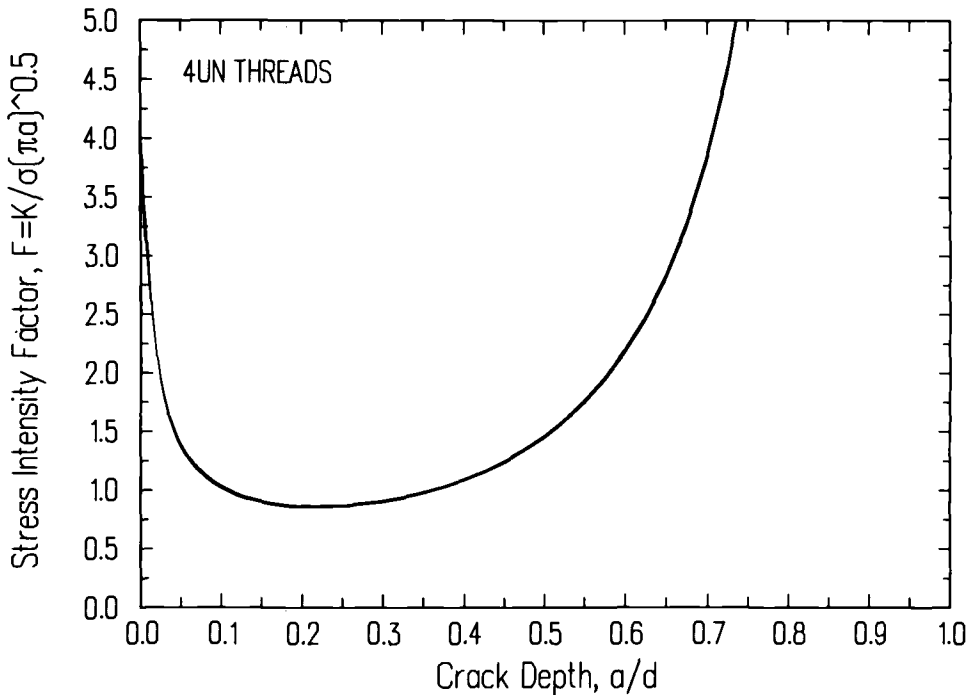


FIG. 7—Nondimensional stress intensity factor for 2½ to 6-in. (6.4 to 15.2-cm)-diameter fasteners with 4UN threads.

value of  $K_I/\sigma(\pi a)^{1/2}$  decreases rapidly with increasing  $a/d$  as the effect of the thread root geometry diminishes. It appears that the overall effect of the thread is nearly gone at a crack depth of  $a/d = 0.25$ . For  $a/d > 0.25$ , the trend in  $K_I/\sigma(\pi a)^{1/2}$  is similar to the behavior of an unnotched bar under pure tension stress.

It also appears from Fig. 7 that the effect of fastener size on  $F$  is small, at least when viewed on the scale shown. Another plot of the limited region  $0 \leq a/d \leq 0.1$  is presented in Fig. 8, where the difference of bolt size can be more clearly discerned. For  $a/d < 0.015$ , bolt size effect is a direct result of the different  $K_I$  values calculated for each bolt geometry. For  $a/d = 0$ , this difference is about 30% between 2½ and 6-in. (6.4 and 15.2-cm) sizes. However, this difference decreases with crack depth and, for  $a/d > 0.02$ , bolt size effects are negligible.

Similar behavior and trends are observed in the calculation of  $K/\sigma(\pi a)^{1/2}$  for 8UN and 12UN threads. Figures 9 and 10 show the results for 1, 1½, 2, 3, 4, 5, and 6-in. nominal diameters (2.5, 3.8, 5.1, 7.6, 10.2, 12.7, and 15.2 cm) for 8UN thread form. Again the effect of the thread discontinuity is limited to  $a/d < 0.25$ ; for cracks larger than  $a/d = 0.25$ , the unnotched solution would provide a conservative determination of  $K_I$ . In the region close to the thread ( $a/d < 0.1$ ), the effect of bolt size again shows that smaller fasteners will have nominally a lower  $K_I$  value and, therefore, a lower  $K_I$  (Fig. 10). The same behavior is observed for the 12UN threads as shown in Figs. 11 and 12.

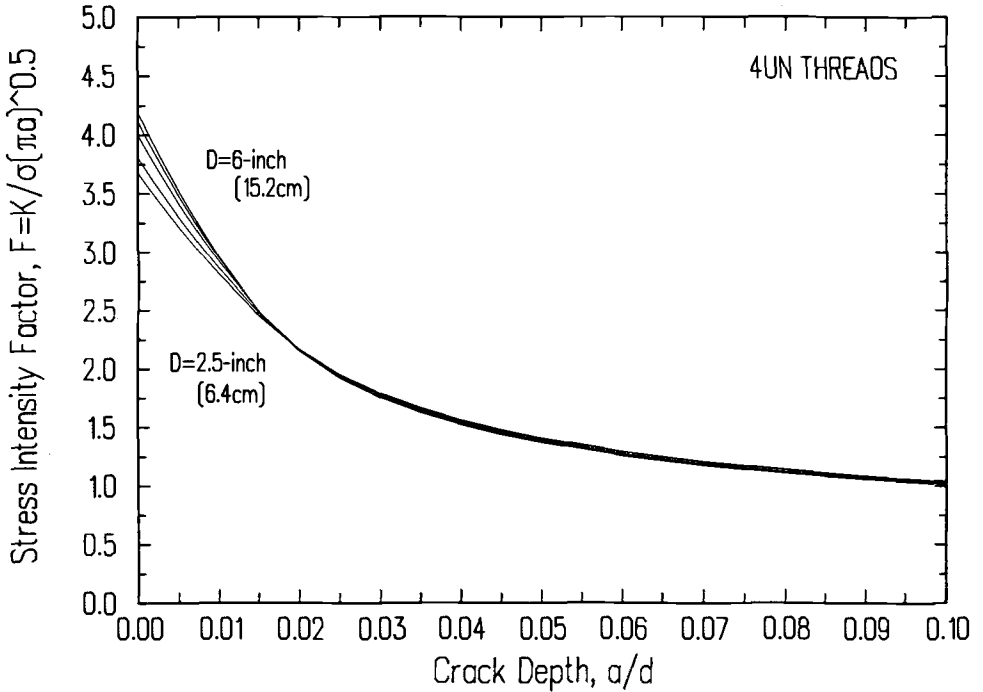


FIG. 8—Nondimensional stress intensity factor for 4UN threaded fasteners—expanded  $a/d$  scale.

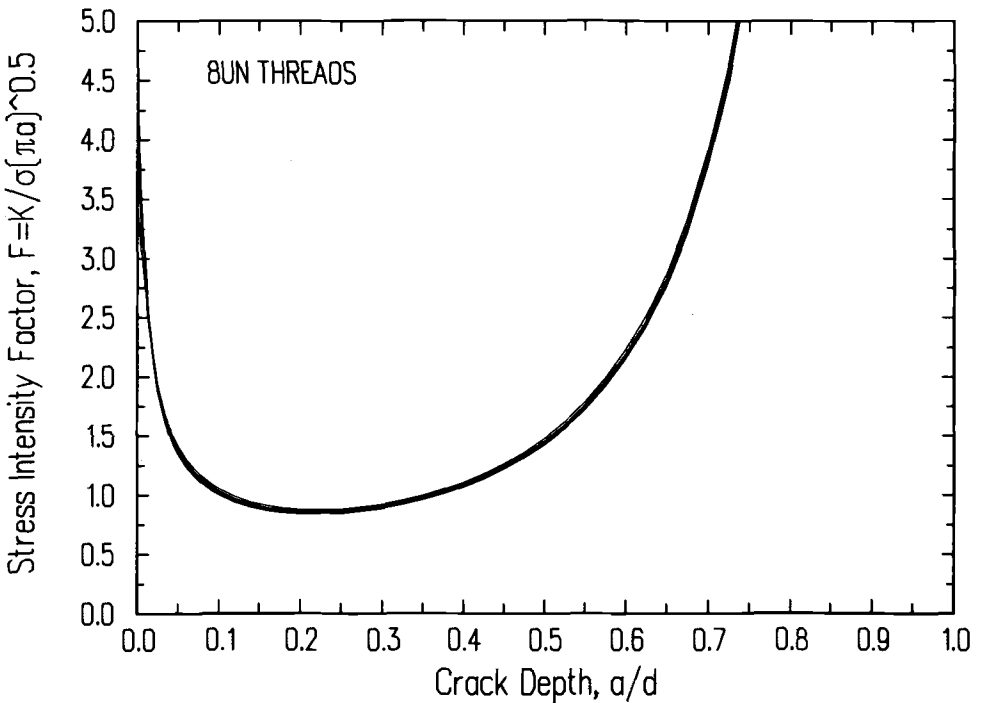


FIG. 9—Nondimensional stress intensity factors for 1-in. to 6-in. (2.5 to 15.2-cm)-diameter fasteners with 8UN threads.

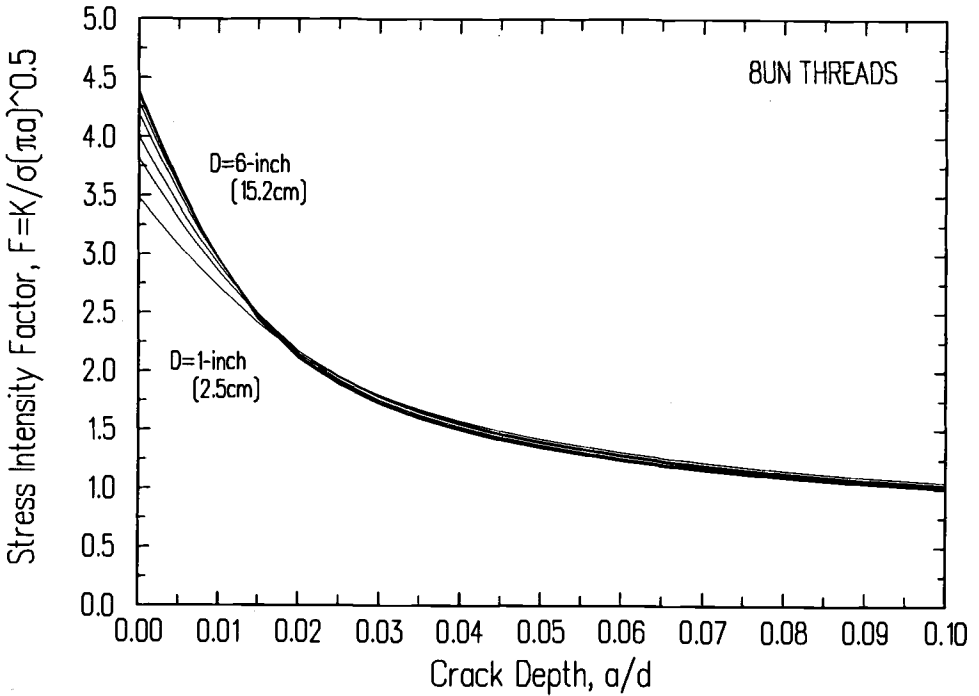


FIG. 10—Nondimensional stress intensity factor for 8UN threaded fasteners—expanded  $a/d$  scale.

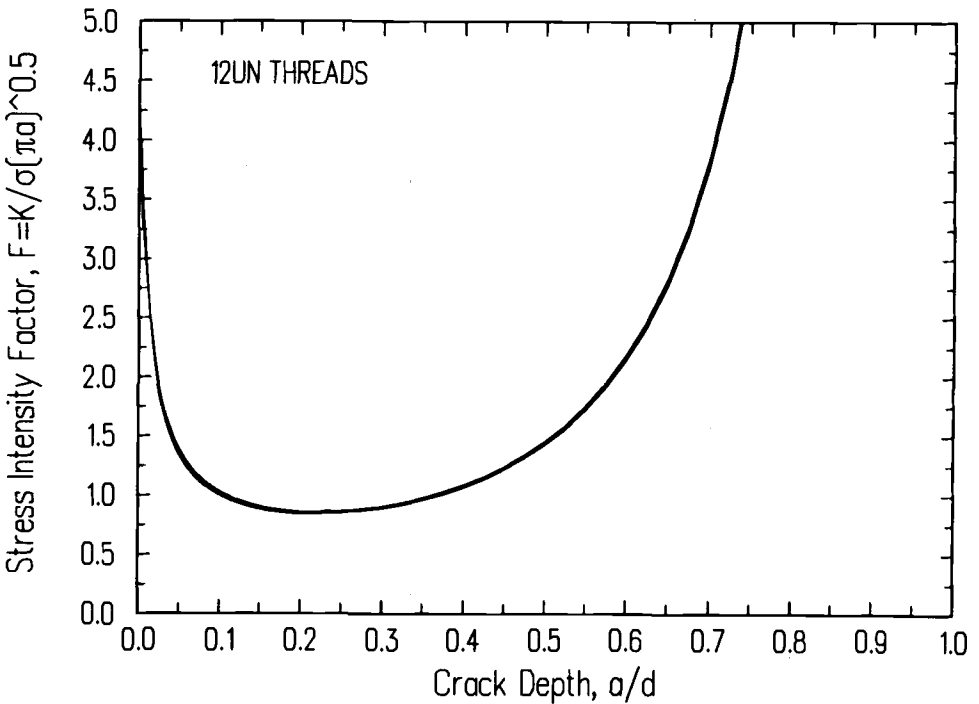


FIG. 11—Nondimensional stress intensity factors for 1-in. to 6-in. (2.5 to 15.2-cm)-diameter fasteners with 12UN threads.

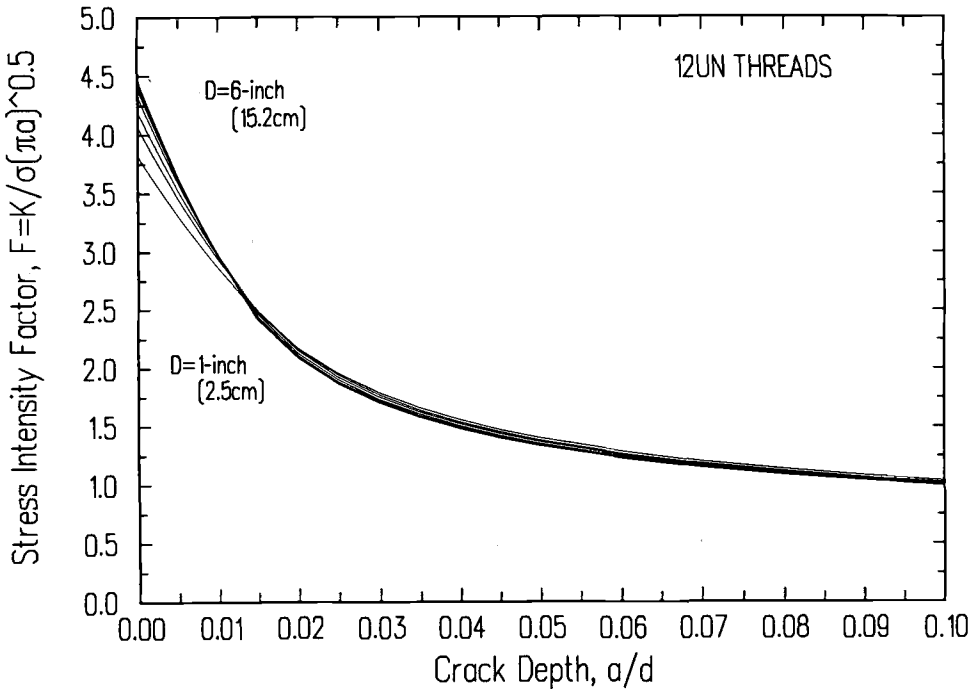


FIG. 12—Nondimensional stress intensity factors for 12UN threaded fasteners—expanded  $a/d$  scale.

### Effect of Thread Radius

The effect of root radius on the computed  $K$  for short cracks was evaluated by comparing the results for four different radii:  $\rho = 0.002, 0.009, 0.018,$  and  $0.036$  in. ( $0.05, 0.23, 0.46,$  and  $0.91$  mm). The comparison is given in Fig. 13 for the case of a  $1\frac{1}{2}$ -in. ( $3.8$ -mm) 8UN fastener. The base case is  $\rho = 0.018$  in. ( $0.66$  mm) as determined from Eq 9. As expected, the sharp radius give rise to the highest stress concentration and, therefore, the highest computed  $K$ . Such a situation could exist locally at some point on the thread helix due to poor fabrication. The other root radius values closer to the base case yield  $K$  values much lower than the assumed “sharp” thread. All local root condition effects are nearly attenuated when  $a/d$  is greater than  $0.015$ .

### Summary and Conclusions

A method for estimating the stress intensity factors for a straight-fronted crack initiating at the root of a thread has been developed that covers the full range of flaw depths. The nondimensional stress intensity factor has a relatively high value for small  $a/d$  where the influence of the thread is dominant. The trend is for  $K/\sigma(\pi a)^{1/2}$  to decrease rapidly with  $a/d$  as the stress concentration of the thread attenuates. The results should be applicable to both engaged and unengaged thread locations; however, the analysis assumptions are most representative of the unengaged threaded length of a fastener. The effect of bolt size and local thread root geometry appear to be only most significant for cracks whose depths are

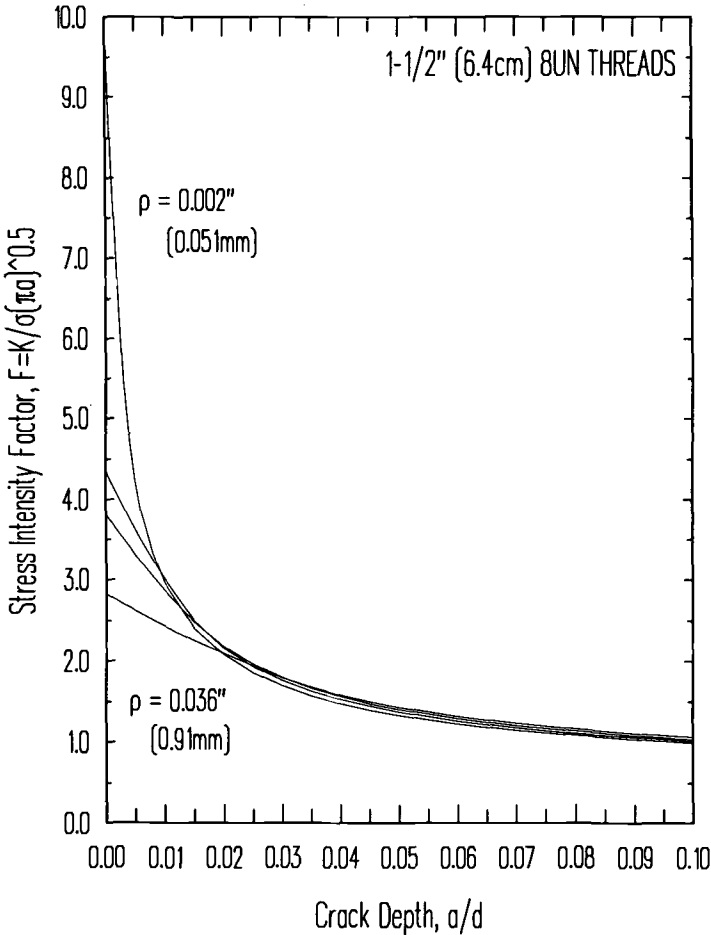


FIG. 13—Effect of thread root radius on stress intensity factor.

within 2% of the net (minor) section. For crack depths exceeding 25%, the global stress concentration effect of the threads is fully diminished and the trend for  $K_1$  follows that of the unnotched bar.

*Acknowledgments*

Some of the reported results had their foundation in work sponsored by the Electric Power Research Institute, Palo Alto, California under RP 2055-5. The author wishes to thank Dr. Lee James for his assistance on obtaining background information. Also the many technical discussions with Mr. Phil Besuner were very helpful in completing the numerical analysis.

**References**

[1] Cipolla, R. C., et al., "Requirements and Guidelines for Evaluating Component Support Materials Under Unresolved Safety Issue A-12," Report NP-3528, Electric Power Research Institute, Palo Alto, CA, June 1984.

- [2] Cipolla, R. C., "Stress Intensity Factor Approximations for Semi-Elliptical Cracks at the Thread Root of Fasteners," *Proceedings*, 1986 ASME Pressure Vessel and Piping Conference, Chicago, 20–24 July 1986, Vol. 26, pp. 49–58.
- [3] "Degradation and Failure of Bolting in Nuclear Power Plants," EPRI NP-5769, Electric Power Research Institute, Palo Alto, CA, April 1988.
- [4] James, L. A. and Mills, W. J., "Review and Synthesis of Stress Intensity Factor Solutions Applicable to Cracks in Bolts," *Engineering Fracture Mechanics*, Vol. 30, 1988, pp. 641–654.
- [5] American National Standards Institute, "Unified In. Screw Threads (UN and UNR Thread Form)," ANSI B1.1-1974, American Society of Mechanical Engineers, New York, 1974.
- [6] Neuber, H., *Theory of Notch Stresses*, 2nd ed., Springer, New York, translated by Office of Technical Services, 1961.
- [7] Peterson, R. E., *Stress Concentration Factors*, Wiley and Sons, New York, 1974.
- [8] Leven, M. M., "Stress Gradients in Grooved Bars and Shafts," *SESA Proceedings*, Vol. XIII, No. 1, Chicago, IL, November 1955.
- [9] Glinka, G. and Shen, G., "Universal Features of Weight Functions for Cracks in Mode I," *Engineering Fracture Mechanics*, Vol. 40, No. 6, 1991, pp. 1135–1146.
- [10] Shen, G. and Glinka, G., "Weight Functions for a Surface Semi-Elliptical Crack in a Finite Thickness Plate," *Theoretical and Applied Fracture Mechanics*, Vol. 15, 1991, pp. 247–255.
- [11] Tada, H., Paris, P. C., and Irwin, G. R., "The Stress Analysis of Cracks Handbook," Del Research Corporation, St. Louis, MO, 1985.
- [12] Besuner, P. M., Peters, D. C., and Cipolla, R. C., "BIGIF—Fracture Mechanics Code for Structures," NP-838, Key Phase Report RP-700-1, Electric Power Research Institute, Palo Alto, CA, 1978.
- [13] Daoud, O. E. K., Cartwright, D. J., and Carney, M., "Strain-Energy Release Rate for a Single-Edge-Cracked Circular Bar in Tension," *Journal of Strain Analysis*, Vol. 13, No. 2, 1978, pp. 83–88.
- [14] Daoud, O. E. K. and Cartwright, D. J., "Strain Energy Release Rates for a Straight-Fronted Edge Crack in a Circular Bar Subject to Bending," *Engineering Fracture Mechanics*, Vol. 19, No. 4, 1984, pp. 701–707.
- [15] Daoud, O. E. K. and Cartwright, D. J., "Strain Energy Release Rate for a Circular-Arc Edge Crack in a Bar Under Tension or Bending," *Journal of Strain Analysis*, Vol. 20, No. 1, 1985, pp. 53–58.

# Behavior of Fatigue Cracks in a Tension Bolt

---

**REFERENCE:** Liu, A. F., "Behavior of Fatigue Cracks in a Tension Bolt," *Structural Integrity of Fasteners, ASTM STP 1236*, P. M. Toor, Ed., American Society for Testing and Materials, Philadelphia, 1995, pp. 126–140.

**ABSTRACT:** A state-of-the-art review of the characteristics of crack growth in a tension bolt has been conducted. Considerations are centered on evaluating the usefulness of the existing stress intensity factors in making fatigue crack growth predictions. The closed-form stress intensity expression of Forman and Shivakumar (for an unnotched round bar) has been validated by making correlations with three sets of experimental data available in the literature. While the James-Mills equation (for a threaded round bar) matches the finite element solutions, the results of the analytical/experimental correlations indicate that an empirical equation, i.e., Eq 9, which was derived from this study, may be used to obtain acceptable life predications.

**KEYWORDS:** tension bolt, threaded cylinder, stress intensity factor, fatigue crack, crack shape, crack growth, metal

## Nomenclature

- b* Half of the crack tip-to-tip circumferential arc, inch (mm)
- d* Minor diameter of a bolt, inch (mm)
- D* Major or minor diameter of a bolt depending on application inch (mm), or coefficient of a polynomial equation
- K* Stress intensity, ksi (MPa)
- N* Number of applied load cycles
- P* Applied load, lbf (N)
- R* Minimum to maximum stress ratio
- S*  $4P/(\pi \cdot D^2)$  or  $4P(\pi \cdot d^2)$ , depending on crack plane geometry, ksi (MPa)
- Y* Stress intensity multiplication factor

During the past decade, much attention in fracture mechanics research has been given to the development of stress intensity factors for cracks in a tension bolt. A review paper by James and Mills [1] listed 38 references covering a period up to the year 1987. Progress made afterwards can be found in Refs 2 through 9. Among the early papers, most dealt only with analytical solutions for part-through cracks in the cylindrical cross section of a solid round bar (i.e., a rod), which can be considered as the shank portion of a bolt. Very limited experimental data have been generated in support of these analytic solutions. For those very few papers that reported stress intensity solutions for cracks originating at the screw thread, the investigations were limited to the area immediately adjacent to the thread (i.e.,  $a/d < 0.09$ ).

---

<sup>1</sup> Senior engineering specialist, Durability and Damage Tolerance, Rockwell International, North American Aircraft Division, P.O. Box 3644, Seal Beach, CA 90740-7644.

The post-1987 studies include: a detailed finite element analysis on the unthreaded bar [2]; a commercially available computer software package, tailor-made for determining  $K$  in a cylinder, including mixed Mode 1 and Mode 2 loading [3]; experimental crack growth data generated from threaded and unthreaded specimens [4,5]; an improved solution for small cracks at the thread [6]; three-dimensional finite element solutions for a threaded bar containing larger-size cracks up to  $a/d = 0.72$  [7–9]. The availability of these new data warrants a second review on this subject.

The objective of the present investigation is to identify those parametric variables that are unique in influencing the characteristics of crack growth in the shank and at the thread of a bolt subjected to uniaxial tension. Attempts have been made to attain a pair of working equations that will produce reliable  $K$  values for the entire range of crack sizes. This has been accomplished by making correlations between those closed-form stress intensity equations proposed in Refs 1 and 10 and the analytical and experimental data recently available in the literature.

### Crack Geometry Consideration

Understanding the crack growth mechanism is a prerequisite in determining stress intensity factors for a crack, that is, the variables that influence crack growth behavior should be identified. The crack model for computing  $K$  should contain such characteristic variables. Taking the classical semielliptical flaw problem, for example, it was originally assumed that crack growth took place at the maximum depth of a shallow crack where the  $K$  value was a maximum. Later, in the 1970s, it was recognized that  $K$  and the crack-shape aspect ratio interact in every incremental step of crack extension, that is, for a given crack,  $K$  values vary along the crack periphery. This causes the crack front to grow a different amount in different directions. As a result, the crack shape continuously changes as the crack extends. Since then, emphasis has been placed on implementing a two-dimensional crack-growth analysis procedure (for structural life prediction) for which a minimum of two  $K$  values (i.e., at the maximum depth and on the surface) are computed for the varying crack size and corresponding aspect ratio [13,14].

Consider an almond-shaped crack in a cylindrical cross section (Figs. 1a and 1b). Due to geometric difference between a cylinder and a plate, this crack cannot be regarded as being similar to a commonly recognizable edge crack, or thumbnail crack, in a rectangular cross section. Geometrical modeling of such a crack has not been sufficiently defined. As shown in Figs. 1b and 1c, the crack can be modeled as a part of an ellipse, or a straight front crack, having its origin fixed on the cylinder's free surface. However, it is generally believed that for a crack originating on the surface of a rod (or at the root of a thread), its crack front will quickly stabilize to the shape of a circular arc (rather than one half of an ellipse), which intersects the free surface of the crack plane at a right angle (i.e., Fig. 1a). As the crack front passes through the center of the rod, the crack front curvature will become flattened, approaching a straight crack front. Experimental observations on crack growth in rods [5,10–12] and specimens containing simulated screw threads [4,5] seem to support this claim. Photographs of two typical examples are shown in Figs. 2 and 3. Therefore, many analytic solutions had been developed from these crack models (i.e., a circular crack front for  $a < D/2$  and a straight crack front for  $a > D/2$ ). Among the circular crack models, the center of the crack curvature was either fixed on the cylinder's free surface, fixed at a point outside the cylinder, or was treated as a floating point that moved between the free surface of the cylinder and a point infinitely far away from the cylinder (i.e., allowing transition of the circular crack to become a straight crack).

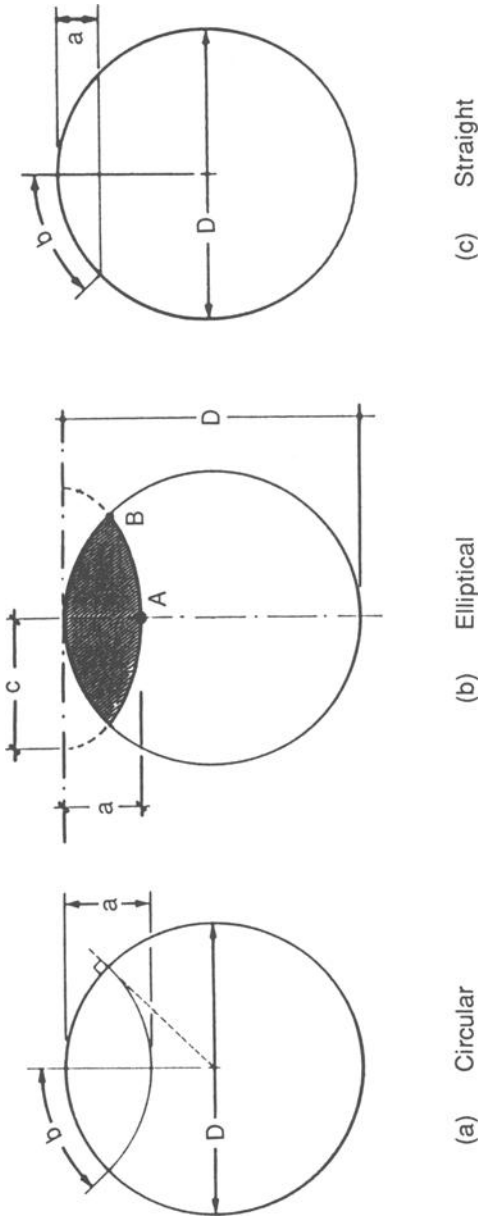


FIG. 1—Crack front shape models.

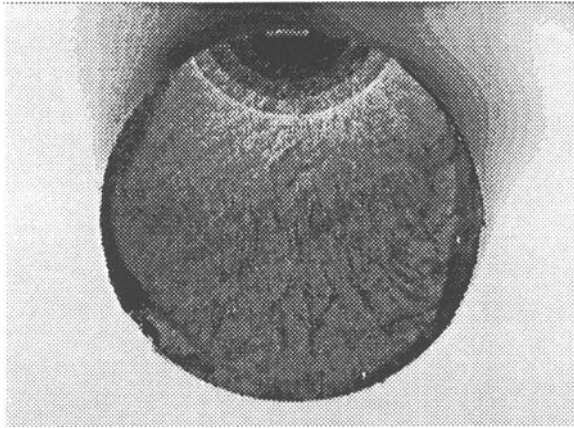


FIG. 2—Crack surface in an unthreaded bar. Courtesy of R. G. Forman.

In the aforementioned experiments [4,5,10–12], special efforts were made (by using marker cycles) to show the crack geometries inside the rod. The marker band data have been reduced from the referenced papers and are presented in Fig. 4. The depth-to-surface length ratio,  $a/b$ , is used to characterize the crack shape. The variation of  $a/b$  is plotted as a function of  $a/D$  or  $a/d$ , where  $D$  and  $d$  are, respectively, the major and minor diameter of the bolt. It is shown that the crack in a smooth rod exhibits a behavior distinctively different from those adjacent to a screw thread. Taking the apparent experimental scatter into consideration, it can be concluded that for  $a/D < 0.5$ , the crack in a smooth rod maintains a constant  $a/b$  ratio of approximately 0.9 (scattered around 0.8 and 1.0). To the contrary, the crack at

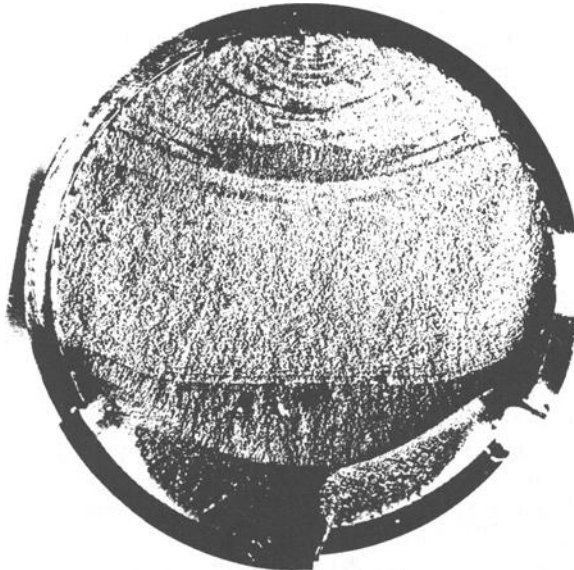


FIG. 3—Crack surface in a threaded bar. Courtesy of R. R. Cervay.

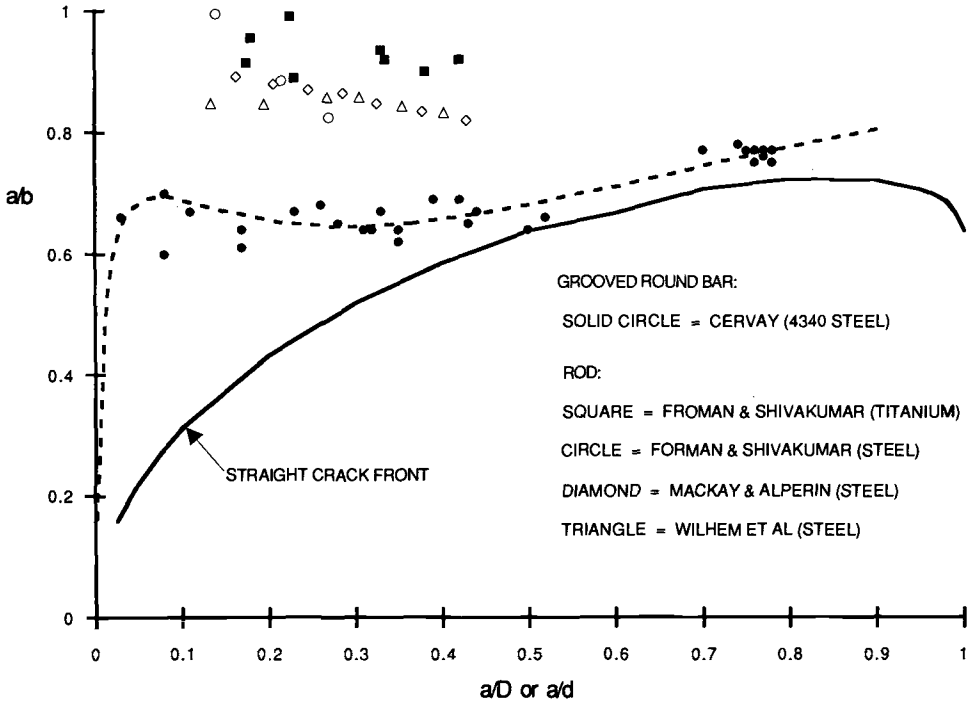


FIG. 4—Measured crack shape aspect ratios.

the screw thread has a constant  $a/b$  ratio of 0.65 up to  $a/d \approx 0.5$ . Using plane geometry, a simple relationship between  $a/b$  and  $a/D$  (or  $a/d$ ) for the straight crack configuration has been derived. It is represented by a solid line in Fig. 4. Comparing the experimental data points with this line, it is seen that the larger cracks in a threaded specimen have made smooth transitions from a curved crack front to a straight crack front. However, there is insufficient data to demonstrate how crack shape transition occurs in unthreaded specimens.

**Selection of Independent Variables**

Generally, the crack tip stress intensity,  $K$ , can be written as

$$K = S \cdot Y \cdot \sqrt{\pi \cdot c} \tag{1}$$

where  $c$  is an appropriate crack dimension for a given specimen configuration, e.g., the  $a$  or  $b$  in Fig. 1, or just  $c$  in a compact specimen. In the remainder of this paper, the crack depth  $a$  is used to characterize the cylindrical specimens. The symbol  $Y$  is the stress intensity multiplication factor, a function of loading condition, crack morphology, and the overall and local geometries of the structure. Its magnitude is determined by analysis, e.g., finite element, boundary integral equation, etc. As demonstrated in a number of papers [15,16], in lieu of using any analytical tool,  $Y$  can be effectively determined by empirical means. For the purpose of providing flexibility in making computerized structural life prediction, it is necessary to separate  $Y$  into a series of dimensionless parametric functions, where each segment represents an explicit boundary condition. Examples showing how to treat  $Y$  as a compounded

function for various types of complicated structural configuration are available in the literature [16–18].

For an almond-shaped crack in a bolt, a large portion of the crack growth activity will take place in only one half of the cylindrical crack plane, i.e., where  $a \leq D/2$  (or  $a \leq d/2$ ), before it becomes critical. As discussed earlier, the crack maintains a circular shape and a constant  $a/b$  ratio in this region. Referring back to the semielliptical flaw problem, a constant flaw shape during crack growth implies that the  $K$  values along the crack periphery are nearly constant. However, this is not the case here because the crack tip on the surface, which travels along the circumference of the cylindrical cross section, has to travel a longer distance than the crack middle point (which propagates in the depth direction) to keep up with the crack-shape aspect ratios. That is,  $db/dN > da/dN$  in each increment of crack extension. This means that the  $K$  value at Point B would be higher than those at Point A. Therefore, a two-dimensional crack-growth scheme is more suitable for this type of crack geometry. However, if the relationship between  $a/D$  and  $a/b$  is clearly established (such as those shown in Fig. 2), and the  $K$  or  $Y$  values at locations on the crack propagation path are specifically determined for the expected crack geometries, crack growth prediction can be accomplished by monitoring only one point on the crack periphery, i.e., by treating the crack configuration as if it were a one-dimensional crack. In the remainder of this paper,  $Y$  will be expressed as a function of  $a/D$  (or  $a/d$ ) for stress intensity factors at Point A.

### Analytically Determined Stress Intensity Factors

In Ref 1, James and Mills divided the analytic solutions into three groups: (1) cracks in a smooth rod having a circular crack front, (2) cracks in a smooth rod having a straight crack front, and (3) small cracks in the vicinity of a screw thread. They synthesized all the data into closed-form expressions representing cracks in unthreaded and threaded cross sections. The equations and the rationale they used to reach the solutions are discussed below.

#### *Stress Intensity Factors for Cracks in a Rod*

In dealing with the first two groups of the analytic data, a curve-fitted equation for cracks having a circular crack front was obtained by Forman and Shivakumar [10]. That is,

$$Y = g(x') \cdot f(x, x') \quad (2)$$

with

$$g = 0.586 \cdot [\tan(x')/x']^{1/2}/\cos(x') \quad (3)$$

and

$$f = 0.752 + 2.02x + 0.37 \cdot (1 - \sin(x'))^3 \quad (4)$$

where  $x = a/D$ , and  $x' = (\pi/2) \cdot x$ . Similarly, a curve-fitted closed-form equation for the straight cracks was developed by James and Mills [1], that is,

$$Y = 0.926 - 1.771x + 26.421x^2 - 78.481x^3 + 87.911x^4 \quad (5)$$

A plot for Eqs 2 and 5 is shown in Fig. 5. It indicates that stress intensity factors for straight cracks are higher than those for circular cracks. It should be noted that for the

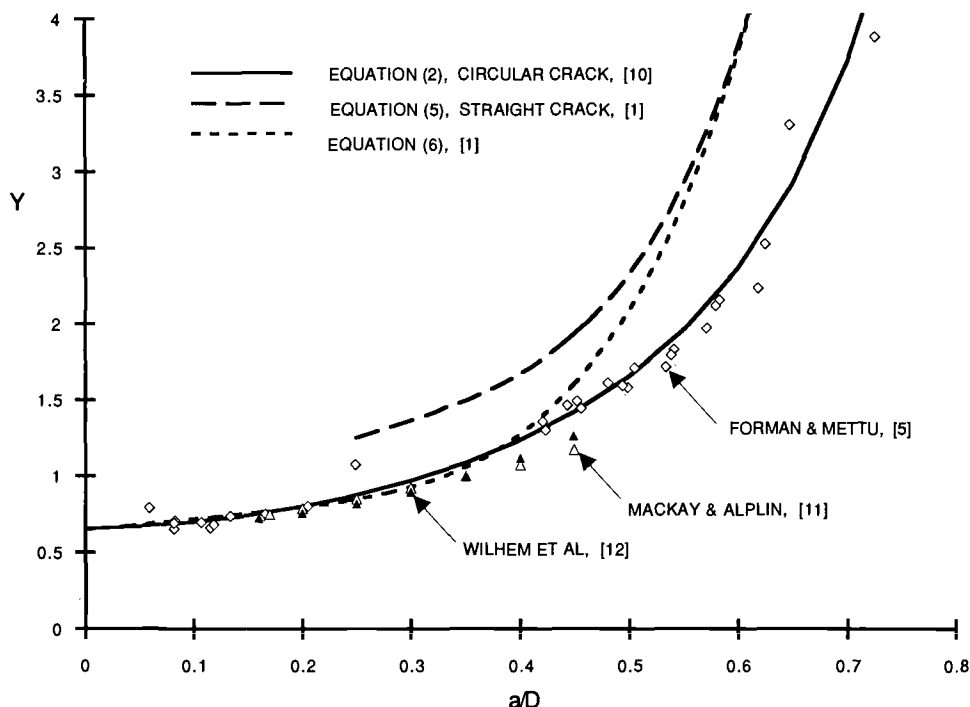


FIG. 5—Stress intensity factors for cracks in an unthreaded bar.

purpose of maintaining clarity, the analytic results that were used to construct these equations are not shown in the figure. The points shown in Fig. 5 are experimentally generated from test data. Discussion on this matter will appear in a later section of this paper.

Believing that a crack begins with a curved crack front and gradually changes to a straight crack front, James and Mills postulated that a single equation representing the entire  $a/D$  range could be derived by connecting these two curves (i.e., Eqs 2 and 5) at transition points near  $a/D = 0.5$ . The resulting equation is

$$Y = C + Dx + Ex^2 + Fx^3 + Gx^4 \quad (6)$$

where  $C = 0.6507$ ,  $D = 0.5367$ ,  $E = 3.0469$ ,  $F = -19.504$ ,  $G = 45.647$ , and  $x = a/D$ . A plot of this equation is also shown in Fig. 5.

It should be noted that the post-1987 finite element solutions for the straight and curved cracks [2] are not shown in Fig. 5. However, it is worth mentioning that the new straight crack solutions closely agree with Eq 5. The new circular crack data match Eq 2 in the intermediate  $a/D$  range but are slightly lower (in magnitude) than Eq 2 in the high  $a/D$  region. Therefore, judging from the apparent diversity between Eqs 2 and 5, it can be said that the  $Y$  functions for the curved and straight cracks do not merge in such a way as James and Mills had anticipated.

*Stress Intensity Factors for Cracks Originated from the Root of a Screw Thread*

Because the local stress concentration induced by the screw thread quickly decreases as  $a/d$  increases, James and Mills further postulated that except for those very small cracks, stress intensity distributions across the diameters of the unthreaded and threaded geometries (i.e.,  $K$ , or  $Y$ , as a function of  $a/D$ , or  $a/d$ ) were similar. In other words, when  $a$  is large (relative to thread depth), the bolt may be satisfactorily approximated as a unnotched round bar. Therefore, Eq 6 was used as the core for a new equation. The curve that fitted through the third group of analytic data (i.e., for small cracks in the vicinity of a screw thread) was jointed with into the synthesized curve of the larger cracks. Consequently, Eq 6 has been modified to become

$$Y = A \cdot \exp[(Bx)] + C + Dx + Ex^2 + Fx^3 + Gx^4 \tag{7}$$

where  $A = 2.043$ ,  $B = -31.332$ , and  $x = a/d$ . The exponential term covers the local stress concentration caused by the screw thread and decays away rapidly as  $a/d$  increases. The other coefficients in Eq 7 have the same values as those in Eq 6.

A plot of Eq 7 is presented in Fig. 6. Again, the analytical results (for the small cracks which James and Mills used to fit the equation) are not plotted in the figure. Those data points around the curve are three-dimensional finite element solutions, reported in Refs 7 to 9. It should be noted that the crack models in Ref 8 were semicircular cracks centered on the free surface of the cylinder ( $0.95 \leq a/b \leq 1.0$ ). However, the crack geometries in Ref

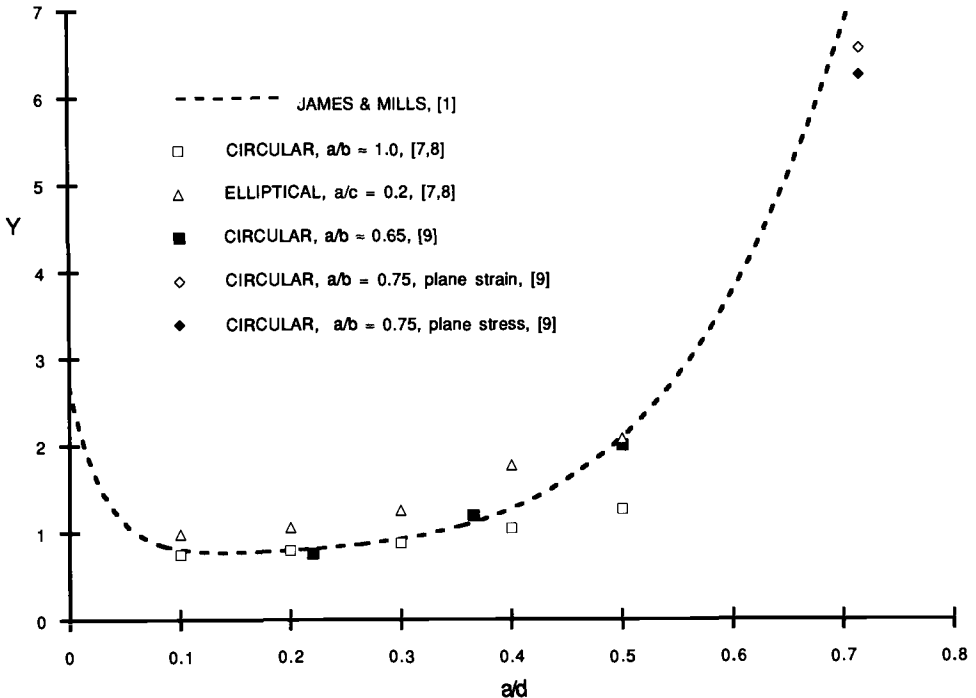


FIG. 6—Analytical stress intensity factors for cracks in a threaded bar.

9 were exactly the same as those found in Cervay's experiments, i.e.,  $a/b$  follows the dotted line in Fig. 4, which is approximately equal to 0.65 for most  $a/d$  ratios (or slightly higher after transition to a straight crack).

For a given  $a/d$  ratio, the crack which has a lower  $a/b$  ratio would have an area larger than a crack of a higher  $a/b$  ratio. Therefore, the  $K$  value for the former would have been higher than the latter. As  $a/d$  increases, the difference in cracked area between the two cracks (of the same  $a/d$  ratio, but different  $a/b$  ratios) increases, thus the difference in  $K$  also increases. This trend is reflected in the finite element solutions shown in Fig. 6. For the same reason, the  $K$  value for a straight crack or an elliptical crack would be higher than a circular crack as is shown in Fig. 5 and Fig. 6, respectively.

In addition to the crack-shape aspect ratio, the influence of crack length on  $K$  should be also considered. Customarily, a plane strain condition is assumed in the middle (i.e., Point A) of a part-through crack. However, for a larger-size crack, e.g., for  $a = 0.64$  in. ( $a/d = 0.72$  with  $a/b = 0.75$ ), the remaining ligament of the crack plane cross-sectional area may not be large enough to constrain the crack tip with a plane strain condition. Therefore, as shown in Fig. 6, two  $Y$  values for this crack have been determined, that is, based on plane stress and plane strain assumptions. As will be discussed later, the plane stress  $Y$  actually correlates better with experimental data.

### Empirically Determined Stress Intensity Factors

By backtracking the crack growth rate behavior from a set of controlled experiments, the  $Y$  factor can be determined from the crack-growth-rate relationship in a constant amplitude test, i.e.,

$$dc/dN = f(\Delta S, c, Y) \quad (8)$$

Since crack growth rates for the crack in a bolt is driven by  $K$ , it can be assumed that  $da/dN$  and  $db/dN$  in the bolt specimen will follow the same crack growth law as those for the basic material. Therefore, if one can separately develop the material baseline crack growth rate using a specimen geometry for which the relationship between  $K$  and  $Y$  is known (i.e., the compact specimen), the values for  $Y$  for the crack in a bolt can be determined by matching the experimental crack growth rate in the bolt to the material baseline crack-growth-rate data. This method is commonly known as the James-Anderson approach [15]. In fact, Mackay and Alperin [11] and Wilhem et al. [12] have used this technique to obtain empirical  $K$  values for unthreaded steel bars. Their results are presented in Fig. 5 along with the Forman-Shivakumar equation.

### Stress Intensity Factors for Cracks in a Rod

In addition to those experimental data for steels (already shown in Fig. 5), Forman and Mettu [5], have conducted similar tests on titanium. Their data set consists of 31 data points, generated from seven specimens (Ti, 6Al-4V, STA, stress relieved,  $D = 22.9$  mm), subjected to six stress levels ( $S_{\max} = 47.7, 75.8, 86.5, 107.8, 129.7,$  and  $162.4$  MPa, with  $R = 0.1$ ). Using the James-Anderson approach, their data have been reduced to  $Y$  versus  $a/D$  format. The results are plotted in Fig. 5. It is seen that agreement between Eq 5 and all the experimentally determined stress intensity factors (for a range of  $a/D$  ratios between 0.05 to 0.7) is excellent. The James-Mills equation, i.e., Eq 6, appears to be conservative for  $a/D > 0.5$ . It should be noted that the Forman-Shivakumar equation was originally used to fit data up

to  $a/D = 0.6$ . It is clear (in Fig. 5) that the applicable range for this equation is actually beyond  $a/D = 0.7$ .

*Stress Intensity Factors for Cracks Originated from the Root of a Screw Thread*

There are two sets of experimental data on fatigue crack growth of threaded specimens. The first set was developed by Cervay [4] in 1988, shortly after the James-Mills review was published. The second set, developed by Forman and Mettu [5], was made available recently.

The Cervay data set consisted of a comprehensive test matrix. It included eight specimens made of 4340 steel (1185 to 1227 MPa heat treat). Each specimen had three machined grooves simulating the 12-UNF-3A screw thread. The major and minor diameters were 25.4 and 22.6 mm, respectively. These specimens were subjected to constant amplitude cyclic stresses with  $R = 0.1$ . In a given test, the maximum stress level was either 262, 276, 290, or 331 MPa. A total of 108 data points, covering a range of  $a/d$  ratio between 0.018 to 0.702, was reduced from the crack length versus cycles record. It should be noted that because the raw data were presented in terms of  $2b$  versus  $N$ , the crack depth,  $a$ , was computed from a fractographically determined  $a$  versus  $2b$  relationship [4], which is shown by a dotted line in Fig. 4. All the empirical  $Y$  versus  $a/d$  data points are plotted in Fig. 7. Curve fitting was performed to obtain a new set of coefficients for Eq 7. As a result, Eq 7 became

$$Y = A \cdot \exp(Bx) + C + Dx + Ex^2 + Fx^3 + Gx^4 \tag{9}$$

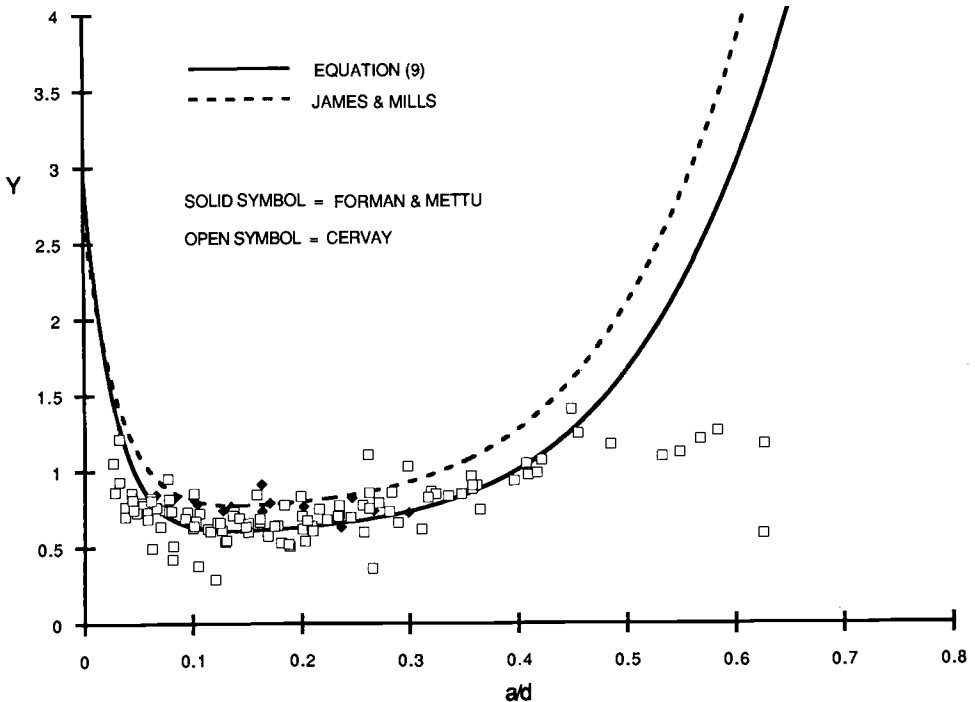


FIG. 7—Comparison of analytical and experimental stress intensity factors for cracks in a threaded bar.

where  $A = 2.4371$ ,  $B = -36.5$ ,  $C = 0.5154$ ,  $D = 0.4251$ ,  $E = 2.4134$ ,  $F = -15.4491$ ,  $G = 36.157$ , and  $x = a/d$ .

This set of coefficients satisfies the criteria, which requires that the  $Y$ 's are capable of reproducing crack growth histories for all the tests while the curve (representing  $Y$ ) maintains a good fit with the plotted  $Y$  versus  $a/d$  data points. The curve for Eq 9, shown here as a solid line, is superimposed on those empirical data points in Fig. 7. The criteria used to measure reproducibility are as follows:

*The Predicted Life*—A stress-intensity-factor equation's ability to predict crack growth life of a test can be demonstrated by calculating the number of cycles,  $N_p$ , required for the crack to propagate from its initial size to the final size (where the test terminates). The ratio of the calculated  $N_p$  to the actual number of cycles in the test,  $N$ , provides a measure of the accuracy of the empirical equation.

To do this, several iterations (in crack growth life prediction) were made. In each iteration, a different set of  $A$  through  $G$  values was assigned to the  $Y$  versus  $a/d$  equation. The calculated  $N_p/N$  ratios (based on Eq 9) are presented in Table 1. It is evident that the correlation is quite good because the average  $N_p/N$  value approaches unity. In addition, the predicted life,  $N_p$ , for each individual test is within  $\pm 20\%$  of the actual value. Judging by the apparent spread in experimental scatter, which is shown in Fig. 7 (for the empirical  $Y$  versus  $a/d$  data points) and later in Figs. 8 and 9 (for  $a$  versus  $N$ ), it is fair to say that this  $N_p/N$  range is quite reasonable.

*The Trend in Predicted Crack Growth History*—Other than matching  $N_p$  with  $N$ , it is also important that the experimental  $a$  versus  $N$  trend (i.e., the shape of the  $a$  versus  $N$  curve) can be reconstructed by analysis. Illustration on this is given in Figs. 8 and 9, where the predicted crack growth histories (based on Eq 9) are plotted against the actual  $a$  versus  $N$  record. For clarity, only one predicted curve per stress level is shown in the figures. Again, it is evident that the correlations are quite good.

The second set of experimental data on crack growth from a screw thread [5] was also reduced to  $Y$  versus  $a/d$  format. There are only 15 data points in this set, representing four specimens (Ti, 6Al-4V, STA, stress relieved,  $D = 22.9$  mm,  $d = 19.8$  mm), subjected to three stress levels ( $S_{\max} = 170.8, 216.3, \text{ and } 288.5$  MPa,  $R = 0.1$ ). The results are also

TABLE 1—Analytical and experimental crack growth lives in threaded specimens.

Specimen No.	Max Stress MPa	Initial ( $a/d$ )	Final ( $a/d$ )	N, 1000 cycles	$N_p/N$
2A	276	0.101	0.409	90	1.113
3A	331	0.046	0.415	100	0.965
5A	290	0.018	0.647	127.5	1.184
6A	331	0.025	0.438	135	0.785
7A	262	0.034	0.702	182.5	1.043
8A	290	0.018	0.685	189	0.805
9A	290	0.025	0.648	177.5	0.838
10A	262	0.027	0.615	202.8	0.961
Mean					0.962
Standard deviation					0.146

NOTE:

(1)  $S_{\min} = S_{\max}/10$  for all tests.

(2)  $N_p$  is computed by using Eq 9, with material properties data given by Ref 4.

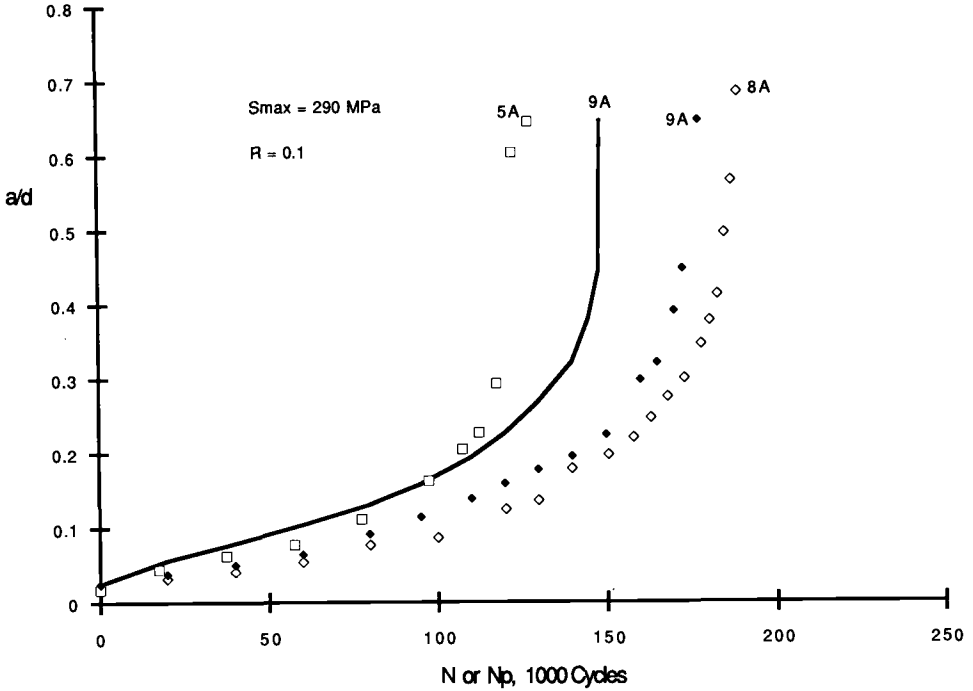


FIG. 8—Analytical/experimental correlations for crack growth in threaded specimens (Part 1).

plotted in Fig. 7. It is seen that the titanium data fall close to the upper bound of the 4340 steel.

For comparison purposes, the James-Mills equation for the threaded configuration (i.e., Eq 7) is also plotted in Fig. 7. It is seen that this equation is very conservative as compared to Cervay's crack growth data (for the 4340 steel), but correlates well with those titanium data of Ref 5. Adding to the confusion, the finite element solutions of Ref 9, which were developed based on crack geometries identical to those cracks found in the 4340 steel specimens, also shown to be conservative as compared to its experimental counterpart, but correlate with Eq 7. Some probable explanations on analytical/experimental correlations are offered as follows.

In reality, for very small and very large cracks, i.e., for  $a$  approaches zero and  $a$  approaches  $d$ , the  $Y$  values for these cracks are highly influenced by the notch geometry, which includes the pitch angle of the thread, the depth of the thread, and the root radius. The notch root radius in the finite element models of Refs 8 and 9 was 0.125 mm and 0, respectively. However, the notch root radius in the 4340 steel specimens was  $0.38 \pm 0.05$  mm. Therefore, it would be unreasonable to expect that the  $Y$  values are the same for all the thread geometries. To elucidate the local stress distribution effect on crack growth rate, a parametric evaluation was conducted on the 4340 steel experiments. By varying the value for the exponential coefficient,  $B$  (which provides a mean for imitating the stress gradient at the notch root), in a range between  $-40.0$  and  $-31.332$  while keeping the other coefficients constant, it is shown in Fig. 10 that the predicted life might be as low as  $-30\%$  (or as high as  $+30\%$ ) of the actual life depending on the  $B$  value.

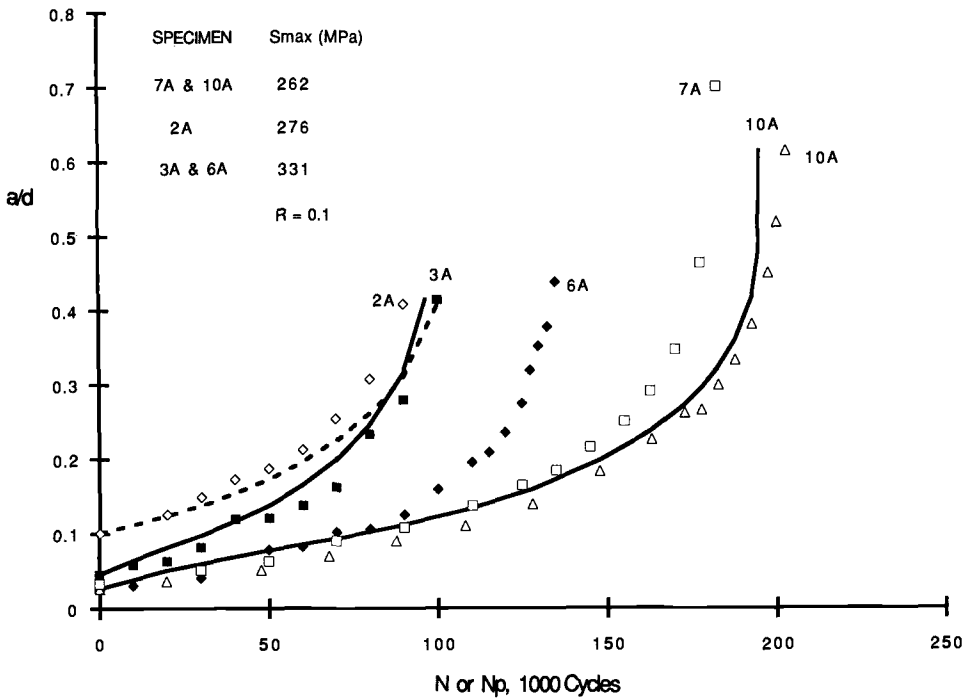


FIG. 9—Analytical/experimental correlations for crack growth in threaded specimens (Part 2).

As discussed earlier, as the crack becomes larger, the crack tip constraint gradually will change to plane stress (from plane strain). In fact, the plane stress solution for the largest crack, i.e.,  $a/d = 0.72$ , has a  $Y$  value of 6.26 (see Fig. 6), which is 5% lower than its plane strain counterpart but only 4% higher than the  $Y$  value computed by using Eq 9. Therefore, it can be considered that in the high  $a/d$  region, the correlation between Eq 9 and the finite element solution is actually quite good.

As shown in Table 1 and Figs. 8 and 9, having approximately the same initial crack lengths, those crack growth data generated at 290 MPa maximum cyclic stress level (Fig. 8) nearly overlap those crack growth data of Fig. 9 of which the applied maximum cyclic stress levels were either much lower (262 MPa) or much higher (331 MPa). Therefore, excessive experimental scatter might have been responsible for the discrepancies encountered here. Since Eq 9 was fitted with only one set of test data, it can be realized that the  $Y$  values in the mid  $a/d$  region would have been higher (approaching those in Eq 7) if the influence attributed to the second data set was also accounted for. In any event, further research in this area is required.

**Conclusion**

A review on the behavior of fatigue crack growth in unnotched and notched round bars under uniaxial tension was conducted. Existing stress intensity equations of Refs 1 and 10, which were developed based on data published prior to the year of 1988, were correlated

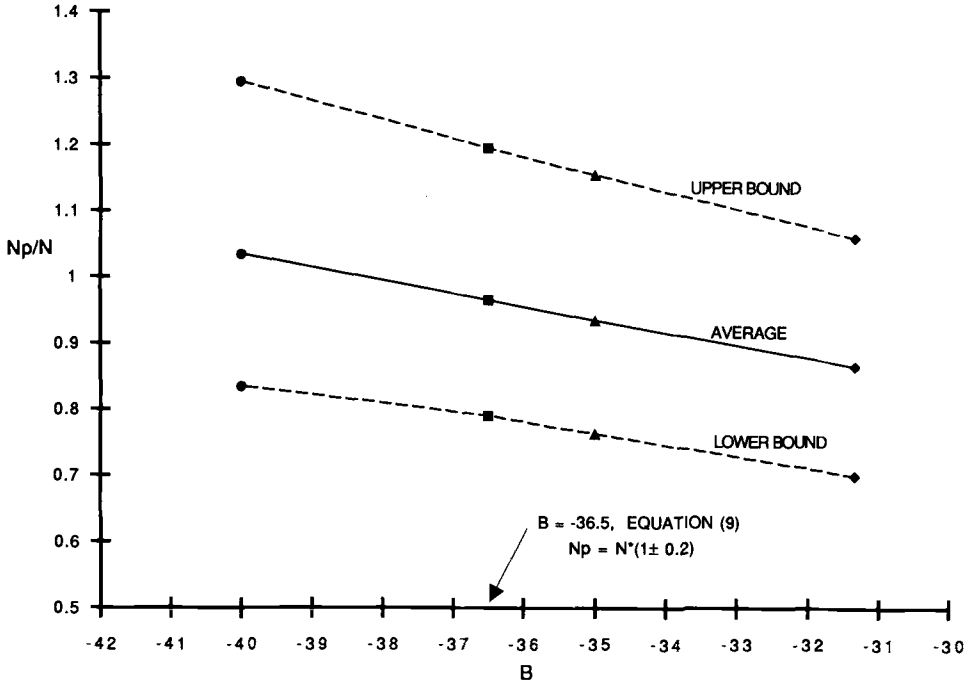


FIG. 10—Analytical/experimental correlations for crack growth in threaded specimens (Part 3).

with a bulk of analytical and experimental data sets recently available in the literature. The highlights of the conclusions drawn from this investigation are given below:

1. Crack front curvature is predominantly circular, not elliptical.
2. Crack front radius increases as crack depth increases and approaches infinity (i.e., becomes a straight crack front) at  $a/D > 0.5$ .
3. Crack growth tests on solid round bar indicates that the crack shape aspect ratios (i.e.,  $a/b$ ) are in between 0.8 to 1.0 for  $a/D < 0.5$ .
4. Cervay's tests on threaded bar indicated that the crack shape aspect ratio is a constant ( $a/b \approx 0.65$ ) for  $a/d \leq 0.5$ . Beyond that, the crack shape is approximated by a straight crack front.
5. One dimensional  $K$ -factors are adequate for life prediction.
6. The Forman-Shivakumar equation (i.e., Eq 2) for the unnotched round bar correlates well with experimental data.
7. The James-Mills equation for the threaded round bar (i.e., Eq 7) has been reconfirmed with the latest finite element solutions but lies on the upper bound of the experimental data. Conceptually, it is impossible to have a single curve for  $Y$  to cover a wide range of thread geometries. The conservatism of Eq 7 was due to the sharp notch models used in the finite element analyses. Pending a more refined, all around solution, Eq 9 may be regarded as an engineering approximation for this rather complex configuration.
8. This paper concerns only the crack in a bolt subjected to uniaxial tension. Stress intensity solutions for bending of a bolt have been published elsewhere (Ref 19).

## References

- [1] James, L. A. and Mills, W. J., "Review and Synthesis of Stress Intensity Factor Solutions Applicable to Cracks in Bolts," *Engineering Fracture Mechanics*, Vol. 30, 1988, pp. 641–654.
- [2] Ng, C. K. and Fenner, D. N., "Stress Intensity Factors for an Edge Cracked Circular Bar in Tension and Bending," *International Journal of Fracture*, Vol. 36, 1988, pp. 291–303.
- [3] Chen, K. L., Kuo, A. Y., and Shvarts, S., "Stress Intensity Factor Solutions for Partial Elliptical Surface Cracks in Cylindrical Shafts," *Proceedings*, 23rd National Symposium on Fracture Mechanics, College Station, TX, 18–20 June 1991.
- [4] Cervay, R. R., "Empirical Fatigue Crack Growth Data for a Tension Loaded Threaded Fastener," AFWAL-TR-88-4002, Air Force Wright Aeronautical Laboratories, Wright Patterson Air Force Base, OH, February 1988.
- [5] Forman, R. G. and Mettu, S. R., "Behavior of Surface and Corner Cracks Subjected to Tensile and Bending Loads in Ti-6Al-4V Alloy," *Fracture Mechanics: Twenty Second Symposium (Volume 1)*, ASTM STP 1131, American Society for Testing and Materials, Philadelphia, 1992, pp. 519–546.
- [6] Cipolla, R. C., "Stress Intensity Factors Approximations for Cracks Located at the Thread Region of Fasteners," this publication.
- [7] Muller-Wiesner, D., "Report on Crack Growth Calculations for Tension Loaded Bolts," ESA Study Contact Report, TN-OT217-029/88, MBB-ENRO, Deutsche Aerospace, Bremen, Germany, May 1988.
- [8] Toribio, J., Sanchez-Galvez, V., and Astiz, M. A., "Stress Intensification in Cracked Shank of Tightened Bolt," *Theoretical and Applied Fracture Mechanics*, Vol. 15, 1991, pp. 85–97.
- [9] Liu, A. F. and Gurbach, J. J., "Application of a p-Version Finite Element Code to Analysis of Cracks," *AIAA Journal*, Vol. 32, 1994, pp. 828–835.
- [10] Forman, R. G. and Shivakumar, V., "Growth Behavior of Surface Cracks in the Circumferential Plane of Solid and Hollow Cylinders," *Fracture Mechanics: Seventeenth Volume*, ASTM STP 905, American Society for Testing and Materials, Philadelphia, 1986, pp. 59–74.
- [11] Mackay, T. L. and Alperin, B. J., "Stress Intensity Factors for Fatigue Cracking in High Strength Bolts," *Engineering Fracture Mechanics*, Vol. 21, 1985, pp. 391–397.
- [12] Wilhem, D., FitzGerald, J., Carter, J., and Dittmer, D., "An Empirical Approach to Determining K for Surface Cracks," *Advances in Fracture Research*, Vol. 1, Pergamon Press, Elmsford, NY, 1981, pp. 11–21.
- [13] Liu, A. F., "Fracture Control Methods for Space Vehicles," *Fracture Control Design Methods*, Vol. 1, NASA CR-134596, National Aeronautics and Space Association, August 1974.
- [14] Rudd, J. L., Hsu, T. M., and Wood, H. A., "Part-Through Crack Problems in Aircraft Structures," *Part-Through Crack Life Prediction*, ASTM STP 687, American Society for Testing and Materials, Philadelphia, 1979, pp. 168–194.
- [15] James, L. A. and Anderson, W. E., "A Simple Procedure for Stress Intensity Calibration," *Engineering Fracture Mechanics*, Vol. 1, 1969, pp. 565–568.
- [16] Liu, A. F. and Kan, H. P., "Growth of Corner Cracks at a Hole," *Journal of Engineering Materials and Technology, Transactions of the ASME*, Vol. 104, 1982, pp. 107–114.
- [17] Waraniak, J. M. and Liu, A. F., "Fatigue and Crack Propagation Analysis of Mechanically Fastened Joints," AIAA Paper No. 83-0839, presented at the AIAA/ASME/ASCE/AHS 24th Structures, Structural Dynamics and Materials Conference, Lake Tahoe, NV, 2–4 May 1983. Synopsis appears in *Journal of Aircraft*, Vol. 21, 1984, pp. 225–226.
- [18] Newman, J. C. and Raju, I. S., "Stress-Intensity Factor Equations for Cracks in Three-Dimensional Bodies," *Fracture Mechanics: Fourteenth Symposium*, ASTM STP 791, Vol. 1, *Theory and Analysis*, American Society for Testing and Materials, Philadelphia, 1983, pp. I-238–I-265.
- [19] Liu, A. F., "Evaluation of Current Analytical Methods for Crack Growth in a Bolt," *Durability and Structural Reliability of Airframes—ICAF 17*, Vol. 2, EMAS Ltd., West Midlands, U.K., 1993, pp. 1141–1155.

# **Structural Integrity Criteria for Fasteners**

## Early Stages of Fatigue Damage of Fastener Holes Monitored by Laser Speckle

---

**REFERENCE:** Chiang, F.-P., Du, M.-L., and Li, S., "Early Stages of Fatigue Damage of Fastener Holes Monitored by Laser Speckle," *Structural Integrity of Fasteners, ASTM STP 1236*, P. M. Toor, Ed., American Society for Testing and Materials, Philadelphia, 1995, pp. 143–154.

**ABSTRACT:** The present work confines itself to the study of the initiation and early propagation of fatigue cracks emanating from simulated fastener holes using a laser speckle method that is a noncontact, nondestructive, and remote sensing technique. When illuminated by a narrow laser beam, the fatigue-induced surface roughness causes the laser beam to diffract into a halo modulated by a random speckle pattern. The fatigue damage information is contained in the speckle diffraction pattern. The half width and cross correlation coefficient of a speckle pattern are chosen to quantify this information. Two kinds of specimens, a thin plate with an open hole in the center and a thin plate with an oversized pin impacted into a central hole, were tested. The fatigue process was monitored by the laser speckle patterns. After crack propagation, the specimens were examined under a scanning electron microscope and their fractographic features correlated with the fatigue process.

**KEYWORDS:** fatigue, roughness measurement, laser speckle pattern

Fatigue damage manifests itself on the surface of cyclically stressed materials in the form of surface roughness. It has been observed [1,2] that repeated compressive and tensile loading produces a random roughening of the surface. As the cumulative strain increases, the valleys between the peaks grow deeper statistically. The deepest valleys may eventually develop into cracks. Significant improvement in fatigue life has been reported for uniaxially fatigued specimens after a surface removal treatment. Improvement is possible even when precycling has been carried to 95% of the fatigue life of a virgin specimen [3]. This indicates that the roughness of materials caused by cyclic fatigue governs the initiation of cracks and may be used to define the development of fatigue damage.

Surface roughness can be measured by using a mechanical profilometer. However, to study the surface roughness evolution using a profilometer, one has to dismount the specimen repeatedly from the test machine during the test. Furthermore, scratches produced by the probe on the specimen surface may be the source of crack initiation in high-cycle fatigue. A reliable means for accurate, noncontact, and nondestructive assessment of cumulative fatigue damage has been sought for many years. In this paper, we propose an improved laser speckle method to assess fatigue damage that has the above-mentioned features.

When illuminated by a narrow laser beam, the fatigue-induced surface roughness scatters the laser beam in a broad spectrum of directions. The reflected wavelets mutually interfere

---

<sup>1</sup> Chair, leading professor of mechanical engineering, and director and <sup>2</sup>research assistants, Laboratory for Experimental Mechanics Research, Department of Mechanical Engineering, State University of New York at Stony Brook, Stony Brook, NY 11794-2300.

to form a random interference pattern called speckles. The spectrum half width technique and cross correlation technique have been shown to be sensitive to surface roughness change. The experimental setup is relatively simple [4].

Fatigue life of a structure with different types of fastener connections (bolts or pins, etc.) has received much attention over the years. Stress analysis of a structure component under remote loading is a complex nonlinear problem involving variable contact between the fastener and the component. Related work includes that by Shah [5] in which approximate stress intensity factors for cracks originating at fastener holes have been derived. Leis et al. [6] presented experimental results on the nucleation and continued growth of corner cracks at circular notches in aluminum sheet specimens. In our present study, two kinds of specimens were investigated. One is an aluminum thin plate with an open hole in the center, and the other is a thin plate of identical dimensions but with an oversized pin impacted into the hole.

### Specimen and Experiment

The specimens were made of Al 5052-H32 with the yield strength  $\sigma_y = 160$  MPa. The rolling direction was parallel to the loading. The stress-strain curve was fitted with the hardening exponent  $n$  being 21 of the Ramberg-Osgood relation as show below [7].

$$\epsilon = \frac{\sigma}{E} \left[ 1 + \frac{3}{7} \left( \frac{\sigma}{\sigma_0} \right)^{n-1} \right] \quad (1)$$

where  $\sigma$  and  $\epsilon$  are the uniaxial stress and strain, respectively,  $E$  is the elastic modulus,  $\sigma_0$  is the nominal yield stress, and  $n$  is the hardening exponent chosen to provide the best fit for the stress-strain curve.

Specimens were made of a thin plate with a hole in the center. The specimen dimensions were 203 mm in length, 44.45 mm in width, and 3.175 mm thick, and the diameter of the central hole was 6.35 mm. Repeated stress-controlled tension-tension tests in a sinusoidal waveform were performed in an Instron machine at room temperature. The specimens were loaded at a frequency of 6 Hz and a stress ratio of  $R = \sigma_{\min}/\sigma_{\max} = 0.1$ . In order to observe the features of the crack tip, some of the specimens were loaded until the cracks had propagated about 5 mm in length. The rest of the specimens were loaded to fracture so that the fractured surface could be observed afterwards by scanning electron microscope (SEM).

The specimens were polished at the interested area to an initial surface with an arithmetic mean roughness  $R_{am}$  of about 0.05  $\mu\text{m}$ . Figure 1 shows the experimental setup. The area near the edge of the hole where the crack initiation would occur was illuminated by a 15-mW He-Ne laser beam. A SP2000 high-speed motion analysis system was used to record and digitize the laser speckle patterns at different loading cycles. The resolution of the digital camera is 238 by 192 pixels. The speed of the camera was set at 200 frames per second. Several speckle patterns were recorded at different loading cycles. First, the initial speckle pattern was recorded. Then the speckle patterns about every tenth of the whole crack initiation life were recorded. Since in the last period the pattern varied at every cycle, the patterns were recorded as frequently as possible. The digitized speckle patterns were processed on a computer through a procedure described in the next section.

### Evaluation of Spectrum Half Width and Cross Correlation

Fatigue processes may roughen the specimen surface by increasing the surface height deviation and decreasing the surface correlation length. When the surface of a fatigued

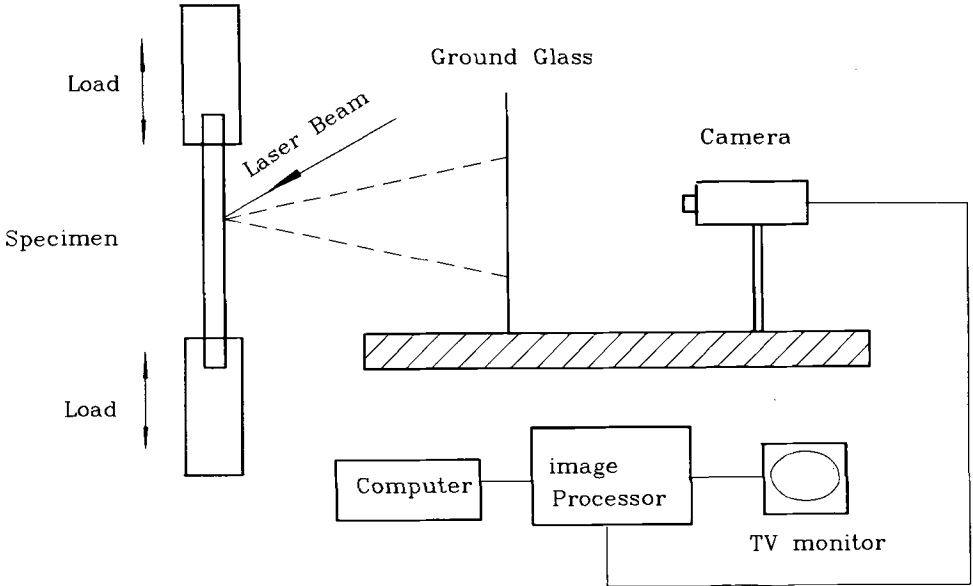


FIG. 1—Experimental setup to monitor fatigue-induced surface roughness by laser speckle.

specimen is illuminated by a laser beam, the reflected and scattered light intensity distribution, in the form of a speckle pattern, indicates surface roughness and hence fatigue damage information [8]. We choose the spectrum half width and cross correlation coefficient of a speckle pattern to quantify this information.

### Preprocess

Before the evaluation of surface damage, a speckle pattern is smoothed by the following procedures. First, the centroid of speckle pattern is determined by a moment method using the following equations

$$i_c = \frac{\sum_{i=1}^{i=m} \sum_{j=1}^{j=n} g(i, j) \times i}{\sum_{i=1}^{i=m} \sum_{j=1}^{j=n} g(i, j)} \quad (2)$$

and

$$j_c = \frac{\sum_{i=1}^{i=m} \sum_{j=1}^{j=n} g(i, j) \times j}{\sum_{i=1}^{i=m} \sum_{j=1}^{j=n} g(i, j)} \quad (3)$$

where  $g(i, j)$  is the digitized intensity levels of the speckle pattern and  $(i_c, j_c)$  is the position of the centroid of a pattern, and  $m$  and  $n$  are the total number of pixels along the  $i$  and  $j$  directions, respectively.

Second, the spatial intensity is averaged by

$$\bar{g}(r_i) = \frac{1}{n_k} \sum_{k=1}^{n_k} g(r_i) \quad (4)$$

where  $r_i$  is the radius measured from the centroid, and  $n_k$  is the number of points dropped on the ring with  $\Delta r_i = r_{i+1} - r_i < 1$ .

Such a spatial averaging may not be sufficient to depress the speckle noise, especially at regions near the centroid, where the number of points used in averaging is less when  $r_i$  is small. Further smoothing is then performed by using

$$g_s(r_i) = \frac{1}{5} \sum_{i-2}^{i+2} \bar{g}(r_i) \quad (5)$$

### *Spectrum Half Width and Cross Correlation*

The spectrum half width is a measure of the extension of a scattered field. It is defined as the radius corresponding to one half of the highest intensity.

The cross correlation coefficient is a measure of the degree of similarity between two different objects. For two-dimensional digitized images, the cross correlation of two arbitrary functions  $g(i, j)$  and  $f(i, j)$  is defined as [9]

$$C_c(g, f) = \frac{\sum_{i=1}^{i=M} \sum_{j=1}^{j=N} g(i, j) \times f(i, j)}{[\sum_{i=1}^{i=M} \sum_{j=1}^{j=N} g^2(i, j) \times f^2(i, j)]^{1/2}} \quad (6)$$

where  $g(i, j)$ ,  $f(i, j)$  are the discrete intensity levels at point  $(i, j)$  of image  $g$  and  $f$ , respectively.  $M$  and  $N$  are total discrete points in  $X$  and  $Y$  directions ( $M = 238$ ,  $N = 192$ ).

## **Results and Discussion**

### *Observation of the Speckle Pattern*

Figure 2 shows a set of experimentally obtained speckle patterns of a specimen at different stages of fatigue damage with  $\lambda = \sigma_{\text{nom}}/\sigma_y = 0.96$ , and  $R = \sigma_{\text{min}}/\sigma_{\text{max}} = 0.1$ , where  $\lambda$  is the ratio of the maximum nominal far field stress  $\sigma_{\text{nom}}$  to the yield stress  $\sigma_y$ . Figure 2a is the initial speckle pattern at  $N = 1000$  cycles. Speckles are distributed around the central spike, and the pattern has a preferred orientation owing to the polishing processes. Figure 2b corresponds to the fatigue cycle number  $N = 20\,000$ . No obvious differences are observed between these two patterns. As the number of loading cycles is increased, the speckles spread out and the speckle pattern becomes more circular when the crack initiation stage is approached as shown in Fig. 2c, when  $N = 29\,800$ . The crack initiation and propagation occurred only a few hundred cycles more from this stage. Figure 2d is the pattern when the crack has propagated near to the laser beam point, which is about 5 mm away from the edge of the hole; we define this cycle number as the failure cycles  $N_f = 32\,600$ .

The crack would have grown faster and the fracture would have occurred within several hundred cycles from this stage if the loading had been continued. The loading was stopped when the crack propagated about 5 mm. We then pointed the laser beam at different distances from the crack tip and recorded the resulting speckle patterns, respectively. Figure 3a is the speckle halo pattern at a distance of  $0.7a$  from the crack tip, where  $a = 4.43$  mm is the crack length; halos in Figs. 3b, 3c, and 3d correspond to the distances of  $1.1a$ ,  $1.9a$ , and  $2.2a$  from the crack tip, respectively. It can be seen that the speckle patterns vary from each other significantly with increasing distance from the crack tip. In the area far from the crack tip as shown in Fig. 3d, the preferred orientation due to surface polishing is seen because the roughness does not change significantly at that position.

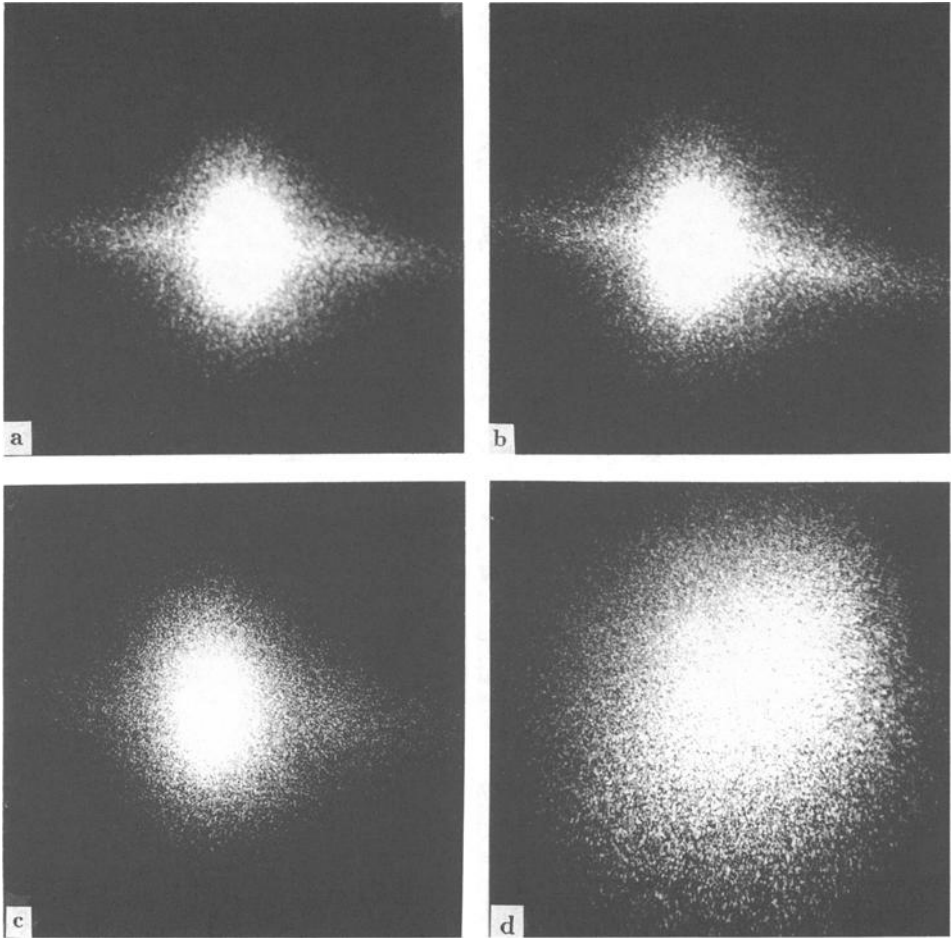


FIG. 2—Successive speckle patterns from a typical specimen at different levels of fatigue damage; (a)  $N = 1000$ , (b)  $N = 20\,000$ , (c)  $N = 29\,800$ , and (d)  $N = N_f = 32\,600$ .

By using the mechanical stylus type of profilometer, we can also show the roughness degradation from the crack tip by the arithmetic mean roughness ( $R_{am}$ ) distribution from the crack tip as shown in Fig. 4.  $R_{am}$  is defined as

$$R_{am} = \frac{1}{N} \sum_{i=1}^N |h(i)| \quad (7)$$

where  $h(i)$  is the variation of a surface profile.  $R_{a0}$  is the far field roughness (or initial roughness). It is seen from Fig. 4 that the roughness distribution from the crack tip is nonlinear.

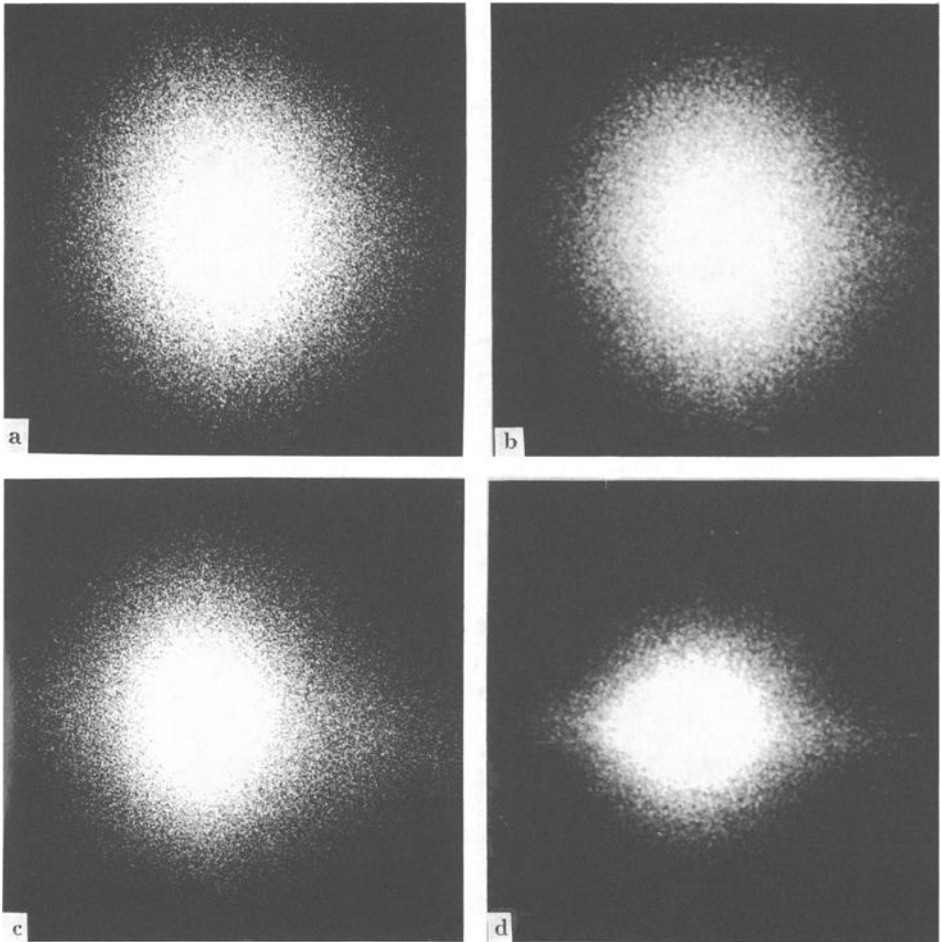


FIG. 3—Successive speckle patterns at different locations along the crack tip direction (crack length  $a = 4.43$  mm) (a)  $r/a = 0.7$ , (b)  $r/a = 1.1$ , (c)  $r/a = 1.9$ , and (d)  $r/a = 2.2$

#### *Relation Between Surface Roughness and Fatigue Damage*

How to quantitatively assess measurement of fatigue damage depends first of all strongly on the definition of damage. There are generally two damage definitions: (1) damage considered as the alteration of material property, and (2) damage considered as the presence of defects. The theory of continuum damage mechanics has been developed for the first concept, which is being applied to engineering materials and structures based on the theory of fracture mechanics [10,11]. The second concept, focused on the physical studies of damage and limited to the microscopic scale, is important in improving the understanding of damage mechanism. However, it presents difficulties in engineering application. Damage caused by fatigue manifests itself on the macroscopic scale through the evolution of surface roughness. Failure due to fatigue damage may be defined in terms of fatigue life. This approach is supported by the fact that crack initiation is preceded by a progressive internal deterioration

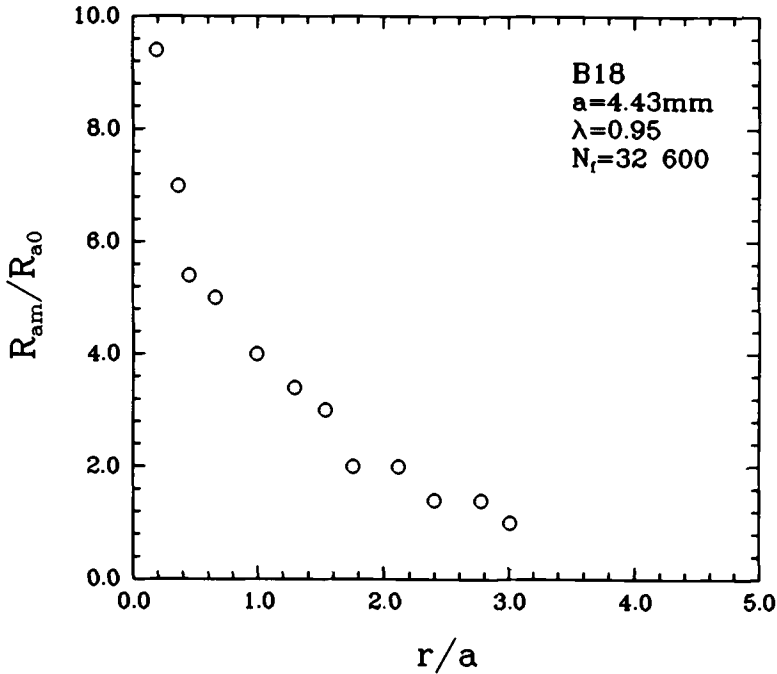


FIG. 4—Mean roughness distribution along crack tip is obtained by a mechanical profilometer.

of the material that induces a surface roughness change. We attempt to relate the fatigue life to the surface roughness through two parameters evaluated from the speckle patterns and monitor the fatigue damage by an improved laser speckle method.

Figure 5 shows examples of the relation between the half spectrum width and the fatigue life ratio  $N/N_f$  (where  $N_f$  is the failure life under periodic loading). The result agrees with that reported in Ref 4 that the spectrum width does not change much at early stages of cyclic loading. However, it jumps drastically near the failure stage. This sudden jump in spectrum half width reflects the drastic surface roughness change resulting from the development of extrusion, intrusion, or slip band due to crack initiation and propagation. This significant change in the spectrum half width may be used as a criterion for the determination of the crack initiation life. Figure 5 shows that the higher nominal stress causes an earlier drastic change in the spectrum, or an earlier crack initiation. For example, the ratio of crack initiation life to the failure life ( $N_i/N_f$ ) for Specimen B16 (with a load ratio  $\lambda = 0.94$ ,  $N_f = 34\ 000$ ) is 0.84, whereas for specimen B24 (with a load ratio  $\lambda = 0.90$ ,  $N_f = 78\ 700$ ), it is 0.94.

As mentioned previously, we introduced a new parameter, the cross correlation coefficient, to evaluate the speckle pattern. This parameter is a measure of the similarity of two speckle patterns representing two different surface roughnesses. The cross correlation coefficient  $C_c$  was evaluated between the initial speckle pattern [ $g(i, j)$  in Eq 6] and the speckle patterns at different fatigue cycles [ $f(i, j)$  in Eq 6] through the whole fatigue life. Figure 6 gives the relation between the cross correlation coefficient and the fatigue life cycle ratio of several specimens. The surface roughness change in terms of the cross correlation coefficient is not linear with respect to the fatigue life cycle ratio and depends on the applied stress as well. The surface roughness changes slowly during most part of the fatigue life except at the end, where it varies drastically. The rate at which the roughness changes under higher nominal

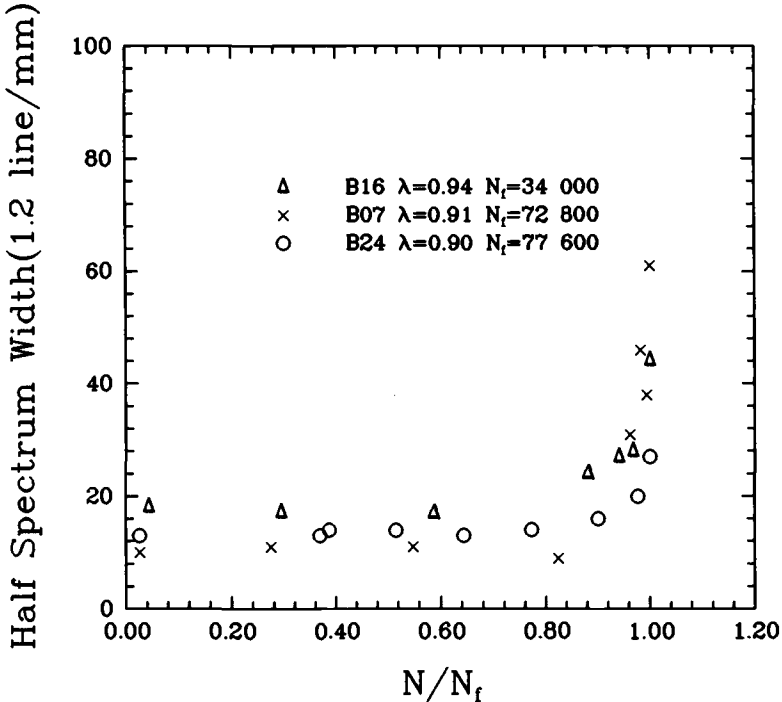


FIG. 5—Half spectrum width versus fatigue life ratio ( $N_i/N_f$ ) for  $0.90 \leq \lambda \leq 0.94$ .

stress is comparatively stable. At the last stage of fatigue life, all the specimens showed quite a drastic change in roughness. Figure 6 also shows that the crack initiation life ratio ( $N_i/N_f$ ) is lower the higher the maximum stress.

*Influence of an Oversized Pin*

The study of failure origins in aircraft structures shows that most flaws originate from fastener holes in the form of corner cracks [12]. In our study, we tested eight specimens with an open hole and nine specimens with a slightly oversized rigid pin impacted into the central hole (average hole diameter = 6.325 mm, and average pin diameter = 6.350 mm) subjected to remote cyclic loading. The relations between the maximum remote stress and failure cycle number, i.e., the conventional S-N curves for the specimens both with and without a pin, are shown in Fig. 7. The fatigue strength of the specimens at  $10^4$  cycles was measured to be 165.5 MPa without the pin and 172.2 MPa with the pin, respectively. The strength of the former is about 4% lower than that of the latter. This is believed partly due to the strain-hardening property of the material, the lack of free surface for the pinned specimens, and the local residual stress caused by the oversized pin [13].

Figure 8 shows the slip bands near the crack tip of a pinned specimen. The repeated cyclic loading roughens the specimen surface randomly, and with the increase of the cumulative strain the valleys between the peaks grow deeper statistically. The deepest valleys may eventually develop into cracks.

The fractured surfaces of the specimens were examined by SEM. Fractography shows that most cracks initiate as corner cracks. As shown in Fig. 9, the fracture surface near the

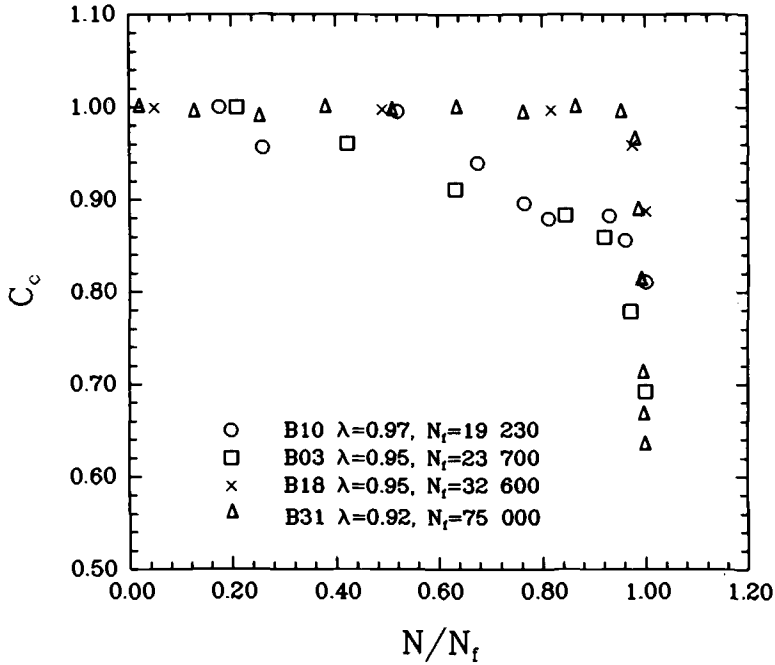


FIG. 6—Cross correlation coefficient versus fatigue life ratio ( $N_i/N_f$ ) for  $0.92 \leq \lambda \leq 0.97$ .

nucleation site is rather coarse, indicating that the crack initiates at a very late stage of the fatigue life. This is supported by the fact that the ratio of crack initiation life to the failure life ( $N_i/N_f$ ) of this specimen reaches 0.94 owing to the relatively lower ratio of the maximum nominal far field stress to the yield stress (i.e.,  $\lambda = 0.9$ ). This kind of crack nucleation has also been observed by Laird [14].

## Conclusions

Fatigue tests on specimens made of A15052-H32 thin plates with a central hole have been performed and evaluated using a laser speckle technique and a high-speed motion analysis system. The surface roughness caused by fatigue damage has been shown to be related quantitatively to the speckle pattern through two parameters, the spectrum half width and the cross correlation coefficient.

The spectrum half width is nearly constant for almost the entire fatigue life. However, a drastic increase takes place at the time of the fatigue crack initiation. The cross correlation coefficient between the speckle pattern of the initial surface and that of the roughened surface is proposed as a new parameter to measure the surface roughness change during the entire fatigue life of the material. The surface roughness change in terms of the cross correlation coefficient is nonlinear with respect to the number of the fatigue cycle ratio  $N_i/N_f$  and depends on the applied maximum stress as well. Both parameters may be used as a criterion to assess fatigue damage in terms of surface roughness change.

The fatigue strength of a specimen with a slightly oversized pin impacted into a hole is slightly higher than that of a specimen with an open hole. This is attributed, in part, to the strain-hardening effect of the material, the lack of free surface, and the residual stress created

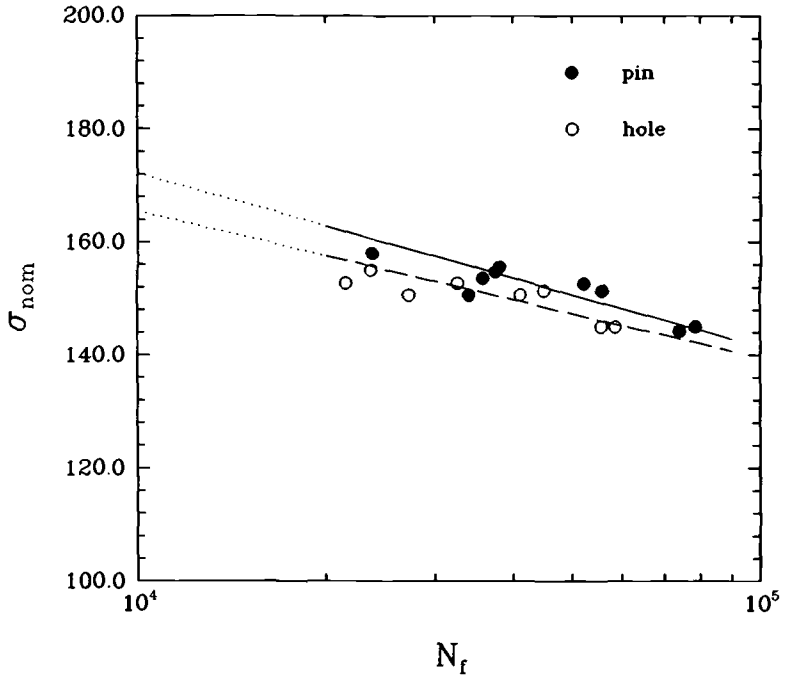


FIG. 7—Variation of remote maximum stress as a function of number of cycles to failure.

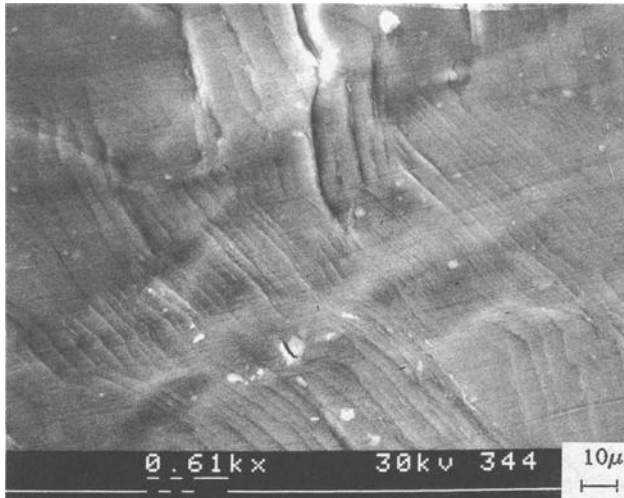


FIG. 8—Slipbands near crack tip of pinned specimen B23 with  $\lambda = 0.98$ .

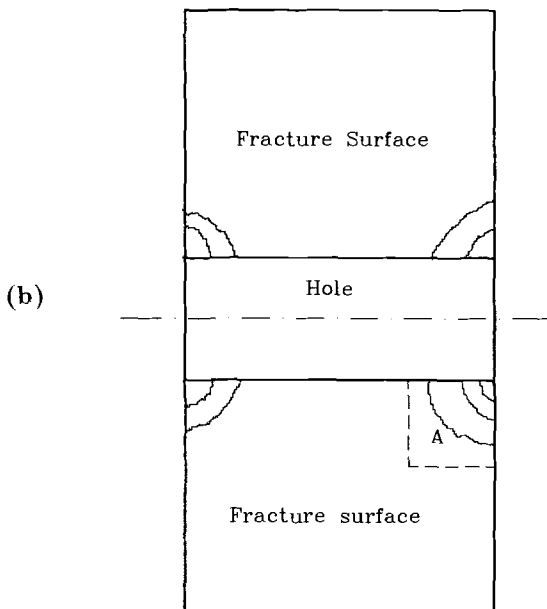
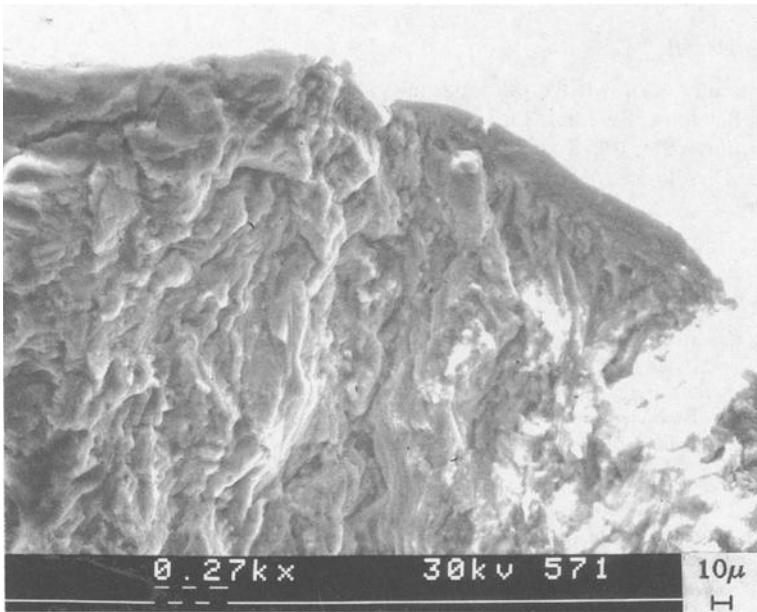


FIG. 9—(a) SEM view of fracture surface near the nucleation site and (b) sketch showing the photographed region as marked by "A" of Specimen B24 with  $\lambda = 0.90$ .

by the oversized pin. Results show that fatigue cracks initiate at the corners of the holes for both pinned and unpinned specimens.

### Acknowledgments

We gratefully acknowledge the financial support of this work provided by the Air Force Office of Scientific Research through the University Research Initiation Program through Grant No. F496209310218 and the encouragement of Dr. Jim C. I. Chang, Director of the Aerospace Directorate.

### References

- [1] May, A. N., "Dislocation Distribution and Prediction of Fatigue Damage," *Nature*, Vol. 185, No. 1, 1960, pp. 303–304.
- [2] Hunsche, A. and Neumann, P., "Crack Nucleation in Persistent Slipbands," *Basic Questions in Fatigue: Volume I, ASTM STP 924*, J. T. Fong and R. J. Fields, Eds., American Society for Testing and Materials, Philadelphia, 1988, pp. 26–38.
- [3] Pangborn, R. N., Weissmann, S., and Kramer, I. R., "Dislocation Distribution and Prediction of Fatigue Damage," *Metallurgical Transactions*, Vol. 12A, No. 1, 1981, pp. 109–120.
- [4] Dai, Y. Z., Kato, A., and Chiang, F. P., "Fatigue Monitoring by Laser Speckle," *International Journal of Fatigue*, Vol. 13, No. 3, 1991, pp. 227–232.
- [5] Shah, R. C., "Stress Intensity Factors for Through and Part-Through Cracks Originating at Fastener Holes," *Mechanics of Crack Growth, ASTM STP 590*, American Society for Testing and Materials, Philadelphia, 1976, pp. 429–459.
- [6] Leis, B. N. and Galliher, R. D., "Growth of Physically Short Corner Cracks at Circular Notches," *Low-cycle Fatigue and Life Prediction, ASTM STP 770*, American Society for Testing and Materials, Philadelphia, 1982, pp. 399–421.
- [7] Huang, W. C., "Theoretical Study of Stress Concentrations at Circular Holes and Inclusions in Strain Hardening Materials," *International Journal of Solids Structures*, Vol. 8, 1972, pp. 149–192.
- [8] Dai, Y. Z. and Chiang, F. P., "Application of Scattering Theory to Plastic Strain Estimation," *Nondestructive Characterization of Materials IV*, C. O. Ruud, J. F. Bussjere, and R. E. Green, Jr., Eds., Plenum Press, New York, 1991, pp. 283–291.
- [9] Rosenfield, A. and Kak, C. A., *Digital Picture Processing*, Academic Press, New York, 1982.
- [10] Chaboche, J. L. "Lifetime Predictions and Cumulative Damage under High-temperature Conditions," *Low-cycle Fatigue and Life Prediction, ASTM STP 770*, American Society for Testing and Materials, Philadelphia, 1982, pp. 81–104.
- [11] Wang, J., "A Continuum Damage Mechanics Model for Low-Cycle Fatigue Failure of Metals," *Engineering Fracture Mechanics*, Vol. 41, No. 3, 1992, pp. 437–441.
- [12] Fujimoto, W. J. and Staff, C. R., "A Multidimensional-Crack-Growth Prediction Methodology for Flaws Originating at Fastener Holes," *Experimental Mechanics*, Vol. 22, 1982, pp. 139–146.
- [13] Broek, D., *The Practical Use of Fracture Mechanics*, Kluwer Academic Publishers, Boston, 1988.
- [14] Laird, C., "The General Cyclic Stress-Strain Response of Aluminum Alloys," *Cyclic Stress-Strain and Plastic Deformation Aspects of Fatigue Crack Growth, ASTM STP 637*, American Society for Testing and Materials, Philadelphia, 1977, pp. 3–35.

Julie A. Henkener,<sup>1</sup> Attibele R. Shamala,<sup>1</sup> Paul L. Carper,<sup>1</sup> Royce G. Forman,<sup>2</sup> and Charles L. Salkowski<sup>2</sup>

## Development of Fracture Control Methodology for Threaded Fasteners in the Space Program

---

**REFERENCE:** Henkener, J. A., Shamala, A. R., Carper, P. L., Forman, R. G., and Salkowski, C. L., "Development of Fracture Control Methodology for Threaded Fasteners in the Space Program," *Structural Integrity of Fasteners, ASTM STP 1236*, P. M. Toor, Ed., American Society for Testing and Materials, Philadelphia, 1995, pp. 155–165.

**ABSTRACT:** High-strength threaded fasteners are used in many critical applications in aerospace hardware. This paper outlines a fracture control methodology that can be applied to prevent their structural failure due to the presence and/or propagation of crack-like defects. In cases where the failure of a single fastener would result in a catastrophic failure, fracture control is usually implemented either by nondestructive inspection followed by a fracture mechanics analysis of life or by a proof test approach. Special nondestructive techniques are usually required for flaw detection at thread roots. This paper discusses the procedures necessary for determining probability of detection values for threaded fasteners, including methods of fabricating threaded fatigue crack specimens and the statistical methods used to reduce reliability data.

**KEYWORDS:** crack propagation, eddy current inspection, fatigue crack growth, fatigue (materials), fracture control, fracture mechanics, nondestructive evaluation, probability of detection, threaded fasteners

High-strength fasteners are used in many critical applications in aerospace hardware. However, throughout the history of the United States space program, no known fastener failures have occurred as a result of the propagation of preexisting, crack-like defects. In fact, because of the tight quality assurance required for space flight, most fastener problems are discovered prior to launch, resulting in very few fastener failures in service. For example, a survey of approximately 80 problem reports issued during the Skylab program indicated that fastener failures during acceptance or qualification tests were largely a result of inadequate design, incorrect preload, improper assembly, or manufacturing and handling damage [1]. While none of these failures were attributed to fatigue, this does not mean that the potential for fastener failure due to crack propagation can be ignored. Fasteners in critical applications that experience a complicated load history require careful analysis, especially if the failure of a single fastener could result in a catastrophic failure.

During the Space Shuttle development, a fracture control approach that included nondestructive evaluation (NDE) and safe-life analysis was not imposed on fasteners. Control was achieved by relying on highly qualified fastener experts working for the prime contractors

---

<sup>1</sup> Lockheed Engineering & Sciences Co., 2400 NASA Rd. 1, Mail Code C62, Houston, TX 77058.

<sup>2</sup> National Aeronautics and Space Administration, Lyndon B. Johnson Space Center, Mail Code EM2, Houston, TX 77058.

and on their ability to control the purchasing of fasteners to meet specification requirements that detailed necessary material selection, traceability, and lot testing. In contrast, because of their large number and unknown fastener expertise, Space Shuttle payload developers are required to demonstrate the structural integrity of fasteners by compliance with fracture control requirements that are documented in Ref 2. Fracture control requirements for Space Station hardware [3] that reflect recent modifications to NASA fracture control methodology and conditions specific to Space Station have also been established.

The primary objectives of this paper are to outline the development of a methodology for applying fracture control to threaded fasteners in current and future manned spaceflight programs and to discuss the development of NDE standards to inspect fasteners for crack-like defects.

### Fracture Control Methodology

The development of NASA fracture control methodology and requirements is a currently ongoing process, especially for fasteners. The NASA Fracture Control Methodology Panel, which includes a member from each NASA center as well as representatives from the international partners, is responsible for establishing the fracture control requirements for space hardware and coordinating development work in fracture control methodology. Fracture control is used to prevent structural failure due to the presence and/or propagation of flaws or crack-like defects. The methodology can be applied to a variety of different types of hardware, including rotating equipment, pressure vessels, batteries, composite structures, and fasteners. Similar to structural hardware, fasteners are categorized as either nonfracture critical or fracture critical, according to the logic diagram shown in Fig. 1.

### Nonfracture Critical Fasteners

Fasteners can be categorized as nonfracture critical for manned spaceflight structures if their failure does not result in a catastrophic failure and if they meet the nonhazardous release, containment, fail-safe, or low-risk criteria. Nonfracture critical fasteners should be processed according to generic quality standards for aerospace hardware. Since nuts are mainly loaded in compression, they are usually classified as nonfracture critical.

#### *Nonhazardous Released Fasteners*

Structural failures resulting in the release of parts, including fasteners, are considered to be safety hazards because of possible impact damage to critical equipment during the high  $g$  launch acceleration. In addition, the failure of a fastener resulting in a high velocity or energy release could present a safety hazard to flight personnel during on-orbit mission operations. A fastener may be classified as a *nonhazardous released part* if the total mass that would be released is less than 113.5 g. If a fastener is made from a material that has a relatively low fracture toughness ( $K_{Ic}/\sigma_{ys} < 1.66 \sqrt{\text{mm}}$ ) and is preloaded in tension, a high release velocity may result from its failure. For this reason, the mass of the fastener released must be less than 13.6 g to be classified as a nonhazardous released part. This requirement encourages designers to select materials such as Inconel 718, A286, and MP35N instead of ultra-high-strength steel or titanium for fastener applications.

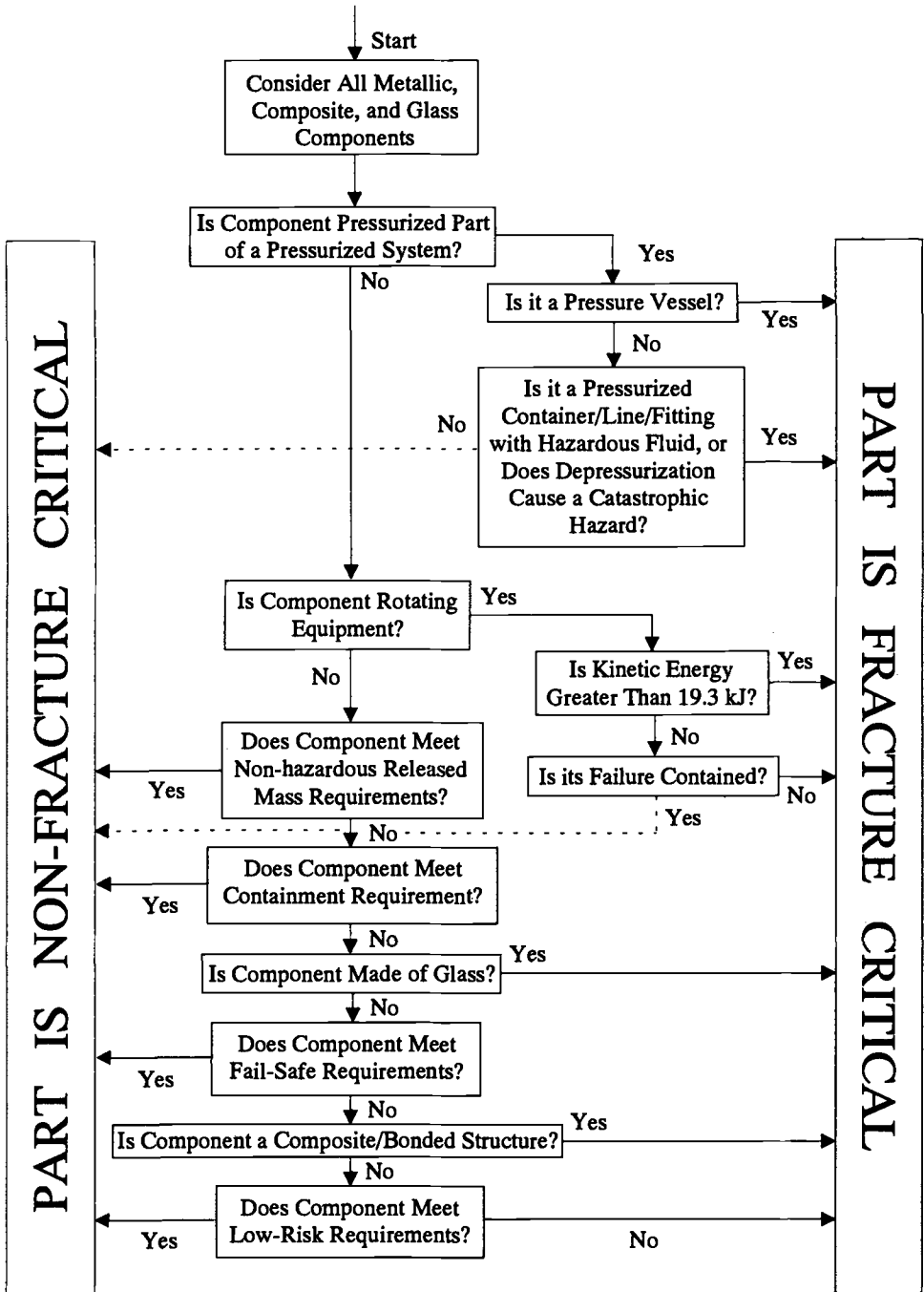


FIG. 1—Logic diagram for the classification of fracture critical parts.

### *Contained Fasteners*

A fastener can be categorized as *contained* if it can be demonstrated that all fragments created by its failure would be contained within the payload or a structural subsystem. Containment can be demonstrated by analysis, testing, or engineering judgment.

### *Fail-Safe Fasteners*

Fasteners are considered to be *fail-safe* when it can be shown by test or analysis that, due to structural redundancy, the structure remaining after a single failure can withstand the redistributed limit loads. In addition, any fragments that would be released from such a failure must meet the nonhazardous release or containment requirements outlined above.

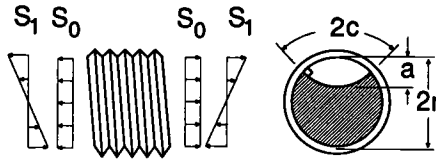
### *Low-Risk Fasteners*

In the past, if a component did not meet one of the above criteria, it was automatically categorized as a fracture critical part, even if the possibility of its failure causing a catastrophic failure was rather remote. The concept of a *low-risk fracture part* has been introduced into NASA fracture control methodology to alleviate this problem and to focus efforts on "truly" fracture critical parts. This approach has significantly reduced the number of parts requiring the costly process of NDE or proof test, safe-life analysis, tracking, and documentation, which is necessary for all fracture critical parts. The rationale for acceptance of a component as a low-risk fracture part is based on showing that the possibility of failure due to the propagation of a crack-like flaw is extremely remote. This is achieved by demonstrating both a remote possibility of the presence of a significant initial crack-like defect and a remote possibility of significant fatigue crack growth.

A remote possibility of a significant crack-like defect is shown by using a well-characterized metal that is not sensitive to stress corrosion cracking and by ensuring that the fastener has not been fabricated using processes that have a recognized risk of inducing crack-like defects. In addition, a low-risk fastener must be manufactured using a relatively tough material ( $K_{Ic}/\sigma_{ys} > 1.66 \sqrt{\text{mm}}$ ) and produced in accordance with applicable military specifications and standards or their equivalent.

To demonstrate a remote possibility of significant crack growth, the fastener must not be subjected to significant cyclic loading. One service mission would normally not be considered a significant exposure to fatigue loading. For more than one service mission, the fastener must possess acceptable resistance to crack growth of potential initial defects caused by thread-forming operations, assembly, and handling. This may be shown from a durability analysis, whereby it is demonstrated that an assumed initial thumbnail crack with a surface length ( $2c$ ) of 1.02 mm, a depth ( $a$ ) of 0.5 mm, and the thumbnail geometry shown in Fig. 2 does not grow to failure in less than four times the number of desired service missions.

It is well known that rolled threads are more resistant than machined threads to the initiation and propagation of fatigue cracks [4]. For this reason, external threads on low-risk fasteners loaded in tension must be rolled, and the threads may not be reworked or remachined. Low-risk fasteners are also required to meet military or aerospace grade specifications and must be traceable to lot testing by the manufacturer. In applications where the failure of a single fastener would directly result in a catastrophic failure, the total tensile stresses in the fastener at limit load must be less than 30% of the material's ultimate tensile strength. Here, limit load is defined to be the maximum expected service load the fastener will experience. This limit load must be computed based on the expected preload, the loads externally applied to the joint, and other factors specific to the joint configuration.

ROLLED THREAD

$2r$  = minor diameter

$2c$  = surface crack length

$a$  = crack depth

$S_0, S_1$  based on minor diameter

FIG. 2—Crack geometry for rolled threads.

### Fracture Critical Fasteners

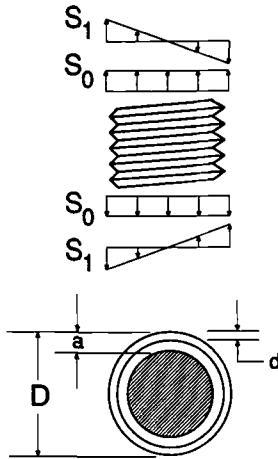
Fracture control on fasteners that are used in fracture critical applications and that cannot be classified as low-risk fasteners is usually accomplished by nondestructive inspection, followed by a fracture mechanics evaluation of life. The analysis method used requires (a) accurate stress intensity factor solutions; (b) appropriate fracture mechanics data, including  $da/dN - \Delta K$  and  $K_{Ic}$  (fracture toughness from part-through cracked specimens) or  $K_{Ic}$  (plane strain fracture toughness) data; (c) a good failure/collapse criterion; (d) a suitable fatigue spectrum; and (e) realistic crack growth models incorporated into a computer code that can be used to calculate life. The safe-life analysis must demonstrate that an initial flaw size screened by NDE and assumed to exist in the most critical location of the component will not propagate to failure within four times the number of desired service missions. One service mission is defined as one application of the Space Shuttle launch and landing fatigue spectrum [5] in combination with any fatigue loading it might see during orbit. Fracture critical shear pins or bolts that primarily carry shear loads require NDE and analysis in the shank area only since it is the most critical location. Tension-loaded fracture critical fasteners usually require NDE overall, but analysis only in the threaded regions.

The crack cases for rolled and machined threaded connections that have been incorporated into the NASA/FLAGRO computer program [6] are shown in Figs. 2 and 3, respectively. A fully circumferential initial flaw depth of 0.13 mm plus the thread depth is assumed for fasteners with machined threads. This initial crack depth is based on the maximum defect size that would be expected due to machining operations. For rolled threads that have been inspected using the dye penetrate technique, a thumbnail crack with a surface length of 1.9 mm is currently proposed.

The stress intensity factor solution for a surface flaw in the rolled thread configuration has been reported in Ref 7. The stress intensity factor solution for the machined thread crack case combines the tension solution proposed by Tada et al. [8] with the bending solution reported by Benthem et. al. [9]. Both the rolled and machined thread solutions assume that the stress is applied remotely and do not account for load transfer through the threads.

An alternate method of implementing fracture control is to perform an acceptance proof test of fracture critical fasteners. This approach involves applying a proof test to the fastener and demonstrating experimentally that an initial flaw surviving the test will not grow to failure within four times the number of desired missions. A test program was conducted at

**MACHINED THREAD**



$D$  = major diameter  
 $d$  = thread depth  
 $a = d + \text{crack depth}$   
 $S_0, S_1$  based on major diameter

FIG. 3—Crack geometry for machined threads.

the Jet Propulsion Laboratory [10] to determine the fatigue life of A286 threaded fasteners that just survive a proof test at 75% of the minimum ultimate strength. In this way, they were able to ensure the safety of fasteners with a specific proof factor where the service loading was between 40 and 60% of the ultimate strength. However, these data are only applicable for a very specific combination of fastener size, material, and loading conditions. A similarly thorough test program would need to be undertaken to qualify each specific fastener application.

Along with proof test or analysis, many hardware-related factors directly affect the successful application of threaded fasteners. It is very important for the bolted joint to be properly designed, and the purchase and installation of fasteners should be carefully monitored by a good quality assurance program. In highly loaded tension joints, special attention must be directed toward achieving the targeted preload. Also, because titanium fasteners have a relatively low fracture toughness and are therefore more susceptible to the formation of cracks due to improper rolling, it is recommended that they not be used in fracture critical tension-loaded applications [11].

**Nondestructive Evaluation of Threaded Fasteners**

The reliable determination of initial flaw size by nondestructive evaluation is one of the most important aspects of fracture mechanics life assessments. Until recently, reliability data for complex geometries such as curved surfaces, bolt holes, and threads have not been widely

available. For this reason, NDE detection limits for such geometries were derived from data accumulated for flaws in flat panels. Also, research in the application of nondestructive inspection to bolted joints using ultrasonic, electromagnetic-acoustic, or eddy current inspection techniques [12–17] has largely focused on the evaluation of inspection system that can detect flaws at bolt holes. Relatively little research has been done regarding the application of NDE techniques for flaw detection in the thread root or shank regions of fasteners.

### *Statistical Analysis of NDE Data*

The smallest flaw size detectable by a given NDE technique is determined by statistical analysis of experimental flaw detection data. At the Johnson Space Center (JSC), improvements in statistical methods for analyzing such data has been an ongoing process aimed at providing more reliable fracture control of space hardware. Initially, detectability curves for the dye penetrant test method were produced by analyzing the Space Shuttle Orbiter inspection data for flat panels using a sorted group ascent technique combined with a Poisson approximation to the binomial distribution. The binomial approximation suggests that a probability of detection (POD) capability of 90% with a 95% statistical confidence level will be obtained if the inspector can correctly detect a specific number of defects in a set of identical flaws, such as 29 out of 29, 46 out of 47, or 61 out of 63. However, this method was altered so that the smallest defect in the largest set of detected flaws from the global set (sorted in descending order) which also met the binomial sample requirements was identified as the inspector's 90/95 POD number. More recently, a method for statistical analysis of probability of detection data was developed at the University of Dayton Research Institute [18]. This research demonstrated that an analysis based on a log-normal maximum likelihood model could provide more information than previous techniques. Therefore this maximum likelihood technique is being used to demonstrate POD capability both for Space Shuttle payloads and Space Station NDE work.

### *Fabrication of Threaded Fastener POD Specimens*

In order to collect reliability data for a particular geometry, a large number of standard specimens containing identical flaws must be manufactured. However, developing a procedure for generating reproducible fatigue cracks in fastener thread roots is difficult because of the stress concentration caused by the threads themselves. Several methods for producing realistic threaded NDE standards were investigated. One attempt involved introducing a starter notch in a threaded specimen, which was then fatigue cracked in bending. However, this method failed to produce controlled crack growth only in the notched location. An attempt was also made to fatigue crack a partially threaded specimen in bending, using special fixtures to concentrate the stress in a specified region. After a crack was grown, the threads would be further machined to remove evidence of the starter notch. Varying degrees of success in producing a single crack per specimen were achieved, and producing cracks of a repeatable size presented a problem.

The thread-root-rib method, depicted in Fig. 4, provided the most successful means of producing a repeatable fatigue crack of a specified size in a threaded specimen. Each specimen was notched to a depth approximately two thirds of the distance between the major and minor diameters using a ram electron discharge machine (EDM). The EDM electrode, which is custom machined from brass shim stock to match the curvature of the raw specimen stock, contacts the specimen at the angle of the anticipated thread pitch. The notch in the electrode leaves a rib that is easily precracked in bending. The specimens are then cycled

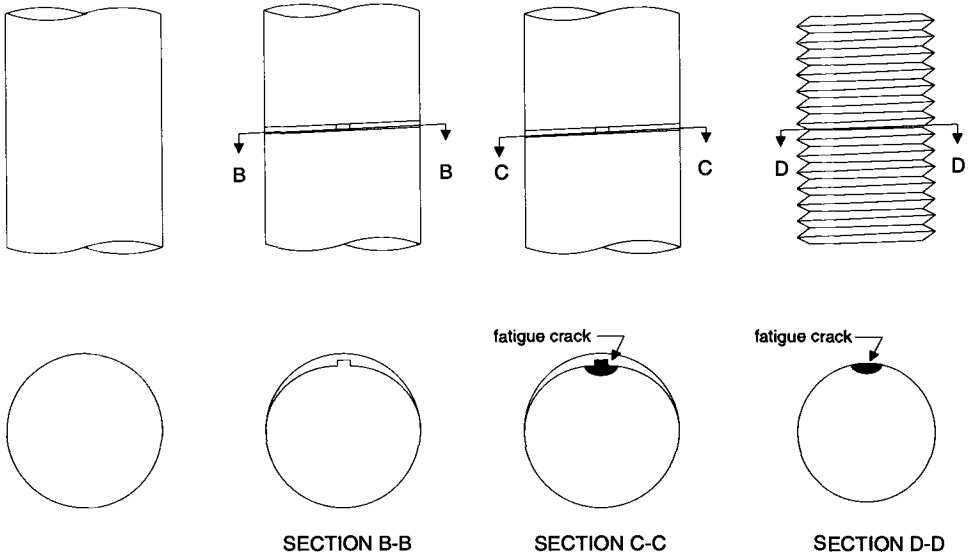


FIG. 4—Procedure for fabricating threaded NDE standards using the thread-root-rib method.

in tension to produce a crack with a more realistic aspect ratio. Since the base of the rib is near the minor diameter, most of the crack depth can be maintained after the final threading operation.

*Inspecting the Fastener Threads*

After manufacturing the fatigue crack standards, an appropriate NDE inspection method must be chosen to detect the flaws. However, the constraints imposed by the fastener thread geometry present a significant challenge to conventional NDE techniques. The inspection technique most commonly applied to fracture critical structural components is the dye penetrant method. However, this procedure cannot be strictly applied to fastener threads that have tight tolerances since the etching required to ensure the method's sensitivity is not permitted. A dye penetrant test can be performed without etching, but the detectable flaw size screened is not well defined. A second method, magnetic particle testing, is only applicable to fasteners manufactured from ferromagnetic materials and becomes increasingly difficult to use on small fasteners with very fine threads. Ultrasonic inspection methods are also very difficult to apply to fastener threads at the desired sensitivity levels because the sound waves interact with the threads, producing an unacceptable noise level. One recently proposed method for thread inspection involves the use of an a-c potential drop technique [19] to measure the potential difference between successive thread crowns. Also, researchers at the European Space Agency [20] have evaluated the application of the eddy current technique to inspect the thread roots of Ti-6Al-4V, Inconel 718, and A286 fasteners.

At JSC, a development program is currently in progress to apply the eddy current method for flaw detection at thread roots. Ten 1/2-13 threaded specimens were machined from 2024-T4 aluminum rod, which was selected for its machinability and suitability for eddy current testing. The specimens were fatigue cracked using the thread-root-rib method and inspected using the eddy current technique. Photographs of the semiautomated eddy current system

are shown in Figs. 5 and 6. A motorized scanner is used to turn the threaded specimen through a fixed holder that supports a custom-wound 0.25 by 1.52-mm eddy current coil. Preliminary results from these specimens indicate favorable repeatability and reliability for finding flaws with surface lengths in the range of 1.3 to 3.2 mm. Future work will include investigation of high-strength fastener materials such as MP35N and A286 and cracked specimens with varying diameters and thread sizes. In addition, changes will be made to the eddy current system in an effort to improve the method's sensitivity.

### Summary

A fracture control methodology that can be applied to prevent the failure of threaded fasteners due to the presence and/or propagation of crack-like defects has been presented. This methodology involves classification of the fastener as either fracture critical or non-fracture critical. Since the failure of a fracture critical fastener would result in a catastrophic failure, fracture control is usually implemented by nondestructive inspection followed by a fracture mechanics evaluation of life. However, the application of NDE techniques to fastener threads is difficult to achieve at desired detection levels. For this reason, development work in the NDE laboratory at JSC is focusing on the fabrication of realistic NDE standards for

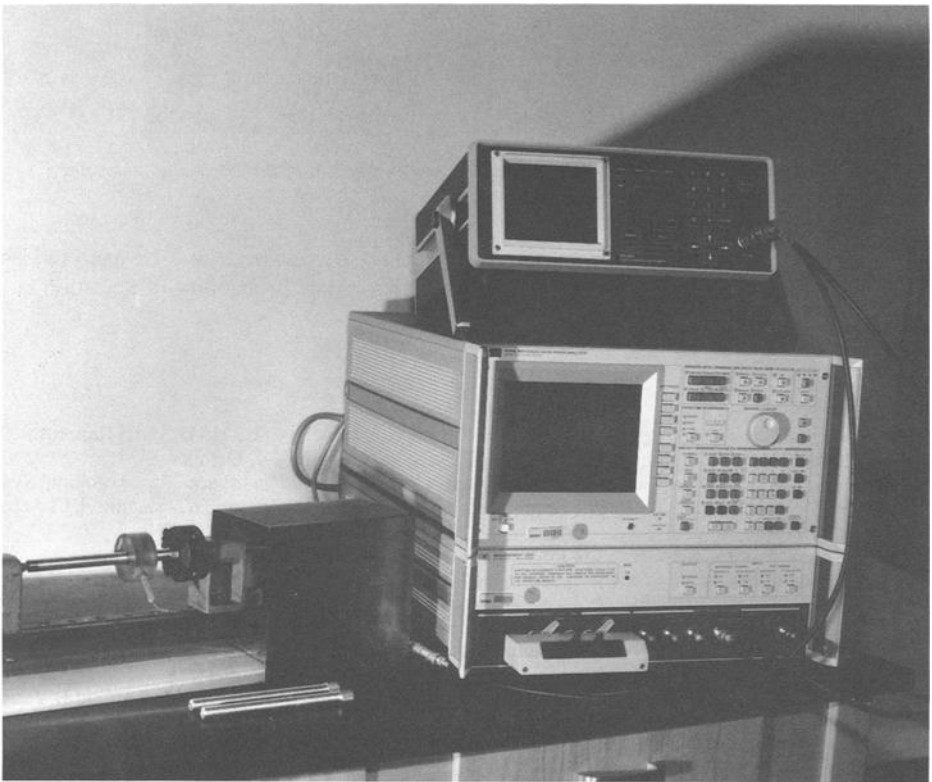


FIG. 5—Overall photograph of semiautomated eddy current inspection system.



FIG. 6—Close-up photograph of eddy current inspection of threaded aluminum rod.

threaded fasteners. Reliability data obtained from these specimens will be analyzed using maximum likelihood techniques to establish the appropriate probability of detection curves for threaded fasteners.

**References**

- [1] "Investigation of Threaded Fastener Structural Integrity," NASA-CR-151541, Final Report for Contract NAS9-15140, Southwest Research Institute, San Antonio, TX, October 1977.
- [2] "Fracture Control Requirements for Payloads Using the National Space Transportation System (NSTS)," NHB 8071.1, National Aeronautics and Space Administration, Washington, DC, September 1988.
- [3] "Fracture Control Requirements for Space Station," SSP 30558, National Aeronautics and Space Administration, Space Station Freedom Program Office, Reston, VA, August 1991.
- [4] Fuchs, H. O. and Stephens, R. I., *Metal Fatigue in Engineering*, John Wiley & Sons, New York, NY, 1980, p. 127.
- [5] Brodeur, S. J. and Basci, M. I., "Fracture Mechanics Loading Spectra for STS Payloads," AIAA-83-2655-CP, Goddard Space Flight Center, Greenbelt, MD, 1983.
- [6] "Fatigue Crack Growth Computer Program 'NASA/FLAGRO'," JSC-22267A, Lyndon B. Johnson Space Center, Houston, TX, May 1994.
- [7] Forman, R. G. and Shivakumar, V., "Growth Behavior of Surface Cracks in the Circumferential Plane of Solid and Hollow Cylinders," *Fracture Mechanics: Seventeenth Volume, ASTM STP 905*, J. H. Underwood, R. Chait, C. W. Smith, D. P. Wilhelm, W. A. Andrews, and J. C. Newman, Eds., American Society for Testing and Materials, Philadelphia, 1986, pp. 789-805.

- [8] Tada, H., Paris, P. C., and Irwin, G. R., *The Stress Analysis of Cracks Handbook*, Del Research Corporation, Hellertown, PA, 1973, pp. 27.1–27.2.
- [9] Benthem, J. P. and Koiter, W. T., “Asymptotic Approximations to Crack Problems,” *Methods of Analysis and Solutions of Crack Problems*, G. C. Sih, Ed., Nordhoff International Publishing, Groningen, The Netherlands, 1973, pp. 131–178.
- [10] Hsieh, C., Hendrickson, J., and Bamford, R., “Development of Methodology for Qualifying Safety Critical A286 Threaded Fasteners,” *Journal of Testing and Evaluation*, Vol. 19, March 1991, pp. 135–148.
- [11] “Threaded Fasteners, 6Al-4V Titanium Alloy, Usage Criteria for Spacecraft Applications,” MSFC-STD-557, George C. Marshall Space Flight Center, Huntsville, AL, September 1979.
- [12] Weinhold, J. H., “Autoscan-I Ultrasonic Fatigue-Crack Detector for Military Aircraft Fastener Sites,” *Proceedings*, Twelfth Symposium on Nondestructive Evaluation, Southwest Research Institute, San Antonio, TX, 1979, pp. 292–298.
- [13] Raney, J. M., “Walking-Gate Spatial Signal Averaging—Signal Processing for Fatigue Ultrasonic Inspection System,” *Proceedings*, Twelfth Symposium on Nondestructive Evaluation, Southwest Research Institute, San Antonio, TX, 1979.
- [14] Martin, J. F., Hodgetts, P. J., and Thompson, R. B., “Investigation of EMAT Base System for the Detection of Bolt Hole Type Cracks,” AFWAL-TR-80-4081, Rockwell International Corp., Thousand Oaks, CA, 1980.
- [15] Cooper, T. D. and Forney, D. M., “Detection of Cracks Under Installed Fasteners in Aircraft Structures,” *Materials Evaluation*, Vol. 41, September 1983, pp. 1178–1185.
- [16] Bell, D. L. and Mih, D. T., “Manufacturing Technology for Advanced Second Layer NDE System Producibility,” AFWAL-TR-85-4095, Systems Research Labs, Inc., Dayton, OH, 1985.
- [17] Fahr, A., Chapman, C. E., Pelletier, A., and Hay, D. R., “Inspection of Aircraft Engine Components Using Automated Eddy Current and Pattern Recognition Techniques,” NRC-LTR-ST-1834, National Research Council of Canada, Ottawa, Ontario, 1991.
- [18] Berens, A. P., “NDE Reliability Data Analysis,” *Nondestructive Evaluation and Quality Control*, Metals Handbook, 9th ed., Vol. 17, ASM International, Metals Park, OH, 1989, pp. 689–701.
- [19] Collins, R. and Lugg, M. S., “Use of A.C. Field Measurements for Non-Destructive Testing,” *Fatigue Crack Measurement: Techniques and Applications*, K. J. Marsh, R. A. Smith, and R. O. Ritchie, Eds., Engineering Materials Advisory Services, Ltd., West Midlands, U.K., 1991, pp. 39–67.
- [20] Müller-Wiesner, D., “NDI of Threaded Fasteners,” presentation at the ESA-NASA Fracture Control Meeting, ESTEC, Noordwijk, The Netherlands, April 1991.

# The Effect of a Tensile Load on the Ultimate Shear Capacity of a Fastener Shank

---

**REFERENCE:** Olson, S. M., "The Effect of a Tensile Load on the Ultimate Shear Capacity of a Fastener Shank," *Structural Integrity of Fasteners, ASTM STP 1236*, P. M. Toor, Ed., American Society for Testing and Materials, Philadelphia, 1995, pp. 166–174.

**ABSTRACT:** When a fastener is simultaneously subjected to a tensile and transverse shear load, it is unclear from the literature whether the tensile load results in a reduced allowable ultimate shear load and, if so, by how much. The relationship was investigated experimentally using test samples of 6Al-4V titanium and 17-4PH stainless steel. The specimens were loaded in tension and then pulled to failure in three-point shear. The tensile load was varied from 0% of the material's ultimate strength (pure shear failure) to 100% (pure tensile failure). In preliminary tests, the tensile load would drop as the specimen was tested due to lengthening of the specimen as a result of the shearing process. This would seem to indicate that in most practical applications, the tensile load will be greatly reduced as the fastener deforms in shear. The final test fixture kept a nearly constant tensile load on the specimens as they were sheared. Analysis of the resulting data revealed that a squared stress ratio interaction curve provided satisfactory estimates of the ultimate shear strength of a fastener shank subjected to a constant tensile load.

**KEYWORDS:** combined loading, stress ratio, shear strength, shear loading, fastener strength

The most commonly used method for determining the effect of combined loading on the ultimate strength of a material is the stress ratio interaction curve, developed by Shanley [1]. In this method, the various stress conditions are represented by stress ratios of the form:

$$R = f/F \quad (1)$$

where  $f$  is the applied stress, and  $F$  is the ultimate stress for the pure loading condition. Here "pure" denotes a single state of stress, for example, a pure shear or tensile load. The general condition for failure may then be written:

$$AR_1^x + BR_2^y + CR_3^z = 1 \quad (2)$$

where  $A$ ,  $B$ ,  $C$ ,  $x$ ,  $y$ , and  $z$  define the general relationships between the stress ratios.

Prior experimentation has determined these coefficients for a variety of common fasteners (see, for instance, Wallaert and Fisher [2]). However, because of the wide variety of fasteners, sufficient data are generally not available to the designer. As a result, many designers use untested interaction curves. One of the most common for the case of a combined tension and shear load on a fastener is the squared interaction curve given as follows:

---

<sup>1</sup> SVG Lithography, 77 Dunbury Rd., Mail Stop 416, Wilton, CN 06897.

$$\left(\frac{\sigma_s}{\sigma_{sult}}\right)^2 + \left(\frac{\sigma_t}{\sigma_{tult}}\right)^2 = 1 \tag{3}$$

where:

- $\sigma_s$  = engineering shear stress at failure,
- $\sigma_{sult}$  = ultimate shear stress of the material,
- $\sigma_t$  = engineering tensile stress at failure, and
- $\sigma_{tult}$  = ultimate tensile stress of the material.

This study attempts to measure the effectiveness of Eq 3 in determining the ultimate shear strength of a fastener in its shank for the materials titanium (6AL-4V) and steel (17-PH H1100). These materials were selected as the test materials because their tensile yield strengths were within 90% of their ultimate strengths. This was necessary because data points were desired at close to 90% of the ultimate strength. The engineering properties of each material are as follows:

	17-4PH Steel	Titanium (6AL-4V)
Young's modulus <sup>a</sup> (GPa):	196	110
Tensile yield <sup>a</sup> (MPa):	960	1000
Tensile ultimate (MPa):	1068	1102
Shear ultimate (MPa):	681	667

<sup>a</sup> Denotes a published value not determined in this study.

It should be noted that the condition of constant tensile load proved very difficult to obtain. Preliminary experiments indicated that the tensile load would be greatly reduced as the fastener deformed in shear. Only the elaborate design of the test fixture allowed the tensile load to be maintained.

### Experimental Procedure

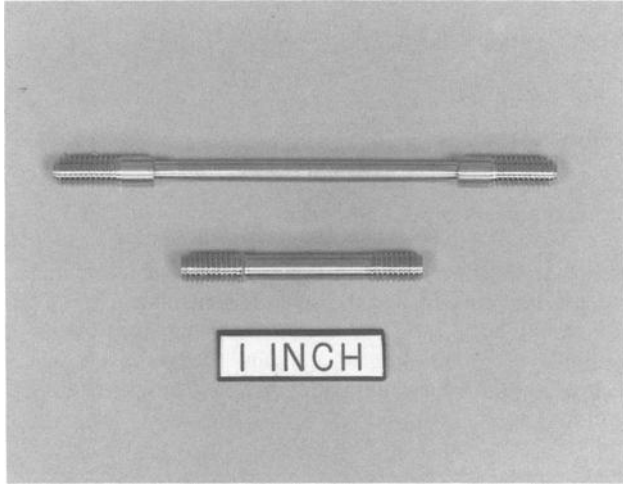
#### *Pure Tension Test Apparatus*

A typical titanium tension specimen is shown at the top of Fig. 1. Each specimen was approximately 7.62 cm long and threaded on each side with No. 10-32 threads. The inner test section was reduced to a diameter of 3.175 mm. Threaded fixtures, which attached to a tension testing machine, were used to pull the specimens to failure in tension.

The steel specimens were identical with one exception: each had an unplanned transverse crack along its length. The crack was approximately 0.1 mm deep at the outset of each test and deepened to approximately 1 mm by the end of the test. These cracks were most likely the result of a manufacturing error in the raw stock. The effect of these cracks on the tensile load-carrying capacity of the fastener is believed to have been small because the cracks were parallel to the axis of the load. The fact that the tensile ultimate stress obtained for the material was in good agreement with the published value seems to confirm this assertion.

#### *Pure Shear and Combined Load Test Apparatus*

A typical titanium specimen used in the pure shear and combined load tests is shown in the lower part of Fig. 1. The steel specimens were identical except for the transverse crack, which is discussed below. The overall length was approximately 3.81 cm, and each side was

FIG. 1—*Specimens.*

threaded with No. 10-32 threads. The center test section was reduced to a diameter of 3.97 mm. This was necessary to ensure that the specimens would not yield in the threads due to the high tensile loads applied during the experiment.

The steel samples each had an unplanned transverse crack along their length that was approximately 0.1 mm deep. In order to minimize the effect of this crack on the data, it was aligned so that it did not carry any shear load during the tests. This method seems to have been effective because experimental values for the shear ultimate stress of the material were in good agreement with the published value.

The fixture used to apply the shear load to the specimens is shown in Fig. 2. It attaches to the tensile testing machine and generates a three-point shear load on the specimens. Its keyhole shape allows the larger threaded section of the specimen to fit through. The smaller part of the keyhole then clamps down on the test section and applies the load.

The apparatus used to apply the tensile load is shown in Fig. 3. It is positioned in the lower part of the shear fixture as it would be during an actual test. Prior to testing, the tensile load-generating spring-plate assembly is compressed to the desired load using the tension testing machine. Then, the bolts on each end of the threaded rods that run through the center of the springs are tightened. This allows the load to be maintained while the spring-plate assembly is positioned around the shear fixture. Next, the device is suspended around the shear fixture in the orientation shown in Fig. 4. Then, the nuts on the tension rods are tightened to transfer the load from the springs to the specimen. The tension rods are torsionally restrained during the tightening to ensure that no torque is applied to the specimen. The tensile force on the specimen is measured with two load cells, as follows:

The load cells shown in Fig. 4 are each composed of a single aluminum cylinder with two strain gages bonded on opposite sides to measure axial strain. The strain gages are connected on opposite legs of a Wheatstone bridge to eliminate the effects of bending. The signal from the Wheatstone bridge was conditioned to an easily measurable voltage with a Vishay strain gage amplifier. The load cells were calibrated in the tension testing machine after every five combined load tests.

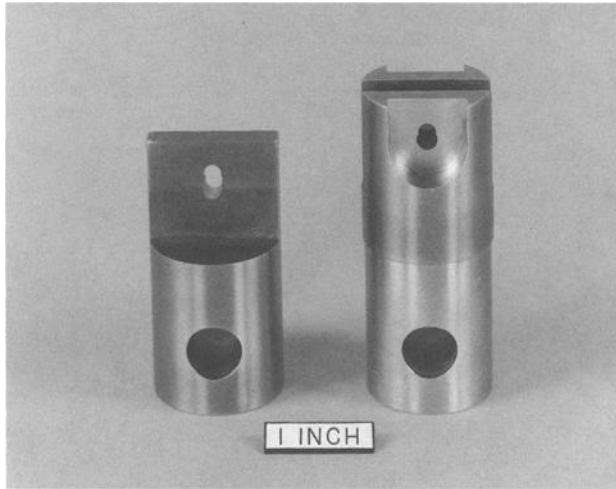


FIG. 2—*Shear fixture.*

The system of pulleys and weights was necessary to balance the weight of the fixture and prevent large bending moments on the specimen. Friction in the system was minimized by using lubricated, TFE-fluorocarbon pulley shafts. The result was an effective weight for the system of 0.5 N, meaning a force of 0.5 N was required to overcome the static friction in the pulleys and cause the fixture to move.

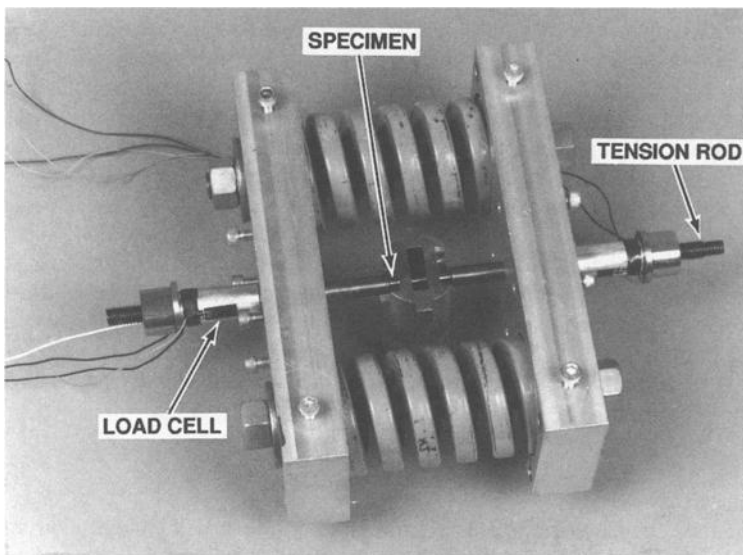


FIG. 3—*Combined load fixture.*

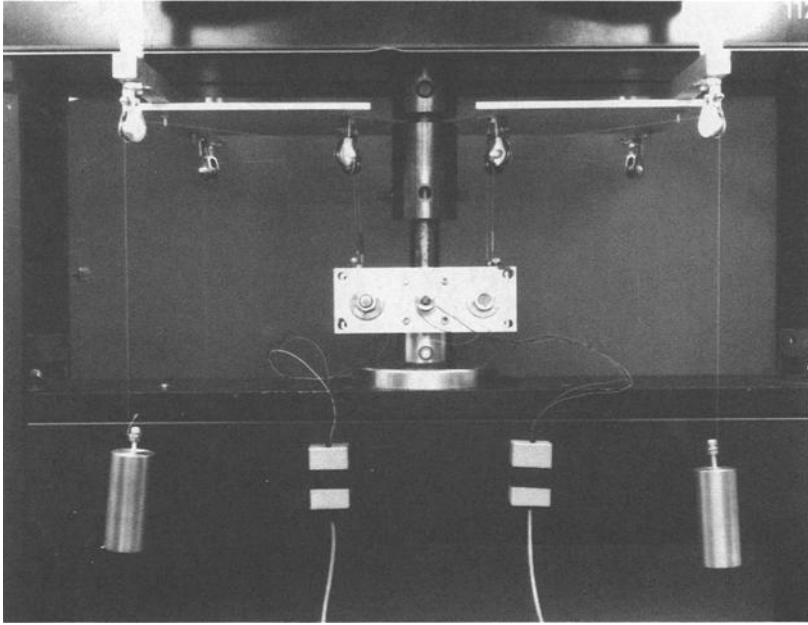


FIG. 4—Testing apparatus orientation.

### Preliminary Experiments

The fixture shown in Fig. 5 was used prior to the development of the one mentioned in the last subsection. It is discussed here not only because it yielded valuable data, but also to give the reader some idea of the evolution of the project.

The preliminary version is very similar to the current fixture except for the method of applying the tensile load. In the preliminary fixture, the tensile load was applied by tightening the nut while torsionally restraining the tension rod. The aluminum load cell then went into compression as the specimen and tension rod went into tension.

This fixture was replaced because it failed to maintain a constant tensile load on the specimen, the stated goal of the project. In testing using this fixture, it was found that the tensile load would drop by as much as 40% as the specimen sheared. The reason behind this behavior was the high effective spring rate of the system, which would cause the load to drop dramatically as the specimen lengthened during the shearing process. For this reason a new fixture was developed using two shorter load cells and adding two comparably low-spring-rate coil springs. This reduced the effective spring rate of the system by a factor of approximately 250. Thus, when the specimen lengthened in the new fixture, the tensile load was kept nearly constant.

### Procedure

Two tension specimens were pulled to failure for each material. Once the ultimate tensile load of the material was determined, the pure shear and combined load testing was begun. The specimens were loaded in tension, from 0 to 90% of the ultimate strength and then pulled to failure in three-point shear. The tensile load was recorded twice, once at the be-

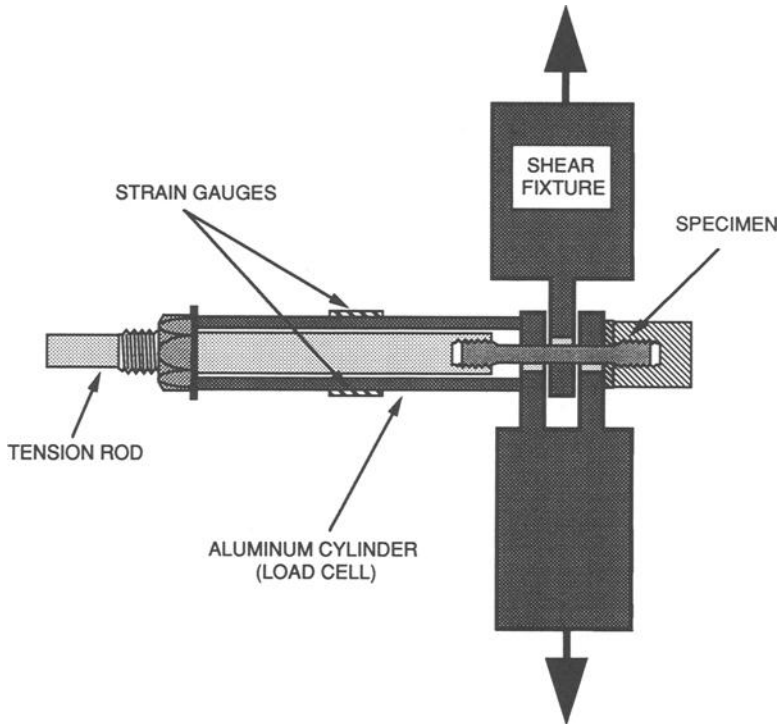


FIG. 5—Preliminary testing apparatus.

ginning of testing and once just prior to failure. The average of these two values was taken to be the tensile preload. In all cases, the stresses calculated were engineering stresses that ignore the reduction in cross-sectional area that occurs as a specimen is strained. It should be noted that the pure shear specimens were set up in a manner identical to those under a combined load, only the springs were not compressed. For both sets of specimens, two pure shear and fifteen combined-load specimens were tested.

The data from the preliminary version of the apparatus were obtained in an identical manner.

## Results

The relationships between the normalized tensile and shear stress ratios for the titanium and steel specimens are shown in Figs. 6 and 7. The curve shown in each figure is a plot of the squared stress-ratio interaction curve defined by Eq 3.

The figures show that the squared curve gives satisfactory predictions of the ultimate shear strength of the specimens. In the case of the titanium, the predicted values become conservative at higher values. Note that these values, where the tensile load is greater than 80% of the ultimate strength, are seldom seen in practice.

Figure 8 is a photograph of one of the sheared 17-4 PH specimens. It failed at a shear stress of 410 MPa (0.60 if normalized in the same manner as the data in the graph) and was subjected to a tensile stress of 875 MPa (0.82). In this specimen the left side yielded first. The arrows shown represent the shear forces present during testing. The angle of failure that

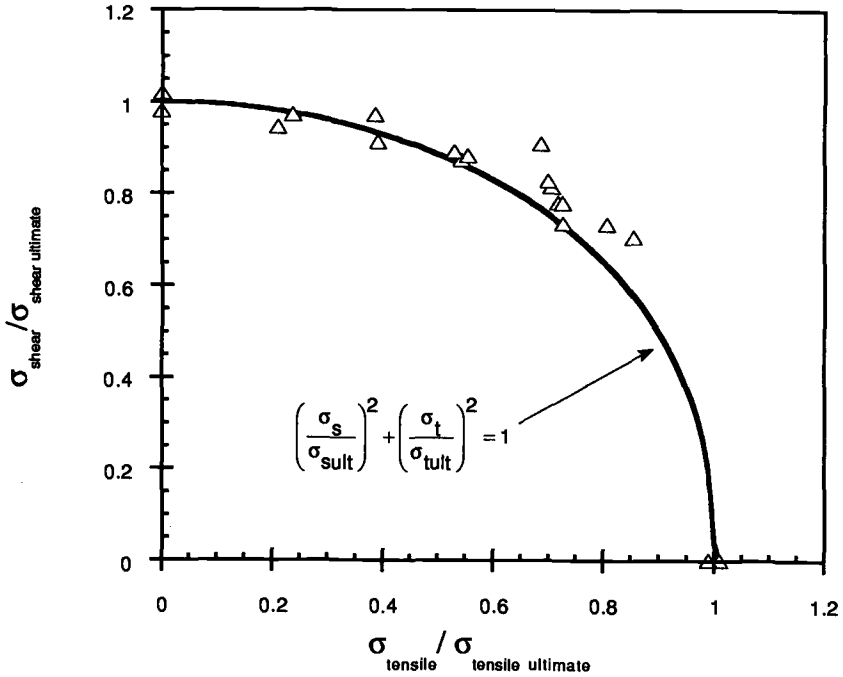


FIG. 6—Ultimate shear stress versus tensile stress for titanium.

appears on the left side of this specimen was present in every sheared specimen. It tended to be more acute the higher the tensile stress. Note that the center and right-hand sections were badly mauled in the second shearing, the removal process making them unfit for analysis.

All the data mentioned up to this point were derived from observations of shear failure under a constant tensile load. However, what follows are data from experiments with titanium where the tensile load was not constant, but instead dropped by as much as 40%. Because two measurements of the tensile load were taken, one at the beginning of the test and one just prior to failure, two sets of data were generated, one based on the initial tensile load and the other on the prefailure load. Plotting both of these values in the same manner as was done in the previous graph (as shown in Fig. 9) reveals two items.

First, the values derived from the prefailure data follow the theoretical equation very well. In fact, they appear very much like the constant load data mentioned earlier. This would seem to indicate that only the tensile stress present at the moment of shear failure is relevant. Second, this graph shows why many textbooks claim that the two quantities can be treated independently. In most testing situations, where the tensile load is applied by a fixture with a high effective spring rate, the tensile stress drops to insignificant levels as the specimen shears. Hence, its effect on the shear strength of the sample is very small. Only when the tensile stress is held constant as the specimen shears will the effect be truly noticeable. For this reason, the theoretical equation will only be applicable in a limited number of circumstance.

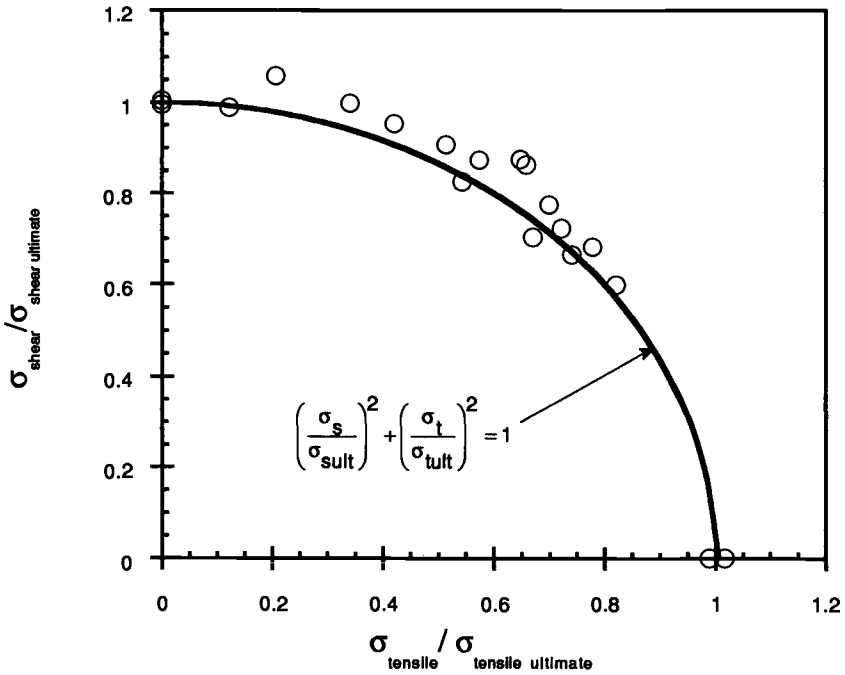


FIG. 7—Ultimate shear stress versus tensile stress for steel.

**Conclusions**

A general, qualitative relation between a constant tensile load and the ultimate shear strength of a fastener has been presented and correlated with three sets of experimental data.

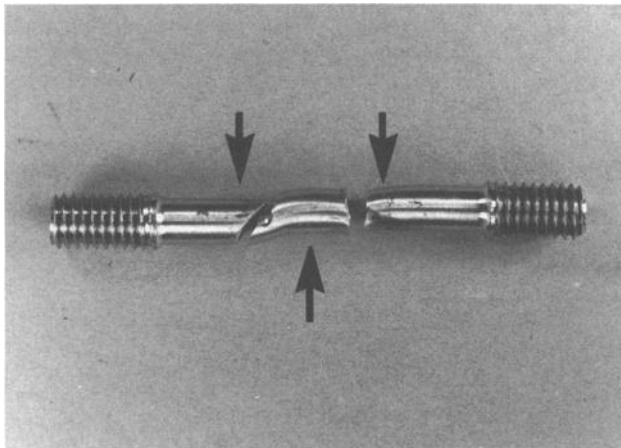


FIG. 8—Sheared specimen.

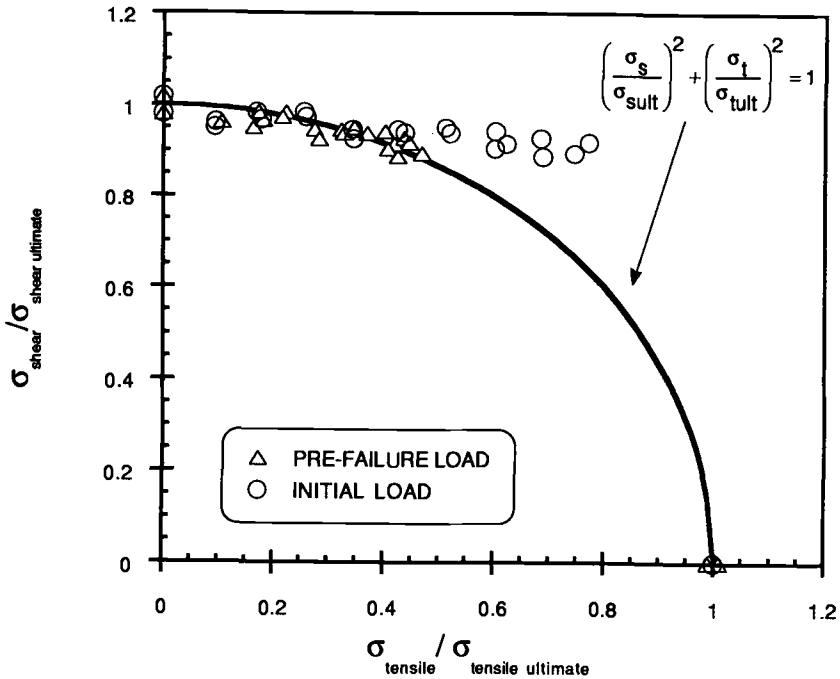


FIG. 9—Ultimate shear stress versus nonconstant tensile stress for titanium.

It has been demonstrated that Eq 3 gives conservative estimates of the ultimate strength. The data also revealed that in most fastener applications the tensile load will be greatly reduced as the material deforms in shear.

It should be noted that while Eq 3 provides good predictions, its range of application is limited. First and foremost, the condition of constant load is not often satisfied in practical situations: the tensile load will generally decrease as the specimen is sheared unless the effective spring rate of the system causing the tensile stress is very low. In addition, Eq 3 is only relevant to situations with high tensile loads. The reduction in the shear ultimate strength of the material will only be truly significant for tensile loads approaching 60% of the ultimate value of the material. For titanium, this means that a tensile stress of 68% of the yield stress will be necessary to reduce the shear ultimate by 20%. For 17-4 PH, the necessary tensile stress will be about the same, 66%. Loads this high are rarely seen in fasteners because of the possibility of failure in the threads.

*Acknowledgment*

This work was sponsored by the Department of the Air Force.

**References**

[1] Shanley, F. R. and Ryder, E. I., "Stress Ratios," *Aviation*, Vol. 36, Issue 36, June 1937, pp. 28-43, 66, 69, 70.  
 [2] Wallaert, J. J. and Fisher, J. W., "Shear Strength of High-Strength Bolts," *Journal of the Structural Division Proceedings of the American Society of Civil Engineers*, Vol. 91, No. ST3, June 1965.

# Pitch Diameter Measurement of Threaded Gages Using a Coordinate Measuring Machine

---

**REFERENCE:** Veale, R., Erber, E., and Borchardt, B., "Pitch Diameter Measurement of Threaded Gages Using a Coordinate Measuring Machine," *Structural Integrity of Fasteners, ASTM STP 1236*, P. M. Toor, Ed., American Society for Testing and Materials, Philadelphia, 1995, pp. 175–185.

**ABSTRACT:** The reference datum for a screw thread is the pitch diameter cylinder. Although a defined method within the United States for pitch diameter measurement exists, it does not follow worldwide procedures, and the complexity and uncertainties associated with this measurement often go unappreciated. Some of the problems associated with using a coordinate measuring machine (CMM) for measurements on both external and internal threads will be discussed.

**KEYWORDS:** CMMs, coordinate measuring machines, measurements, pitch diameter, screw threads, thread measurement, threaded fasteners, threads

## Nomenclature

*Pitch diameter*—The basic dimension for all the elements of a thread is the pitch diameter that serves as the datum from which measurements are made. The pitch diameter of a straight threaded gage is defined as the diameter of the cylinder passing through the points where the width of the material of the thread ridge and the width of the groove between the threads are equal.

*Pitch*—The pitch (sometimes incorrectly called lead) is the distance from one point on a thread to the corresponding point on the next adjacent thread, measured in an axial plane at the pitch line. Unfortunately, pitch has another meaning in thread terminology. For threads specified in the English system of units, pitch is used to indicate the number of threads per inch. A 10-32 bolt, which has 32 threads per inch, is often identified as having 32 pitch and has its pitch diameter measured using a 32-pitch set of thread wires. This confusion does not exist in the metric series where the pitch is specified in millimeters.

*Lead*—Lead is the amount of axial distance moved by the part in relation to the amount of angular rotation.

*Flank angle or half angle*—The flank angle is the angle between the thread flank and the perpendicular to the axis of the thread, measured in an axial plane. The angle is nominally 30° for most threads.

*Helix angle*—On a straight thread, the helix angle is the angle made by the helix of the thread with the thread axis at the pitch line.

---

<sup>1</sup> Metrologist, U.S. Department of Commerce, National Institute of Standards and Technology (NIST), Manufacturing Engineering Laboratory, Precision Engineering Division, Mid-Scale & Complex Form Metrology Group, Gaithersburg, MD 20899.

*Functional diameter*—Functional diameter is the diameter of the actual pitch diameter plus the effects of pitch errors, flank errors, out-of-roundness, taper, and variations in the helix angle.

## Introduction

More interest in thread measurement exists now than at any time in the past 35 years. The increased interest probably stems from three factors:

1. The passage of Public Law 101-592 (also known as the Fastener Safety Act).
2. The General Accounting Office report reaffirming the validity of the Air Force military specification (MIL-S-8879C) that requires single element inspection of critical fasteners.
3. The increased interest in quality ISO standards (especially the 9000 series), the creation of the European Economic Community, and the Metric Use Act. The Metric Use Act was part of the 1988 Omnibus Trade and Competitiveness Act, which was followed by an Executive Order instructing all government agencies to develop and implement a plan for converting to metric by the end of Fiscal Year 1992.

Although Mil-S-8879C refers only to the United Controlled Radius Root (UNJ) threads, a fundamental change is required in some of the measurement methods previously used. Mil-S-8879C has created a need for accurate measurement of master ring gages, which can be used to set variable gaging. This paper will discuss only one aspect of the measurement of threaded fasteners, specifically the measurement of the pitch diameter with emphasis on the use of a coordinate measuring machine (CMM).

## Three-Wire Pitch Diameter Method

The pitch diameter of external threads is commonly measured using wires. The wires are placed in the threaded grooves with two on one side and one on the opposite side as shown in Fig. 1. The diameter over the wires,  $M_w$ , is measured using an instrument having two flat parallel contacts. To simplify computation and minimize variations caused by errors in the pitch and half angle, a standard series of "best size" wires is used. A "best size" wire is one that touches the flank at or near the pitch diameter cylinder. For purposes of computing the "best wire size," it is assumed that the threads consist of annular grooves around the cylinder. Using this simplification, the "best size" can be computed from

$$\text{"Best size wire"} = 0.5p \sec(\alpha) \quad (1)$$

where  $\alpha$  is the half angle, and  $p$  is the thread pitch.

When measuring pitch diameter using wires, better repeatability is obtained if a force is used to compress the wires into the groove. The force tends to align the wires with the helix angle and minimizes the nonrepeatability associated with poor surface finish. The force to be used has been standardized and varies from 0.56 N (2 oz-force) for threads with pitch greater than 140 to 11.1 N (2.5 lb-force) for threads of 20 pitch and coarser. The elastic deformation at the point contact between the thread flank and the wire is not insignificant. For example, the elastic deformation for a 1/2-13 thread when measured using wires under the specified force of 11.1 N (2.5 lb-force) is 4  $\mu\text{m}$  (156  $\mu\text{in.}$ ).

It is the U.S. custom to calibrate the wires so that it is unnecessary to correct for deformation when measuring the pitch diameter. The wires are measured between a flat anvil and a steel cylinder. The force used in measuring the wires and the diameter of the cylinder are

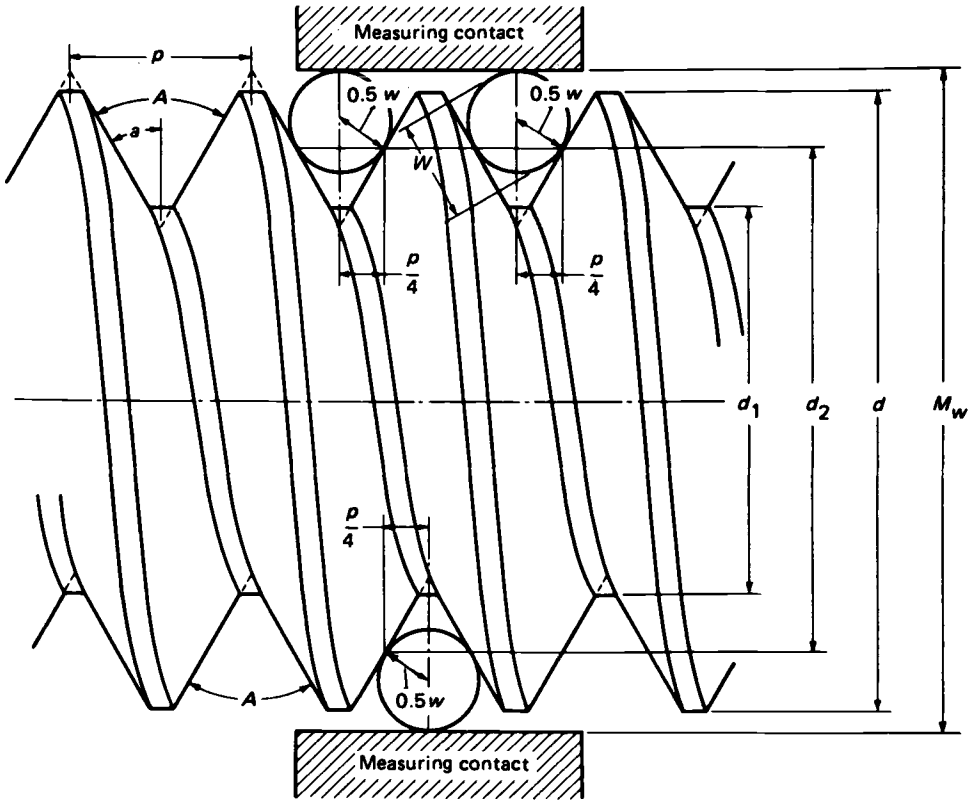


FIG. 1—A three-wire method of measuring pitch (thread groove) diameter of thread plug gages.

chosen so the elastic deformation in the measurement process is approximately the same as when the pitch diameter measurement is made.

The specifications for the wires as listed in the American National Standards Institute ASME B1.2 [1] document are in Table 1.

The wires are measured and sold with a “C” correction shown on the label. The “C” correction is the value to subtract from the measurement over the wires to get the pitch diameter on external threads. It is computed from the equation

$$C = w(1 + \operatorname{cosec}(\alpha)) - 0.5p \cotan(\alpha) \tag{2}$$

TABLE 1—Measuring conditions for thread wire calibrations.

Threads, in.	Measuring Force, ± 10%	Cylinder Diameter in inches, mm
20 or less	2.5 lb (11.1 N)	0.750 (19.05 mm)
Over 20 but not over 40	1 lb (4.4 N)	0.750 (19.05 mm)
Over 40 but not over 80	8 oz (2.2 N)	0.125 (3.175 mm)
Over 80 but not over 140	4 oz (1.1 N)	0.050 (1.27 mm)
Over 140	2 oz (0.56 N)	0.020 (0.508 mm)

where  $w$  is the mean diameter of the wires, and  $\alpha$  is the thread half angle. It is derived from Jeffcott's simplified pitch diameter formula [2]

$$d_2 = M_w + 0.5p \cotan (\alpha) - w(1 + \operatorname{cosec} (\alpha)) \tag{3}$$

The measured pitch diameter,  $d_2$ , is the measurement over the wires minus the "C" correction.

The standard practice in the United States is to ignore the effect of the helix angle of a pitch diameter measurement unless it exceeds  $3.8 \mu\text{m}$  (0.000 15 in.).

**Coordinate Measuring Machines (CMMs)**

The same principle is used when measuring pitch diameter with a CMM. A stylus ball is chosen that is near the "best wire size"—in this case "best ball size." Jeffcott [2] and Tomlinson [3] have shown that measurements made using either balls or wires give the same results.

A length measurement made with a CMM having an infinitely stiff probe shaft gives the distance between the centers of the stylus ball. The diameter of a cylinder, for example, would be too large by the diameter of the ball. To get the correct diameter of the cylinder, subtract the ball diameter from the CMM measurement.

But CMM styli are not infinitely rigid; the shaft holding the stylus ball bends when a part is contacted. The amount of the bending depends on the length, shape, and material of the shaft holding the ball and the force used to measure the part. As shown in Fig. 2, the amount of the bending must be added to the machine reading (after the ball diameter has been subtracted) to get the correct answer.

Ordinarily, the bending is not calculated. The procedure for most CMMs is to measure a known standard, usually a master ball, to obtain an effective stylus ball diameter. For the type of probe used for the measurements listed in this paper, the effective diameter is the real ball diameter minus the amount of bending. On touch-trigger-type probes, the difference may also include probe pretravel.

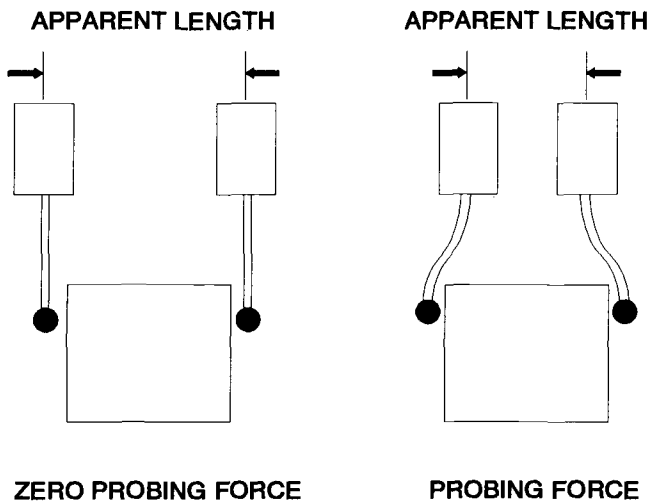


FIG. 2—Probe shaft bending.

Assuming the master is of the same material as the part being measured, any elastic deformation at the point of contact can be ignored. Even if the parts are not the same, e.g., a carbide master and a steel part, the deformation correction for a 2-mm carbide ball when using a force of 1 N (which is larger than most machines would ever use) would only be 0.08 μm.

For the highest accuracy, the stylus ball should be calibrated on a standard similar to the part to be measured. Because most probes exhibit some form of lobing (variation in pre-travel), the measurements should be made at the same positions on the part as on the master. This is seldom practical to do, however, and the common practice is to calibrate the effective diameter of the stylus ball by measuring a master ball. It should be noted that even though the stylus ball is calibrated by measuring a master ball, the effective diameter can be used for both external and internal measurements. The correction is as follows

$$\begin{aligned} \text{external} & \quad (- \text{ stylus ball diameter} + \text{ bending}) \\ \text{internal} & \quad (+ \text{ stylus ball diameter} - \text{ bending}) \end{aligned}$$

The absolute value of the terms between the parentheses is the same for both internal and external measurements if the bending of the shaft is not direction dependent (which is safe in all cases except perhaps specially designed styli), and no errors are introduced due to lobing of the probe.

The CMM used to measure the gages described in this paper has a self-centering mode which allows the stylus ball to seat itself in the thread groove before triggering. This is similar to the unrestrained wires seating themselves when using the standard three-wire method. The axis of the gage should be located by measuring several points on the major diameter (minor diameter for an internal thread). Using this axis, collect data points near the pitch diameter cylinder along and around the gage. The CMM software computes the location of the axis and diameter of the cylinder that passes through the collected data points. As in the case of measuring a plain cylinder, correct for the stylus shaft bending. It is easiest to calculate this correction by assuming the measurement of a plain cylinder for an external thread and a plain ring for an internal thread. Take the case of the external thread first.

Calibrate the stylus ball and tell the CMM it is measuring a cylinder. Any shaft bending can be ignored because the machine software automatically corrects for both the shaft bending and the stylus ball diameter. This correction is done by subtracting the effective diameter from the measured cylinder, thus giving the diameter of the cylinder at the bottom of the ball. (The measurement at the bottom of the ball,  $M_b$ , for a thread measurement is defined as the distance between the points on the ball closest to the thread axis, as shown in Fig. 1). Add twice the ball diameter to this value to obtain a measurement similar the traditional three-wire method—the measurement over the wires, or in this case, the measurement over the balls.

But the diameter added to the measurement must be the actual stylus ball diameter, not the effective diameter determined by measuring the master ball. This is one of the few cases where the true diameter of the stylus ball must be known in a CMM measurement.

Remembering that the pitch diameter is determined by subtracting the “C” correction

$$C = w(1 + \operatorname{cosec}(\alpha)) - 0.5p \cotan(\alpha) \tag{4}$$

from the measurement over the wires, get the pitch diameter in this case by first adding  $2w$  and then subtracting the “C” correction. For  $30^\circ$  threads  $(1 + \operatorname{cosec} \alpha) = 3$ , to correct from the bottom of the ball,  $M_b$ , to the pitch line cylinder add

$$2w - [3w - 0.5p \cotan(\alpha)] \quad (5)$$

The equation for the pitch diameter,  $d_2$ , then becomes

$$d_2 = M_B - w + 0.5p \cotan(\alpha) \quad (6)$$

where  $w$  in this equation is the actual diameter of the ball.

An alternate way to achieve the same results is to have the coordinate measuring machine do a least squares fit of a cylinder through the measured data points. This measurement gives the diameter of a cylinder passing very nearly through the stylus ball centers at the recorded measured positions. To get the pitch diameter cylinder, add the stylus shaft deflection and subtract an amount to correct for the fact that the pitch cylinder is not the same as the cylinder passing through the center of the stylus ball positions. If  $\delta$  is twice the deflection, which is the true diameter of the ball minus the measured or effective diameter,  $w_{\text{eff}}$ , the pitch diameter,  $d_2$ , becomes

$$d_2 = M_C + 0.5p \cotan(\alpha) - 2w + \delta \quad (7)$$

$$d_2 = M_C + 0.5p \cotan(\alpha) - 2w + w - w_{\text{eff}} \quad (8)$$

$$d_2 = M_C + 0.5p \cotan(\alpha) - w - w_{\text{eff}} \quad (9)$$

$M_C$  is defined as the position at the center of the stylus ball (see Fig. 1).

### External Thread Measurement Results

NIST has been measuring the pitch diameter of 4, 5, and 8-pitch American Petroleum Institute (API) gages on a CMM for more than ten years with good results. To test the procedure with smaller gages, 15 American Petroleum Institute (API) 10-pitch sucker rod plug gages, ranging from 15 to 30 mm in diameter, were measured. The results are shown in Table 2.

The results were disappointing. The lack of agreement is more significant than random error because the differences were all positive with a mean difference of 3.1  $\mu\text{m}$ .

Two methods to measure pitch diameter with a CMM were used. One technique uses a double-ended gage or four styli at right angles to each other, all in the  $xy$  plane. Separate measurements of the test ball determine effective diameter and the relative location of each stylus ball (see Fig. 3).

NIST predominantly uses another method involving only one stylus with the CMM interfaced to a rotary table that holds the gage near the center of the table. This method was used to measure the sucker rod gages. The technique consists of determining the center of rotation of the rotary table by measuring the test ball at the 0, 90, 180, and 270° positions. Points on the major diameter of the gage (minor diameter for internal threads) are then measured to establish the part coordinate system. If the part coordinate system is not aligned with the gage, diameter measurements can be wrong because the length of the measured line will be a chord, not a diameter. The pitch diameter is then measured using the self-centering mode by moving the stylus ball into the thread groove. The table is rotated with readings taken at each 90° position. These points are either used directly, or the CMM software fits a cylinder to the measured points (see Fig. 4).

Next, a 15.24071-mm master cylinder with a diameter known to an uncertainty of 0.1  $\mu\text{m}$  was measured. The purpose of this measurement was to determine the effective stylus ball

TABLE 2—External threads.

Gage	CMM	Three-Wire Value	Difference
1-B4	33.0808	33.0774	3.4
1-P3	33.5018	33.4975	4.3
7/8-P3	28.7304	28.7254	5.0
7/8-B4	28.3322	28.3289	3.3
5/8-B2	22.1813	22.1790	2.3
5/8-P1	22.1290	22.1259	3.1
3/4-B2	25.3553	25.3548	0.5
3/4-P1	25.3040	25.3009	3.1
7/8-B2	28.5288	28.5265	2.3
7/8-P1	28.4886	28.4737	4.9
1-B2	33.2930	33.2892	3.8
1-1/8-B2	38.0566	38.0522	4.4
1-1/8-P1	38.0009	37.9979	3.0
1-P7	33.2356	33.2354	0.2
1-P1	33.2362	33.2336	2.6

NOTE: Comparison of CMM and three-wire pitch diameter measurements on external thread gages. Values are in millimetres for the pitch diameter and micrometres for the differences.

diameter by a method other than measuring a test ball. The values obtained by the two methods differed by  $2.5 \mu\text{m}$ .

The most reasonable explanation is that in the measurement of the master cylinder on the rotary table, the probe force is always directed in the axial direction of the probe stylus shaft. Therefore, the deflection which occurs when the ball is measured is not the same as when the master cylinder or the threaded gages are measured. This means  $W_{\text{eff}}$  in the previous equation was too small. The result after applying this correction agrees better with the expected values (see Table 3). The lesson learned is always to calibrate the probe as closely as possible in the same manner as the measurements are to be made.

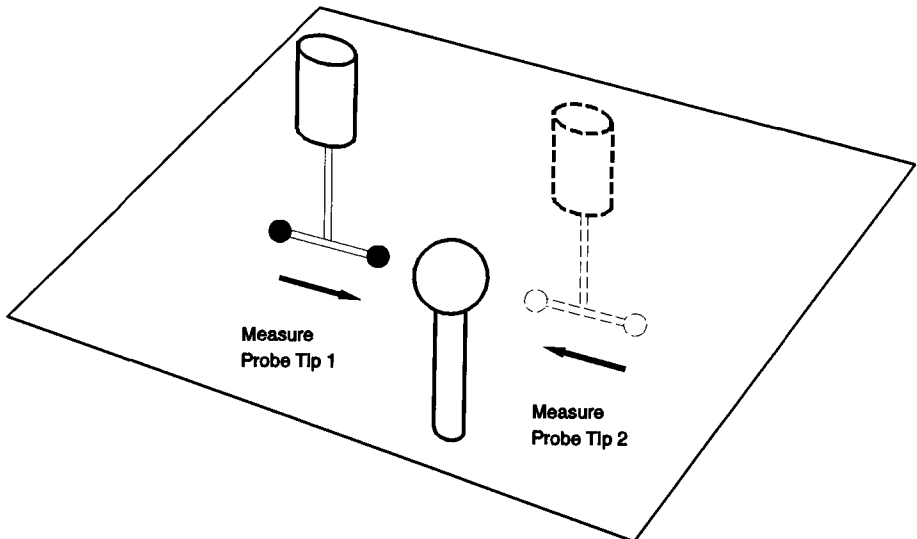


FIG. 3—Calibration of probe tips.

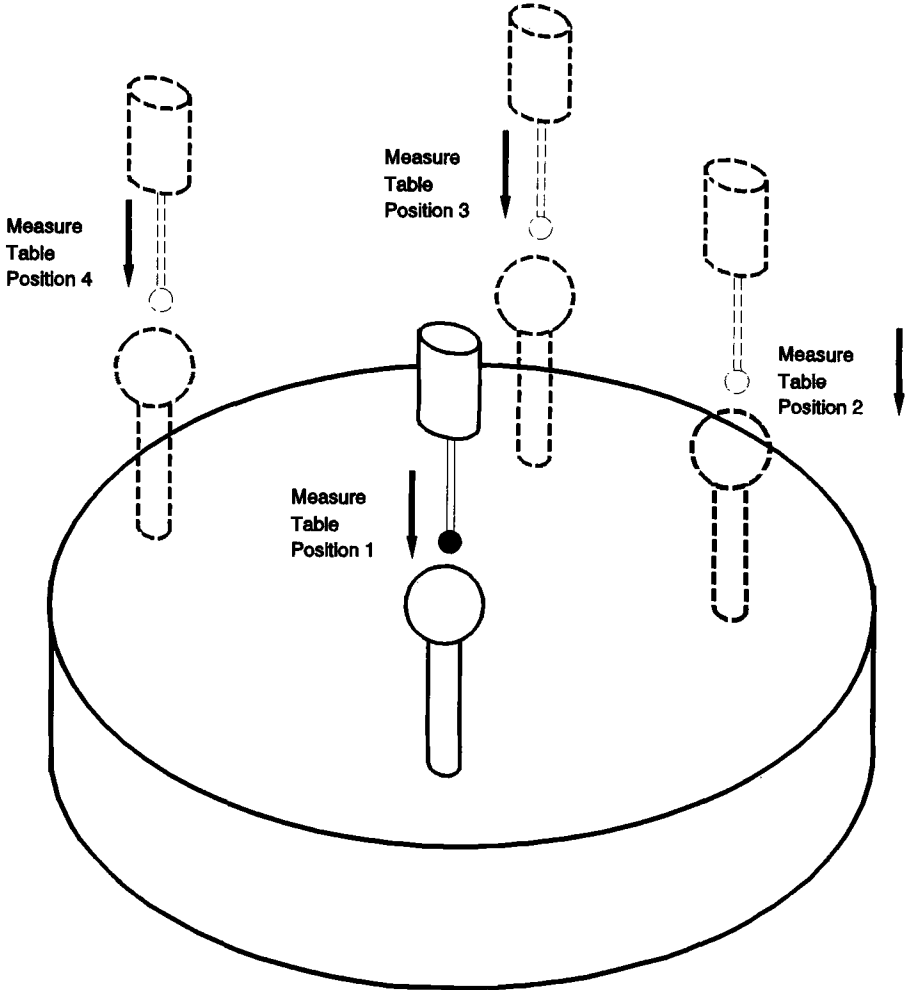


FIG. 4—Calibration of rotary table.

The pitch diameters in Tables 2 and 3 were calculated using Eq 7. To illustrate, the 1-B4 plug gage, having a nominal pitch diameter of 33.0759 mm, was measured with a ball having a true diameter of 1.499 74 mm. The effective diameter as determined by measuring a 25-mm ball on the coordinate measuring machine was 1.496 94 mm, and the effective diameter as determined by measuring the master cylinder was 1.499 51, thus giving a deflection or  $\delta$  of 2.8  $\mu\text{m}$  and 0.2  $\mu\text{m}$ , respectively. The diameter of the measured cylinder  $M_C$  was 33.8777 mm. The calculated pitch diameter as shown in Table 3 was

$$d_2 = 33.877\ 73 + 2.199\ 69 - 2.999\ 49 + 0.000\ 23 \tag{10}$$

TABLE 3—External threads.

Gage	CMM	Three-Wire Value	Difference
1-B4	33.0782	33.0774	0.8
1-P3	33.4993	33.4975	1.8
7/8-P3	28.7279	28.7254	2.5
7/8-B4	28.3296	28.3289	0.7
5/8-B2	22.1788	22.1790	-0.2
5/8-P1	22.1264	22.1259	0.5
3/4-B2	25.3528	25.3548	-2.0
3/4-P1	25.3014	25.3009	0.5
7/8-B2	28.5262	28.5265	-0.3
7/8-P1	28.4724	28.4737	-1.3
1-B2	33.2905	33.2892	1.3
1-1/8-B2	38.0540	38.0522	1.8
1-1/8-P1	37.9984	37.9979	0.5
1-P7	33.2331	33.2354	-2.3
1-P1	33.2336	33.2336	0.0

NOTE: Comparison of CMM and three-wire pitch diameter measurements on external thread gages applying stylus correction. Values are in millimetres for the pitch diameter and micrometres for the differences.

or

$$d_2 = 33.0782 \text{ mm} \quad (11)$$

The mean value was 0.3  $\mu\text{m}$  larger than the value obtained using the three-wire method.

Soon after, in an unrelated project, the pitch diameters of 18½-13 UNC-2A setting plug gages were measured by both the three-wire method and the CMM. The probe was calibrated by measuring a master 12.7-mm cylinder located on the rotary table rather than using the CMM manufacturer's recommended method of measuring a master ball. The agreement between the two results was within the uncertainty limits of the two methods. It took less than half the time to measure the gages on the CMM rather than using the more traditional method. In addition to the time saved, the CMM data also gave the deviations from nominal pitch and some information on variation in the helix angle. The pitch diameter values are shown in Table 4.

### Internal Thread Measurement Results

Good methods already exist for measuring the pitch diameter of plug gages. While using the CMM for external thread measurement is advantageous, the primary intent of the work was to find a fast and accurate method of qualifying threaded ring gages.

The procedure for measuring a ring on the CMM is similar to the procedure for measuring a plug gage. If the computer measures an internal bore, the equation used to obtain the pitch diameter from this number is

$$d_2 = M_B + w - 0.5p \cotan(\alpha) \quad (12)$$

$M_B$  is the diameter of the bore reported by the computer that has subtracted the effective stylus ball diameter from the machine reading.

If the alternate method is used where the machine gives us the diameter of the cylinder at the center of the stylus ball, the equation for the pitch diameter becomes

TABLE 4—*External threads.*

Gage	CMM	Three-Wire Value	Difference
201G	11.3922	11.3906	1.6
202G	11.3888	11.3876	1.2
203G	11.3911	11.3904	0.7
204G	11.3878	11.3883	-0.5
205G	11.3909	11.3909	0
206G	11.3922	11.3901	2.1
207G	11.3868	11.3886	-1.8
208G	11.3878	11.3901	-2.3
209G	11.3904	11.3916	-1.2
201N	11.2735	11.2712	2.3
202N	11.2692	11.2667	2.5
203N	11.2725	11.2712	1.3
204N	11.2674	11.2667	0.7
205N	11.2679	11.2677	0.2
206N	11.2677	11.2667	1.0
207N	11.2641	11.2646	-0.5
208N	11.2682	11.2685	-0.3
209N	11.2641	11.2641	0

NOTE: Comparison of CMM and three-wire pitch diameter measurements on 18½-13 UNC-2A thread gages. Values are in millimetres for the pitch diameter and micrometres for the differences.

$$d_2 = M_C = 0.5p \cotan(\alpha) + w + w_{\text{eff}} \quad (13)$$

To test the reliability of this technique, nine 1/2-13 "W" tolerance master ring gages were measured. Single point measurements using the rotary table were made. As a check, the rings were also measured on a SIP 305.<sup>2</sup> Table 5 shows the results. When this comparison was made, the CMM gave nonrepeatable and inconsistent results due to excessive flexure occurring in the smaller probe stylus shafts. As explained earlier, in interfacing the rotary table to the CMM coordinate system, the procedure requires finding the center of the master

TABLE 5—*Internal threads.*

Gage	SIP	CMM Value	Difference
102	11.4642	11.4653	1.1
103	11.4283	11.4276	-0.7
104	11.4300	11.4316	1.6
105	11.4497	11.4486	-1.1
106	11.4346	11.4324	-2.2
107	11.4244	11.4236	-0.8
109	11.4322	11.4325	-0.3
110	11.4356	11.4351	-0.5
111	11.4297	11.4293	-0.4

NOTE: Comparison of Calibrated and CMM pitch diameter measurements on 9½-13 UNC-2A thread gages. Values are in millimetres for the pitch diameter and micrometres for the differences.

<sup>2</sup> Certain commercial equipment, instruments, or materials are identified in the paper to adequately specify the experimental procedure. In no case does such identification imply recommendation or endorsement by NIST, nor does it imply that the material is necessarily the best available for the purpose.

ball at four different positions. It is possible to touch only about half of the surface of the ball in locating its center. Shaft bending gives a systematically wrong center position of the ball [4]. Because the stylus lies in the  $xy$  plane, the bending causes an incorrect  $xy$  center position of the rotary table. This causes an error in measurements made on a part when using the rotary table if the rotary table is aligned with this procedure. The solution is to realign the rotary table carefully using a two-headed probe. Each position of the ball on the rotary table is measured with both ends of the probe to avoid a systematic shift of the ball center. To obtain repeatable measurements, the alignment of the rotary table is critical. When the time between alignment and measurement is too long, the thermal drift of the machine moves the apparent center of rotation and invalidates the measurements. When the measurements are made promptly after alignment and the alignment is done using the two-headed probe, the results are quite good. Table 5 shows the results obtained. The average difference between the SIP 305 and the CMM measurements is  $0.8 \mu\text{m}$ , with a worst case of  $2.2 \mu\text{m}$ . No systematic bias exists between the two sets of measurements.

### Conclusion

It is shown that a CMM can be used for high-accuracy measurement of threads where there is negligible bending of the shaft holding the stylus ball. For smaller sizes where there is shaft flexure, it will be necessary to use a "star probe." It is believed that a CMM will give an accuracy comparable to some of the best available existing equipment.

A more important result of the work is to show that pitch diameter on small internal threads can be measured using either a CMM or other equipment to an accuracy that will satisfy the majority of users.

### Acknowledgments

Partial funding for the work in this paper was provided by the Navy Manufacturing Technology Program through the NIST Automated Manufacturing Research Center (AMRF). The authors thank Janet L. Land for editing advice.

### References

- [1] ANSI/AMSE B1.2: Gages and Gaging for United Screw Threads, American Society for Mechanical Engineers, New York, 1983.
- [2] Jeffcott, H. H., "Notes on Screw Threads," *Proceedings of the Institute of Mechanical Engineers*, December 1907, pp. 1067–1108.
- [3] Tomlinson, G. A., "Correction for Rake in Screw Thread Measurement," National Physical Laboratory Notes, December 1927.
- [4] Phillips, S. D., Borchardt, B., Doiron, T., and Henry, J., "Static and Dynamic Properties of Free Standing Ball Bars," *Proceedings*, Sixth Annual Conference of the ASPE, 1991, pp. 33–36.

# Summary

---

The papers in this publication were divided into four major sections:

1. Fatigue in Fasteners.
2. Failure Evaluation and Criteria.
3. Fracture Mechanics in Fasteners.
4. Structural Integrity Criteria for Fasteners.

## **Fatigue in Fasteners**

Fatigue evaluation is generally used to predict crack initiation under complex service load histories for a complex structural component sometimes under an aggressive environment. The most important consideration is to ensure the accuracy of cyclic stresses or strains at a local point of interest. This is achieved by finite element analyses (two or three dimensional). Engineering structural components have discontinuities (in the form of notches, holes, and grooves, etc.) that are the sites of high stress concentration.

Allaei presented an effect of nonuniformities in fasteners on localized vibration and fatigue. The work discussed is ongoing research and development of an efficient and effective mathematical model that will be capable of incorporating the dynamic characteristics of fasteners and their interface with the host structure. Endo et al. presented test methods for turbine blade fasteners to verify the use of peak stress calculated by three-dimensional elastic finite element model analysis. Skochko and Herman reviewed the factors that affect fatigue strength of low-alloy steel fasteners. The paper discussed the influence of machining and thread rolling on fatigue strength and provides design guidelines.

## **Failure Evaluation and Criteria**

Johnson and Davis presented the United States Nuclear Regulatory Commission's approach to fastener integrity in the nuclear industry. Failure criteria and limiting states for cracked bolts were discussed by Kagan. A step-by-step discussion was given on design consideration, material selection, load selection, and fatigue prediction and crack propagation procedure. Nathisan and Porr presented the effect of grain boundary carbon on the hydrogen-assisted intergranular failure of nickel-copper Alloy K-100 fastener materials.

## **Fracture Mechanics in Fasteners**

Zhao and Atluri presented the stress intensity factor solutions for surface and corner-cracked fastener holes. They employ a three-dimensional weight function method. Examples of the method were given for remote tension, biaxial tension, wedge loading in the hole, and simulated pin loading. In addition, the effect of the residual stress field following cold expansion was considered.

Cipolla presented the nondimensional stress intensity factor solution for a straight-fronted crack using an influence function. Several analytical approximations are examined in the development of the weight function. Cipolla concluded that the effect of bolt size and thread

form are only important when the crack size is small and suggested that this effect is limited to crack depth within 2% of the net section. He also suggested that the contribution of thread to elevate  $K_1$  diminishes for cracks extending beyond 20% of the minor diameter. A companion paper by A. F. Liu presented a state-of-the-art review of the existing stress intensity factors applicable to tension bolts. Using the analytical and experimental data sets from the literature, a stress intensity equation is suggested as an engineering approximation. Liu also applied this equation to the experimental results of the ASTM task group E08.04.07 round robin evaluation of the three grooved round bar crack growth results. Liu concluded that in these tests the crack shape aspect ratio is constant ( $a/b = 0.65$ ) for  $a/d \leq 0.5$ . Beyond that, the crack shape is assumed to be a straight crack front.

### Structural Integrity Criteria for Fasteners

Chang and Du presented a laser speckle method for characterizing fatigue crack initiation in conditions of high-cycle fatigue. The authors claim this procedure is noncontact, non-destructive, and remote sensing. The fatigue damage information is contained in the defraction pattern, which reflects the surface roughness change as a result of fatigue-induced slip bands. The relation between the stress amplitude and the number of cycles to crack initiation is described by the authors.

Henkener et al. presented fracture control methodology for threaded fasteners in the space program. The fracture control plan classifies the fasteners as either fracture control or non-fracture critical. The authors stated that fracture control is implemented by nondestructive inspection, followed by crack growth evaluation. It is acknowledged that application of the nondestructive evaluation (NDE) technique to fastener threads is difficult to achieve. Therefore, a fabrication of NDE standards for threads is being developed, and the probability of detection using the maximum likelihood technique is recommended.

Olsen presented a general, quantitative relation between a constant tensile load and the ultimate shear strength of a fastener. He also experimentally observed that the tensile load in the fastener is greatly reduced as the material deforms in shear. The reduction in shear strength is only significant for tensile loads approaching 60% of the ultimate strength of the material. Veale et al. presented a criterion for pitch measurements of threaded gages using a coordinate measuring machine (CMM). The authors stated that, although a defined method within the United States for pitch measurement exists, it does not follow worldwide procedures. The application of CMM for measurements on both external and internal threads is discussed. This technique is still in the development stage and needs additional work.

*Pir M. Toor*

Bettis Laboratory  
West Mifflin, PA 15122  
Task Group Chairman and Editor

ISBN 0-8031-2017-6